Vrije Universiteit Brussel

Faculty of Engineering Sciences
Department Electronics and Informatics

Processing of Geostationary Satellite Observations for Earth Radiation Budget Studies

PhD. thesis submitted in partial fulfillment of the requirements for the degree of Doctor in Engineering Sciences

Nicolas Clerbaux

Promotor: Prof. Steven Dewitte (KMI)
Prof. Jan Cornelis (VUB)

25 November 2008

In collaboration with the
Royal Meteorological Institute of Belgium,
Department of the Observations,
Division of Remote Sensing from Space

RMI

Acknowledgements

First of all, let me show my gratitude to my supervisor Steven Dewitte, and more recently also to Jan Cornelis, for their valuable opinions and recommendations. Many thanks also to all my GERB colleagues working at the RMIB, the Imperial College and the Environmental Systems Science Centre (ESSC) for their great support. Needless to say I am most grateful to Jacqui Russell for the critical review of most of the works compiled in this document. I am also thankful to all my colleagues from the GERB and the CERES Science Teams, from the Climate Monitoring SAF, and from EUMETSAT for their close collaboration. I feel particularly grateful both to the CM–SAF project team who gave me time to work out this thesis and to Yves Govaerts at EUMETSAT for the support given concerning the MVIRI and SEVIRI calibrations.

Abstract

Accurate measurements are needed to improve our understanding of the Earth Radiation Budget (ERB). Despite continuous efforts to improve the observation systems, models remain necessary to convert the raw measurements in a form usable by the scientific community. These models concern the spectral, the angular, the spatial, and the temporal properties of the radiation leaving the Earth at the top of the atmosphere. The geostationary orbit allows to resolve the full diurnal cycle and consequently there is no need for any temporal modeling. This is the main motivation to include the Geostationary Earth Radiation Budget (GERB) instrument on the Meteosat Second Generation satellites. However, using the geostationary orbit the spectral, angular, and spatial models are still needed. In this work, we address these modelings in the case of the GERB project.

Assumptions about the spectral signature of the observed scene are necessary to compensate the telescope and detector spectral responses. This is especially important for geostationary observations as the distance implies the use of a powerful telescope. We describe the method used to unfilter the GERB shortwave (SW) and longwave (LW) measurements. Another spectral modeling problem that we address is the narrowband–to–broadband techniques for the SEVIRI imager. These broadband estimates are useful to model spatially the repartition of the energy within the large GERB footprints. This allows to compensate for the point spread function of the instrument, to enhance the spatial resolution, and to produce the "GERB–like" products. Finally, angular modeling of the radiation field is needed to convert the directional radiation measurement in hemispheric flux. This step is very important for geostationary observation as a point of the Earth is always observed from the same direction.

We discuss the rationale of what is implemented for the Edition-1 GERB data processing. These modeling steps should be done and validated carefully. Indeed, any model error is likely to introduce biases in the GERB products. The errors that these models introduce in the final GERB products are theoretically quantified using radiative transfer computations. Further high–level validations are given by comparison of the GERB and CERES radiances and fluxes for the SW and LW radiations. Recommendations for the future Edition–2 of the GERB processing are made in the present document and a summary is given in the conclusions.

Contents

Chapter 1

Introduction

Context

In 1958, the Royal Meteorological Institute of Belgium (RMIB) established a small team to study the components of the Earth Radiation Budget (ERB). At that time, it was believed that a better understanding of the ERB could improve the accuracy of the weather prediction, the 'core business' of a meteorological institute like the RMIB. Fifty years later, this decision proves premonitory although the main implications of the ERB studies are more in the field of climatology than in operational meteorology. The team, led by Dr. Dominique Crommelynck, started its works with the measurement of the solar irradiance and its variation. Accurate measurements were made possible by the design and operation of space instruments. In parallel, routine spaceborne observation of the Earth started in the 70'ies allowing the measurement of the energy leaving the Earth by reflection and thermal emission, the 2 other components of the budget (Figure 2.1). Since 1992, the team has been co–investigator for a new space instrument mission, the Geostationary Earth Radiation Budget (GERB, Harries *et al.*, 2005). The GERB instrument is designed to perform accurate broadband (BB) measurement of the reflected solar radiation and the emitted thermal radiation from the Meteosat Second Generation (MSG, Schmetz *et al.*, 2002) satellites on geostationary orbits. In this framework, the RMIB is responsible for a large part of the ground segment. For this purpose, the "RMIB GERB team" has been set up in 1997 under the leadership of Steven Dewitte who made a preliminary study of the GERB challenges during his PhD thesis (Dewitte, 1997). Later, the responsibilities of the team have been broadened through its participation to the EUMETSAT Satellite Application Facility (SAF) on Climate Monitoring (CM-SAF, Woick *et al.*, 2002). This PhD work outlines my contribution to the GERB and CM–SAF projects.

Problems statement and objectives of the thesis

Measurement of the Earth radiation budget at the top of the atmosphere is performed with spaceborne broadband radiometers. Requirements from the user community (e.g. climate modelers) concern the absolute calibration and the stability of the measurements (Ohring *et al.*, 2005) as well as the spatial, temporal, spectral and angular sampling of the radiation field leaving the Earth (Rieland & Raschke, 1991). An excellent temporal sampling is possible with the geostationary orbit but, unfortunately, this orbit is not very efficient in terms of spatial, spectral, and angular sampling. In this context, our PhD work focuses on different objectives.

During this PhD thesis we have defined, implemented and validated what was considered the best–suited algorithms for the Edition 1 of the GERB data processing. At this level our personal contribution covers the algorithms that are applied to the narrowband (NB) measurements of the Spinning Enhanced Visible and InfraRed Imager (SEVIRI, Schmetz *et al.*, 2002), the multispectral imager on the MSG satellites. The GERB unfiltering for the shortwave (SW) and longwave (LW) channels, the GERB scene identification and the GERB radiance–to–flux conversions are processing steps based on the SEVIRI NB measurements.

To this end, we have investigated some specific problems introduced by the geostationary orbit. At this level, our personal contribution mainly concerns the detection of biases introduced during the radiance–to–flux conversions. For example, we have quantified the error that is introduced on the GERB LW flux by using models which are symmetrical in azimuth angle.

The work also addresses some specific problems introduced by the GERB instrument design. Here our personal contribution mainly concerns the unfiltering of the GERB SW and LW measurements, and the pixel–to–pixel variability between the 256 GERB detector elements.

A large part of the work involves the estimation of the broadband unfiltered radiance from the NB measurements of SEVIRI. This is what we call the "GERB–like" product. The GERB–like estimate plays a major role within the GERB and CM–SAF projects. It is used to tune the GERB footprint geolocation by matching. It allows to enhance the spatial resolution of the GERB products and to correct for the GERB Point Spread Function (PSF). It allows performing more accurate unfiltering and angular conversions at a higher spatial resolution than the large GERB footprint. The GERB–like is also used to fill gaps in the GERB database, for example to build monthly means for the Climate Monitoring SAF (Caprion *et al.*, 2005). The possibility to estimate GERB–like data from the long dataset of Meteosat first generation observations is also addressed. Empirical GERB–like can be derived for the overlap period (2004–2006) between the 2 generations of Meteosat satellites. In the future, these GERB–like products are foreseen to be used to extend back the CM–SAF Earth radiation budget databases in the past, back to 1982.

Finally, the accuracies of the GERB unfiltered radiances and fluxes are analyzed at regional scale by comparison with the Clouds and Earth's Radiant Energy System (CERES, Wielicki *et al.*, 1996) data. These validation activities are done on the Edition 1 data and result in recommendations for a future Edition 2 processing of the database.

Outline of the thesis

In accordance to this introduction, the manuscript is structured as follows.

Chapter 2 states the relevant **scientific background** for this work. Basis of the Earth radiation budget science (Section 2.1) and previous ERB missions like ERBE, ScaRaB and CERES are presented (Section 2.2). Then, different aspects of the processing of ERB data are addressed: the calibration and LW estimation (Section 2.3), the unfiltering (Section 2.4), the radiance–to–flux conversion (Section 2.5), the scene identification (Section 2.6), the spatial and temporal processings (Section 2.7). Finally, Section 2.8 gives the scientific background for the narrowband–to–broadband technique.

Chapter 3 describes the main **instruments and data used** in this study: the GERB and the SEVIRI instruments on MSG, the MVIRI imager of the Meteosat first generation satellites, and the CERES instruments on the Tropical Rainfall Measurement Mission (TRMM), Terra and Aqua satellites.

Chapter 4 is dedicated to the **spectral modeling of the reflected solar radiation** field. Section 4.1 introduces the problems we face that require to model the radiation in its spectral aspect. The factors that affect the spectrum are discussed in Section 4.2. Based on that analysis, radiative transfer computations are done to simulate spectra for various scene types at different viewing and solar geometries (Section 4.3). These simulations are then used to address the spectral modeling problems in Sections 4.4 to 4.9. Section 4.4 presents the direct unfiltering of the GERB SW measurement. The operational unfiltering is described in Section 4.5 with comprehensive theoretical validations. Section 4.6 reports on further validations by comparison of the GERB and CERES unfiltered SW radiances. The effect of the variability of the individual detector spectral response is discussed in Section 4.7. Shortwave narrowband–to–broadband conversions are finally analyzed for the SEVIRI and the MVIRI instruments, respectively in Sections 4.8 and 4.9. Section 4.10 summarizes this first part of the work dedicated to the spectral modeling of the SW radiation.

Chapter 5 treats the **spectral modeling of the emitted thermal radiation** field. This chapter is organized using the same structure as for the solar radiation, respectively: problem statement (Section 5.1), study of the factors affecting the TOA spectrum in the infrared (Section 5.2), radiative transfer computations (Section 5.3), direct unfiltering of the GERB LW measurements (Section 5.4), operational unfiltering and theoretical validation (Section 5.5), GERB/CERES LW radiances comparison (Section 5.6), pixel–to–pixel variability (Section 5.7), NB–to–BB for the SEVIRI (Section 5.8) and for MVIRI (5.9), summary in Section 5.10.

Chapter 6 is dedicated to the **angular modeling of the solar radiation** field. The problem is stated in Section 6.1. In Section 6.2 we review the main factors that affect the TOA anisotropy for the SW radiation field. Section 6.3 presents the SEVIRI scene identification implemented within the GERB data processing. Section 6.4 describes the SW radiance–to–flux conversion implemented for GERB. The method relies on the fine–scale SEVIRI scene identification to infer the flux using the CERES–TRMM SW Angular Dependency Models (ADMs). This is further validated by comparison of the GERB and CERES collocated fluxes (Section 6.5). Section 6.6 summarizes this part of the work.

Chapter 7 is dedicated to the **angular modeling of the thermal radiation** field. As for the previous chapters, the problems are first stated (Section 7.1) and the factors affecting the anisotropy of the thermal radiation field are discussed (Section 7.2). The correlation between spectral and angular behaviors of the thermal radiation is analyzed in Section 7.3. This early work (published in 2003) forms the basis of the Edition 1 GERB LW radiance–to–flux conversion which is detailed in section 7.4. Validations with collocated CERES fluxes are reported in Section 7.5. The comparison with CERES provides evidence that the GERB LW angular modelings suffer from a series of limitations. These limitations, and the way to solve them in the future Edition 2, are discussed in Section 7.6 (cirrus clouds anisotropy) and 7.7 (azimuthal dependency of LW radiation field). Section 7.8 summarizes this chapter dedicated to the anisotropy of the LW radiation.

Finally, Chapter 8 concludes this work and provides recommendations for further developments, including the improvements that should be implemented in the future Edition 2 of the GERB.

Related documents

When possible, we provide references to works published in the peer–reviewed literature. However, this was not always possible, and for the sake of conciseness, we also refer to the technical notes of the GERB project. These notes are referred to as (TNxx) in the text and are available on the RMIB GERB website at the address

http://gerb.oma.be/gerb/Documentation/documentation.html.

Verbal presentations done during the GERB and CERES sciences team meetings are not compiled in proceedings. They are however available for download at the following URLs, respectively for the GERB and CERES meetings:

http://www.sp.ph.ic.ac.uk/~gerb/gerbteam/gistmeetings/

http://asd-www.larc.nasa.gov/ceres/meetings.html

Chapter 2

Scientific Background

2.1 Radiation budget components and processes

The **Top–Of–Atmosphere (TOA) radiative fluxes** densities[1] are defined as the quantities of radiant energy entering and leaving the Earth–atmosphere system from and to space. The incoming energy is the **TOA Incoming Solar radiation (TIS)** F_{tis} which varies at different time scales: the diurnal cycle due to the Earth's rotation (24 hours), the seasonal cycle (365 days) due to the precessing of the Earth axis and the eccentricity of its orbit. This flux is also dependent on the solar brightness which is called the Total Solar Irradiance (TSI), the irradiance at 1 Astronomical Unit. This quantity also presents cycles due to change in solar activity (e.g. the 11 years cycle). The order of magnitude of the TSI is 1365 Wm^{-2} (Wilson, 1993). Taking into account the Earth's sphericity, the global average of the TIS is only a quarter of this value, i.e. 341.25 Wm^{-2}. The spectral signature of the incoming solar energy follows in good approximation the Planck's law for a blackbody at 5800K.

A part of this incoming solar radiation, the **reflected solar flux** F_{sol}, is reflected back toward space by the clouds, the Earth surface and the atmospheric constituents. As the reflected radiation mainly contains wavelength shorter than 5μm it is often referred to as **shortwave flux**. The reflected fraction, about 30% in global average (Kiehl & Trenberth, 1997), is called the **TOA albedo**. By definition, reflection is done without modification of the wavelength of the radiation. However, as the strength of the reflection depends on the wavelength, the spectrum of the reflected radiation departs significantly from the incoming solar spectrum. This is the reason behind the need of spectral modeling of the reflected solar radiation.

The Earth is heated by the part of the TIS which is not reflected (thus about 70%). This

[1]The adjective "densities" stipulates that the radiant flux refers to unit surface ($1m^2$) at the TOA. Like most of the authors, we omit this adjective in the following of the text. As it is no possible to define a height for the TOA, the $1m^2$ surface is defined at the surface level (except otherwise stated)

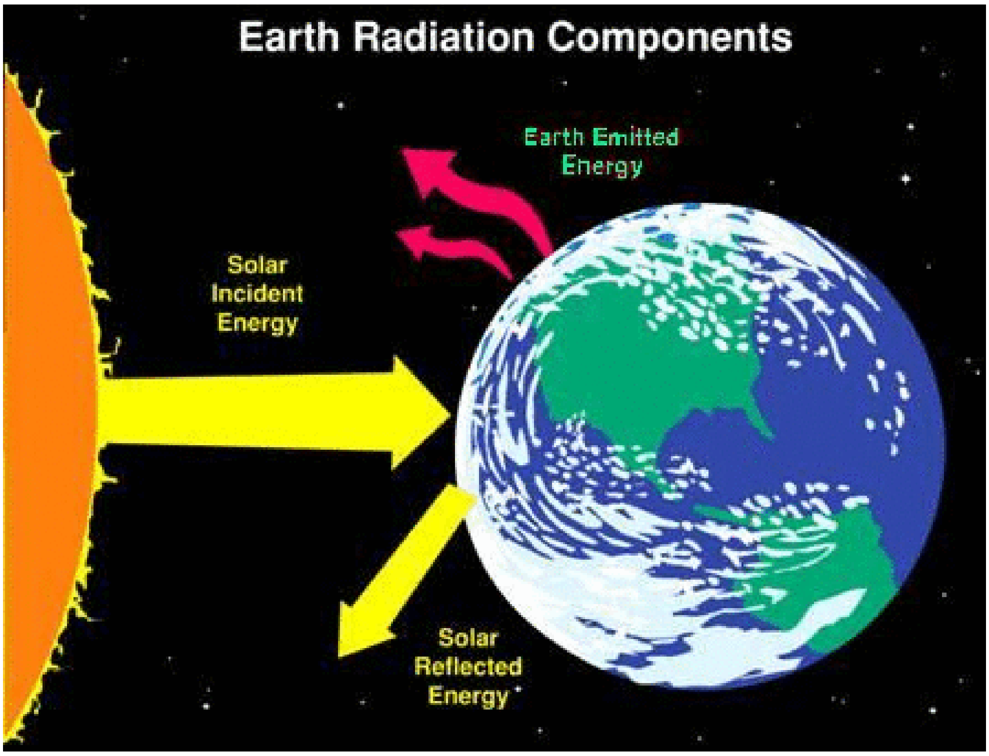

Figure 2.1: The 3 components of the Earth radiation budget: the solar incident energy, the solar reflected energy and the Earth emitted energy.

induces thermal emission and an escape of energy to space at the TOA. This flux is called the **emitted thermal flux** F_{th}, **Outgoing Longwave Radiation (OLR)**, or **longwave flux**. Its global mean value reaches about 235 Wm^{-2} as estimated by Kiehl & Trenberth (1997) from ERBE data. The spectrum of the thermal emission by a blackbody is well–known (Planck's law). However, for the Earth–atmosphere system the spectrum differs from the blackbody curve due to spectral structures in surface emissivity, atmospheric absorption, and differences of temperature in the system. Spectral modeling makes assumptions about the shape of this emitted spectrum.

For Earth radiation budget studies, these fluxes are integrated over all the wavelengths to get the total amount of radiant energy. Figure 2.1 illustrates these fluxes. The **net flux** or **budget** is defined as the difference between the incoming and the outgoing energies

$$F_{net} = F_{TIS} - F_{sol} - F_{th} \tag{2.1}$$

To illustrate these quantities, Figure 2.2 shows the budget for the month of June 2006 derived at RMIB in the frame of the Climate Monitoring SAF project. Accurate estimation of these fluxes at adequate temporal and spatial resolutions is of great importance in meteorology and climatology. The budget presents excesses or deficits up to 200 Wm^{-2} at regional scale (Harrison *et al.*, 1993). These imbalances are the motor of the atmospheric circulations and ocean currents. In this frame, the hydrological cycle of evaporation/precipitation is an efficient transfer mechanism between the regions with positive and negative net budget. When averaged over a sufficiently long time period (e.g. several years) the planetary budget should be close to the equilibrium. Current observations of the increase in ocean heat storage are consistent with an imbalance of $0.85 \pm 0.15 \mathrm{Wm}^{-2}$ due to climate change (Hansen *et al.*, 2005). A global dataset of ERB components should agree with this closure condition. For CERES Edition 2, the imbalance is much higher ($6.5\mathrm{Wm}^{-2}$) and a method has been proposed by Loeb *et al.* (2008) to balance the budget. The global mean adjusted solar and thermal fluxes are $99.5\mathrm{Wm}^{-2}$ (i.e. albedo of 29.3%) and $239.6\mathrm{Wm}^{-2}$. These values are no more direct observation but instead the result of an objective adjustment within their range of uncertainty to remove the inconsistency with the $0.85 \pm 0.15\mathrm{Wm}^{-2}$.

The incoming and outgoing TOA fluxes show pronounced **diurnal cycle** (variations during the 24–hour cycle). Persistent diurnal variation of the albedo is observed over regions with strong convection where the clouds develop mainly during the afternoon. Over cloud free land surface, the thermal radiation is highly dependent on the surface skin temperature and maximum is observed in the early afternoon around 14:00 solar time.

Figure 2.3 (from Kiehl & Trenberth (1997)) illustrates the main processes of interaction between radiation and the planet. The **Earth surface** plays a major role by reflection of the incoming solar radiation and by thermal emission. The reflection strongly depends on the type and state of the surface. Surface albedo ranges from 6% for a water surface to nearly 80% in case of fresh snow. Desert areas are widely represented in the Meteosat Field–Of–View (FOV). This scene is of importance for ERB studies due to its important albedo (about 40%) and surface skin temperature. Figure 2.2 shows that the deserts present negative net flux F_{net} values and therefore cool our climate like the Polar Regions.

The **atmosphere** also plays an important role through scattering, absorption, and thermal emission of the radiation. Cooling by escape of infrared radiation is lessened by the greenhouse effect due to water vapor, CO_2, O_3, CH_4, N_2O, CFC, and many other atmospheric constituents. Except for CO_2 and O_3, the concentrations of these constituents are difficult to model.

The atmosphere contains more or less **aerosol** which affects the radiation by reflection (cooling effect in the SW) and absorption (warming effect in the SW and LW). A distinction can be done between natural aerosols (e.g. desert dust, oceanic aerosols) and man–made (e.g. polution, biomass burning, ...). At this level, the Meteosat observations are of prime interest as the FOV includes most of the planetary biomass burning and desert dust sources (Forster *et al.*, 2007). A series of volcanoes presents also frequent activity in the Meteosat FOV. They are the sources of rapid release of important aerosol concentration (sulfate, black carbon).

Clouds are major components of our climate system through their direct effect on the radiation budget (absorption, scattering) and on the hydrological cycle. They are the main source of variability of the radiation balance. With a global mean annual coverage of about 67.5% (Rossow

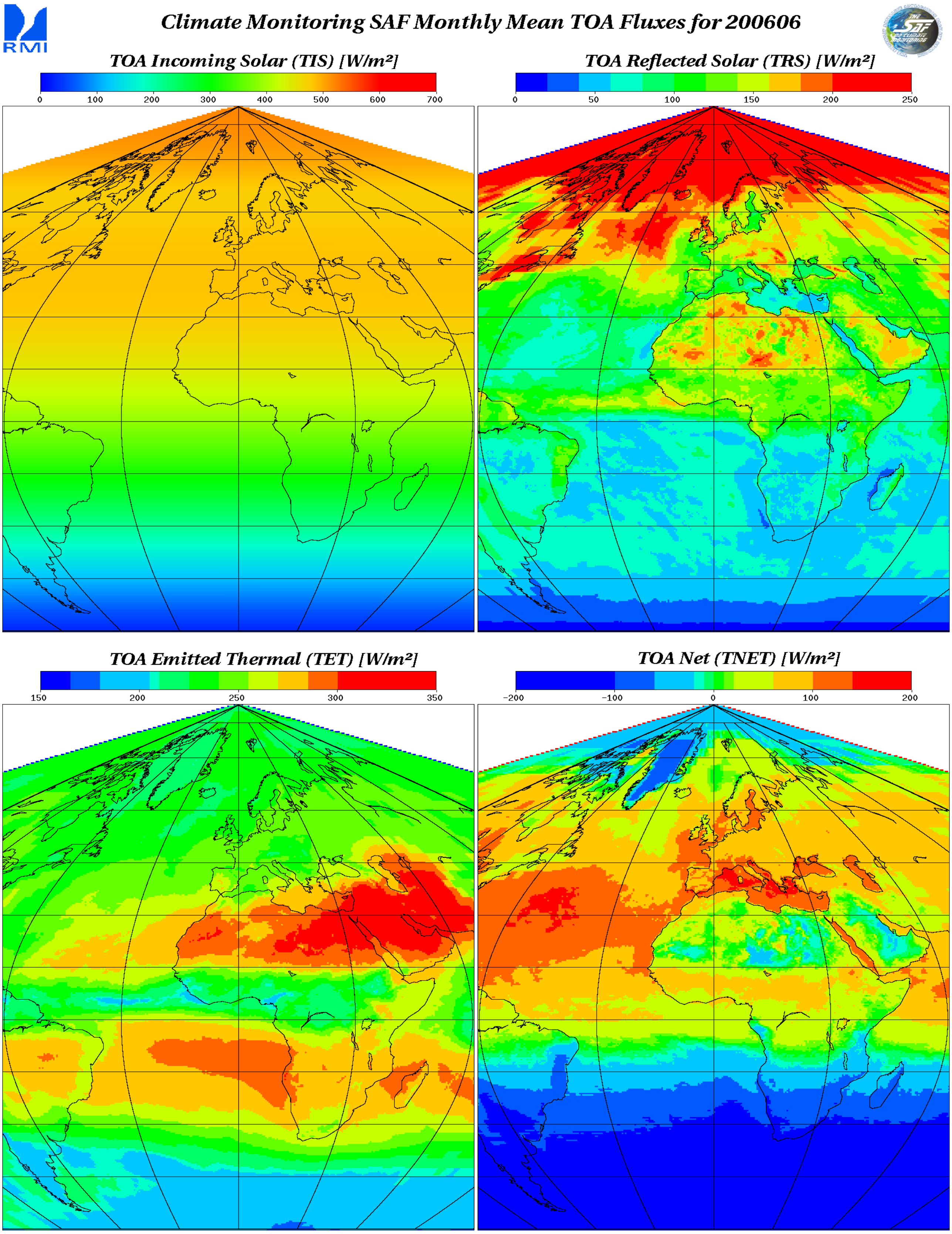

Figure 2.2: June 2006 monthly mean Earth Radiation Budget components produced by the Climate Monitoring SAF from GERB, GERB–like (SEVIRI) and CERES data.

& Schiffer, 1999) the cloudiness is mostly abundant. Both the micro–physical properties (drop size distribution, liquid water content) and the macro–physical properties (cloud optical depth τ, liquid water path, cumuliform or stratiform shape, height of the cloud bottom and top) affect the radiation budget. **Low level clouds** (e.g. stratus, marine stratocumulus, fog) have generally a cooling effect on our climate. They are indeed characterized with high reflectivity but have a limited effect on the thermal flux (Allan *et al.*, 2007). The net cooling effect is maximum over dark surface (e.g. the ocean) due to the albedo increase. It was early recognized that modest changes in this type of cloudiness could potentially offset warming due to greenhouse gas increases (Slingo, 1990). On the other hand, the **high semi–transparent clouds** (e.g. cirrus, cirrostratus, ...) have a (smaller) warming effect on the climate by the greenhouse effect in the infrared. For **deep convective tropical systems** the cooling in the SW and the warming in the LW have about the same magnitude. Different dynamical mechanisms have been proposed to explain this cancellation of the overall forcing (Futyan, 2005). As a matter of fact, each particular cloud system is the cause of a specific perturbation of the radiation budget. The forcing is directly dependent on the latitude zone and season through the incoming solar radiation in the SW and the atmospheric humidity in the LW. Similarly, the radiative effects of the cloudiness is strongly different during day and night time. This stresses the need of detailed cloud classification/characterization for ERB studies. Satellite cloud products and climatology are available from the International Satellite Cloud Climatology Project (ISCCP, Rossow & Schiffer, 1999). Synergetic use of ISCCP and ERBE data have permitted the first observational studies of the effect of cloud type on the radiation balance (e.g. Hartmann *et al.*, 1992). Significant advances in climate science are expected from high quality ERB observations and corresponding accurate cloud characterization. This allows quantifying the **cloud radiative forcing** in regard to the type of cloud system and consequently to model more accurately the potential cloud feedbacks in the climate. It is generally accepted that a significant part of the uncertainty in climate prediction could be attributed to the interactions between clouds and radiation. So, in addition to the determination of the TOA fluxes, a large part of the present days ERB missions is dedicated to the retrieval of macro– and micro–physical properties of the clouds and aerosol layers.

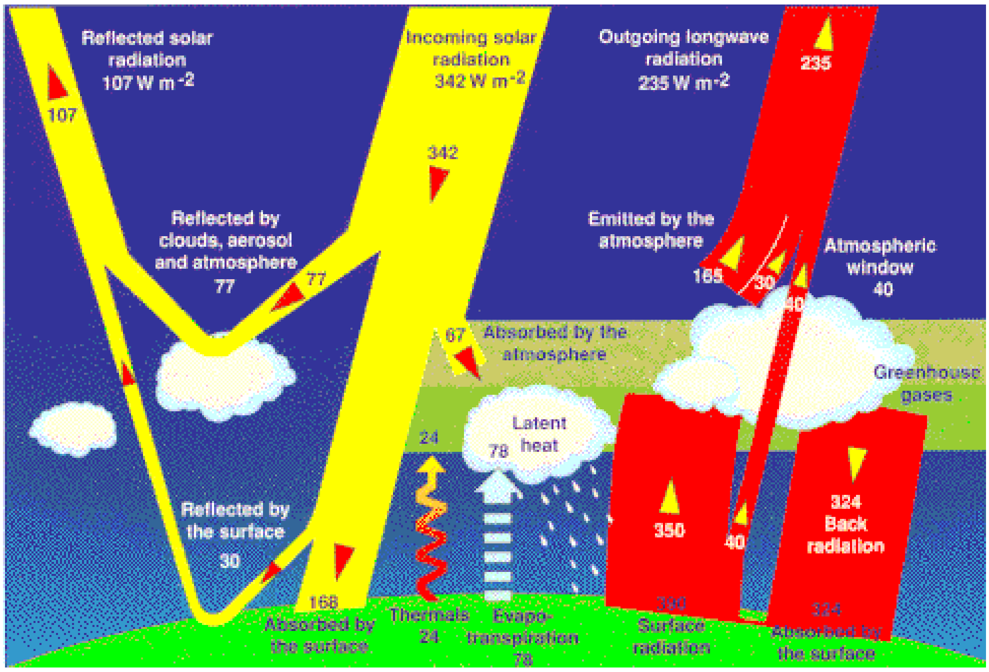

Figure 2.3: Atmospheric processes. Reproduced from Kiehl & Trenberth (1997).

2.2 Satellites missions for ERB studies

The first spaceborne measurements of the Total Solar Irradiance (TSI) with an active cavity radiometer were taken in 1976 on a NASA sounding rocket. Long–term space monitoring has started with the Earth Radiation Budget (ERB, Jacobowitz *et al.*, 1984) experiment on the Nimbus-7 spacecraft which provided 14 years (1978 to 1993) of TSI measurements. The following TSI measurement missions are not detailed here, although the RMIB played a pioneering role with the development of the differential cavity method (Crommelynck & Dewitte, 1999).

The ERB experiment on the Nimbus-7 was also the first successful attempt to measure the 2 other components of the Earth radiation budget: the reflected solar flux and the emitted thermal flux. The instrumentation included both wide FOV sensors and a narrow FOV bi–axial scanning radiometer. The 9–years wide FOV data were mainly used for climate studies over large areas. The 20–months scanner data proved to be useful for regional climate studies and, thanks to the bi–axial scanning, to derive the first set of empirical Angular Dependency Models (ADMs, Suttles *et al.*, 1988, 1989). An ADM is a model of the anisotropy of the radiance field at the TOA which allows converting a directional radiance into a hemispheric flux.

Limitations of the Nimbus–7 ERB data have been identified at the level of the absolute calibration and stability of the measurement. Using geostationary weather satellite data it was shown that the sun–synchronous orbit of the satellite introduces a systematic error over regions that present persistent diurnal variations (Minnis & Harrison, 1984a,b,c). These weaknesses motivated the development of the Earth Radiation Budget Experiment (ERBE, Barkstrom, 1984). For this mission, the ERBE instrument flew simultaneously on 3 satellites: the Earth Radiation Budget Satellite (ERBS) and the sun–synchronous NOAA–9 and –10 satellites. The ERBS is on a sun–precessing orbit that spans all the local time during a cycle of 36 days. Combining improvements in instrumentation and in data processing (see next section) allowed ERBE to achieve its science goals which was the provision of accurate monthly and seasonal mean fluxes.

Dedicated ERB missions have been carried forward with the Scanner for the Radiation Budget (ScaRaB, Kandel *et al.*, 1998), the Cloud and Earth Radiant Energy System (CERES, Wielicki *et al.*, 1996), and the Geostationary Earth Radiation Budget (GERB, Harries *et al.*, 2005). Different aspects of these missions inherit from what has been learned from ERBE. A first point is that the radiometers do not include anymore a LW channel. Indeed, the use of a diamond filter for this channel introduced important variation of spectral sensitivity. Since ERBE, it is known that the LW radiation is more accurately derived by subtraction of a SW measurement (obtained with a quartz filter) from a total channel. It was also demonstrated that flatter spectral response curve can be obtained in the SW part of the spectrum by using silvered mirrors for the telescope optics instead of aluminum. Another point is that scanner data with relatively small footprint size are necessary to quantify the cloud forcing. At this level, the wide FOV non–scanner data presented limited usefulness (the non–scanner data was however useful in constructing and understanding long term record of radiative fluxes, as by Wielicki *et al.* (2002)).

Two ScaRaB instruments have been operated on Russian satellites during limited time periods in 1994/1995 and 1998/1999. These data are however valuable to transfer the absolute calibration to other sensors like weather satellite imagers. Another interest is that in addition to the SW and total (TOT) channels, ScaRaB provides visible and infrared narrowband measurements in channels similar to the ones of weather satellites. As discussed in Section 2.8, the ScaRaB measurements have been used to improve narrowband–to–broadband techniques.

In 1998, ERB measurements over the tropical belt were available from the CERES Proto–Flight–Model (PFM) aboard the Tropical Rainfall Measurement Mission (TRMM) precessing satellite. Unfortunately, an instrument failure obliged to switch off the instrument after only 9 months of observation. Detailed analysis of the CERES–PFM data allowed building ADMs for a large set of Earth–atmosphere conditions (Loeb *et al.*, 2003b). These models are of particular interest in this work because they have been selected for the GERB SW radiance–to–flux conversion. Since 2000 and 2002 respectively, CERES instruments provide broadband (BB) measurements from the Terra and Aqua sun–synchronous polar satellites. These independent simultaneous observations are of primary interest for GERB validation. Section 3.3 provides the characteristics of the CERES observations and the methodology followed for the GERB/CERES comparisons.

The geostationary Earth observation began with ATS–1, the first geostationary "weather" satellite launched on 7 December 1966. Figure 2.4 shows the first picture obtained. This satellite was the pioneer of a long series of geostationary weather satellites (more than 50 have been launched since then) observing the Earth with visible and infrared sensors. For ERB studies, these historical geostationary observations suffer from poor absolute calibration and stability, poor characterization and rapid aging of the spectral responses, and inherent errors introduced by the needed narrowband–to–broadband conversions. For these reasons, EUMETSAT and ESA selected the GERB instrument as secondary passenger on the Meteosat Second Generation satellites. With the launch of MSG–1 on 28 August 2002, the calibrated BB observation of the Earth has been performed for the first time from the geostationary orbit. A second GERB instrument was launched on MSG–2 on 21 December 2005.

Currently (mid–2008), broadband ERB measurements are available through 4 CERES instruments (but only 3 for the SW radiation as the SW channel of FM4 failed on 30 March 2005) and 2 GERB instruments (although a single instrument is operated most of the time).

In the coming years, ERB measurement will continue with the GERB on MSG–3 and MSG–4. A ScaRaB instrument is expected to fly on MeghaTropique, an Indo–French satellite mission for the study of the tropical convective systems. The launch is foreseen at the end of 2009. Since

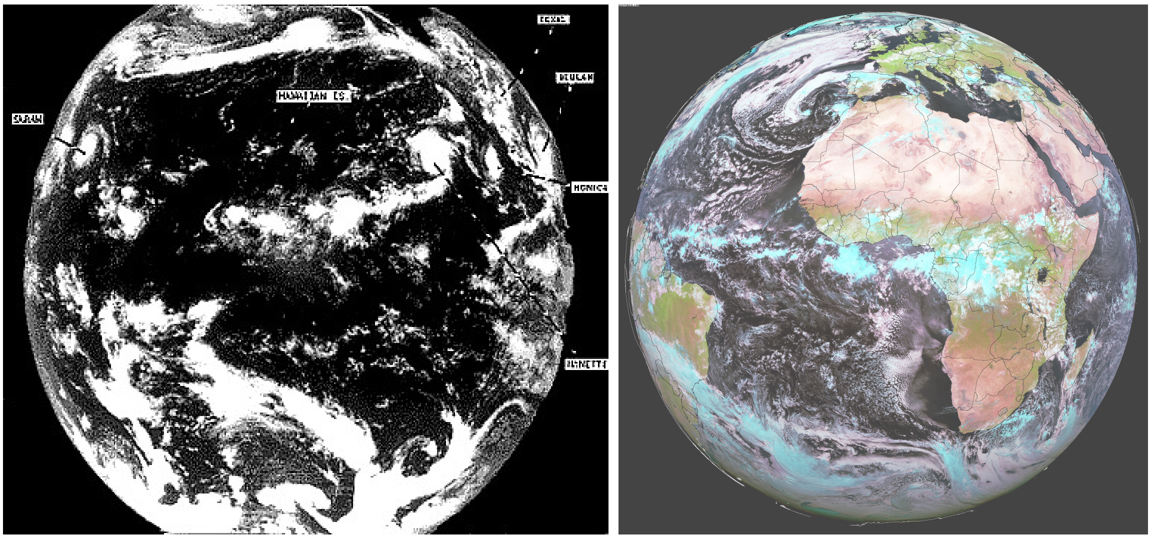

Figure 2.4: Left: first cloud-cover pictures taken from ATS-1 in 1966. Right: images from MSG-1 in 2007.

2006, China has shown an interest in participating in geostationary ERB measurement. In this context, a Chinese delegation visited the Imperial College and the RMIB in April 2006. A first Chinese broadband radiometer, called the Earth Radiation Budget Unit (ERBU), has been launched on 27 May 2008 on the FY-3A polar satellite. Concerning the follow-up of GERB, it is unlikely that broadband radiometers will operate either on the Meteosat Third Generation (MTG) or on the Post–EPS programme (although there is still some possibility to ensure a global coverage by the European countries). Finally, some of the National Polar–orbiting Operational Environment Satellite System (NPOESS) US satellites, scheduled for launch as from 2011, will continue the CERES mission with the Earth Radiation Budget Sensor (ERBS), a redesign of the CERES instrument. In the meantime, it was decided that the spare CERES instrument (FM5) will fly on the NPOESS Preparatory Program (NPP) satellite to reduce the probability of a gap in the global dataset.

In parallel to these broadband measurements, several space instruments provide valuable data for ERB studies. The NOAA/NESDIS supplies operational Outgoing Longwave Radiation (OLR) estimation from the High-resolution InfraRed Sounder (HIRS) measurements (Ellingson *et al.*, 1989). A complete reprocessing of the entire TIROS–N series of NOAA satellites from 1979 up to now is foreseen (Lee *et al.*, 2007). The long–standing Advanced Very High Resolution Radiometer (AVHRR) database is also interesting for climate studies.

Finally, reprocessing of geostationary weather satellite observations provides climate–long databases (i.e. more than 30 years) of ERB estimation. Such reprocessing effort with state–of–the–art algorithms and calibration has been performed by EUMETSAT for the Meteosat–2 to –7 period (1982–2006).

2.3 Broadband radiometer data processing: from raw data to filtered radiances

Absolute **calibration and stability** are key elements of ERB missions (Ohring *et al.*, 2005). Since the ERBE, all missions have aboard a blackbody at known temperature for the calibration. The LW channel (ERBE) and the LW part of the TOT channel are calibrated using this blackbody. This allows targeting an absolute accuracy of 0.5% for the LW radiance. The calibration of the SW channel relies on the ground characterization of the SW quartz filter transmission and on the spectral response of the instrument. As the filter and the detector are subject to aging, a relative calibration device is desirable, as a minimum requirement. For ERBE and CERES the SW drift is checked using a solar diffuser called mirror attenuator mosaic. For GERB the drift is monitored with an integrating sphere illuminated by the sun.

For a BB instrument having a SW and a TOT channels, the **LW radiance** is estimated by subtraction: LW = TOT $-$ $A \times$ SW. The factor A is usually set in such a way that the LW radiance is exactly equal to zero for a blackbody spectrum at 5800 K (idealized solar spectrum). The subtraction assumes that the measurements are simultaneous and that the footprints are accurately collocated. For ERBE, CERES and ScaRaB, the lines of sight of the 2 channels are carefully aligned on–ground (the PSF is however often a bit larger for the TOT than for the SW channels, due to diffraction of infrared radiation). To check that the SW contribution is correctly subtracted from the TOT channel, the LW radiances are usually validated (e.g. by comparison with other instruments) during day and night separately. In the case of the ERBS scanner instrument radiances, Green & Avis (1996) reported a drift of 1.4 % in 4 years for the SW part of the TOT channel. This drift affected the LW estimation during daytime, especially over bright scenes. Difficulties arise when the TOT and SW measurements are not realized exactly over the same footprint or at the same time, as it is the case for GERB. The problem affects mainly the areas with strong contrast in the SW channel like the borders of the clouds. The daytime GERB LW images seem noisy and a dedicated filtering was implemented to reduce the magnitude of this noise (Dewitte *et al.*, 2008). A **separation of the solar and thermal** radiation is also needed to remove any signal due to emitted thermal radiation in the SW channel and due to reflected solar radiation in the LW (synthetic) channel. This separation, and the associated errors, can be addressed theoretically, using radiative transfer computations. For ERBE (Green & Avis, 1996) and CERES (Loeb *et al.*, 2001), these contaminations are estimated as linear combination of the TOT and SW signals. For GERB, the contaminations are estimated as regressions on the NB channels of SEVIRI (Clerbaux *et al.*, 2008a,b). The SW measurements realized during the night allow deriving an empirical estimate of thermal contamination in the SW channel. This approach is adopted by CERES which uses an empirical nighttime regression between the SW radiance and the infrared window channel. This regression is then used to estimate the thermal contamination in the SW channel during the day.

2.4 Broadband radiometer data unfiltering

It is not possible to manufacture a broadband radiometer that has perfectly equal sensitivity at all the wavelengths. The thermal detector elements themselves show some spectral structure in their responses. The throughput of the optics of the instrument also presents spectral variations. If the effect of a single silvered mirror is limited, the combined effects of multiple mirrors optics can be significant. To give an example, the transmission for the GERB-1 telescope at 0.5μm is 15% lower than at 2.5μm. The transmission of the optics typically drops at short wavelengths ($\lambda < 0.4$ μm). This is however not a problem for an ERB instrument as the reflected solar radiation at these wavelengths is small due to the strong absorption by atmospheric ozone.

The signal provided by the instrument is a radiance filtered by the spectral response of the instrument ($L_{fil} = \int L(\lambda)\phi(\lambda)d\lambda$). The conversion in unfiltered radiance ($L = \int L(\lambda)d\lambda$) requires an accurate characterization of the instrument spectral response $\phi(\lambda)$ but also some assumptions about the spectral signature $L(\lambda)$ of the observed scene. The spectral response curves $\phi(\lambda)$ of the different channels are usually carefully characterized on–ground. They can afterward vary slowly due to aging and deposition of pollutants. The challenges, and unfortunately also the errors introduced during the unfiltering, are proportional to the existing spectral variability in the response. The ratio of the unfiltered and filtered radiances is called the unfiltering factor.

In general, unfiltering factors are derived from radiative transfer simulations for different scene types in the instrument footprint. The ERBE unfiltering (Smith *et al.*, 1986) is based on a set of such factors obtained for 5 surface types and for an overcast cloudiness. An interpolation is realized for partly cloudy and for coastal pixels. The factors depend on the viewing and sun geometry. Validation of the ERBS scanner instrument radiances has been done by Green & Avis (1996).

Viollier *et al.* (1995) derived spectral correction factors for the ScaRaB instrument. They suggested not to apply spectral correction in the longwave domain and to use only a +4.5% correction in the SW channel for clear and partly cloudy ocean. This correction compensates for the lower sensitivity of the instrument at the short visible wavelengths.

Loeb *et al.* (2001) developed the unfiltering method for the CERES instrument data. As for ERBE, the method relies on a set of radiative transfer simulations. However, regressions between unfiltered and filtered radiance are used instead of a fixed ratio as for ERBE. The regression coefficients are function of viewing and solar geometry, of the surface type (ocean, land, snow), and of the presence of cloud (clear or cloudy). For the CERES PFM instrument, Loeb *et al.* (2001) estimate unfiltering errors of less than 1% for the SW radiances and less than 0.2% for LW radiances. For the subsequent CERES instruments (FM-1, -2, -3, and -4), the SW unfiltering error is further reduced to less than 0.5% thanks to a spectral response in ultra violet ($0.3 - 0.4$ μm) that is flatter than the one of the PFM. The CERES unfiltering is also used to generate the CERES ERBE–like products (processing of the CERES observations with the ERBE algorithms) because the original ERBE method fails to process correctly the CERES data (Loeb *et al.*, 2001).

The operational unfiltering method developed for GERB (Clerbaux *et al.*, 2008a,b) follows a different approach. The method relies on some information about the spectral signature provided by the narrowband measurements of the SEVIRI imager. The method is described and validated in Sections 4.5 (SW) and 5.5 (LW) of this work. An alternative unfiltering method is also proposed to permit the processing of the GERB data in case of unavailability of SEVIRI imager data. This method, called "direct unfiltering", is similar to the CERES unfiltering and is described in Sections 4.4 (SW) and 5.4 (LW).

2.5 Radiance–to–flux conversions

The unfiltering process generates unfiltered solar (SW) and thermal (LW) radiances which are spectrally integrated energies leaving the Earth in direction of the satellite. These directional values are of limited interest for most of the scientific community which requires hemispheric fluxes[1]

$$F = \int_{\mathrm{VZA}=0}^{\frac{\pi}{2}} \int_{\mathrm{VAA}=0}^{2\pi} L(\mathrm{VZA}, \mathrm{VAA}) \cos(\mathrm{VZA}) \sin(\mathrm{VZA})\, d\mathrm{VZA}\, d\mathrm{VAA} \tag{2.2}$$

where VZA and VAA are the Viewing Zenith Angle and the Viewing Azimuth Angle. These angles are ilustrated in Figure 2.5. It is worth noting that this hemispheric flux can be "directly" measured with wide field–of–view instruments, as it was done during ERBE (Barkstrom, 1984). Although these limb–to–limb measurements could be useful for climate monitoring, they prevent to study processes at local scale, in particular to separate clear and cloudy regions. For narrow field–of–view instruments like the ERBE scanner radiometer, the ScaRaB, the CERES or the GERB, the flux F must be inferred from a single directional radiance L measurement[2].

For an isotropic (Lambertian) radiance field, the radiance–to–flux conversion is trivial, the Eq.(2.2) reduces to $F = \pi L(\mathrm{VZA}, \mathrm{VAA})$. However, this is not the case for real scenes and a characterization of the anisotropy is needed in the conversion from radiance to flux. The anisotropy factor R is defined as the ratio of the equivalent Lambertian flux (πL) to the hemispheric flux F

$$R(\mathrm{VZA}, \mathrm{VAA}) = \frac{\pi L(\mathrm{VZA}, \mathrm{VAA})}{F} \tag{2.3}$$

The Eq.(2.3) is widely used to infer the flux F from the directional measurement $L(\mathrm{VZA}, \mathrm{VAA})$ after angular modeling of the TOA radiance field via a model $R(\mathrm{VZA}, \mathrm{VAA})$. The selection of the best–suited model to infer the flux from the radiance with Eq.(2.3), requires a characterization of the observed scene.

In the **empirical approach**, the anisotropy models R are derived from multiangle BB instrument observations themselves. Two methodologies have been identified: the Sorting by Angular Bins (SAB) method (Taylor & Stowe, 1984) and the Radiance Pairs Method (RPM, Green & Hinton, 1996). Loeb *et al.* (1999) have compared the 2 methods and concluded that the SAB

[1] As an exception, the directional radiance measurement L is usually used for instrument calibration and validation activities (e.g. instrument comparison). The directional measurement can also be directly assimilated in weather or climate models or used to validate the radiative scheme of the model.

[2] The case of multi–angular observations of a same scene is not discussed here although this technique is implemented in some current (i.e. Polder, MISR, CERES in along–track scanning mode) and future missions like the ESA Earth Explorer EarthCARE mission.

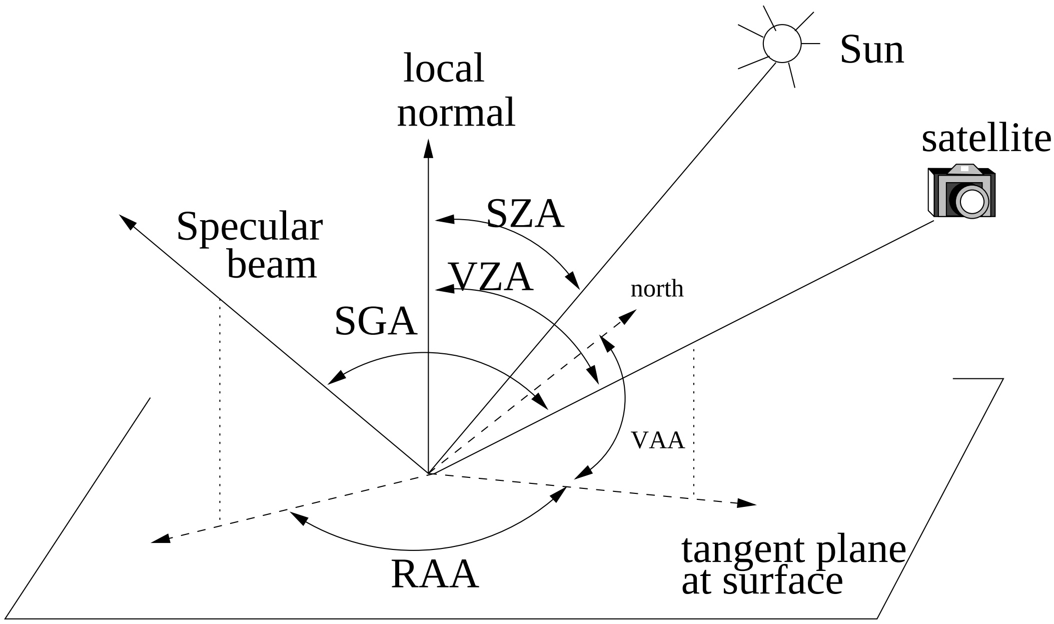

Figure 2.5: Definition of the Solar Zenith Angle (SZA), Viewing Zenith Angle (VZA), Relative Azimuth Angle (RAA), and Sun Glint Angle (SGA).

gives better (i.e. unbiased) TOA flux estimates, while the RPM method provides better estimate of the true mean angular model. The SAB method is used to construct the ERBE and CERES models. Although relatively high instantaneous errors may affect the flux F, the empirical approach allows reducing the average error (i.e. the bias) to a very low level value. This assumption is verified by comparing the ADM derived flux with the Direct Integration (DI) flux (Loeb *et al.*, 2003a).

A **theoretical approach** is also possible, based on radiative transfer computations to model the anisotropy of the radiance field at TOA. This presents both advantages and disadvantages with respect to the empirical ADMs. The approach does not require the full angular sampling of the observations needed to derive the empirical ADMs (which is obviously impossible to achieve with a geostationary instrument). On the other hand, theoretical ADMs are more likely to introduce biases in the inferred fluxes, especially where the scene presents 3–dimensional effects that are difficult to model with the existing computer programs (e.g. broken cloud field, mountain region). For the shortwave radiation, the theoretical approach also transfers a part of the difficulties from the TOA to the Earth surface level. Indeed, the radiative transfer model needs the characterization of the Bidirectional Reflectance Distribution Function (BRDF) of the surface. Radiative transfer computations have been demonstrated to be useful for improving and/or filling gaps in an empirical ADM set. For instance, Loeb *et al.* (2003b) propose a theoretical adjustment of the clear ocean empirical CERES–TRMM ADM to account for the presence of aerosols. Due to the infrequent observation of snow, CERES–TRMM does not provide an empirical model for this surface type. In this case, CERES suggests to use theoretical models constructed by Kato & Loeb (2005). Another theoretical approach involves **geometric models**. In this case, simulations of 3–dimensional objects permit to model the anisotropy at the earth surface level (Roujean *et al.*, 1992) or at the TOA due to the cloudiness, e.g. the model of broken cloud field by Duvel & Kandel (1984).

For a long time, the best available sets of empirical models were derived using the SAB method from the Nimbus–7 ERB instrument data by Suttles *et al.* (1988) for the SW and Suttles *et al.* (1989) for the LW. Manalo-Smith *et al.* (1998) have derived analytical forms of the SW models. These ADMs have been used to process ERBE, ScaRaB, and the CERES ERBE–like data. However, it became evident that the fluxes inferred using the ERBE models are affected by significant biases for some scene types. Concerning the effect of the viewing geometry, it is observed that the ERBE models underestimate as well the SW limb–brightening as the LW limb–darkening (Suttles *et al.*, 1992). Geostationary data like Meteosat or GOES (the Geostationary Operational Environmental Satellite) have been widely processed with these models. For the GERB data processing, Dewitte & Clerbaux (1999b) have however suggested to use improved models like the ones under development for CERES–TRMM. Models from the ScaRaB or from the POLarization and Directionality of the Earth's Reflectances (POLDER) instruments were also considered at that time. The CERES–TRMM ADMs (Loeb *et al.*, 2003b) are derived from the CERES–TRMM data in Rotating Azimuth Plane Scan (RAPS) mode using scene type information from the Visible and InfraRed Scanner (VIRS) imager. The improvement compared to the previous ERBE models is significant (Loeb *et al.*, 2003a). In particular, the viewing and solar zenith angles dependencies that affected the ERBE fluxes are strongly reduced. The regional (1°) instantaneous accuracies are estimated to 9.8 Wm^{-2} in the SW and 3.5 Wm^{-2} in the LW. As the TRMM satellite is on a sun–precessing orbit, these models span the Solar Zenith Angle (SZA) range, from the terminator (SZA $\sim 90°$) to the nadir illumination. This makes the CERES–TRMM models well–suited to process geostationary satellite observations. The use of the CERES–TRMM models for the GERB SW radiance–to–flux conversion is described in Section 6.4. Later on, models have been developed from (and for) the CERES observations on the Terra and Aqua sun–synchronous spacecrafts (Loeb *et al.*, 2005). They are very accurate to process data taken at approximately the same solar time, respectively 10:30 and 13:30.

The selection of the best–suited model to convert the radiance in flux requires the characterization of the scene type in the footprint because each scene has a particular anisotropy. The scene identification is discussed in the next Section 2.6. To avoid relying on explicit scene identification, Loukachine & Loeb (2004) suggest to estimate the flux with neural networks. The only information needed is the SW and LW unfiltered radiances. The strength of the approach is to allow retrieval of the fluxes even when no imager data is available. Some teams have focused their efforts on the development of anisotropy models for particular scene types. In the future, dedicated models are expected to become available for challenging situations like desert dust clouds, semi–transparent high clouds, semi–arid regions, ... Table 2.1 provides a non–exhaustive list of SW anisotropy models.

Scene types	author (year)
all	Suttles (1988) (ERBE models) Loeb (2003) (CERES–TRMM models) Loeb (2005) (CERES Terra/Aqua) Loukachine (2004) (neural network)
all surface	Roujean (1992)
sea surface	Cox and Munk (1954)
forest	Duchemin (1999)
glacier ice	Knap (1998)
snow	Kato (2005)
clouds	Staylor (1985)
stratiform cloud	Loeb (1998)
broken cloud field	Duvel (1984)
marine bound.l. clouds	Chambers (2001)
desert surface	Capderou (1995, 1998)

Table 2.1: Non–exhaustive list of SW anisotropy models. (first author and year).

It is generally observed that the best–suited observation angle to convert radiance in flux is close to VZA $\sim 52°$ (Otterman *et al.*, 1997). Figure 6.1 in Chapter 6 shows that this condition is only fulfilled over a small part of the GERB field–of–view. For the shortwave radiation, the ADM is also dependent on the Solar Zenith Angle (SZA) and on the Relative Azimuth Angle (RAA) between the Sun and the observer. The model of bidirectional distribution is consequently written $R(\mathrm{SZA}, \mathrm{VZA}, \mathrm{RAA})$.

On the other hand, the **thermal radiation** field does not present systematic dependency neither on the SZA nor on the viewing azimuth. Indeed, surface emission and atmospheric absorption do not present preferred azimuthal direction. The LW model is therefore written $R(\mathrm{VZA})$ and is sometimes called limb–darkening function as the radiance usually decreases at increasing VZA values, due to the increase of the atmospheric absorption with the atmospheric path ($\sim 1/\cos(\mathrm{VZA})$). A number of other effects are making the radiance field anisotropic: scattering by atmospheric constituents, surface reflection, 3-dimensional effects at the Earth surface and cloudiness,... they are discussed in Section 7.2. The ERBE LW models (Suttles *et al.*, 1989) are stratified according to the ERBE scene type, the colatitude bin (18° bins from North Pole to South Pole), and the meteorological season (DJF, MAM, JJA, SON). CERES–TRMM provides a set of 1035 LW models (Loeb *et al.*, 2003b). The scenes are stratified in terms of surface type (ocean, land, desert), cloudiness (clear, broken cloud field, overcast), precipitable water, cloud fraction, vertical temperature change (in clear sky) or temperature difference between the surface and the cloud layer (in case of cloudiness), and IR emissivity of the cloud (infrared transparency). These empirical LW models are not used for the GERB processing because the model selection relies on ancillary information from numerical models (precipitable water, surface and vertical temperature profile). Furthermore, a nighttime cloud retrieval is needed and this is not available in GERB Edition 1.

The theoretical approach for the radiance–to–flux conversion has often been used to estimate the LW flux from a set of NB measurements. The parameterizations are carried out using radiative transfer calculations with different atmospheric profiles. The first multispectral thermal flux estimation technique was used by Raschke *et al.* (1973) on data from the Nimbus 3 radiometer. Ellingson *et al.* (1989) proposed and validated (Ellingson *et al.*, 1994) a method based on 4 of the 19 High resolution InfraRed Sounder (HIRS) NB measurements. Schmetz & Liu (1988) parameterized regressions to estimate the flux from the Meteosat water vapor and infrared channels. In these studies, the problem of the angular conversion is not isolated from the problem of the NB–to–BB conversion. Recently, the Meteorological Products Extraction Facility (MPEF) at EUMETSAT has published regressions to estimate the OLR from SEVIRI. The method is similar to what has been implemented for Meteosat first generation with the exception that, nowadays, 3 distinct regressions are proposed for clear sky, opaque clouds, and semi–transparent clouds. For these different NB instruments, it is worth noting that the flux is estimated without intermediate estimation of the BB radiance. For the ScaRaB data processing, Stubenrauch *et al.* (1993) proposed an new technique to estimate the anisotropy factor directly as a function of the BB and a window infrared NB radiances. This technique is discussed in Section 7.3.4. The theoretical approach is adopted for the GERB LW radiance–to–flux conversion, described in Section 7.4. The anisotropy factor $R(\mathrm{VZA})$ is a function of a subset of the SEVIRI thermal channel observations.

The **validation** of the radiance–to–flux conversion involves different aspects. When empirical ADMs are used, the first validation should be done at the scene identification level. The GERB/SEVIRI scene identification has proved to be in agreement with the corresponding products derived from the VIRS data by the CERES cloud team (Ipe *et al.*, 2004, 2008). Second type of validation consists in the comparison with fluxes derived from other directions of observation. In this frame, the CERES observations are of prime interest. A methodology has been set up to extract, from the observed difference between the GERB and CERES LW fluxes, the part which is due to the angular modeling. In this frame, the CERES Rotating Azimuth Plane Scan (RAPS) mode should be preferred, as it provides a better angular sampling than the standard cross–track mode. For infrequent scene type (e.g. desert dust), more accurate LW ADM validation could be obtained by using only the CERES fluxes derived from observations with VZA $\sim 52°$. At these angles, the CERES ADM error is neglected, and therefore CERES is an excellent reference for flux comparison. Finally, when a same quantity is estimated from 2 geostationary satellites having an intercepting FOV, the validation of this quantity is possible in the common area. This can be done with the fluxes estimated from Meteosat–7 (before its relocation over the Indian Ocean) and Meteosat–5 (located at 63° east) following the method of Govaerts *et al.* (2004b) for the validation of surface albedo.

2.6 Scene identification

Scene identification is an important point for all the current ERB missions. Thorough information about the scene type is needed at various processing steps: to select the best–suited ADM for the angular conversion, to select the unfiltering factors, and to infer the clear sky fluxes. Moreover, a precise characterization of the observed scene is requested by the user community in addition to the TOA fluxes (Wielicki *et al.*, 1996). Most of the time, the scene identification is based on the collocated NB radiances provided by multispectral imagers. For some current missions, more detailed retrievals become possible by spaceborne RADAR and LIDAR.

For ERBE and ERBE–like, the scenes are stratified in 12 classes. According to the footprint geolocation, the ERBE surface type is extracted from a constant map of the following geotypes: ocean, land, desert, snow, and coast. The cloudiness is estimated based on the broadband SW and LW radiances themselves with the maximum likelihood method (Wielicki & Green, 1989). This defines 4 classes of cloudiness: clear, partly cloudy, mostly cloudy, and overcast. Clearly, the method does not fulfill neither the current requirements for the ADM selection (too coarse scene stratification) nor the wishes of the users.

A complex cloud retrieval has been implemented by Minnis *et al.* (1999) for CERES. The scheme involves multispectral tests on the VIRS or on the Moderate resolution Imaging Spectroradiometer (MODIS) data. The retrieved cloud characteristics at the imager spatial resolution are: the visible optical depth, the thermodynamic phase, the IR emissivity, the cloud top pressure and the particle size distribution (effective radius). These quantities are then convoluted with the CERES PSF to obtain averaged cloud characteristics in the CERES footprints.

For GERB, different sources of cloud information have been identified: the development of a dedicated cloud identification based on SEVIRI, the use of the MPEF cloud products, or the use of the Nowcasting–SAF cloud software (Derrien & Le Gléau, 2005). After long discussions, it was decided to rely on our own scene identification. The main motivation behind this choice is the need to use "frozen" cloud products for Edition GERB data. The RMIB GERB Processing (RGP) scene identification is detailed in Section 6.3. The retrieval is based on the visible NB observations of the SEVIRI imager, consequently it does not work during nighttime. Ipe *et al.* (2003) focused their work on the best possible estimate of the clear sky reflectance in the 0.6μm and 0.8μm channels of the imager. Updated weekly, these clear sky reflectance maps allow a reliable cloud detection and characterization in terms of visible optical depth. There is however a request from the user community to extend the cloud retrieval to nighttime situations using the thermal channels of the imager. This IR cloud detection could also resolve some bottleneck detected in the data processing, like the processing in the sun–glint region.

The SAF nowcasting cloud programs have been installed and configured to process full–disk SEVIRI data. This provides valuable cloud/dust products in support of GERB research and validation activities. In this context, a visiting scientist activity at the *Centre de Météorologie Spatiale* of Météo-France in Lannion took place in April 2005. The nowcasting SAF cloud mask is also of importance as it is the official cloud mask within the Climate Monitoring SAF. For the sake of consistency between the different products, there is a request from the CM–SAF steering group to reprocess the TOA radiative products using the nowcasting SAF cloud retrieval. This is a request to be addressed during the coming years.

2.7 Spatial and temporal processing

The ERBE and CERES ERBE–like instantaneous products are averaged over $2.5° \times 2.5°$ latitude and longitude boxes and over time periods of 1 hour. The spatial processing consists in a simple selection and average of the observations falling in the region. For the CERES products, the spatial resolution is enhanced to a $1° \times 1°$ grid. This is made possible by the increased sampling rate of the instrument (100 observations per second instead of 30 for ERBE) and the smaller footprint size (10 km on TRMM and 20 km on Terra and Aqua instead of 40 km for ERBE). In both cases, there is no correction for the PSF of the instrument.

Temporal processing infers the daily, monthly and annual means from the instantaneous measurements. More or less complex temporal interpolation schemes must be implemented in accordance with the frequency of observations over a given Earth location. In general, for a Sun–synchronous satellite, two observations are carried out every day: one during daytime and one during the night. In this case the daily mean must be inferred from a single measurement (2 for the longwave). Ellingson & Ba (2003) have estimated that the Root Mean Square (RMS) error on the OLR due to temporal sampling when observations are available on a 12–hourly interval is about 14 Wm^{-2}. When observations are available from 2 polar satellites (6–hourly observations), the temporal sampling error decreases to about 7 Wm^{-2}. For a polar satellite the temporal sampling problem is worse in the tropics than at the Poles. On the other hand, worldwide observation of the tropics and mid–latitude regions is provided by the geostationary weather satellites. CERES takes advantage of this synergy. The temporal interpolation methods for ERBE and CERES are described and compared by Young *et al.* (1998). The introduction of geostationary data in the CERES temporal processing improves the accuracy by 68% for LW flux and 80% for SW flux.

The GERB sampling distance is about 45 km at sub–satellite point. The GERB Averaged Rectified Geolocated (ARG) products are obtained by linear interpolation between the measurements on a regular 44 km grid. Based on ancillary fine–scale estimates of BB radiation from the SEVIRI imager, a series of complex processing steps allows to correct for the GERB PSF and to generate the Binned Averaged Rectified Geolocated (BARG) and High Resolution (HR) products (described in Section 3.1.5).

With about 255 daily SW and TOT observations GERB is not subject to significant temporal interpolation error. Linear variation could be assumed between the observations. They are indeed separated by 338s at a maximum. Nevertheless, temporal processing is necessary to derive the GERB clear sky fluxes (Futyan & Russell, 2005; Russell *et al.*, 2004) and to deal with missing GERB data. An alternative approach of temporal processing is to rely on the GERB–like data in case of absence of GERB data.

2.8 Narrowband–to–broadband techniques

The broadband (BB) unfiltered radiance can be estimated using regressions on a set of narrowband (NB) measurements. Compared to the unfiltering of a BB instrument data, a higher error level is expected for NB–to–BB techniques, because the NB observations sample only a limited part of the spectrum. As for the radiance–to–flux conversion, empirical and theoretical approaches are possible. The empirical regressions rely on collocated coangular NB and BB observations. The theoretical approach is based on radiative transfer computations to simulate a database $L(\lambda)$ of spectra. The simulated NB and BB radiances are obtained by spectral convolution with the spectral response of the NB channel(s). The regressions are then adjusted to the simulated radiances.

This technique allowed the early studies of Earth radiation budget from multispectral instruments like Meteosat, GOES, the AVHRR, the HIRS sounder, and many others, from either geostationary or polar satellites. In general, a single regression gives sufficiently accurate results, at least with respect to the absolute accuracy and stability of the NB measurements. However, dedicated regressions for some kinds of scenes have also been proposed. Table 2.2 gives non–exhaustive lists of NB–to–BB methods for the SW and LW radiation.

The empirical approach can combine NB and BB measurements taken by instruments on different satellites. In this case, the statistics of coangular observations are in general limited. For some couples of instruments the NB and BB radiances are measured from the same spacecraft, providing much better statistics. This is the case of VIRS and CERES on the TRMM satellite, MODIS and CERES on the Terra and Aqua satellites, and SEVIRI and GERB on the MSG satellites.

In Earth radiation budget studies, the estimated BB radiance from geostationary satellites is useful for the temporal processing of the polar satellite instrument (e.g. CERES). In the case of the GERB project, while the NB–to–BB techniques are not required for the temporal processing, they are used in the processing: (i) to perform the unfiltering and the angular conversions at finer spatial resolution than the large GERB footprint, (ii) to correct for the GERB PSF in the BARG product, (iii) to generate a GERB product at finer spatial resolution, and (iv) to tune the geolocation of the GERB footprint. In addition to this, the "GERB–like TOA fluxes" products could be used to fill gaps in the GERB dataset. This is of special interest to build the monthly mean products. The GERB–like fluxes could also enlarge the GERB dataset back in the past, by using the long Meteosat first generation archive. For climate applications, the NB–to–BB conversion is useful to monitor the relative calibration of the BB and NB instruments and to detect possible instrument drifts.

An interesting issue to address concerns the error which is introduced by the NB–to–BB conversion for a multispectral state–of–the–art imager. A concrete statement concerning this error

Instrument	SW	LW
General paper	Laszlo (1998), Li(1992,1999), Liang(1999,2000) (for surface albedo)	
Landsat TM	Knap(1999) (glacier), Greuell(2003) (glacier)	
HIRS		Ellingson (1989, 1993), Ba(2003), Lee(2004)
AVHRR	Wydick(1987), Jacobowitz(1991), Li(1992), Valiente(1995), Hucek(1995), Godoy(2002), Hollmann(1998), Greuell(2003) (glacier), Feng(2005)(ScaRaB)	Gruber (1978,1984,1990,1994), Ohring (1984), Bess(1989), Liebmann(1996), Hollmann(1999)
PolDER	Javioc(2002), Jacob (2002)	
MISR	Sun(2006), Stroeve(2002)(snow), Greuell(2003) (glacier)	
MODIS	Liang(2002)(surface albedo), Loeb and Manalo-smith (2005) (aerosol over ocean), Greuell(2003) (glacier)	
VIIRS	Liang(2005)(surface albedo)	
ScaRaB (NB)	Feng(2005)	Chen(2002)
GOES	Minnis (1984), Briegleb(1986), Li(1992), Chakrapani(2003), Doelling(1997,1998), Khaiyer(2002)	Minnis (1984, 1991), Brooks(1989), Young(1990), Khaiyer(2002), Doelling (2003), Ba(2003), Lee(2004, 2008)
Meteosat 1st Gen.	Gube(1982), Stum (1985), Nacke (1991), Duvel (1985),Valiente(1995)	Saunders (1980), Duvel (1985), Schmetz (1988), Gube(1988), Kandel(1988,1990) ,Cheruy (1989,1991)
Meteosat-5 (IODC)	Viollier (2004)	Viollier (2004)
MSG	Geiger(2003,2005), Clerbaux(2002), Marsouin(2005), Clerbaux(2005), Cros (2006), Lorenz(2008)	Clerbaux(2002), Lee(2008)
GMS	CERES team	Collins(1997), CERES team

Table 2.2: Non–exhaustive list of estimation of BB unfiltered SW and LW radiances from NB observations. First author and year are given.

is indeed a prerequisite to decide if geostationary BB observations must continue on Meteosat Third Generation (MTG) or if abundant and accurate NB observations are sufficient. The SEVIRI NB–to–BB conversions have been analyzed using both theoretical and empirical approaches, as reported in Sections 4.8 (SW) and 5.8 (LW). Similar investigations are done for the Meteosat first generation satellites (Sections 4.9 and 5.9).

Chapter 3

Instruments and Data Used

3.1 The Geostationary Earth Radiation Budget (GERB)

3.1.1 Mission

The main purpose of operating a broadband radiometer on the geostationary orbit is to measure the Earth radiation budget in a quasi–continuous manner. As already stated, this can not be achieved with a low Earth orbit instrument. Measurements at high frequency are needed to understand processes that develop over short time periods, like the tropical convection, and might involve feedback mechanisms that last over short–time periods. These new data could provide a better understanding of the phenomena and improve the modeling of the climate system, especially in its temporal variability. The initial science plan for GERB (Harries & Crommelynck, 1999) identified 5 main areas of use of the GERB data: radiation budget studies, evaluation of numerical models, meteorological and other exploitations, Earth observation science, education and public understanding. Table 3.1 reviews the exploitation of the data at the beginning of 2008, about 4 years after commissioning the first GERB instrument and 2 years after the Edition 1 data release. The first GERB instrument was developed as an ESA/EUMETSAT co–passenger opportunity for the SEVIRI imager on MSG–1. Later, EUMETSAT decided to fund additional GERB instruments for the next 3 MSG satellites. The GERB dataset will therefore extend over more than 15 years. This should allow direct observation of the climate variability and possible trends in the radiation balance. Harries *et al.* (2005) provide the full description of the GERB mission and instrument.

In regard to the previous broadband radiometers like the ERBE scanner, the CERES, or the ScaRaB, the design of the GERB instrument and of its data processing system gives rise to a set of challenges to be tackled. The critical piece of the instrument is the de–spin mirror which is necessary to counteract the spin stabilization of the Meteosat satellites (100 rpm). The characterization of the instrument is also complex as it is based on an array of 256 detectors.

Each detector has its specific gain, time constant, and spectral and spatial response functions. Concerning the data processing, the unfiltering is challenging because the instrument shows greater spectral structure in its SW and LW responses, for instance compared to CERES. This is due to the 5 mirrors arrangement of the optics that is made necessary by the orbit distance. Innovative spatial and temporal modeling is needed to estimate the LW from the TOT and SW measurements, because they are neither simultaneous (time difference up to 170s) nor taken at the same place. As a given place on the Earth is always observed from a same direction, the GERB radiance–to–flux conversion is especially challenging because any error at this level is likely to introduce biases in the GERB flux.

Four identical GERB instruments (G1 to G4) have been built and characterized. Before the launch of MSG–1, it was decided to assemble the G2 on the satellite and to re–characterize the G1 instrument. G1 was launched on MSG–2 in August 2005. The current plan is to launch the G3 and G4 instruments at the beginning of 2011 and 2013, respectively on MSG–3 and MSG–4.

3.1.2 The GERB instruments

The GERB detector is an array of 256 bolometers covered with an absorbing black paint coating. The detector array is exposed during 40ms to a vertical portion of the FOV. As the Meteosat satellites are spin–stabilized, a de–spin mirror is set in the optical path of the instrument to "freeze" the observed region during the 40ms acquisition time. This mirror is rotating in the reverse direction at half the angular velocity of the satellite. At each rotation of the satellite, the vertical stripe is moved in the left–right direction. An image of 282 columns by 256 lines is constructed in 169.2s (282 satellite revolutions). During the following 169.2s, a quartz filter is set in the optical path to transmit only the SW radiation at wavelength lower than about 5μm. Figure 3.1 shows an example of a GERB SW image (with the filter) and a TOT image (without the filter). The telescope is a three mirrors anastigmatic system that performs the appropriate magnification. This part of the instrument was designed and manufactured in Belgium by the AMOS and OIP companies. A fifth mirror is added to reduce the sensitivity to the polarization of the incoming radiation.

The whole system observes successively: the Earth (40ms), the SW calibration monitor (integrating sphere) and the thermal blackbody. The Earth view count is converted in filtered radiances using, for each detector, a gain and an offset derived from the thermal blackbody and space views. Although the gain of each detector can be evaluated for each Earth view, it has been demonstrated that better in–flight performances are obtained by temporal filtering of the gain values. For the SW measurement, the transmission of the quartz filter must be taken into account. This transmission and the responses of the detectors to the visible light have been characterized on–ground using the VISible Calibration Source (VISCS), a tungsten

Field	Applications
Radiation Budget Studies	• **Climate monitoring:** monthly means TOA fluxes are built operationally in the frame of the CM–SAF (Woick *et al.*, 2002). Methodology and first results are described in (Caprion *et al.*, 2005; Dewitte *et al.*, 2002a,b; Nicula *et al.*, 2002). • **Regional climate:** the data is used in regional climate campaigns like the RADAGAST component of the AMMA (Miller & Slingo, 2007). Summer 2006 ERB anomaly over Europa has been demonstrated (Dewitte *et al.*, 2007). • **Cloud feedbacks:** Futyan (2005) and Futyan & Del Genio (2007) used GERB(-like) data to study the convective clouds forcing. A methodology to derive clear sky fluxes is developed (Futyan & Russell, 2005). Futyan *et al.* (2005) have demonstrated the interest of geostationary observation to quantify cloud radiative forcing according to cloud type. GERB observations of the radiative properties of low level stratus clouds are used by Daniela Nowak (MeteoSwiss, Payerne). • The **diurnal cycle** of water vapor, of convection, and of land surface temperatures is addressed with Empirical Orthogonal Functions (EOFs) by Comer *et al.* (2007) at ESSC. This work started with the OLR. Nowicki & Merchant (2004) studied the diurnal cycle of deep convective cloud forcing with GERB–like data. • **Surface radiation budget and albedo:** The CM–SAF Surface Radiation Budget (SRB) is based on GERB (Hollmann *et al.*, 2006). Similar SRB in the land and ocean SAFs could use GERB data in Near Real–Time (NRT) or "off-line" for validation of NB–to–BB conversions. • **Aerosol forcing:** Haywood *et al.* (2005) have studied the forcing due to a large Sahara dust outbreak. Similar studies are performed at Imperial College (Brindley & Ignatov, 2006; Brindley & Russell, 2006), Environmental Systems Science Centre (Slingo *et al.*, 2006) and RMIB in the frame of the CM–SAF(De Paepe *et al.*, 2008). Quantifying radiative effect of volcanoes eruptions is another application of GERB data (Bertrand *et al.*, 2003).
Evaluation of Numerical Models	Continuing previous analysis done with Meteosat–7 (Slingo *et al.*, 2004), Allan *et al.* (2005, 2007) routinely compare the GERB and the UK Met–Office model fluxes since the beginning of the GERB observations. This already showed that the model radiative scheme presents inaccuracies over: marine stratocumulus, Saharan vegetation, mineral dust aerosol, cirrus outflow, and convective clouds. Bertrand *et al.* (2002) showed that surface albedo from GERB/Meteosat could improve the skill of a NWP model (e.g. ALADIN).
Meteorological and other exploitation	The near real–time generation of the GERB products allows their use in meteorological applications, for problems where accurate radiative fluxes are needed. While different uses have been analyzed they remained at the level of idea or proposal, like the use of GERB data in a 1–dimensional fog model.
Earth Observation Science	• The analysis of the GERB radiances on their own is done in the CAL/VAL activities. Velazquez-Blazquez *et al.* (2007) validate forward modeling of TOA fluxes at the Valencia Anchor Station (Lopez-Baeza *et al.*, 2004) using GERB observations. • Attempts have been done to retrieve/validate instrument spectral response from the GERB observations (Glyn Spencer at Leicester University). • The analysis of the GERB radiance in conjunction with the SEVIRI NB observation allowed deriving accurate empirical NB–to–BB regressions (see this work). Similar developments are done for the Meteosat first generation (Clerbaux *et al.*, 2007). • In conjunction with CERES data, GERB is of help in the study of angular reflectance characteristics (ADMs) and allows detecting angular conversion problem (Bertrand *et al.*, 2008).
Education and Public Understanding	At the Belgian level this covers: a permanent near real–time display of GERB and SEVIRI data at the federal planetarium and at the EuroSpaceCenter, different contributions in the press and in books, university lessons. Similar efforts are done by our colleagues in UK.

Table 3.1: GERB science plan and main realizations as at beginning of 2008. Prior to the Edition1 data release, some of these works were done using GERB–like data from Meteosat–7 (the authors indicated however interest in GERB).

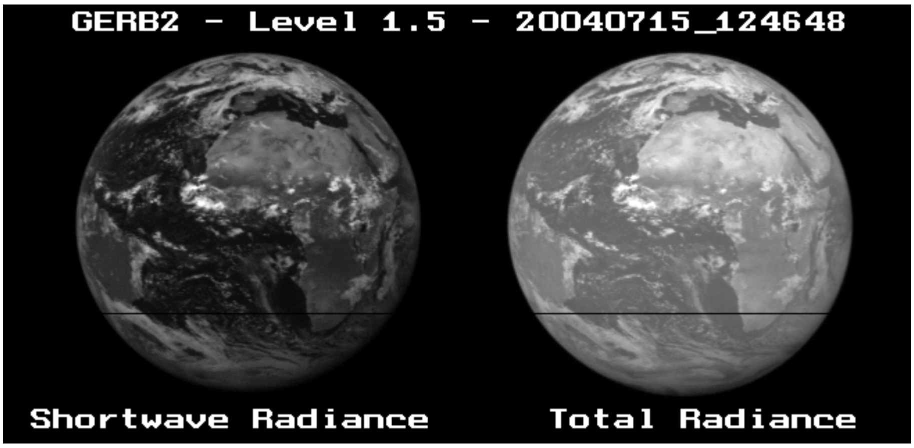

Figure 3.1: Illustration of the GERB SW and TOT broadband images.

lamp that emits like a 3000K blackbody. Figure 3.2 (right) shows that the VISCS peaks in the near infrared at a longer wavelength than the visible radiation. For this reason, the absolute calibration of the GERB SW channel may suffer from any error in the spectral response determination between the visible and the near–infrared.

The preflight characterization of the instrument spectral responses is done at the Earth Observation Characterization Facility (EOCF) of the Imperial College (UK). They use the detector characterization performed at Leicester University and at UK National Physical Laboratory. For GERB–2, it has been observed that the spectral responses show nonrealistic variations between the individual detectors . These variations have been attributed to random errors introduced during the characterization process of the detector elements. Therefore, it was decided not to use the individual detector spectral response but to use instead the average response over all the detectors. Furthermore, as the variability due to the different optical paths in the optics is small, the individual system level responses ϕ^{det} have been replaced by their average

$$\phi_{sw}(\lambda) = \frac{1}{256}\sum_{det=1}^{256}\phi_{sw}^{det}(\lambda) \tag{3.1}$$

$$\phi_{lw}(\lambda) = \frac{1}{256}\sum_{det=1}^{256}\phi_{lw}^{det}(\lambda) \tag{3.2}$$

$$\phi_{tot}(\lambda) = \frac{1}{256}\sum_{det=1}^{256}\phi_{tot}^{det}(\lambda) \tag{3.3}$$

Figure 3.2 illustrates these average spectral response curves for the G2 instrument. The pixel–to–pixel variability in spectral response is problematic, because in the Edition 1 data processing the LW is estimated by spatial and temporal interpolation of the TOT channel at the SW time and PSF location. This interpolation implicitly assumes that all the lines in the TOT image correspond to an identical filtered radiance quantity. This problem is addressed in the technical note (TN31) and summaries are given in Sections 4.7 (SW) and 5.7 (LW).

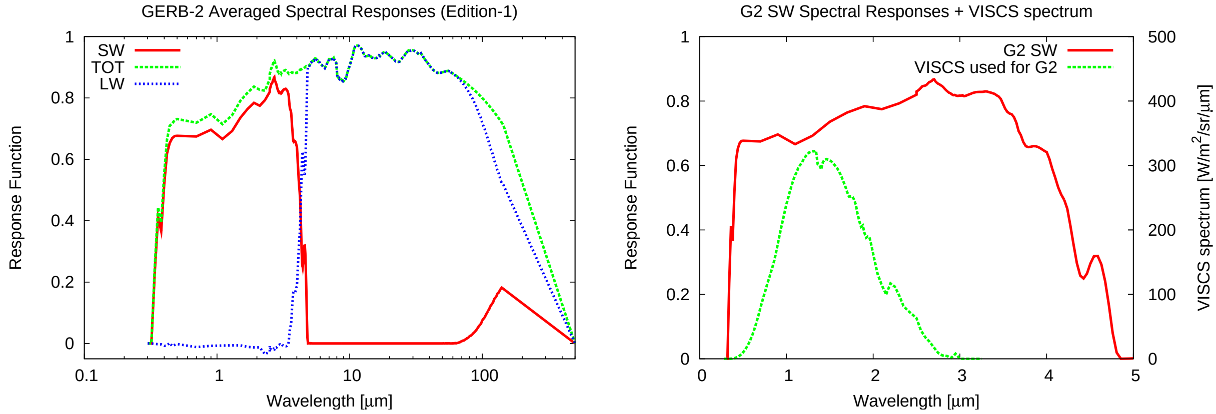

Figure 3.2: Average spectral response curves for GERB–2 (left) and details in the SW with the spectrum of the VISCS (right).

The GERB observations are made over Point Spread Functions (PSF) with (in average) a full–width half maximum of 68km east–west × 38km north–south at satellite nadir. The tails of the PSF extend much further (e.g. 140km × 71km for the full–width at the 10% sensitivity level).

3.1.3 The GERB data processing

The ground processing is organized between the Rutherford Appleton Laboratory (RAL, UK) and the RMIB. The RAL receives the raw GERB packets from EUMETSAT and performs data calibration and geolocation. The resulting level 1.5 Non–Averaged Non–Rectified Geolocated (NANRG) is then transferred to the RMIB where the level 2 data are derived. The RMIB tasks cover: (i) the estimation of the LW radiance by subtraction of the SW radiance from the TOT radiance, (ii) the estimation of the BB SW, LW and TOT radiances from SEVIRI (narrowband–to–broadband), (iii) the tuning of the RAL geolocation by matching of the GERB footprint measurements in the images of SEVIRI estimate, (iv) the estimations of the contaminations (thermal radiation in the SW channel and solar radiation in the LW channel), (v) the unfiltering of the SW and LW channels, (vi) the scene identification, (vii) the conversion of solar and thermal radiances in fluxes, (viii) the rectification on the ARG grid, (ix) the enhancement of the spatial resolution to the High–Resolution (HR) grid using estimated BB radiances from SEVIRI, (x) the spatial and temporal processings to the BARG grid. The level 2 products are then made available in near–real time to the scientific community via the RMIB On-Line Short-term Service (ROLSS) FTP site. On a regular basis, various tests and quality controls (including human inspection) are performed on the near-real time data. The data with the nominal quality are renamed "Edition" and are archived at the RAL in the GGSPS (GERB Ground Segment Processing System). Dewitte *et al.* (2008) give an overview of the RMIB part of the processing which is called the RMIB GERB Processing (RGP). Details are available in technical notes, proceeding papers (Clerbaux *et al.*, 2003a,b; Dewitte *et al.*, 2003; Gonzalez *et al.*, 2000), and in journal papers: (Bertrand *et al.*, 2005) for the ADM issues, (Clerbaux *et al.*, 2008a,b) for the unfiltering, (Ipe *et al.*, 2008) for the cloud retrieval.

3.1.4 The GERB level 1.5 data (NANRG)

The level 1.5 data (NANRG) consists essentially of instantaneous filtered SW and TOT radiances with the corresponding characteristics of the acquisition, including the geolocation of the footprint. The geolocation is estimated at the RAL from information about the MSG satellite location and attitude, the angular position of the de–spin mirror, and an optical model of the instrument (optical path of the radiation within the instrument). The accuracy of the geolocation in the NANRG data is unfortunately out of the targeted accuracy of 0.1 pixel (Bates *et al.*, 2004). Consequently, a tuning of the geolocation has been implemented in the RGP by matching each GERB column in the SEVIRI BB estimate images. The error on the matched geolocation is unbiased and presents a noise with standard deviation of about 0.25 GERB pixel (Russell, 2006).

The level 1.5 NANRG data are not foreseen to be used by the scientific community as they provide only instrument filtered radiances. However, the NANRG data are useful for validation activities and to study the pixel–to-pixel variability. Directly unfiltered GERB data (Sections 4.4 and 5.4) can be produced at the detector level from the NANRG files.

3.1.5 The GERB level 2 data (ARG, BARG and HR)

The GERB level 2 data provide TOA unfiltered radiance and flux for the SW and LW. The level 2 data are available in 3 formats that differ in the spatial and temporal processing applied to the GERB observations. Although the geolocation of the GERB footprint (PSF) is changing at each scan, the level 2 data are always provided on constant rectified geostationary grids. Therefore, the production of the GERB level 2 data involves rectification processes which are different for the 3 formats as described in (Dewitte *et al.*, 2008) and summarized hereafter.

The **Averaged Rectified and Geolocated (ARG)** data are an average of three successive GERB scans (covering a period of approximately 17 minutes) presented on a regular (in viewing angle) grid with a sampling distance of 44km × 44km at nadir. The ARG values are obtained by bilinear interpolation of the original observations. As no attempt is made to correct for the GERB PSF the radiance and flux values at each grid point are representative of the energy from a larger region than the grid spacing. Additionally, the GERB geolocation noise and the linear interpolation of the observations will affect the radiance and flux values at each point.

The **Binned Averaged Rectified and Geolocated (BARG)** products are averages over fixed 15 minute time intervals (00:00 to 00:15 UTC, 00:15 to 00:30 UTC, etc) presented on a regular (in viewing angle) grid with a spacing of 45km × 45km at nadir. The processing is considerably more complex than for the production of the ARG data. It attempts to remove the effect of the PSF, and also provides corrections for errors that may have been introduced in the ARG by the geolocation and rectification processes. This is achieved by using fine scale estimates of the broadband SW and LW radiances inferred from NB measurements made by the SEVIRI instrument on the same MSG satellite. The SEVIRI narrowband–to–broadband estimation is described in (Clerbaux *et al.*, 2005) and in Sections 4.8 (SW) and 5.8 (LW). Merging the GERB BB observations and the fine–scale SEVIRI BB estimates results in level 2 BARG radiances and fluxes which are representative of the radiation from exact 15 × 15 SEVIRI pixel areas (i.e. 45km × 45km).

Finally, the **High Resolution (HR)** product is presented on a grid with a spacing of 3 × 3 SEVIRI pixels (i.e. 9km × 9km at nadir). It is provided every 15 minutes as instantaneous values at the time of the SEVIRI observations. As for the BARG, fine scale estimates of the BB radiances from SEVIRI are combined with GERB observations to produce the GERB High Resolution data. The GERB HR product is requested to study the radiation budget at relatively small scales (e.g. valley fog).

The current state–of–the–art version of the GERB–2 data is the 'Version 3' (V003). After validation and manual quality checks, the Version 3 is relabeled 'Edition 1' and is put in the GERB archive. Currently validated Edition 1 data only exist for the ARG format. However, Version–3 BARG and HR data have been made available for validation activities in anticipation of their future release.

It can be demonstrated that, in all sky condition, the 3 GERB formats are in mutual agreement when the radiances or the fluxes are averaged over sufficiently large areas and long time interval. These averages are needed to account for the differences in PSF and in time definition. Methodology and results are provided in the technical notes (TN43). Figure 3.3 shows the result of the spatial average for the GERB–1 solar radiance $L(t)$ (left) and flux $F(t)$ (right) for the 5th of May 2007 over a large area. Similar plots can be made for the thermal radiation. The curves for the 3 GERB formats cannot be discriminated on the graph. When integrated over hourly time interval, the 3 GERB formats match very well, with observed random differences below 0.2% (TN43).

It is also evident that differences between the GERB formats occur when the data is interpolated over a given location. The problem has been experienced by our colleagues at the MeteoSwiss aerological station in Payern. They used GERB data to validate radiative transfer simulations in fog and low stratiform cloudiness over the Swiss Plateau in winter conditions. Figure 3.4 shows the GERB fluxes during 4 days when this type of cloudiness was observed at Payern. The diurnal cycles of solar and thermal fluxes show significant differences between the HR format on the one hand and the BARG and ARG formats on the other hand. The color composite

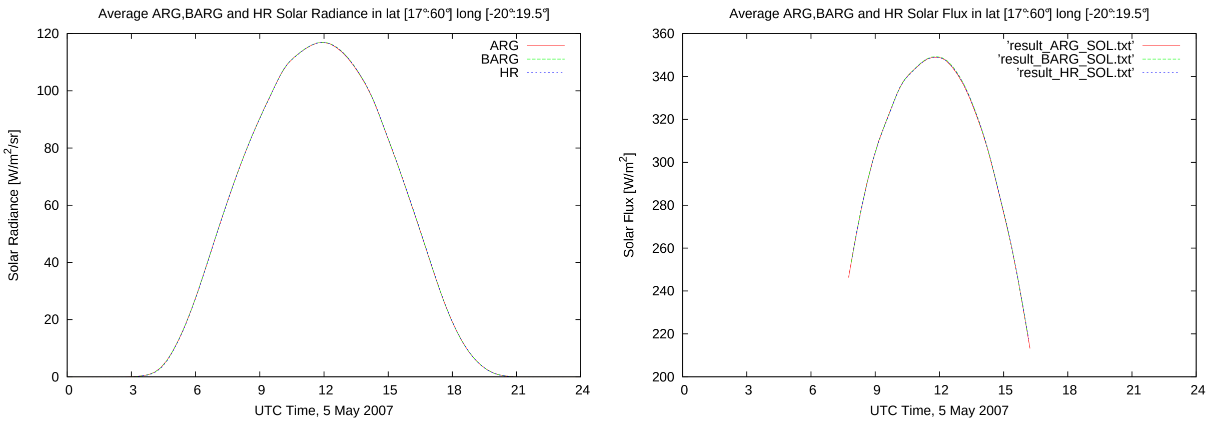

Figure 3.3: Equivalence of average ARG, BARG and HR solar radiance (left) and flux (right) over the area (−20°W to 19.75°E and 17°N to 60°N).

images on the left show that the BARG and ARG pixel sizes are too coarse with respect to the studied phenomena. The 9km × 9km spatial resolution of the HR format is clearly an asset to study local scale objects.

The GERB/CERES comparisons reported in (Clerbaux *et al.*, 2008c), and in Sections 4.6, 5.6, 6.5, and 7.5 of this document, provide evidence of another difference between the GERB formats. The statistical analysis of the ratio GERB/CERES shows higher scene type dependency for the ARG than for the BARG and HR formats. This will be discussed in more detail in Section 4.6.

3.1.6 Accuracy of the GERB radiances

The aimed absolute accuracy of the GERB products is 1% at 1 Standard Deviation (SD) for both the unfiltered SW and LW radiances. However, the theoretical accuracy of the Edition 1 GERB products does not meet this target for the SW channel. The sources of uncertainty are quantified in terms of maximum error in the Quality Summary for the GERB level 1.5 ARG products (Russell, 2006). In terms of 1 SD error, the uncertainties translate to (Jacqui Russell, pers. comm.): the absolute calibration (SW=0.22% and LW=0.05% at 1 SD), spectral response characterization (SW=1.9% and LW=0.9% at 1SD), and unfiltering process (SW=0.56% and LW=0.06% at 1 SD). A root mean square sum of these errors leads to uncertainties at 1 SD of 1.99% (SW) and 0.9% (LW). In both cases, the main source of the uncertainty is the characterization of the GERB spectral sensitivity. It is worth noting that there are ongoing studies relating to the ground characterization of the GERB–2 spectral response which may result in changes to this parameter for the GERB Edition–2 processing. This could modify the absolute level of the GERB SW channel.

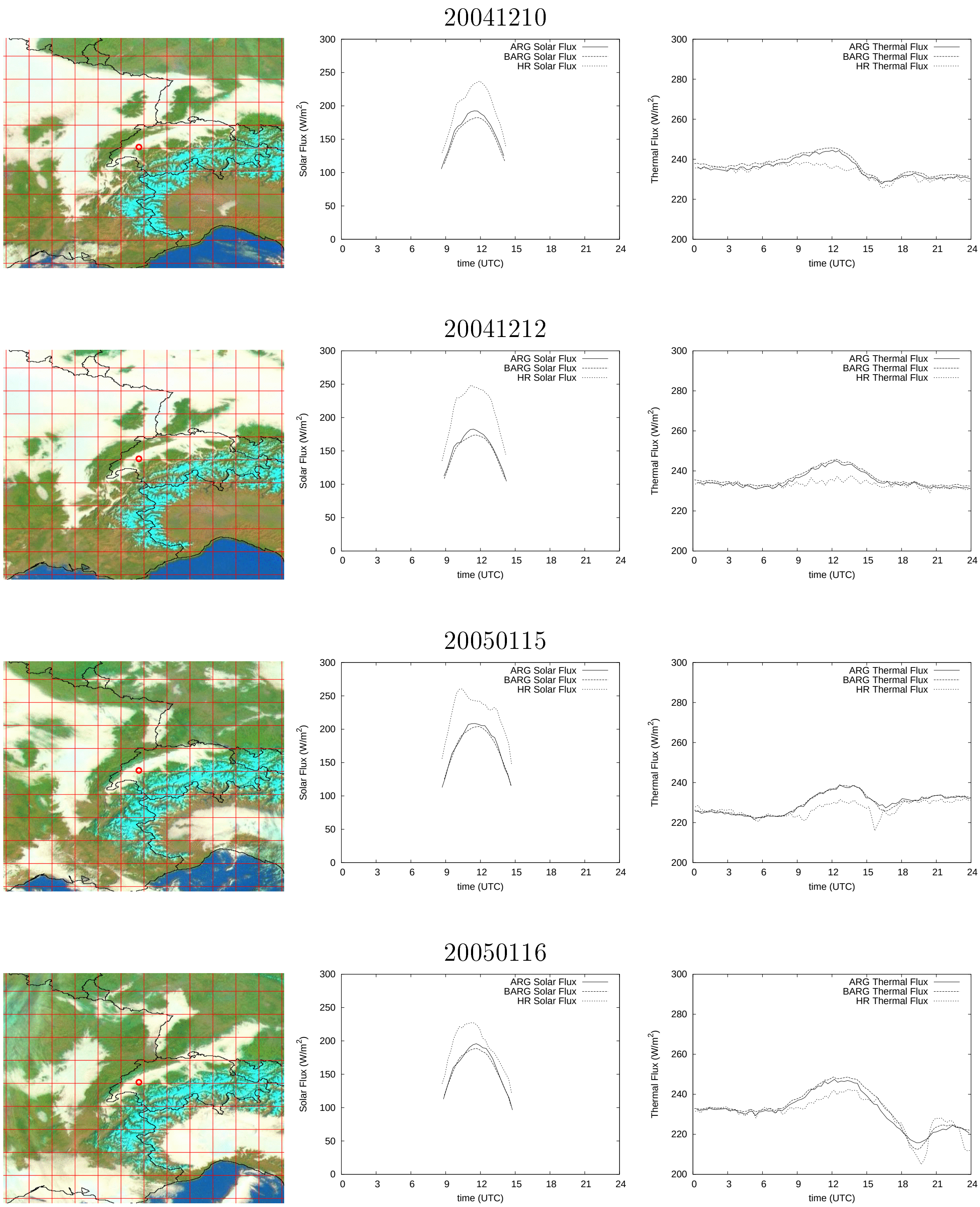

Figure 3.4: Comparison of the GERB ARG, BARG and HR formats over Payern (Switzerland) during 4 days with stratiform low clouds. The left images are SEVIRI "natural color" (RGB composite of the 0.6μm (blue), 0.8μm (green) and 1.6μm (blue) channels) at 12:00 UTC with the BARG grid and the station position (red).

3.2 The Meteosat imagers

3.2.1 Mission

Although initially developed by the French Centre National d'Etudes Spatiales (CNES) in the 70'ies, the first Meteosat satellite was realized by the European Space Research Organization (ESRO). Its prime mission is the imagery from the 0° geostationary longitude for operational meteorology in the frame of the Coordination Group for Meteorological Satellites (CGMS). In parallel, backup and redundant Meteosat satellites have supported the INDian Ocean EXperiment (INDOEX, Ramanathan & coauthors, 2001), the rapid scanning service (more frequent scan of a limited latitude band), and the Atlantic Ocean coverage during a period of unavailability of a GOES satellite. To date, the Meteosat series includes 9 satellites. Their launch dates and the periods when they have been in charge of the operational 0° service are given in Table 3.2.

On the first generation of Meteosat satellites (Meteosat–1 to –7), the imaging instrument is the Meteosat Visible and InfraRed Imager (MVIRI) which provides 30 minute's observations in 3 spectral bands (VIS, WV, IR). On the Meteosat second generation satellites, the Spinning Enhanced Visible and Infrared Radiometer Imager (SEVIRI, Schmetz *et al.*, 2002) provides 15 minute's observation in 12 spectral bands. It was early recognized that the SEVIRI images could be valuable for many more geophysical applications than strictly the meteorology. For this reason, EUMETSAT introduced the concept of Satellite Application Facilities (SAF). The Climate Monitoring SAF is one realization of EUMETSAT in the framework of the enlarged convention of the organization to include operational climate–oriented missions[1].

Satellite	Launch	Operational service
Meteosat-1	23/11/1977	09/12/1977 – 25/11/1979
Meteosat-2	19/06/1981	16/08/1981 – 11/08/1988
Meteosat-3	15/06/1988	11/08/1988 – 19/06/1989
Meteosat-4	06/03/1989	19/06/1989 – 04/02/1994
Meteosat-5	02/03/1991	04/02/1994 – 13/02/1997
Meteosat-6	20/11/1993	13/02/1997 – 03/06/1998
Meteosat-7	02/09/1997	03/06/1998 – 01/02/2004
Meteosat-8	28/08/2002	01/02/2004 – 10/04/2007
Meteosat-9	22/12/2005	10/04/2007 – onward

Table 3.2: Meteosat First and Second Generations: launch date and period in charge of the operational 0° imagery service. Rigollier *et al.* (2002) provided a detailed history up to 2002, including the numerous switches to the backup spacecraft during decontamination or failures.

[1]"The primary objective of EUMETSAT is to establish, maintain and exploit European systems of operational meteorological satellites, taking into account as far as possible the recommendations of the World Meteorological Organization. **A further objective of EUMETSAT is to contribute to the operational monitoring of the climate and the detection of global climatic changes**." from the amended EUMETSAT convention.

3.2.2 The Meteosat Visible and InfraRed Imager (MVIRI) instrument

The acquisition mechanism exploits the spin stabilization of the satellite platform. At each revolution of the satellite there is acquisition of 1 water vapor (WV) line, 1 infrared (IR) line, and 2 visible (VIS) lines (with 2 detectors). The sampling distances are 5km for WV and IR and 2.5km for the VIS.

The spectral responses of the successive MVIRI instruments are available from EUMETSAT and show some variations between the different instruments. The visible (VIS) spectral response is relatively broad, ranging from 0.5μm to 1.1μm. Govaerts (1999) suggests and justifies that for Meteosat–5 and –6 the "official" VIS spectral response provided by EUMETSAT would better be replaced by the curves of Meteosat–7. This suggestion is followed in this work. It is also suggested to extrapolate the VIS channel spectral response in the near infrared. Indeed, the characterization is done up to 1.1μm but the instrument still presents some sensitivity at higher wavelength.

EUMETSAT IMage Processing Facility (IMPF) produces the level 1.5 data by: (i) equalization of detector's response, (ii) compensation of non–linearity, and (iii) rectification on a constant grid. Data are distributed as 8 bits[1] photometric counts that can be converted in physical radiance units using the calibration coefficients.

To use Meteosat pictures for Earth radiation budget studies, an accurate absolute calibration is necessary. State–of–the–art calibration coefficients for Meteosat first generation have been reprocessed recently by EUMETSAT in support of different climate–oriented programs (e.g. ECMWF reanalysis). In this context, the vicarious calibration method developed for SEVIRI (see hereafter) has been applied to the Meteosat first generation VIS channel. Govaerts *et al.* (2004a) describe the application of the SEVIRI Solar Channel Calibration (SSCC) method to the VIS channel of Meteosat–7 and –5. The EUMETSAT website provides the best coefficients to estimate the calibration coefficient in the form of a value at the launch date and a linear daily drift. These calibration coefficients must be adapted in case of modification of the gain level of the channel as was done during the Meteosat–2 and –3 lifetime. The method provides, for the first time, consistent calibration parameters for the full Meteosat dataset (except Meteosat–1). These values are in good agreement with the calibration derived at RMIB by unfiltering of the Meteosat–5 and –7 VIS channels and comparison with CERES data. This work is described in (Govaerts *et al.*, 2004a) and the unfiltering of the Meteosat VIS channel is addressed in Section 4.9. Figure 3.5 shows the agreement between the SSCC and the RMIB calibration for Meteosat–7. The RMIB calibration coefficients are systematically 3% higher than the EUMETSAT values. The SSCC calibration is also in good agreement with the calibration derived at CMS Lannion for the Ocean and Sea Ice (OSI) SAF (Le Borgne *et al.*, 2004), both in terms of absolute calibration

[1]For the pre–operational Meteosats (–1 to –4), the visible channel resolution is only 6 bits.

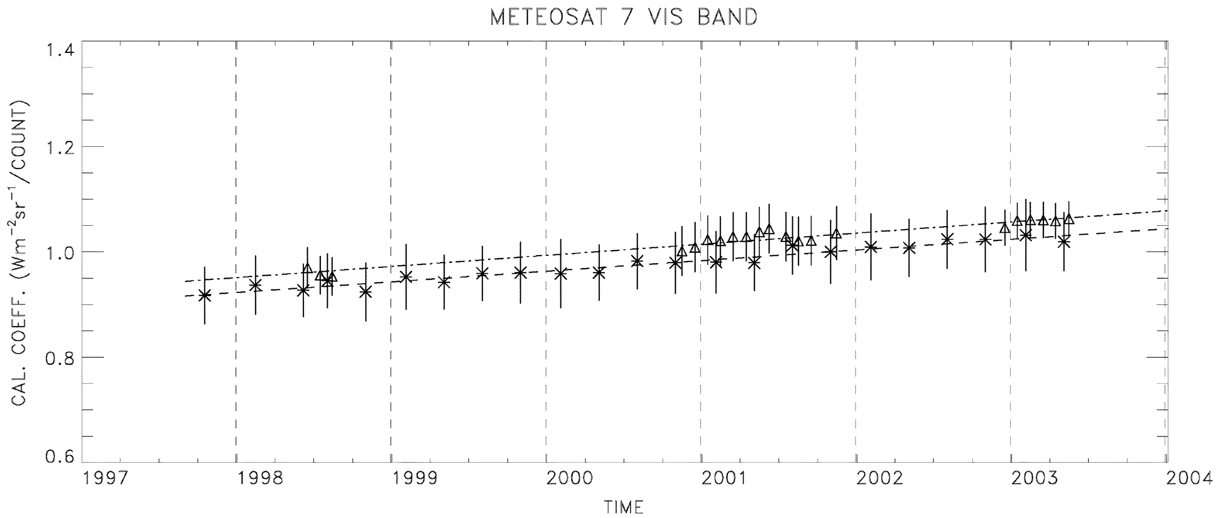

Figure 3.5: Meteosat–7 sensor calibration and drift derived with the operational EUMETSAT method (* symbol) and derived at RMIB from CERES comparison (Δ symbol). From (Govaerts *et al.*, 2004a).

and degradation. Viollier *et al.* (2004) have calibrated the Meteosat–5 VIS channel over the Indian Ocean. Finally, based on comparison with NOAA, Desormeaux *et al.* (1993) provide the calibration for the different Meteosat satellites that are used for the ISCCP. A relative calibration method is proposed by Rigollier *et al.* (2002) based on the percentiles 5% (dark scenes) and 80% (bright scenes) of the count value. Day–to–day fluctuation of the calibration coefficient of ±5% is observed. All these works are of lesser achievement compared to what is currently available from EUMETSAT with the SSCC method.

For the WV and IR channels, a vicarious calibration has been used for a long time. The calibration of the IR channel is based on clear sky ocean scenes with sea surface temperature from the NCEP model. The WV channel is calibrated from radiances simulated by a radiative transfer model based on atmospheric profiles provided by radiosondes. For Meteosat–7, on board blackbodies allow the absolute calibration of the WV and IR channels . This absolute calibration level is then transferred to Meteosat–5 by cross calibration.

3.2.3 The Spinning Enhanced Visible and Infrared Radiometer Imager instrument (SEVIRI)

As for the MVIRI, the acquisition mechanism exploits the spin stabilization of the platform (Pili, 2000b). Observations are done in 12 spectral channels using 3 detectors per standard channel and 9 detectors for the High Resolution Visible (HRV) channel. The SEVIRI channels are listed in Table 3.3 together with a short description of their application in this work. Despite careful on–ground checks, it is not possible to totally prevent failures of some of the 42 detectors. This was the case for a WV 6.2μm detector of MSG–2 which provided excessively noisy signals.

Channel	type	λ_{cen}	λ_{min}	λ_{max}	accuracy	Use in this work
HRV	VIS	BB [0.4 – 1.1] μm			5%	channel calibration/validation of the SSCC method (§4.9).
VIS 0.6	VIS	0.635	0.56	0.71	5%	cloud detection and optical depth over land (§6.3), SW NB-to-BB (§4.8), GERB SW unfiltering (§4.5), GERB clear ocean unfiltering (§4.5).
VIS 0.8	VIS	0.81	0.74	0.88	5%	cloud detection and optical depth over ocean (§6.3), SW NB-to-BB (§4.8), GERB SW unfiltering (§4.5).
IR 1.6	NIR	1.64	1.50	1.78	5%	cloud phase (§6.3), SW NB-to-BB (§4.8), GERB SW unfiltering (§4.5).
IR 3.9	WIN	3.90	3.48	4.36	0.35K@300K	not used in this work due to the difficulty to separate solar and thermal radiation in the channel.
WV 6.2	WV	6.25	5.35	7.15	0.75K@250K	LW NB-to-BB (§5.8), GERB LW unfiltering (§5.5), LW ADM (§7.4).
WV 7.3	WV	7.35	6.85	7.85	0.75K@250K	LW NB-to-BB (§5.8), GERB LW unfiltering (§5.5).
IR 8.7	WIN	8.70	8.30	9.10	0.28K@300K	LW NB-to-BB (§5.8), GERB LW unfiltering (§5.5).
IR 9.7	0_3	9.66	9.38	9.94	1.5K@255K	LW NB-to-BB (§5.8), GERB LW unfiltering (§5.5).
IR 10.8	WIN	10.8	9.8	11.8	0.25K@300K	LW NB-to-BB (§5.8), GERB LW unfiltering (§5.5), LW ADM (§7.4), cirrus detection (§7.5), cloud phase (§6.3).
IR 12	WIN	12.0	11.0	13.0	0.37K@300K	LW NB-to-BB (§5.8), GERB LW unfiltering (§5.5), LW ADM (§7.4), cirrus detection (§7.5).
IR 13.4	$C0_2$	13.4	12.4	14.4	1.8K@270K	LW NB-to-BB (§5.8), GERB LW unfiltering (§5.5), LW ADM (§7.4).

Table 3.3: The spectral channels of SEVIRI, the accuracy requirements for the calibration (Pili, 2000b) and the applications of the channels in this thesis (symbol § means Section).

A software patch has been implemented in the IMPF processing to correct this detector using the signals from the adjacent detectors. It was checked that this does not impact the GERB processing. However, it would be more annoying if such a failure happens to affect a visible channel detector used for cloud detection (0.6μm or 0.8μm).

At the sub–satellite point, the spatial sampling of the instrument is 3km (1km for HRV) while the instantaneous FOV of the detectors is 4.8km (1.67km for the HRV). The spatial co–registration requirement is 0.75km between the thermal channels and 0.6km between the solar channels. This is an important feature as multispectral techniques implicitly assume a precise co–registration of the spectral bands (although some co–registration errors can be resolved by the level 1.5 rectification).

The spectral responses are provided by EUMETSAT. After 5 years of operating SEVIRI, there is no evidence of characterization error or of significant aging affecting these curves. For the thermal channels the calibration is performed using the internal blackbody as warm source (Pili, 2000a). The deep space is used as the cold source. A particularity of the SEVIRI instrument is that the warm calibration source is not observed through the front optic. This necessitates to correct the blackbody calibration by the front optic spectral transmission. The requirements

Satellite	From (YYYYMMDDhhmm)	VIS 0.6μm	VIS 0.8μm	NIR 1.6μm	HRV
Met-8	200401010000	0.022717	0.029433	0.023239	0.031333
-	200402111730	0.022950 (+1%)	0.029216 (-0.7%)	0.023279 (+0.2%)	0.031376 (+0.1%)
-	200504010945	0.023128 (+0.8%)	0.029727 (+1.7%)	0.023622 (+1.5%)	0.031999 (+2%)
Met-9	200609250645	0.020135	0.025922	0.022258	0.029499

Table 3.4: Calibration coefficients for the visible channels of Meteosat–8 and –9 provided in NRT in the SEVIRI header. The coefficients are given in $\mathrm{mWcm^{-2}sr^{-1}(cm^{-1})^{-1}/DC}$, with DC = Digital Count. The adjustments of the coefficients are also given as percentage in parenthesis.

concerning the absolute accuracy of the calibration are given in Table 3.3.

For the solar channels, including the HRV, a calibration based on radiative transfer computations over bright desert targets is performed on a regular basis by Govaerts *et al.* (2001). This method is called the SEVIRI Solar Channel Calibration (SSCC). Its accuracy is assessed to be better than 5% after one year of operation (10 % during the first year). As an independent validation of the SSCC approach, we have performed a cross calibration of the HRV channel with the broadband observations from the CERES FM2 instrument. The results obtained are in close agreement with the SSCC calibration. Differences of +3.3% and +1.5% for August and November 2003 are reported in the technical note EUM/MSG/TEN/04/0024[1]. It is worth noting that this does not prove that the SSCC method performs correctly when it is applied to the narrow channels of SEVIRI. When necessary, the calibration coefficients distributed in the header file to the NRT users are adapted. Consequently, the calibrations of the visible channels present "jumps" instead of slow drifts that could be expected by aging. Table 3.4 and Figure 3.6 give the NRT SEVIRI calibration used within the GERB processing. On 11 Feb. 2004, some days after the satellite was declared operational, a first change was done. A second change of the visible channel calibration took place on the 1st of April 2005. This affects directly the GERB–like products which present similar jumps (Section 4.8).

It was discovered that, for the thermal channels of the SEVIRI, the IMPF provided **spectral radiance** (i.e. at defined wavelength) instead of the standard **effective radiance** (i.e. integral over the spectral band). As most of the users expect effective radiance, and to comply with international standard, the IMPF decided to switch its operational chain from spectral to effective radiance on 5 May 2008. Later on, the earlier Meteosat–8 and Meteosat–9 data archived in the Unified Meteorological ARchive Facility (UMARF) will be reprocessed in effective radiance. A flag is added in the SEVIRI header file to establish the radiance type. The change of radiance definition only concerns the SEVIRI thermal channels, the solar channel images have always been disseminated as effective radiances. From 21 January to 17 March 2008, parallel dissemination of SEVIRI data in spectral and effective radiance was done. We used these parallel data to address the impact of the planned change on the GERB level 2 unfiltered radiances and fluxes. Methodology and results are provided in the technical note (TN44).

[1]MSG–1/SEVIRI Solar Channels Calibration Commissioning Activity Report. Prepared by Y. Govaerts and M. Clerici. Ref. EUM/MSG/TEN/04/0024. Available on the EUMETSAT website.

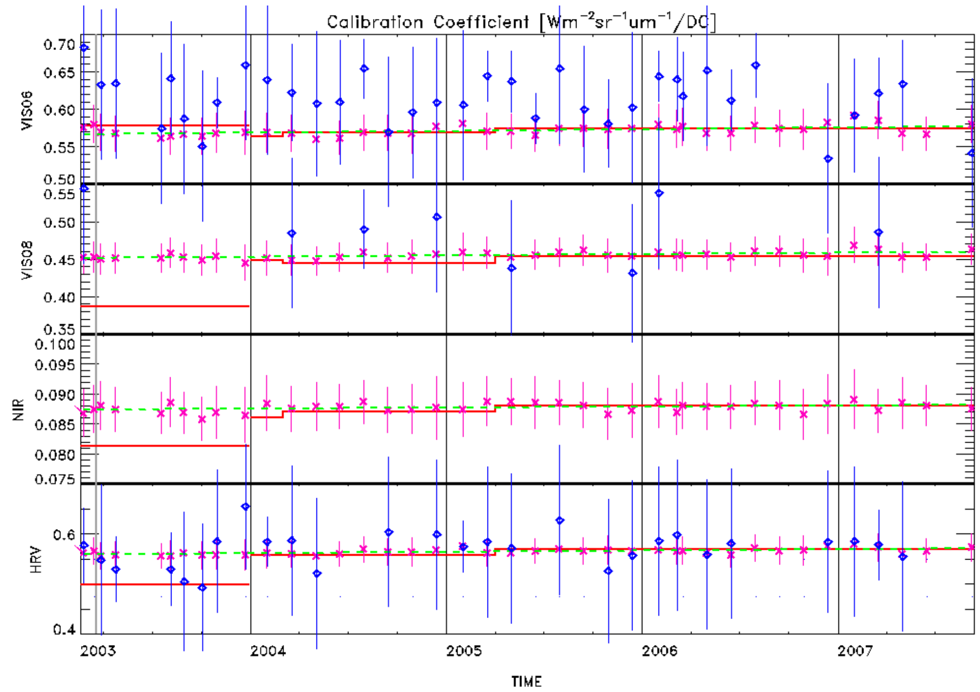

Figure 3.6: Calibration coefficient for Meteosat–8 (pers. comm. Y. Govaerts, EUMETSAT). '×' and '◊' symbols are desert and ocean targets respectively. Dashed lines gives the best linear fits and solid lines the calibration disseminated in NRT in the SEVIRI prologue file.

Figure 3.7 shows the impacts on the GERB radiance and flux due to the change in SEVIRI radiance definition. Although the change only concerns the thermal channels of SEVIRI, some impacts are observed in the GERB reflected solar radiance and flux. Histograms in Figure 3.7 show that there is nearly no systematic difference (bias), but a standard deviation of about 0.1 Wm^{-2} (SW) and 0.2 Wm^{-2} (LW) for the GERB fluxes. To avoid any discontinuity in the GERB–1 and GERB–like datasets it was decided to convert back the new effective radiances in spectral radiances. This conversion is realized using a series of 3rd order polynomial fits provided by EUMETSAT[1].

3.2.4 Use of Meteosat data in this work

During the period June 1998 – November 2003, NRT GERB–like data have been generated from Meteosat first generation images using theoretical NB–to–BB regressions. This activity was performed as part of the implementation and testing of the RMIB GERB ground segment. Later, the early GERB–2 commissioning data have been processed using the Meteosat–7 imager due to delay in the availability of SEVIRI following the commissioning activities and the failure of the MSG–1 direct dissemination. These G2/MET7 data suffer from a relatively poor quality due to parallax problems: MSG–1 was located at 10.5° west while Meteosat–7 provided the

[1]"A simple Conversion from Effective Radiance back to Spectral Radiance for MSG Images". Ref: EUM/OPS-MSG/TEN/07/1053

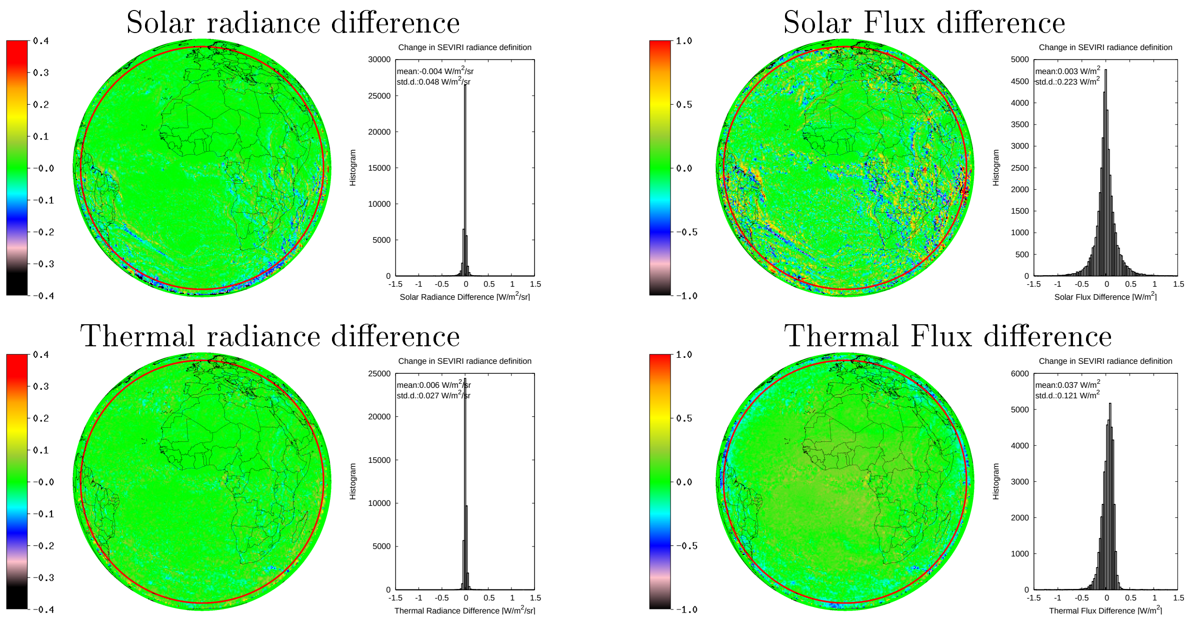

Figure 3.7: Effect of the change in SEVIRI radiance definition on the GERB-1 solar (top) and thermal (bottom) level 2 products. Left panels are for radiance and right panels for flux. Images and histograms are averaged BARG pixel values for the 23 January 2008. The red circle indicates the VZA = 70°.

operational imagery service from 0°.

In the frame of our involvement in the CM–SAF there is an attempt to extend the GERB–like database toward the past, possibly up to 1982 (Meteosat–2). To that end, GERB–like empirical regressions for Meteosat–7 have been derived and evaluated (Sections 4.9 and 5.9). The Indian Ocean Data Coverage service (the EUMETSAT contribution to INDOEX) is currently performed with Meteosat–7. The IODC data could be used for the future extension of the CM–SAF databases eastward. The GERB–like data over the Indian Ocean could profit from the empirical narrowband–to–broadband regressions derived with GERB. The absolute calibration could be provided by corresponding comparison with GERB–1 data on the meridian band located between the 2 satellites.

Similar geostationary instruments located at different longitudes provide valuable simultaneous observations to validate retrieved geophysical quantities. This has been the case of Meteosat–5 and –7 during the period 1998-2007. The data could be used to assess the MVIRI GERB–like angular modelings in a method similar to the validation of the Meteosat surface albedo product (Govaerts *et al.*, 2004b).

Regarding SEVIRI, Table 3.3 gives the different uses of the channels in this thesis. In addition to the level 1.5 images, some higher level products are used in this work. It is the case of the MPEF cloud mask that is used to provide nighttime cloud information in the GERB level 2 products as an interim solution for the Edition 1 (a dedicated infrared cloud mask is under development for the Edition 2).

3.3 The Cloud and Earth's Radiant Energy System (CERES)

3.3.1 Mission

Four main objectives are assigned to CERES (Wielicki *et al.*, 1998): (i) the continuation of the ERBE data set, (ii) the generation of improved estimates of the TOA fluxes both at the TOA and at the Earth surface (twice the accuracy with respect to ERBE), (iii) to provide long term databases of these fluxes in the atmosphere (depending on funding), and (iv) to provide cloud properties consistent with the fluxes. To the exception of the generation of long–term databases, these objectives are already achieved. The first objective is realized with the generation of the CERES ERBE–like products (ES-8, ES-9, ...). The second one is met by the development of improved instruments, ground characterization procedures, and data processing systems. The last one is realized with state–of–the–art cloud properties retrieval implemented and validated based on VIRS and MODIS data. The CERES PFM instrument flew on the TRMM satellite (see Section 2.2). CERES FM1 and FM2 are currently operating on the EOS Terra satellite and FM3 and FM4 on Aqua. The FM5 instrument will fly on the NPP satellite.

3.3.2 The CERES instrument

The CERES scanner is an improved version of the ERBE scanner radiometer that can perform biaxial scanning. The instrument measures radiative energy in three channels. The broadband shortwave (SW) and total (TOT) channels are similar to the GERB and the longwave (LW) is obtained by subtraction. In addition, CERES has a third channel (WIN) that measures thermal radiation in the infrared window between 8.1μm and 11.79μm.

As CERES is primarily a climate instrument, great attention is paid to its absolute calibration and stability. Concerning the unfiltered radiances, the required absolute accuracy at 1 SD is 1% for the SW and 0.5% for the LW (Wielicki *et al.*, 1996). Recently, Loeb *et al.* (2008) performed a detailed analysis of the uncertainty of the CERES measurements. They evaluate at 1% and 0.75% the accuracies of the SW and LW channels at 1 SD. The LW accuracy is better during the night (0.5% at 1 SD) than during the day (1% at 1 SD) due to the TOT - SW separation.

Uncertainties in measured radiances are generally below the 0.5% level. Szewczyk *et al.* (2005) have proved that the likelihood of agreement within 1% between FM1 (Terra) and FM4 (Aqua) SW radiances is higher than 95% over most scene types. Similar comparisons have been done with the other CERES instruments, including the comparison between PFM and FM2. The errors in the instantaneous estimated fluxes of SW (13 Wm^{-2}) and LW (4.3 Wm^{-2}) radiation are mainly due to errors in the application of the angular distribution models. This inaccuracy comes in part from errors in scene identification.

Each CERES instrument can be operated on different scanning modes. The standard cross–track mode is used to maximize the geographic coverage. On each EOS satellite, one CERES instrument is operating in this mode. In the Rotating Azimuth Plane Scan (RAPS) mode, the scanning plan is rotating in azimuth. This provides a full sampling of the anisotropy of radiation in the complete upper–hemisphere.

Between 2000 and 2004 a drop of 2% of the FM1 and FM2 SW flux has been observed. Investigations have shown that the drop must be attributed to a deposition of pollutant on the optics that results in a "spectral darkening" of the SW channel. This aging is faster in RAPS mode than in the normal cross–track mode. This motivated the discontinuance of regular RAPS mode observation. The CERES team published a table of multiplicative factors to compensate for this spectral darkening in the Edition 2. An Edition–3 of the CERES datasets is in preparation. This edition would correct for observed darkening of the SW quartz filter more completely than addressed by the Edition–2 Rev1 used in this study.

3.3.3 The CERES instantaneous products: ES8 and SSF

The state–of–the–art instantaneous radiance measurements are available in both ES8 (ERBE–like S8) and Single Scanner Footprint (SSF) files. The 2 formats differ by the involved angular modeling: the ES8 uses the old ERBE angular models, while the SSF uses the new CERES models. Successive Editions of these products correspond to improvement in the calibration, spectral response aging and set of ADMs. While the ES8 data is released shortly after the acquisition (about 45 days) much more time is needed to release the SSF. For this reason, the first GERB/CERES comparisons were based on ES8 data, assuming that the average fluxes should be close when CERES is operated in RAPS mode. To verify this assumption, a comparison between average ES8 and SSF fluxes was done (TN38). The couples of (ES8, SSF) data have been averaged in $1° \times 1°$ latitude–longitude boxes and the ratio of the 2 averages is analyzed. Figure 3.8 shows images of the monthly mean SW (top) and LW (bottom) ES8/SSF flux ratio for December 2002. The LW flux is in good agreement, with a slight overestimation ($\sim$ 1%) of the ES8 over the tropical cloudiness. For the SW flux, higher disagreement is observed, especially at the northernmost latitudes which have low illumination during December.

3.3.4 Methodology and data for the GERB/CERES comparisons

Introduction

Whenever possible, comparisons of Earth radiation budget data from different spaceborne instruments should be made as they are important steps in the overall validation process. Comparisons are also key elements to compile long–term climate datasets by merging data from

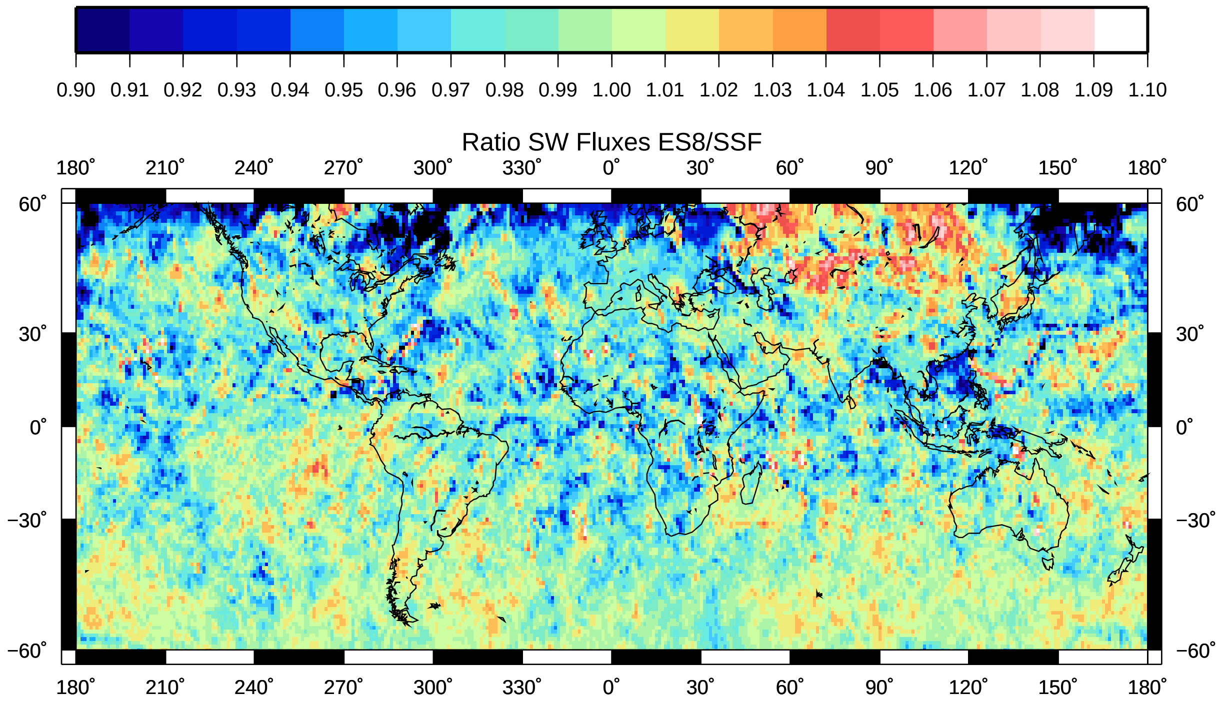

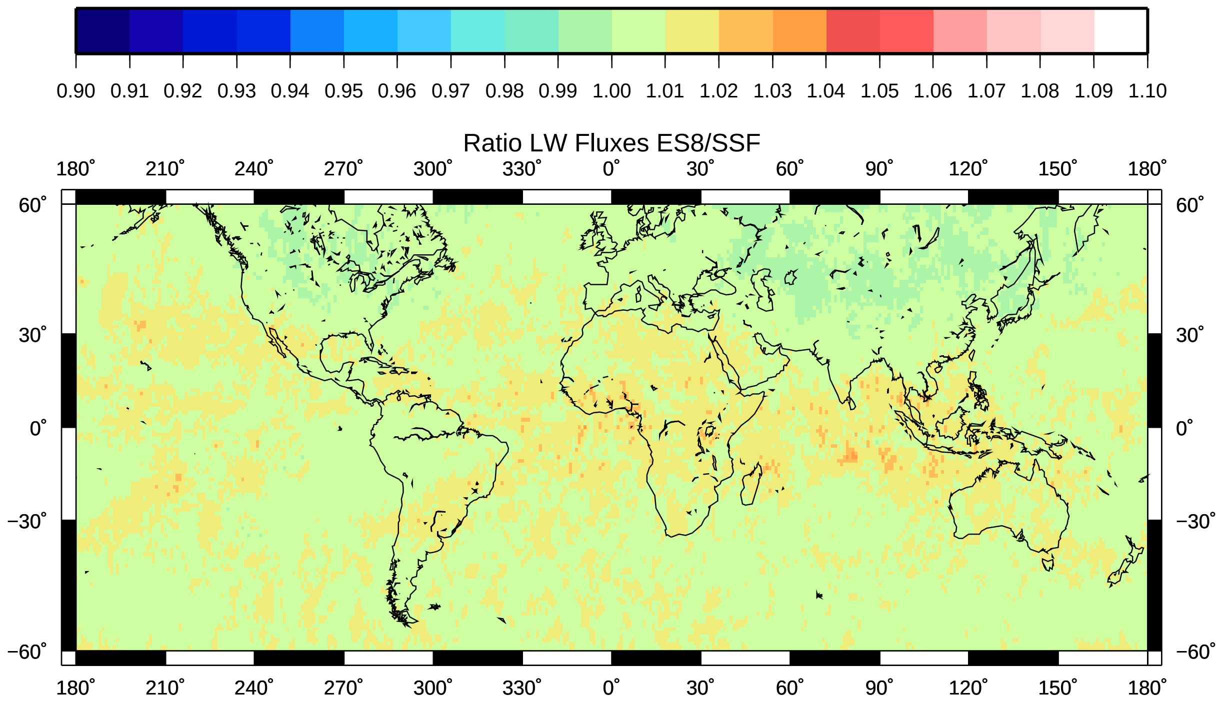

Figure 3.8: Ratio of the monthly means SW (top) and LW (bottom) TOA fluxes as provided by the CERES ERBE–like (ES8) and SSF products, for December 2002. The monthly means only consider the CERES observations in Rotating Azimuth Plane Scan (RAPS) mode.

several instruments. In this thesis, the GERB Edition 1 and CERES Edition 2 data are compared for June and December 2004. The comparisons concern shortwave and longwave radiance and flux at the top–of–atmosphere. Three different GERB level 2 data products with differing space–time characteristics are compared with data from the 4 CERES instruments. This Section presents the comparison data and the methodology. Results are given in the Sections 4.6 and 5.6 respectively for the SW and LW radiances, and in Sections 6.5 and 5.6 for the SW and LW fluxes. These comparisons have been published as a paper in *Remote Sensing of Environment* (Clerbaux *et al.*, 2008c).

CERES data

GERB/CERES comparisons have been made for the months of June and December 2004. In addition to providing maximum difference in solar illumination, these months embrace two special observation campaigns when the CERES Flight Model–2 (FM2) instrument was operated in a special scanning mode that optimizes the frequency of coangular observations with GERB (Smith *et al.*, 2003). During these campaigns the azimuth of the scanning plan of CERES is oriented parallel to the GERB line–of–sight. As these campaigns extended into the beginning of the following months, the 1st to 10th of July 2004 and January 2005 have been added to the June and December periods for the FM2 radiance comparisons. All the other comparisons are based on the 30 days of June 2004 and the 31 days of December 2004.

The best instantaneous TOA radiances and fluxes are available in the Edition 2 of the "Single Scanner Footprint TOA/Surface Fluxes and Clouds" (SSF) product. The correction for the SW quartz filter darkening has been performed as recommended by the CERES team to obtain the "Revision 1" data. For the clear ocean CERES footprints, the specific Revision 1 correction is applied. So, CERES SSF Edition2/Rev1 is used for these comparisons. For the flux comparison, a scaling factor of $(r_e+20\text{ km})^2/r_e^2 = 1.00629$, where r_e is the Earth Equatorial radius, is applied to the CERES SSF fluxes to scale them from the 20km reference level used for the CERES SSF TOA fluxes (Loeb *et al.*, 2002) to the surface reference level used for GERB.

During June and December 2004 the CERES FM1 and FM4 instruments were operated in cross–track mode while the FM2 and FM3 instruments were mainly operated in Rotating Azimuth Plane Scan (RAPS) mode. As already stated, the FM2 instrument has been operated in Programmable Azimuth Plane Scan (PAPS) mode during a few orbits to maximize the number of coangular observations with GERB . FM1 and FM2 are on the sun–synchronous Terra satellite providing measurements close to 10:30 and 22:30 local time. FM3 and FM4 are on the sister Aqua satellite and provide measurements close to 13:30 and 01:30. Therefore GERB/CERES LW comparisons concentrate over 4 blocks of local time and the SW over the 2 daytime blocks.

Collocation methodology

In a first step, databases of corresponding GERB and CERES observations are built by spatial average of the observations of one instrument in the footprint of the second one. The choice is made according to the respective size of the CERES footprints (20km at nadir) and GERB level 2 pixel size (44km for ARG, 45km for BARG and 9km for HR).

For the ARG and the BARG formats, the CERES observations that fall within each pixel are averaged. For the HR, the opposite is done: the GERB HR values that fall within the CERES PSF are averaged. In this case, the CERES PSF in the HR grid is modeled as a disk with radius of $(20\text{km}/\cos(\text{VZA}_{\text{ceres}}))/(9\text{km}/\cos(\text{VZA}_{\text{gerb}}))$ HR pixels. It is known that there is no correction for the PSF in the ARG format and thus the ARG radiance at each grid point will contain contributions from regions outside the grid spacing. In the comparison we treat this ARG product as a representation of a uniform average of the radiance and flux within each grid point as it is expected to be primarily employed (J.E. Russell, pers. comm.).

Concerning the temporal matching, only the CERES observations that fall within the ARG and BARG averaging periods (17 and 15 minutes respectively) are considered. Sensitivity studies have been done to demonstrate that the comparison results are not dependent on the temporal matching criteria. For the matching with the instantaneous HR product, a maximum difference of 5 minutes is allowed for the CERES observations.

This collocation methodology is applied to the radiance and flux and, as described below, also on the cloud fraction, the cloud optical depth, and the viewing angles.

Coangularity criteria

For the radiance comparisons, observations which are not 'coangular' are rejected before being averaged. For this, a threshold value is applied on the angle α between the GERB and CERES directions of observation. Databases of coangular radiances have been extracted using different values for the threshold: $\alpha < 2°$, $\alpha < 5°$, and $\alpha < 8°$. While a strict criteria of coangularity is desirable to improve the radiance matching for highly anisotropic scenes, it provides poorer statistics of matched points. The radiance comparisons presented in this work are mostly based on the $\alpha < 5°$ coangularity criteria. However, the $\alpha < 2°$ and $\alpha < 8°$ criteria have been used to demonstrate that the comparison results are not sensitive to the chosen threshold value.

Figure 3.9 shows the location of the GERB/CERES coangular observations in June and December 2004. Coverage of the full GERB field of view is only possible with the CERES instrument in RAPS mode. Coangular observations for CERES instruments in cross-track mode are restricted to the tropical belt. As the CERES VZA is mostly limited to about 63° due to the

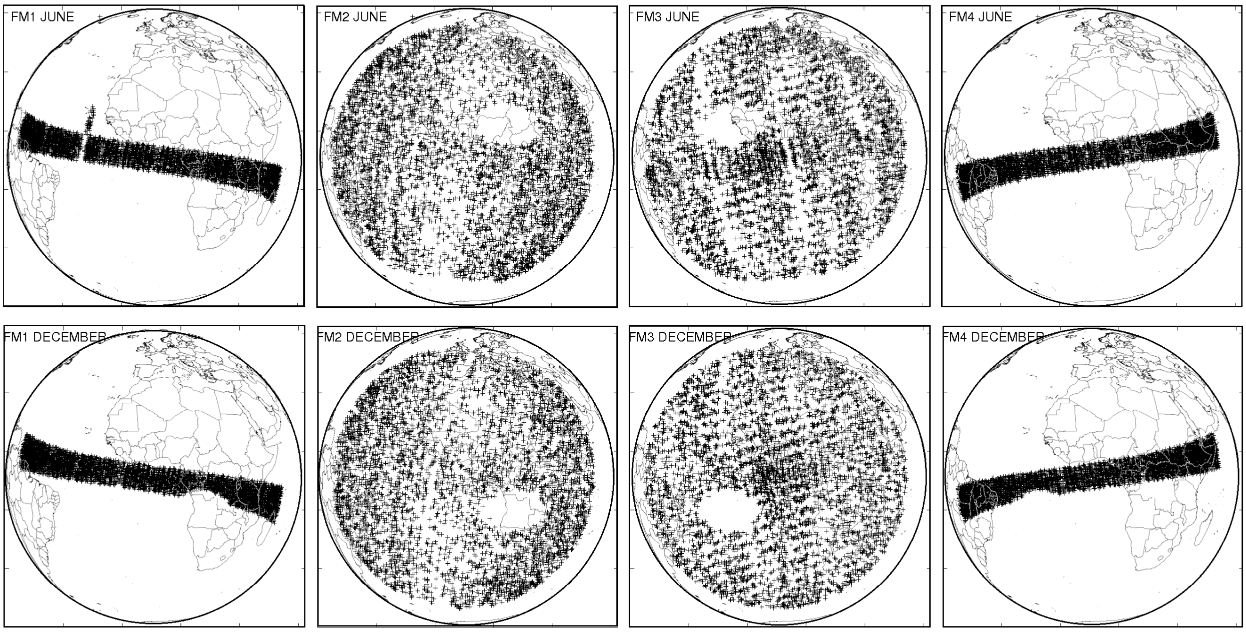

Figure 3.9: Positions of the daytime GERB/CERES coangular observations ($\alpha < 5°$) for the FM1, FM2, FM3, FM4 in June and December 2004 (subsets of 5000 points are shown for clearness). During the night, there is no more sun–glint area and the patterns are inverted (FM1 looks like FM4 and vice–versa).

needed coverage with the Moderate Resolution Imaging Spectroradiometer (MODIS) imager, the statistical analysis considers only the GERB observations with VZA $< 60°$.

Table 3.5 gives the numbers of observation pairs for the different CERES instruments, the 3 GERB data formats, and the 2°, 5°, and 8° thresholds for α. The value of the special scanning mode used for the FM2 during the GERB campaigns is obvious, especially when a strict coangularity criteria is used (i.e. $\alpha < 2°$). The last columns of the table provide the statistics without any coangularity criteria, indicating the number of matches for the flux comparisons.

Cloud type dependency

The fraction of cloud cover and the mean cloud optical depth τ at 0.6μm are available in the GERB level 2 data (ARG, BARG, HR) as well as in the CERES SSF files. These quantities are averaged during the collocation processing in a similar way as the radiance and flux (the smaller pixels are averaged up to the bigger pixels). To address scene type dependency that may affect the GERB/CERES comparison, these cloud retrievals are combined using an "AND" logical operator. For instance, a matched GERB/CERES observation pair is said "clear" if both GERB and CERES data have cloud fraction of 0%. A pair is said "overcast" if both data have cloud fraction of 100% and cloud optical depth higher than 7.39.

The GERB cloud fraction and optical depth are based on the SEVIRI solar channels (Ipe

Number of shortwave observation pairs												
	$\alpha < 2°$			$\alpha < 5°$			$\alpha < 8°$			Flux		
	ARG	BARG	HR	ARG	BARG	HR	ARG	BARG	HR	ARG	BARG	HR
FM1	4311	4085	8065	19677	18486	48801	45498	42563	122336	2488934	2351097	10876945
FM2	74378	70860	178231	147785	139949	478060	218491	206734	768378	2514313	2392723	14839086
FM3	6767	6640	7835	32176	31308	47029	74553	72201	120409	2378288	2328791	11852073
FM4	4369	4145	8093	20125	18906	49042	46533	43908	124137	2499618	2401754	11008608

Number of longwave observation pairs												
	$\alpha < 2°$			$\alpha < 5°$			$\alpha < 8°$			Flux		
	ARG	BARG	HR	ARG	BARG	HR	ARG	BARG	HR	ARG	BARG	HR
FM1	11478	8267	16374	53326	38177	98975	123889	88665	250902	7140077	5154527	23544997
FM2	112533	81116	201756	240593	172238	577490	378152	270975	985685	7422034	5407764	32057576
FM3	18596	13845	15903	88230	65589	96321	203982	150750	247574	6540438	4960310	25242110
FM4	11794	8420	16310	53923	38739	100255	125384	90237	254416	7108241	5161206	23581383

Table 3.5: Numbers of coangular radiance pairs and collocated flux pairs for the SW (top) and LW radiation (bottom).

et al., 2008) and are therefore not available during nighttime. For this reason, the cloud type dependency for the LW comparison is only based on the CERES cloud information. For the clear scenes, separate comparisons are made according to the surface type provided in the GERB files.

Regional analysis

Regional analysis (Figures 6.2 and 7.5) is performed by averaging the GERB and CERES values within $S \times S$ BARG pixel regions and computing the ratio of these values. For the radiance comparison, $S = 10$ (i.e. 450km size at nadir) is used. For the flux comparison, the values $S = 7$ and $S = 4$ are used for the SW and LW radiation, respectively. The regional analysis is performed for all sky and clear sky conditions. Clear sky is here defined as cloud fractions lower than 10% for both GERB and CERES observations[1]. If the number of observation pairs in a box is lower than 20, the box appears in grey on the regional comparison images. For the regional comparison of the coangular radiance the criteria $\alpha < 8°$ is used rather than $\alpha < 5°$ to have better statistics in each box.

Statistical analysis

Comparisons of radiometric instruments can be expressed as differences (e.g. in $Wm^{-2}sr^{-1}$) or as ratios. As the GERB/CERES scatterplots indicate that most of the disparity is explained by multiplicative factors, the second option is adopted in this work. The ratio of the average GERB and CERES quantities is estimated on a daily basis

$$m_{day} = \frac{< v_{gerb} >}{< v_{ceres} >} \tag{3.4}$$

[1] 10% is used rather than 0% to provide sufficient numbers of clear data in most of the boxes. It was however demonstrated that the results are not significantly affected by that 10% threshold

where the quantity v can be SW or LW radiance or flux. The daily basis is adopted because this time period is the time needed by a CERES instrument to scan the whole Meteosat FOV. Therefore the daily m_{day} values are expected to be stable day after day, even if there are regional patterns in the GERB/CERES ratio. The daily value m_{day} is estimated only if the number of GERB/CERES observation pairs is higher than 5. This number is always reached in all sky conditions but may not be reached for radiance comparison in some restrictive conditions. Let N be the number of daily ratio values, the best estimate of the GERB/CERES ratio m and the associated uncertainty are

$$m = \mu(m_{day}) \pm \frac{3\sigma(m_{day})}{\sqrt{N-1}} \tag{3.5}$$

where

$$\mu(m_{day}) = \frac{1}{N}\sum_{day=1}^{N} m_{day} \tag{3.6}$$

$$\sigma(m_{day}) = \sqrt{\frac{1}{N}\sum_{day=1}^{N} (m_{day} - \mu(m_{day}))^2} \tag{3.7}$$

are the mean and standard deviation of the daily values. The factor 3 in Eq.(3.5) is used to have a likelihood of 99% (assuming a normal distribution of the m_{day}). It is worth considering that GERB/CERES ratios observed over very dark (SW) or cold (LW) scenes correspond to small absolute differences and will then vanish in the averaging process. For this reason, the average GERB radiance $< L_{gerb} >$ or flux $< F_{gerb} >$ is provided in addition to the average ratio to allow conversion of the ratio m to an absolute difference.

Chapter 4

Spectral modeling of the reflected solar radiation

4.1 Introduction

In this chapter, we address different problems that require assumptions about the spectral signature $L_{sol}(\lambda)$ of the reflected solar radiation. As for these problems the full spectrum is not measured, it must be modeled based on information about the observed scene. In general, the available information includes a characterization of the surface type and some retrieved information about the cloudiness. For these modelings, one must take into account the viewing and solar geometries (VZA, SZA, RAA) as they modify the spectrum at the TOA. Additional information is often provided by a series of NB radiance measurements at some places in the electromagnetic spectrum $\{L_{nb}\}$. Similarly, in the frame of Earth radiation budget, a rough indicator of the scene type can be obtained by the broadband measurements of a BB radiometer.

Section 4.2 enumerates the factors that govern the spectrum $L_{sol}(\lambda)$ of reflected solar radiation at the TOA. Based on this analysis, a database of simulated spectra has been built by radiative transfer computations, as described under Section 4.3. The simulations are done for a set of 750 realistic scene types under different viewing and solar geometries. This database is used to address spectral modeling problems, for instance to fit regressions on simulated data or for validation purposes.

The first problem we address is the unfiltering of the GERB SW channel. It consists in the estimation of the unfiltered solar radiance $L_{sol} = \int L_{sol}(\lambda)d\lambda$ from the filtered solar radiance in the radiometer SW channel $L_{sw,sol} = \int L_{sol}(\lambda)\phi_{sw}(\lambda)d\lambda$. The problem is illustrated in Figure 4.3 (left) that shows the variability of the unfiltering factor $\alpha_{sw,sol} = L_{sol}/L_{sw,sol}$ according to the scene type. Even with a perfectly known spectral response $\phi_{sw}(\lambda)$, the unfiltering factor depends on the spectrum $L_{sol}(\lambda)$ of the observed scene which must therefore be modeled. Two unfiltering methods have been developed. The direct unfiltering (Section 4.4) is based on a coarse surface type classification and on the GERB SW measurement itself. Although it does not meet the targeted accuracy of 1% for the unfiltering, the method proved to be suitable for different purposes. The (operational) Edition 1 GERB SW channel unfiltering is described in Section 4.5. The method relies on spectral information provided by the 0.6μm, 0.8μm, and 1.6μm SEVIRI channels. Using the database of simulated spectra, theoretical validations of the method have been carried out that show that the unfiltering error remains within the accuracy objective of 1%.

As reflected solar and emitted thermal radiations coexist around 4μm, a filter can not totally separate the two types of radiation. There are therefore solar and thermal contaminations respectively in the LW and SW channels that must be subtracted before unfiltering. The estimation of the solar contamination in the GERB LW channel $L_{lw,sol} = \int \phi_{lw}(\lambda) L_{sol}(\lambda) d\lambda$ is another spectral modeling problem of the reflected solar radiation (addressed in Section 5.5.3).

Section 4.6 reports the results of comparisons of collocated and coangular GERB and CERES unfiltered SW radiances. These high level validations embrace the effects of the instrument calibration, the on–ground characterization of the SW spectral response, and the unfiltering algorithm. The last 2 points could be separated from the absolute calibration by analyzing the GERB/CERES ratio according to the scene type.

For the GERB instrument, an additional challenge comes from the variability in spectral response between the 256 detector elements. In the current design of the RGP, it is not foreseen to perform pixel–level unfiltering. The processing assumes that all the GERB pixels have the same spectral sensitivity. The error which is introduced by this assumption and a method to reduce the pixel–to–pixel differences are analyzed in Section 4.7.

Narrowband–to–broadband conversions, i.e. the inference of the BB radiance from a set of NB measurements, also involves spectral modeling techniques. In this work, we focus our efforts on the narrowband–to–broadband conversions for the SEVIRI (Section 4.8) and the MVIRI (Section 4.9) instruments. Since 1998, theoretical regressions have been derived and used to generate the GERB–like products. In this work, these regressions have been validated by comparison with the GERB Edition 1 product. We also present empirical regressions that produce GERB–like data. These empirical regressions are foreseen to be used in the Edition 2 processing.

Section 4.10 summarizes this first part of the work.

4.2 Factors affecting the TOA reflected solar spectrum

At the TOA, the spectrum of reflected solar radiation $L_{sol}(\lambda)$ depends on the incoming spectral irradiance, the absorption and scattering by atmospheric constituents and clouds, and the reflection of the land or water surface. A considerable literature exists (e.g. Lintz & Simonett, 1976) on this topic often designated by "optical remote sensing" (e.g. optical remote sensing of land surface, optical remote sensing of clouds, of sea ice, of air quality, ...).

In the **atmosphere**, the Rayleigh scattering by diatomic molecules mainly concerns the short visible wavelengths (intensity proportional to λ^{-4}). Diatomic oxygen (O_2) presents absorption lines like in the A–band (0.76μm to 0.77μm) in the visible spectrum. The atmospheric water vapor presents similar absorption lines (e.g. at 0.94μm). The stratospheric ozone is an efficient absorber of the ultraviolet radiation. Consequently, little ultraviolet contribution is present in the reflected solar radiation at the wavelengths below 0.3μm. Of course, these atmospheric absorptions and scatterings are proportional to the optical path and therefore depend on the VZA and SZA.

For a given place on the Earth, the main source of variability of the spectrum is the **cloudiness**. The effect on the spectrum varies as the logarithm of the cloud optical thickness (Nakajima & King, 1990). To a lesser extent, the spectrum depends on the particle size distribution which modifies the extinction efficiency, the single scattering albedo, and the asymmetry factor. At wavelength below 1μm, there is nearly no absorption and the extinction is only due to scattering. The scattering is stronger for small particle size than for large particles and the asymmetry factor is lower (more isotropic scattering). At higher wavelength, in the near infrared, the cloud thermodynamic phase plays a major role with absorption by ice crystals around 1.6μm and 2.2μm. The height of the cloud layer does not modify significantly the spectrum, except in the oxygen absorption band. For higher clouds the atmosphere above it is smaller and thus also the O_2 absorption is smaller.

The interaction between photons and **land surface** involves both electronic and vibrational transitions. The spectrum is mainly dependent on the vegetation cover (absorption in the green) and the humidity (absorption at all wavelengths). These characteristics present short term, seasonal, and inter–annual variations. The soils composition and its absorption features affect the SW part of the spectrum. Actual spectral reflectance data for a large number of soils and rocks samples are available in the ASTER spectral library. Strong modification of the spectrum arises in case of snow cover and sea ice (infrequent in the Meteosat FOV). Similar change is observed over seasonal lakes that happen to present water spectrum and sometimes sand/vegetation spectrum (e.g. lake Chad).

The **ocean** surface absorbs efficiently most of the SW radiation but also shows strong specular reflection ("sun glint"). The strength and the angular distribution of the reflection depends on the sea state and thus, at least statistically, on the wind speed (Cox and Munk, 1954). The wind is also responsible for whitecaps, foam, and spray generation, all elements that make the ocean brighter. In coastal areas, the ocean color is also dependent on detritus coming from the rivers and on the phytoplankton due to their content in chlorophyll (absorption peaks at 0.665μm and 0.465μm). For clear sky ocean, the reflected radiation at the TOA mainly contains Rayleigh scattering radiation. The spectrum is "blue" with more than 60% of the energy below $\lambda < 0.5$ μm. In the specular reflection beam the spectrum is close to the incident solar spectrum (white). This causes difficult detection of the cloud cover in the sun glint region. Over clear ocean, the spectrum is also modified in presence of atmospheric aerosols, due to biomass burning and desert dust outflow.

4.3 Radiative transfer computations

4.3.1 Introduction

The development and/or the validation of spectral modelings can be based on a realistic set of spectral radiance curves $L(\lambda)$ susceptible to be observed. These curves can be simulated using radiative transfer computations based on the optical properties of the surface and of the atmosphere. For the GERB data processing, the Santa Barbara DISORT Atmospheric Radiative Transfer (SBDART, Ricchiazzi *et al.*, 1998) has been widely used. The Streamer model (Key & Schweiger, 1998) is used for the GERB cloud retrieval (Section 6.3). The MODerate resolution atmospheric TRANsmission (MODTRAN, Berk *et al.*, 1999), the Second Simulation of the Satellite Signal in the Solar Spectrum (6S, Vermote *et al.*, 1997), and the GENLN2 models have been used for validation purposes. Although it is not totally free of implementation errors and shortcomings, SBDART has been selected by us as the best–suited model for spectral modeling. The model permits fine line–by–line simulation in an acceptable computation time. A posteriori comparisons of radiative transfer models by Halthore & al. (2005) have confirmed this choice. Hereafter, we provide a brief description of these simulations. The work is fully described in the technical note (TN30) with a rough validation by comparing the distributions of simulated NB radiances with the corresponding distributions of SEVIRI observations.

4.3.2 Simulations

A large database of simulated spectral radiance curves $L_{sol}(\lambda)$ is built using the Version 2.4 of SBDART. The database contains simulations for 750 realistic conditions of the Earth surface, the atmosphere and the cloudiness. For the generation of this database we did not try to mimic the statistics of observed scenes in the Meteosat field–of–view but rather to simulate as much as possible the variability in spectral signature of the scenes. For this reason, the input parameters for the radiative transfer computations are randomly selected using uniform distribution of probability over extended ranges instead of using climatology of observed values.

The surface is either one single or a mixture of 2 of the following geotypes: ocean, vegetation, soil, rocks and snow. For the land surface, the spectral reflectance curve $\rho_{surf}(\lambda)$ of the surface is selected randomly within the ASTER spectral library[1], as detailed in Table 4.1. The Rocks geotype is representative for the sandy surface which is widely present in the Meteosat field of view. In the case of mixture, the spectral reflectance curve at the surface $\rho_{surf}(\lambda)$ is constructed as

[1]Courtesy of the Jet Propulsion Laboratory, California Institute of Technology, Pasadena, California. ©1999.

primary geotype	number	secondary geotype	number	ASTER library surface reflectance models
Ocean	301	Ocean	301	SBDART 'sea water' model
Vegetation	137	Ocean Vegetation Soils Rocks Snow	14 82 28 0 13	conifers,deciduous,drygrass,grass
Soils	138	Ocean Vegetation Soils Rocks Snow	14 29 89 0 6	87P3665c, 79P1530c,87P3671c, 79P1536c,87P3855c, 82P2230c,87P4264c ,82P2671c,87P4453c , 82P2695c, 87P473c,84P3721c , 87P706c, 85P3707c,87P707c, 85P4569c,87P757c, 85P4663c,87P764c, 85P5339c, 88P2535c,86P1994c,88P4699c, 86P4561c,88P475c, 86P4603c,89P1763c, 87P1087c,89P1772c, 87P2376c, 89P1793c, 87P2410c,89P1805c, 87P313c ,90P0142c, 87P325c ,90P128sc, 87P337c ,90P186sc, 87P3468c
Rocks	150	Ocean Vegetation Soils Rocks Snow	14 44 38 45 9	greywa1f, limest1f, limest2f, limest3f, limest4f, limest5f, limest6f, limest7f, sandst1f, sandst2f, sandst3f, sandst4f, sandst6f, sandst7f, shale1f, shale2f, shale3f, shale4f, shale5f, shale6f, shale7f, siltst1f, siltst2f, traver1f, greywa1c, limest1c, limest2c, limest3c, limest4c, limest5c, limest6c, limest7c, sandst1c, sandst2c, sandst3c, sandst4c, sandst6c, sandst7c, shale1c, shale2c, shale3c, shale4c, shale5c, shale6c, shale7c, siltst1c, siltst2c, traver1c
Snow	24	snow	24	coarse,medium,fine,frost

Table 4.1: The 5 geotypes used for the radiative transfer computations and the number of simulations having primary and secondary geotypes. For each geotype, the surface reflectance curves from the ASTER spectral library are given in the last column.

$$\rho_{\mathrm{surf}}(\lambda) = a_1\rho_{\mathrm{surf},1}(\lambda) + a_2\rho_{\mathrm{surf},2}(\lambda) \tag{4.1}$$

where $\rho_1(\lambda)$ and $\rho_2(\lambda)$ are the primary and secondary curves from the ASTER library. The mixing coefficients a_1 and a_2 are randomly selected between 0 and 1 using a uniform distribution of probability (i.e. each value in the range has the same probability). The coefficients are then scaled in such a way that the sum $a_1 + a_2$ follows a uniform distribution of probability in the range $0.8 - 1.2$. These limits make it possible to reduce or boost by 20% the overall reflectance of the surface with respect to the samples stored in the ASTER library. In the case of a pure surface, the $\rho_2(\lambda)$ is taken equal to the $\rho_1(\lambda)$. Table 4.1 provides the number of simulations for the different primary and secondary geotypes. For instance, the database contains 138 simulations with 'Soils' as primary geotype. Among these 'Soils' simulations, 14 have 'Ocean' as secondary geotype, 29 'Vegetation', 89 'Soils' and 6 'Snow'.

For the ocean, the internal 'sea water' SBDART reflectance curve is used with additional specification of the concentration of chlorophyll pigment. The pigment concentration affects the Bidirectional Reflectance Distribution Function (BRDF) of the ocean for wavelengths between 0.4 and 0.7 μm. This concentration is selected in the range $0.01 - 10.0$ mg m^{-3} with the base–10 logarithm of the concentration following a uniform distribution of probability between

-2 and $+1$. This distribution has been selected from the monthly chlorophyll concentration climatology produced by the SeaWIFS project.

The reflection of the ocean surface follows the internal BRDF implemented in SBDART. This BRDF is based on the Cox and Munk model and is dependent on the wind speed which is selected at random using a uniform distribution of probability in the range $1 - 10$ m s^{-1}. The upper limit is selected according to the global climatology of wind velocity derived from the Special Sensor Microwave Imager (SSM/I) instrument (Atlas *et al.*, 1996). The lower limit is needed to avoid radiative transfer instabilities for wind speed below 1 m s^{-1}. The reflection of the land surfaces is isotropic as no surface BRDF is used for the simulations. The use of land surface BRDF would have been desirable but this was recognized as out of the scope for this work as SBDART does not provide BRDF for land surfaces and that BRDF measurements are not available for the ASTER library samples. The effect of not modeling the BRDF for land surface is however expected to be an acceptable approximation because the effect is of secondary importance for spectral modeling problems.

For each simulation, the atmospheric profile of pressure, temperature, humidity and ozone is selected randomly with an equal probability among the 6 internal profiles of SBDART. These ones are the well-known Mac–Clatchey profiles (tropical, mid-latitude summer, mid-latitude winter, sub-arctic summer, sub-arctic winter) with the addition of the US62 profile. Boundary layer aerosols are also simulated. The type of aerosol is selected at random with an equal probability within: none, rural, urban, oceanic and tropospheric. The optical thickness at 0.55 μm of the aerosol is selected at random between 0.01 and 1, with a uniform distribution of probability for the logarithm of the optical thickness. This distribution has been selected according to a climatology of aerosol optical thickness retrieval from Total Ozone Mapping Spectrometer (TOMS) data inversion (King *et al.*, 1999). Finally, the intensity of the Rayleigh scattering is multiplied by a random factor with a uniform distribution of probability in the range $0.8 - 1.2$. This is implemented to enlarge the dispersion of spectrum $L(\lambda)$ over the dark oceanic scenes by altering the intensity of the atmospheric scattering by $+/-20\%$.

Clouds are added in the simulations with a probability of 50%. For a cloudy simulation, the cloudiness can be made of up to 3 overlapping layers. The probabilities of these layers are 50%, 40% and 30%, respectively for the low–, mid– and high–level clouds. The altitude of the low–level cloud is set at random with a uniform distribution of probability in the range $0.5 - 3.5$ km, the mid–level in $4 - 7$ km and the high–level in $7.5 - 16$ km. These threshold values are selected to match the ISCCP cloud height classification (Rossow & Schiffer, 1999). The optical thickness at 0.55 μm of a cloud layer is selected at random between 0.3 and 300, with a uniform distribution of probability for the base–10 logarithm of the optical thickness between -0.523 and $+2.477$. The low–level clouds are always composed of water droplets and the high–level clouds of ice crystals. The phase of the intermediate layer can be either water or ice, with an equal probability. The drop size distribution follows a gamma distribution that can be stretched using a single parameter called the effective radius (Ricchiazzi *et al.*, 1998). For a water cloud layer, the droplets effective radius is selected at random within $2-25$ μm with a uniform distribution of probability. The effective radius of ice particles is selected within $15-128$ μm also with a uniform distribution of probability.

The Discrete Ordinate Radiative Transfer (DISORT) computations are performed using 20 streams to obtain an accurate representation of the dependency of the scene spectral signature $L(\lambda)$ with the Sun–target–satellite geometry. The SZA varies between nadir (SZA $= 0°$) and SZA $= 80°$ in steps of $10°$. The viewing geometry is defined by the VZA ($0°$ to $85°$ in steps of $5°$) and the RAA ($0°$ in the forward direction with respect to the incident sunlight to $180°$ in the backward direction in steps of $10°$). The simulations cover the wavelength interval $0.25-5\mu$m with the following spectral resolution: $\Delta\lambda = 0.005\mu$m over $0.25-1.36\mu$m, $\Delta\lambda = 0.01\mu$m over $1.36-2.5\mu$m and $\Delta\lambda = 0.1\mu$m over $2.5-5\mu$m. All the radiative transfer computations have been performed with the thermal emission turned off in order to simulate only the radiance $L_{sol}(\lambda)$ due to the reflection of the incoming solar radiation.

The database of spectral radiance curves is then weighted with instrument's spectral response filters to get, for each simulation $L_{sol}(\lambda)$, the simulated BB and NB radiances. As an example, in the case of the GERB/SEVIRI instruments on MSG–1, these radiances are

$$\begin{aligned}
L_{sol} &= \int_{0.25\mu\mathrm{m}}^{5\mu\mathrm{m}} L_{sol}(\lambda)d\lambda \\
L_{sw,sol} &= \int_{0.25\mu\mathrm{m}}^{5\mu\mathrm{m}} L_{sol}(\lambda)\phi_{sw}(\lambda)d\lambda \\
L_{0.6} &= \int_{0.25\mu\mathrm{m}}^{5\mu\mathrm{m}} L_{sol}(\lambda)\phi_{0.6}(\lambda)d\lambda \qquad (4.2)\\
L_{0.8} &= \int_{0.25\mu\mathrm{m}}^{5\mu\mathrm{m}} L_{sol}(\lambda)\phi_{0.8}(\lambda)d\lambda \\
L_{1.6} &= \int_{0.25\mu\mathrm{m}}^{5\mu\mathrm{m}} L_{sol}(\lambda)\phi_{1.6}(\lambda)d\lambda
\end{aligned}$$

where $\phi_{sw}(\lambda)$ is the GERB–2 average shortwave spectral response defined by Eq.(3.1) and $\phi_{0.6}(\lambda)$, $\phi_{0.8}(\lambda)$ and $\phi_{1.6}(\lambda)$ are the spectral responses of the visible channels of the SEVIRI instrument on MSG–1, available from EUMETSAT.

4.3.3 Validations

Ricchiazzi *et al.* (1998) report on the validations which have been done for the SBDART model. In–situ spectral observations have been successfully compared with the model outputs based on detailed characterization of the atmosphere state. This validates the accuracy of the model.

Nevertheless, it must also be verified that the simulations are in agreement with what is observed in the Meteosat field–of–view. An important point is that the set of simulations encompasses most of the scenes likely to be observed in the FOV. This ensures the robustness of regressions derived from the simulations. Figure 4.1 shows scatterplots of simulated (green) and observed (red) couples of SEVIRI solar channel radiances at the BARG pixel resolution (45km $\times$ 45km). The top–left graph shows that for the ocean some observations with reflectances in the 0.6 and 0.8 channels $\rho_{0.6} \sim 0.1$ and $\rho_{0.8} \sim 0.2$ are not simulated. It can be shown that these observations correspond to ocean BARG pixel with a significant fraction of land (coastal pixel). This case was not simulated in the database but instead the opposite case (land pixel with water fraction up to 50%) has been simulated. The graphs at the right hand side demonstrate that the simulated reflectance in the NIR 1.6 channel is often significantly lower than the observations. A large number of simulated clouds (e.g. $\rho_{0.6} > 0.6$) have simulated NIR reflectance $\rho_{1.6}$ lower than 15% whilst this is never observed in the FOV. The bottom graphs are scatterplots of the simulated reflectances with respect to the ISCCP cloud classification (Rossow & Schiffer, 1999). These graphs show that the abnormally low simulated $\rho_{1.6}$ reflectances correspond to deep convective and nimbostratus clouds which are optically thick clouds with ice crystals in the upper cloud layer. Similarly, clear bright desert scenes have high $\rho_{1.6}$ observed reflectance which are not sufficiently simulated in the database.

The comparisons of scatterplots of simulated and observed radiances suggest possible improvements for a further edition of the radiative transfer simulations. In addition, the scatterplots of Figure 4.1 can be seen as a rough validation of the MSG–2 visible channel calibration.

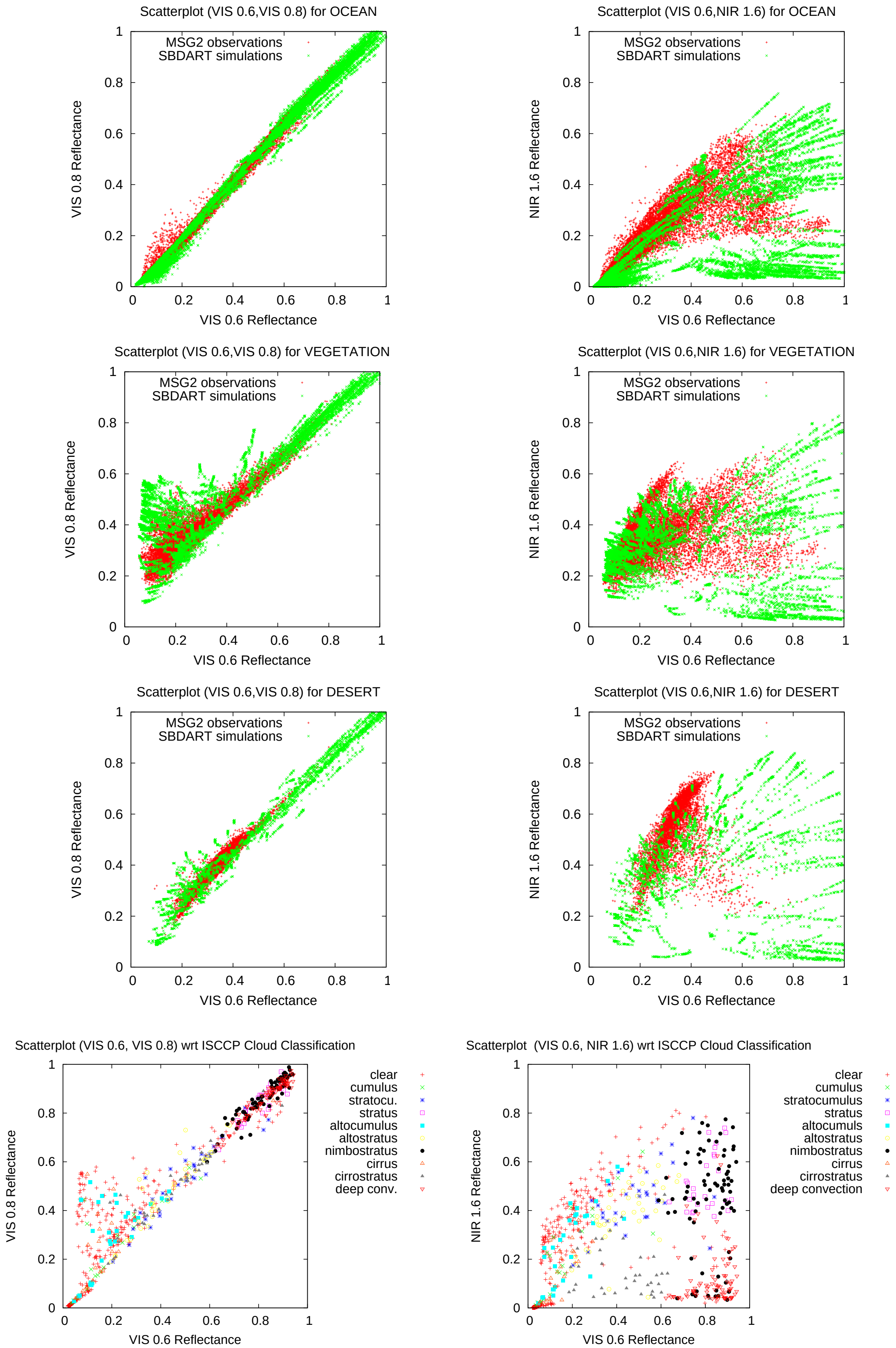

Figure 4.1: Scatterplots $\rho_{0.6}/\rho_{0.8}$ (left) and $\rho_{0.6}/\rho_{1.6}$ (right) of MSG–2 observations for 5 June 2007 12:00 UTC (red) and simulated radiances (green) for ocean (top), vegetation (2nd row), desert (3rd row) surfaces. The bottom graphs provided the simulated radiances according to the ISCCP cloud classification.

4.4 Direct unfiltering of the GERB SW channel

For GERB, we define *direct unfiltering* as the method that estimates the unfiltered radiances from the filtered measurements of the instrument, without using spectral information from SEVIRI. This method, close to the CERES unfiltering (Loeb *et al.*, 2001), is not used in the GERB processing operational chain. The operational GERB unfiltering is based on spectral information provided by SEVIRI as described in the next section. The direct unfiltering is however useful for various purposes. First, it allows unfiltering of GERB footprints with inaccurate geolocation as the method does not require precise co–registration of GERB and SEVIRI observations. Second, it also permits unfiltering of the data at the detector level. This is needed to assess the performances of each individual detector of the GERB instrument (Mlynczak *et al.*, 2006). Third, it makes possible to unfilter the data even in case of unavailability of corresponding SEVIRI observations. This happens during SEVIRI commissioning activities and decontaminations as well as during regular activation of the GERB instrument on the backup MSG satellite(s) (for GERB instrument intercomparisons). Finally, the direct unfiltering method was used to validate the radiative transfer simulations. For this, the direct unfiltering method is applied to the CERES filtered radiances and the resulting unfiltered radiances are compared to the CERES ones. Systematic difference can be the symptom of problems affecting the RTM simulations. The technical note (TN35) fully describes the direct unfiltering method for the GERB–2 and GERB–1 instruments. An outline of the method is given here.

The mean filtered radiances L and unfiltering factors α are estimated for the clear ocean (L_{oc} and α_{oc}) and for the cloudy (L_{cl} and α_{cl}) simulations. These values serve to define the normalized filtered radiance x and the normalized unfiltering factor y as

$$x = \frac{L - L_{oc}}{L_{cl} - L_{oc}} \tag{4.3}$$

$$y = \frac{\alpha - \alpha_{cl}}{\alpha_{oc} - \alpha_{cl}} \tag{4.4}$$

These normalized values usually lie in the range $0 - 1$. Slightly negative y values are however observed over land surfaces that present lower unfiltering factor than clouds. The following curve is proposed to estimate the normalized unfiltering factor y from the normalized filtered radiance x

$$y = c_0 + \frac{c_1}{(x + c_2)} + \frac{c_3}{(x + c_2)^2} \tag{4.5}$$

with the additional constraints that the curve must pass over the "clear ocean point" $(x, y) = (0, 1)$ and over the "cloudy point" $(x, y) = (1, 0)$. So, only 2 free parameters remain in the set $\{c_i\}$. For each SZA (0°, 10°,... ,70°), the parameters are derived as best fit on the database

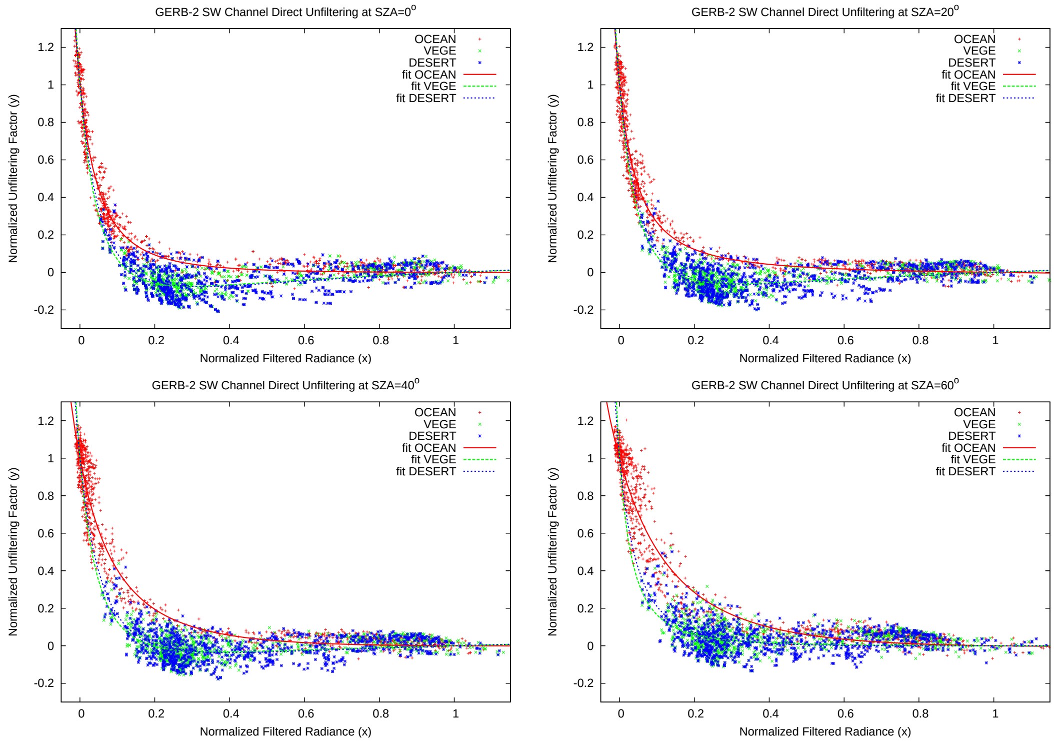

Figure 4.2: Scatterplots of normalized filtered radiance x (Eq. 4.3) and normalized unfiltering factor y (Eq. 4.4) for SZA $= 0°$, $20°$, $40°$, and $60°$. The curves show the best fits of Eq.(4.5).

of SBDART simulations. Distinct fits are derived for ocean, vegetation and desert surfaces. Although it is possible to derive unfiltering fits dependent on the full angular geometry (SZA, VZA, RAA), the improvement compared to fits that depend only on the SZA is small.

In practice, the clear ocean features (L_{oc} and α_{oc}) are first estimated as the averaged L and α values for the clear ocean scenes in the database. Similarly, the cloud features (L_{cl} and α_{cl}) are estimated as the averaged L and α values on the 10% brightest cloudy scenes in the database. Then, an optimization under constraints finds the best parameters $\{c_i\}$ of Eq.(4.5) by minimization of the RMS error on y.

Figure 4.2 illustrates the scatterplots of (x, y) values for the 3 surface types and the corresponding best fits for the SZA $= 0°$, $20°$, $40°$, and $60°$. We can see that the 3 fits intersect on the $(x, y) = (0, 1)$ and $(1, 0)$ points. This aims to limit the errors in case of incorrect surface type characterization, for example due to an incorrect geolocation. The various parameters and RMS errors are given in (TN35) for GERB–2 and GERB–1. The RMS error is about 1% for cloudy scenes, between 1% and 2% for clear land, and between 2% to 3% for clear ocean. These error levels are out of the targeted accuracy of 1% for the GERB SW channel unfiltering. The next section shows how the unfiltering error is reduced using spectral information from SEVIRI.

4.5 Edition 1 GERB SW unfiltering

4.5.1 Introduction

This section presents the unfiltering method used for the Edition 1 GERB data. This work has been published in the *Journal of Atmospheric and Oceanic Technology* (Clerbaux *et al.*, 2008b). The GERB unfiltering problem is illustrated in Figure 4.3 that shows the variability of the unfiltering factors $\alpha_{sw,sol} = L_{sol}/L_{sw,sol}$ according to the scene type for GERB–2 (left) and CERES FM2 (right). As a result of its optics, the relative difference between the ocean and the cloud unfiltering factors (divided with the mean unfiltering factor) is about twice as big for GERB (22%) than for CERES (10%).

Due to ground data processing constraints (Dewitte *et al.*, 2008), the unfiltering is realized in 2 steps. In a first step, the NB measurements in the 0.6μm, 0.8μm and 1.6μm channels of the SEVIRI imager are used to estimate, at the 3×3 SEVIRI pixel resolution (i.e. 9km $\times$ 9km at nadir), the broadband unfiltered radiance L'_{sol} and the filtered shortwave radiance L'_{sw}. The primes ($'$) indicate that these broadband radiances are estimated from SEVIRI through narrowband–to–broadband (NB–to–BB) conversions. The L'_{sw} is a SEVIRI estimate of the filtered radiance that would have been measured by the GERB SW channel and includes the solar and thermal contributions $L'_{sw} = L'_{sw,sol} + L'_{sw,th}$. The NB–to–BB conversions done during this first step use SEVIRI data along with unfiltering factors based on radiance simulations for a wide variety of scenes, and are totally distinct from the GERB measurements. In the second step, the 2 SEVIRI estimates are convolved with the GERB dynamic PSF and temporally interpolated to match the GERB measurements. The GERB unfiltered solar radiance is finally obtained by multiplying the filtered measurement L_{sw} by a factor equal to the ratio of the SEVIRI estimated unfiltered and filtered radiances

$$
\begin{aligned}
L_{sol} &= L_{sw} \left(\frac{L'_{sol}}{L'_{sw,sol} + L'_{sw,th}} \right) && (4.6) \\
&= L'_{sol} \left(\frac{L_{sw}}{L'_{sw,sol} + L'_{sw,th}} \right) && (4.7)
\end{aligned}
$$

This radiance can be interpreted either as the GERB measurement L_{sw} multiplied by a spectral correction factor (L'_{sol}/L'_{sw}) derived from SEVIRI (Eq. 4.6) or equivalently, as the SEVIRI estimate of the broadband unfiltered radiance L'_{sol} corrected by the GERB instrument through the ratio L_{sw}/L'_{sw} (Eq. 4.7). Using this formulation, modeling errors should be annihilated for the most part, as long as the spectral response is broadband and relatively flat.

This approach is well–suited to the unfiltering of BB radiances collected over a large footprint as it is the case for GERB. Indeed, most of the 68km $\times$ 38km footprints contain a mixture

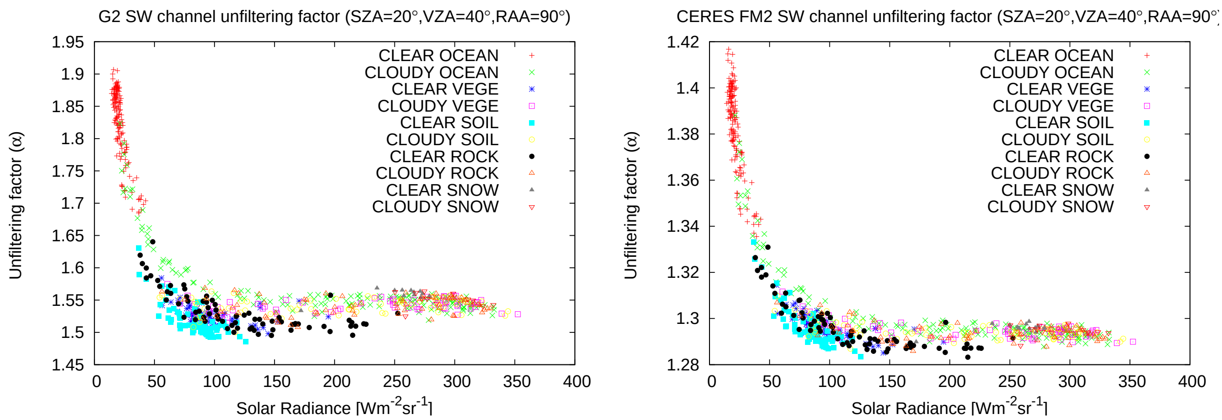

Figure 4.3: SW unfiltering factor $\alpha_{sw,sol}$ for GERB–2 (left) and CERES FM2 (right) according to the unfiltered solar radiance. The dots correspond to SBDART simulations at the geometry (SZA $= 20°$, VZA $= 40°$, RAA $= 90°$).

of scenes with different unfiltering factors, and this situation is taken into account with the SEVIRI fine scale information.

The NB–to–BB conversions used to estimate L'_{sol} and L'_{sw} can be either theoretical (i.e. based on radiative transfer computations) or empirical (i.e. based on corresponding NB and BB observations). However, it is critical that the unfiltered L'_{sol} and filtered L'_{sw} estimates are mutually consistent so that most of the (scene dependent) NB–to–BB conversion error cancels in Eq.(4.6).

It must be recognized that the thermal contamination $L'_{sw,th}$ is not properly taken into account in Eq.(4.6). Indeed, it would have been more rigorous to estimate the unfiltered GERB radiance as

$$L_{sol} = (L_{sw} - L'_{sw,th}) \left(\frac{L'_{sol}}{L'_{sw,sol}} \right) \tag{4.8}$$

so that the result does not depend on the absolute SEVIRI calibration that affects similarly the L'_{sol} and $L'_{sw,sol}$ (calibration error vanishes in the ratio). The unfiltering error introduced in the Edition 1 GERB data due to the use of Eq.(4.6) instead of Eq.(4.8) is quantified on real data under Section 4.5.6.

4.5.2 Theoretical regressions

The regressions estimate the broadband radiances L'_{sol} and $L'_{sw,sol}$ as second order polynomial regressions on the SEVIRI visible channel radiances

$$\begin{aligned} L'_{sol} = \quad & b_0 + b_1 L_{0.6} + b_2 L_{0.8} + b_3 L_{1.6} + b_4 L_{0.6}^2 + b_5 L_{0.8} L_{0.6} + \\ & b_6 L_{0.8}^2 + b_7 L_{1.6} L_{0.6} + b_8 L_{1.6} L_{0.8} + b_9 L_{1.6}^2 \end{aligned} \tag{4.9}$$

$$\begin{aligned} L'_{sw,sol} = \quad & c_0 + c_1 L_{0.6} + c_2 L_{0.8} + c_3 L_{1.6} + c_4 L_{0.6}^2 + c_5 L_{0.8} L_{0.6} + \\ & c_6 L_{0.8}^2 + c_7 L_{1.6} L_{0.6} + c_8 L_{1.6} L_{0.8} + c_9 L_{1.6}^2 \end{aligned} \tag{4.10}$$

The regression coefficients $\{b_i\}$ and $\{c_i\}$ are estimated as a best fit on the database of spectral radiance curves for each SZA = 0°, 10°,..., 80°. The fit is performed over the 750 Earth–atmosphere conditions and over a subset of viewing geometries (VZA = 0°, 20°, 40°, 60° and RAA = 0°, 60°, 120°, 180°). These NB–to–BB conversions are only dependent on the SZA and are neither dependent on the VZA, the RAA, the surface type, nor the cloudiness. The Table 4.2 provides the coefficients $\{b_i\}$ and $\{c_i\}$ for the GERB–2 instrument, and the RMS error of the fit in %. The coefficients for SZA = 90° are copied from the SZA = 80° coefficients, except the intercepts which are set to zero ($b_0 = c_0 = 0$) at SZA = 90°. Before fitting the Eqs.(4.9) and (4.10) on the simulations, the NB radiances $L_{0.6}$, $L_{0.8}$, $L_{1.6}$ are modified at random with a noise having Gaussian distribution with a standard deviation equal to 5% of the average radiance in the channel. This is necessary to avoid that the fits exploit excessively slight correlations between the simulated SEVIRI channels (overfitting of the data). The 5% value is selected as representative of the SEVIRI visible channels calibration accuracy (Govaerts *et al.*, 2001). When the Eqs.(4.9) and (4.10) are used for arbitrary SZA values, the parameters $\{b_i\}$ and $\{c_i\}$ are linearly interpolated in SZA.

The theoretical regressions (4.9) and (4.10) have been used for the generation of the pre–released GERB–2 data. Different limitations have been identified on these early products. First, the estimate of $L'_{sw,sol}$ over desert surface exhibited overestimation of about 15% according to the actual GERB observation L_{sw} when the non–reprocessed spectral response was used (i.e. before 28 October 2005). This overestimation did not introduce error in the unfiltered radiance but was the source of problems in other parts of the processing (e.g. the enhancement of the GERB spatial resolution). This overestimation affected the clear desert scene which is widely present in the Meteosat field of view (Sahara, Kalahari, and Arabian deserts). A second limitation is that the same set of regressions is used whatever the surface type. This was recognized as a drawback as it makes impossible improving the unfiltering for one surface type without modifying the unfiltering results over all the other geotypes. Finally, for dark scenes like clear ocean the unfiltering factor was obtained as the ratio of 2 small quantities and was affected by

SZA	b_0	b_1	b_2	b_3	b_4	b_5	b_6	b_7	b_8	b_9	RMS error $Wm^{-2}sr^{-1}$(%)
0°	14.366	4.943	6.524	-1.032	-0.033	0.021	0.079	0.280	-0.289	0.107	6.41 (4.20%)
10°	14.214	4.961	6.540	-1.123	-0.034	0.017	0.087	0.295	-0.323	0.137	6.32 (4.22%)
20°	13.597	5.000	6.481	-1.053	-0.037	0.021	0.092	0.302	-0.324	0.125	6.12 (4.28%)
30°	12.765	5.088	6.348	-0.909	-0.043	0.020	0.113	0.331	-0.358	0.103	5.77 (4.34%)
40°	11.587	5.291	5.875	0.030	-0.056	0.030	0.142	0.328	-0.294	-0.164	5.34 (4.46%)
50°	10.192	5.563	5.218	1.573	-0.077	0.058	0.167	0.291	-0.077	-0.836	4.82 (4.67%)
60°	6.829	6.721	3.695	3.481	-0.041	-0.191	0.513	0.083	-0.384	-0.091	4.84 (5.82%)
70°	4.955	6.891	3.076	5.193	-0.038	-0.415	0.969	0.325	-1.012	-0.346	3.64 (6.30%)
80°	2.730	6.563	3.931	5.523	-0.001	-0.151	0.512	-0.971	1.285	-1.903	2.16 (7.53%)
90°	0.000	6.563	3.931	5.523	-0.001	-0.151	0.512	-0.971	1.285	-1.903	-

SZA	c_0	c_1	c_2	c_3	c_4	c_5	c_6	c_7	c_8	c_9	RMS error $Wm^{-2}sr^{-1}$(%)
0°	7.129	3.177	4.351	-0.042	-0.026	0.021	0.052	0.173	-0.199	0.113	4.14 (4.19%)
10°	7.072	3.181	4.375	-0.127	-0.027	0.021	0.055	0.181	-0.220	0.137	4.06 (4.20%)
20°	6.719	3.201	4.342	-0.079	-0.030	0.025	0.059	0.186	-0.224	0.133	3.93 (4.26%)
30°	6.274	3.252	4.259	0.034	-0.035	0.026	0.072	0.206	-0.251	0.121	3.69 (4.30%)
40°	5.678	3.360	3.966	0.627	-0.044	0.036	0.091	0.209	-0.227	-0.030	3.39 (4.39%)
50°	4.993	3.511	3.560	1.604	-0.060	0.062	0.105	0.187	-0.101	-0.437	3.03 (4.55%)
60°	3.086	4.205	2.643	2.923	-0.042	-0.075	0.307	0.062	-0.290	-0.036	3.02 (5.63%)
70°	2.245	4.292	2.328	3.880	-0.054	-0.159	0.539	0.184	-0.620	-0.220	2.27 (6.09%)
80°	1.297	4.042	2.920	4.034	-0.096	0.244	0.049	-0.752	1.042	-1.291	1.35 (7.30%)
90°	0.000	4.042	2.920	4.034	-0.096	0.244	0.049	-0.752	1.042	-1.291	-

Table 4.2: Coefficients $\{b_i\}$ and $\{c_i\}$ for the theoretical regressions (Eqs. 4.9 and 4.10). The $\{c_i\}$ are valid for GERB-2 SW channel. The last column gives the residual Root Mean Square (RMS) error of the regressions.

numerical instabilities. Due to the first and second limitations, the theoretical regressions are not used anymore as the primary method for the unfiltering. They have been replaced by a new set of empirical regressions that we have called the "Dubrovnik" regressions, as they were presented during the 2005 EUMETSAT Meteorological Satellite Conference at the medieval city. These empirical regressions are detailed in the next section. To address the dark scene problem (third limitation), a specific unfiltering has been implemented for the clear ocean. The theoretical regressions are still used but only in case of mixed ocean/land pixels and when the SZA > 80°, near the terminator.

4.5.3 Adjustment of the regressions

Clerbaux *et al.* (2005) propose the following empirical regressions to estimate the broadband reflectances ρ'_{sol} and $\rho'_{sw,sol}$ as functions of the SEVIRI NB reflectances

$$\rho'_{sol} = d_0 + d_1\rho_{0.6} + d_2\rho_{0.6}^2 + d_3\rho_{0.8} + d_4\rho_{1.6} + d_5\mathrm{SZA} + d_6\mathrm{SGA} \quad (4.11)$$

$$\rho'_{sw,sol} = e_0 + e_1\rho_{0.6} + e_2\rho_{0.6}^2 + e_3\rho_{0.8} + e_4\rho_{1.6} + e_5\mathrm{SZA} + e_6\mathrm{SGA} \quad (4.12)$$

where SGA is the Sun Glint Angle[1] in degree. The reflectances $\{\rho\}$ are the corresponding

[1] $\cos(\mathrm{SGA}) = \cos(\mathrm{VZA})\cos(\mathrm{SZA}) + \sin(\mathrm{VZA})\sin(\mathrm{SZA})\cos(\mathrm{RAA})$

surface	d_0	d_1	d_2	d_3	d_4	d_5	d_6	RMS
ocean	0.015985	0.247134	0.004561	0.518540	0.015142	0.000129	0.000265	5.25%
dark vege.	0.007039	0.447929	-0.018466	0.373205	-0.007576	0.000379	0.000099	4.13%
bright vege.	0.006219	0.465640	-0.036540	0.359887	-0.011129	0.000357	0.000169	4.64%
dark desert	0.012397	0.403222	0.009855	0.398442	-0.028190	0.000207	0.000132	4.62%
bright desert	0.036945	0.238924	0.075104	0.477670	-0.069874	0.000566	0.000097	2.69%
snow	-0.117821	0.301393	-0.077451	0.670340	0.092932	-0.000197	0.000263	2.04%
surface	e_0	e_1	e_2	e_3	e_4	e_5	e_6	RMS
ocean	0.011928	0.177863	0.000715	0.588210	0.026470	0.000125	0.000214	0.38%
dark vege.	0.001095	0.440421	-0.023079	0.384094	0.009912	0.000381	0.000052	0.53%
bright vege.	0.001588	0.459780	-0.041845	0.368241	0.006747	0.000357	0.000119	0.62%
dark desert	0.005892	0.378195	0.002321	0.429143	-0.010994	0.000205	0.000088	0.56%
bright desert	0.029765	0.217151	0.067063	0.506242	-0.052025	0.000567	0.000052	0.51%
snow	-0.107395	0.208925	-0.059788	0.727045	0.106943	-0.000197	0.000226	0.24%

Table 4.3: Coefficients $\{d_i\}$ and $\{e_i\}$ and RMS error [%] for the adjusted regressions (Equations 4.11 and 4.12)

radiances L normalized by the incoming solar radiance, the cosine of SZA and the Earth–sun distance ($\rho = L/(L_{solar}cos(\text{SZA})/d^2)$). The regression coefficients $\{d_i\}$ and $\{e_i\}$ are not dependent on the SZA (which is already accounted for in the regression) but instead on the surface type. The surface type is extracted from an invariant 6–classes map derived from the 1 kilometer dataset of the International Geosphere and Biosphere Program (IGBP) classification (Townshend *et al.*, 1994). The classes (ocean, dark vegetation, bright vegetation, dark desert, bright desert, and snow) are the same as the ones used for the GERB SW radiance–to–flux conversion using the CERES TRMM ADMs (Loeb *et al.*, 2003b). Table 4.3 gives the regression parameters $\{d_i\}$ as empirically derived by Clerbaux *et al.* (2005) and the RMS error [%] for the 6 surface types. All these values are derived from a large database of coangular SEVIRI and CERES observations. As coefficients for snow are not provided in (Clerbaux *et al.*, 2005), they were derived as best fit of Eq.(4.11) on the SBDART simulations with snow geotype. The parameters $\{e_i\}$ are obtained as best fit on the SBDART simulations of

$$\frac{e_0 + e_1\rho_{0.6} + e_2\rho_{0.6}^2 + e_3\rho_{0.8} + e_4\rho_{1.6} + e_5\text{SZA} + e_6\text{SGA}}{d_0 + d_1\rho_{0.6} + d_2\rho_{0.6}^2 + d_3\rho_{0.8} + d_4\rho_{1.6} + d_5\text{SZA} + d_6\text{SGA}} = \frac{\rho_{sw,sol}}{\rho_{sol}} \tag{4.13}$$

where the $\{\rho\}$ are the simulated reflectances. Specific fits are done for the 6 surface types using the appropriate geotypes in the database of simulations as indicated in Table 4.4. The simulations with SZA $= 0°, 10°, 20°, ..., 70°$, VZA $= 0°, 10°, 20°, ..., 60°$ and RAA $= 0°$, $10°$, $30°$, $60°$, $90°$, $120°$, $150°$, $170°$, $180°$ are used. This is a subset of 504 sun–target–satellite geometries among the 3249 which have been simulated. The regression coefficients $\{e_i\}$ are given in Table 4.3 as well as the RMS error of the fit.

The adjusted empirical regressions (Eqs. 4.11 and 4.12) replace the theoretical regressions (Eqs. 4.9 and 4.10) over the complete FOV except for snow and mixed ocean/land pixels, and at the terminator (SZA $> 80°$).

Surface type	Categories used	Number of simulations
ocean	Ocean	301 × 504
dark vegetation	Vegetation	137 × 504
bright vegetation	Vegetation and Soils	(137+138) × 504
dark desert	Soils and Rocks	(138+150) × 504
bright desert	Rocks	150 × 504
snow	Snow	24 × 504

Table 4.4: Categories and numbers of simulations used to fit Eq.(4.13) for the 6 surface types.

4.5.4 Clear ocean unfiltering

The GERB unfiltering for clear ocean scene may be subject to important relative error due to the drop off in sensitivity of the instrument at wavelengths shorter than 0.45μm and also because the unfiltering factor is obtained in this case as the ratio of 2 small quantities. Furthermore, the clear ocean spectra $L_{sol}(\lambda)$ show more dependency on angular geometry: in the backward direction the spectrum is more "blue" than in the forward direction (more "white"). Therefore a specific unfiltering method is implemented for clear ocean pixels. Additionally, this may ease the improvement of the clear ocean unfiltering for subsequent Editions of the GERB database. The RMIB GERB cloud detection (Ipe *et al.*, 2008) is used to classify the ocean pixel as clear or cloudy.

For clear ocean, the unfiltering factor α_{sw} is estimated as a second order regression on the inverse of the SEVIRI reflectance $\rho_{0.6}$ in the bluest channel of the instrument. The reflectance value $\rho_{0.6}$ is first "clamped" between a minimum $\rho_{0.6,min}(\mathrm{SZA}, \mathrm{VZA}, \mathrm{RAA})$ and a maximum $\rho_{0.6,max}(\mathrm{SZA}, \mathrm{VZA}, \mathrm{RAA})$ value, which are dependent on the full angular geometry. This clamping means that a value lower than the minimum is replaced by this minimum and a value higher than the maximum is replaced by this maximum. This prevents using the highly non–linear regression out of the domain of simulations. The clamped reflectance is then used in the regression

$$\alpha_{sw} = f_0(\mathrm{SZA}, \mathrm{VZA}, \mathrm{RAA}) + \frac{f_1(\mathrm{SZA}, \mathrm{VZA}, \mathrm{RAA})}{\rho_{0.6}} + \frac{f_2(\mathrm{SZA}, \mathrm{VZA}, \mathrm{RAA})}{\rho_{0.6}^2} \tag{4.14}$$

The regression parameters are derived from the 301 ocean simulations in the database including, for the sake of robustness, the ones with cloudiness. For each angular geometry $(\mathrm{SZA}, \mathrm{VZA}, \mathrm{RAA})$, the $\rho_{0.6,min}$ and $\rho_{0.6,max}$ are the 5% and 95% percentiles of the simulated $\rho_{0.6}$ reflectances and the $\{f_i\}$ can be derived as best fit of Eq.(4.14) over the simulations for each set of SZA, VZA, and RAA values. Figure 4.4 illustrates the clear ocean unfiltering for the two angular geometries: $\mathrm{SZA} = 30°, \mathrm{VZA} = 40°$ and $\mathrm{RAA} = 30°$ (forward observation) and $\mathrm{RAA} = 150°$ (backward observation). A significant difference in unfiltering factor between these two geometries is apparent in clear sky conditions.

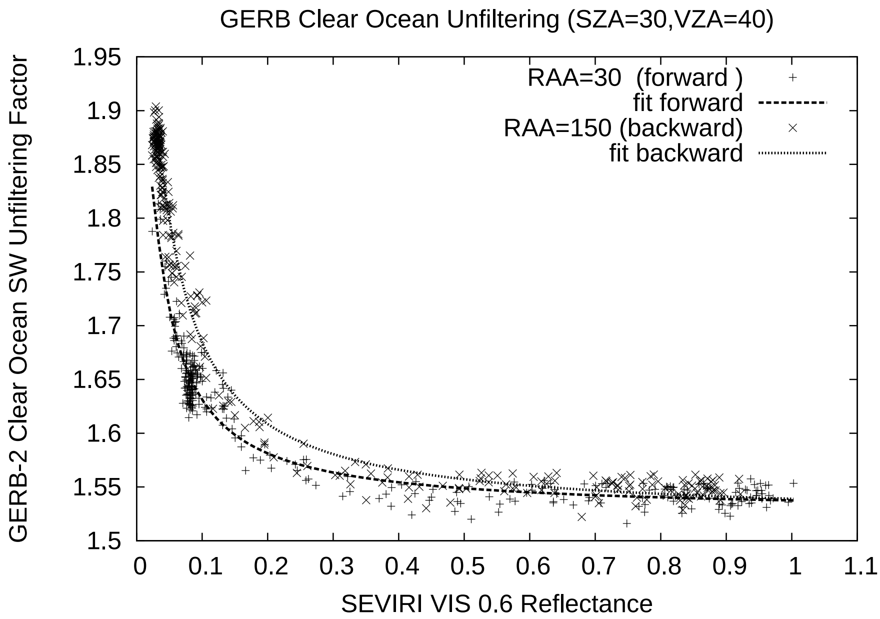

Figure 4.4: Illustration of the GERB–2 clear ocean unfiltering with Eq.(4.14) fit on the SBDART simulations for 2 particular geometries, one in the forward direction the other in the backward direction ("bluer" spectrum with higher unfiltering factor).

When the Eq.(4.14) is used for clear ocean unfiltering, the parameters $\{f_i\}$, $\rho_{0.6,min}$ and $\rho_{0.6,max}$ are tri–linearly interpolated in SZA, VZA and RAA. For SZA or VZA higher than 60°, the regression coefficients for 60° are used. This is needed as the radiative transfer computations provide doubtful results over clear ocean at grazing illumination and/or viewing angles. In these conditions, more robust results are obtained using the regression between $\rho_{0.6}$ and α_{sw} derived from the 60° simulations.

4.5.5 The GERB SW channel contamination by thermal radiation

The contribution of thermal radiation in the GERB shortwave filter must be estimated and subtracted. This is a typical spectral modeling problem of emitted thermal radiation. The problem is discussed here instead of in Chapter 5 as it affects the unfiltered SW radiance. This contribution is estimated from the 7 thermal channels of the SEVIRI instrument, using a regression similar to Eq.(5.5)

$$\begin{aligned} L'_{sw,th} = \quad & c_0 \quad + c_1 L_{6.2} + c_2 L_{7.3} + c_3 L_{8.7} + c_4 L_{9.7} + c_5 L_{10.8} + c_6 L_{12} + c_7 L_{13.4} + \\ & c_8 \quad L_{6.2}^2 + c_9 L_{7.3} L_{6.2} + c_{10} L_{7.3}^2 + c_{11} L_{8.7} L_{6.2} + c_{12} L_{8.7} L_{7.3} + \ldots + c_{35} L_{13.4}^2 \end{aligned} \tag{4.15}$$

with the coefficients $\{c_i\}$ of the regression being dependent on the VZA. Clerbaux *et al.* (2008a) provide the $\{c_i\}$ values and RMS errors of the regression at VZA = 0°, 25°, 50° and 75°. As

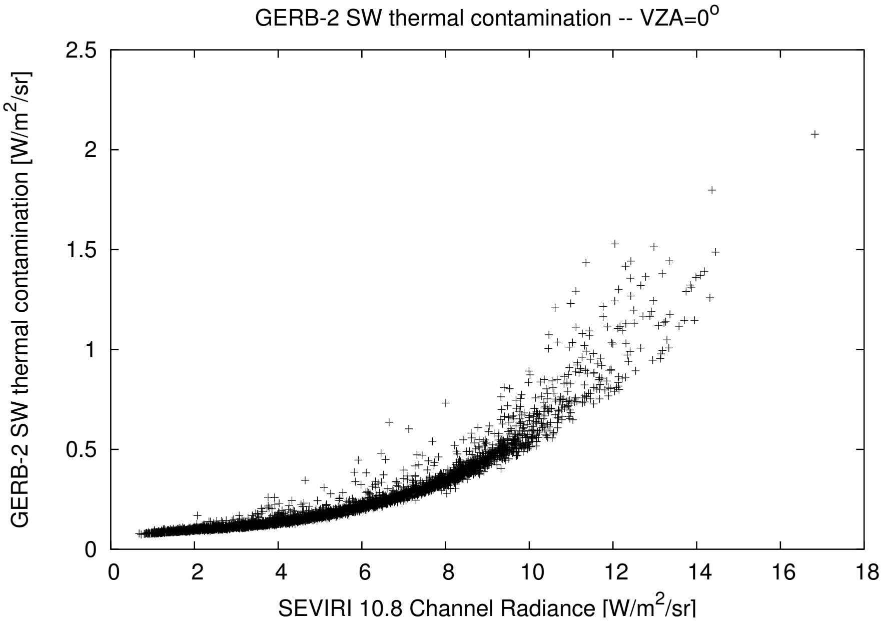

Figure 4.5: Scatterplot of the thermal contamination in the GERB–2 SW channel ($L_{sw,th}$) according to the SEVIRI 10.8 μm channel radiance. Each dot is a SBDART thermal simulations at viewing zenith angle VZA $= 0°$.

for the regressions on the visible channels (see Section 4.5.2), and for the same reasons, the simulated NB thermal radiances are modified at random with a random noise (5%) before the regression is fit on the simulated data. The Figure 4.5 provides an illustration of the magnitude of this contamination.

4.5.6 Theoretical assessment of unfiltering errors

In the following sections, the different sources of errors that affect the unfiltering process are addressed using radiative transfer simulations. Errors are expressed as the difference between the estimated and the actual unfiltered radiances. So, positive (negative) error means that the unfiltering process overestimates (underestimates) the resulting GERB unfiltered radiance.

Error due to the NB–to–BB regressions

Although the SEVIRI NB–to–BB theoretical regressions Eqs.(4.9) and (4.10) (or Eqs.(4.11) and (4.12) after adjustment) are affected by about 4.5% RMS errors (Tables 4.2 and 4.3), the unfiltering error is much smaller. This assumption is verified in this section on the database of simulations for the adjusted regressions (Section 4.5.3) and for the specific regression in case of clear ocean (Section 4.5.4). The not–adjusted theoretical regressions (Section 4.5.2) lead to similar unfiltering errors (not discussed here as these regressions are almost not used for the GERB unfiltering).

For each simulated scene $L_{sol}(\lambda)$, the BB (L_{sol}, $L_{sw,sol}$) and the NB ($L_{0.6}$, $L_{0.8}$, $L_{1.6}$) radiances are computed with Eqs.(4.2) and the unfiltering error is evaluated as

$$\epsilon[\%] = 100.0 \frac{L_{sw,sol}\frac{L'_{sol}}{L'_{sw,sol}} - L_{sol}}{L_{sol}} \tag{4.16}$$

where L'_{sol} and $L'_{sw,sol}$ are estimated through the NB–to–BB from the simulated SEVIRI NB radiances. Figure 4.6 shows the scatterplots of the unfiltering error ϵ versus L_{sol} for the 6 surface types and for a given sun–target–satellite geometry (SZA = 30°, VZA = 30°, RAA = 90°). The figure also provides the unfiltering bias (the average of the unfiltering error) and RMS error

$$\text{bias} = \frac{1}{N}\Sigma_{i=1}^{N}\epsilon_i \tag{4.17}$$

$$\text{rms} = \sqrt{\frac{1}{N}\Sigma_{i=1}^{N}(\epsilon_i - \text{bias})^2} \tag{4.18}$$

where the summations are done on the simulations that belong to a particular scene type. The figure shows that the unfiltering does not introduce significant bias in cloudy conditions and is affected by a small RMS error of less than half a percent. In clear sky condition, up to 2% unfiltering error is observed for some simulations. However, for this particular geometry, the bias and the RMS error for each of the 6 surface types are limited to 0.5% and 0.8%, respectively.

Similar scatterplots, biases and RMS errors are obtained at the other sun–target–satellite geometries. Table 4.5 provides the unfiltering bias and RMS error for the 6 surface types and the clear and cloudy conditions averaged over the following subset of 14 geometries

$$\begin{aligned}(\text{SZA}, \text{VZA}, \text{RAA}) = \quad & (0,0,90), (0,30,90), (0,60,90), (30,0,90), (30,30,20),\\ & (30,30,90), (30,30,160), (30,60,20), (30,60,90), (30,60,160),\\ & (60,0,90), (60,30,20), (60,30,90), (60,30,160)\end{aligned} \tag{4.19}$$

When the SBDART simulations for all the geometries are considered together, the table shows that the biases and RMS errors are respectively less than 0.2% and 0.8% for the different surface types and cloudiness. However, for all the scenes the bias is dependent on the geometry. The second part of Table 4.5 gives the biases and RMS errors for the 'worst' geometry in the set defined by Eq.(4.19). This 'worst' geometry is the one that presents the highest absolute value of the bias (|bias|). For these worst cases, the biases lie between −0.85% and +0.88% and are positive in clear and negative in cloudy conditions.

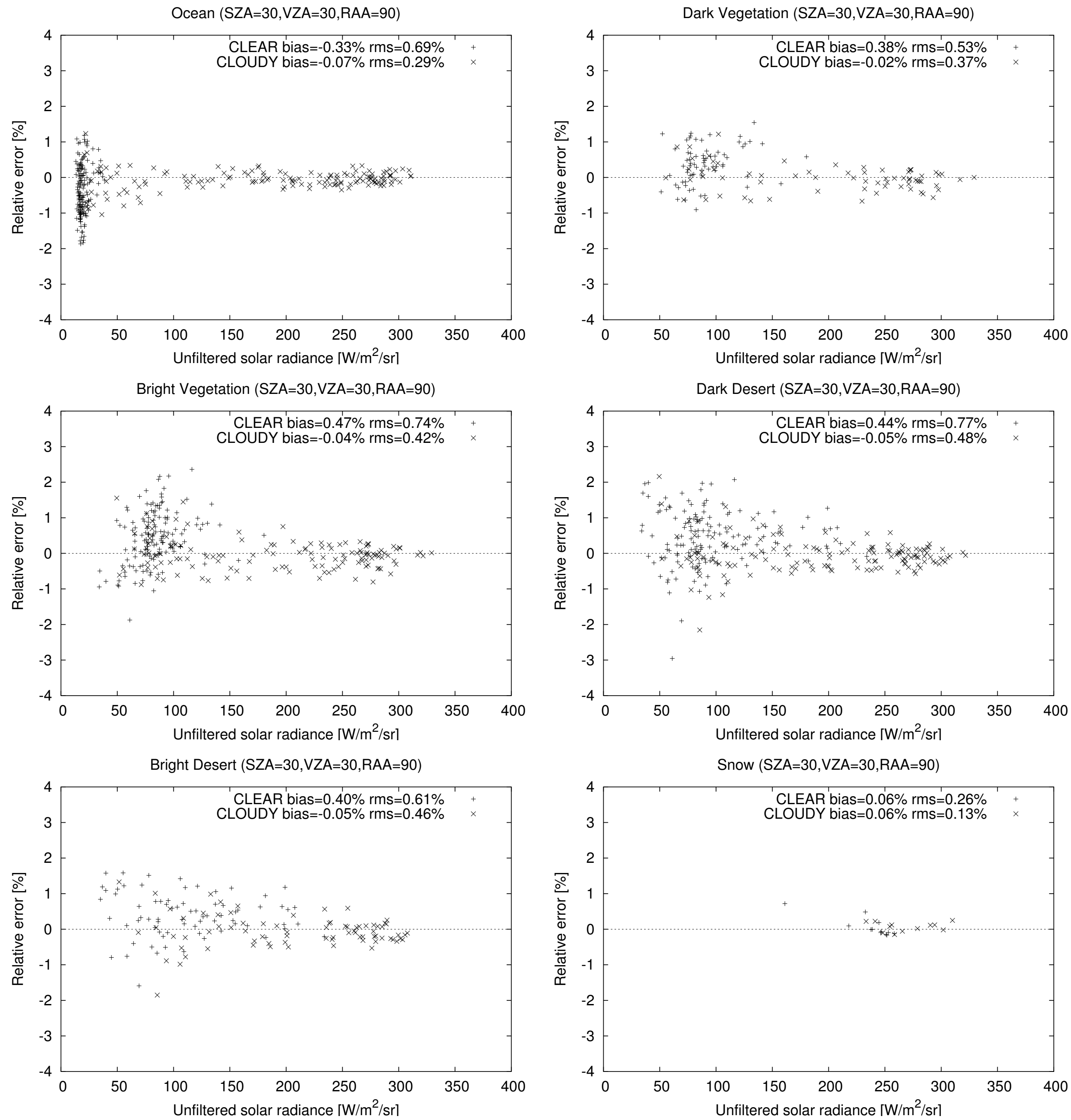

Figure 4.6: Scatterplots of unfiltering error ϵ versus the BB radiance L_{sol} for the adjusted regressions at the (SZA = 30°, VZA = 30°, RAA = 90°) geometry. The scatterplots are built up from the SBDART simulations classified in 6 surface types and for clear (+) and cloudy conditions (×).

Scene Type		RTM	All geometries together bias [%]/RMS [%]	Worst geometry bias [%]/RMS [%] (SZA, VZA, RAA)
ocean	clear	SBDART	-0.12 / 1.16	0.45 / 0.99 (00,00,090)
	clear	6S	0.38 / 1.08	1.22 / 1.33 (00,00,090)
	clear -continental	6S	-0.27 / 0.76	1.17 / 1.35 (00,00,090)
	clear - maritime	6S	0.66 / 0.52	1.22 / 0.20 (00,00,090)
	clear - urban	6S	1.15 / 1.00	2.08 / 1.43 (00,00,090)
	clear - desert	6S	1.07 / 0.56	1.41 / 0.17 (00,00,090)
	clear - biomass	6S	-0.69 / 0.96	-1.30 / 0.75 (00,00,090)
	cloudy	SBDART	0.03 / 0.33	-0.85 / 0.76 (00,00,090)
dark vegetation	clear	SBDART	0.13 / 0.60	0.48 / 0.53 (00,60,090)
	clear	6S	0.41 / 0.44	0.71 / 0.31 (00,60,090)
	cloudy	SBDART	-0.01 / 0.43	-0.60 / 0.42 (00,00,090)
bright vegetation	clear	SBDART	0.18 / 0.79	0.53 / 0.66 (00,60,090)
	clear	6S	0.37 / 0.62	0.76 / 0.43 (00,60,090)
	cloudy	SBDART	-0.04 / 0.49	-0.73 / 0.50 (00,00,090)
dark desert	clear	SBDART	0.19 / 0.79	0.52 / 0.77 (00,60,090)
	clear	6S	0.50 / 0.60	0.85 / 0.64 (00,60,090)
	cloudy	SBDART	-0.05 / 0.51	-0.69 / 0.59 (00,00,090)
bright desert	clear	SBDART	0.20 / 0.66	0.63 / 0.76 (00,60,090)
	clear	6S	0.39 / 0.52	0.88 / 0.69 (00,60,090)
	cloudy	SBDART	-0.04 / 0.49	-0.62 / 0.57 (00,00,090)
snow	clear	SBDART	0.06 / 0.25	-0.25 / 0.30 (00,00,090)
	cloudy	SBDART	0.05 / 0.19	-0.25 / 0.17 (00,00,090)

Table 4.5: Average bias [%] and RMS [%] of the unfiltering error ϵ for various scene types. The unfiltering is realized with the adjusted regressions except for the clear ocean for which the specific regression is used. The first column of numbers provides the errors when all the geometries are considered together whilst the last column is for the 'worst' geometry in terms of bias. This geometry is given in parenthesis (SZA, VZA, RAA).

The subset of geometries does not contain grazing solar and viewing geometries. Figure 4.7 provides a more complete analysis of the dependency of the unfiltering errors (bias and RMS error) as a function of the SZA and VZA angles. Panels (a)–(d) provide separate analyses according to the scene types, with different VZA and RAA considered together. Panel (a) shows a systematic decrease of the bias at increasing SZA for the different surface types in clear sky condition. At high solar zenith angle, this clear sky bias reaches $\sim -0.8\%$. Panel (c) shows the opposite dependency for cloudy conditions but to a smaller extent. Panels (e)–(h) provide the SZA dependency for the different angles of observation VZA, with the different surface types and RAA considered together. Panel (e) shows that the decreases of the bias observed in clear sky condition in panel (a) is due to the simulations at high VZA. For nadir observation (VZA $\sim 0°$) the clear sky bias does not present significant SZA dependency. To summarize Figure 4.7, the GERB unfiltering method has a tendency to underestimate the unfiltered radiance: (i) in clear sky conditions at grazing observation and illumination angles (bias of about -2% for SZA $\sim 70°$ and VZA $\sim 70°$) and (ii) in cloudy conditions at nadir sun and observation (bias of about -0.5% for SZA $\sim 0°$ and VZA $\sim 0°$).

For more confidence, the error introduced during the unfiltering has been assessed on an independent set of spectral radiance curves $L_{sol}(\lambda)$ generated at Imperial College (pers. comm. Helen Brindley) using the 6S (Vermote *et al.*, 1997) radiative transfer model. The database contains only clear sky simulations performed for the same geometries as given in Eq.(4.19). The land surface reflectance curves are extracted from the ASTER library. For the ocean simulations, the internal 6S model is used for 3 wind speed values (1, 5 and 10 ms^{-1}), 5 aerosol types (continental, maritime, urban, desert, biomass), and 6 aerosol optical thickness (0.1, 0.2, 0.4, 0.6, 0.8 and 1). Figure 4.8 shows the scatterplots of the unfiltering error for the 6S simulations at the (SZA $= 30°$, VZA $= 30°$, RAA $= 90°$) geometry. The scatterplots present similar error levels as the ones of Figure 4.6.

The average and worst case biases and RMS errors of the unfiltering using the 6S RTM are given in Table 4.5. As for the SBDART simulations, the unfiltering errors for spectra simulated with 6S show positive biases for clear sky conditions. All geometries together, the bias lies between 0.37% and 0.5% according to the surface type. For the 'worst' geometry the bias lies between 0.71% and 1.22%. The 6S simulations are used to quantify the unfiltering error introduced by tropospheric aerosol over clear ocean surface. For the worst geometry, the error remains less than $|\epsilon| < 2.08\%$ (urban aerosol). All geometries together, biases are dependent on the type of aerosol. Negative biases are observed for continental (-0.31%) and biomass (-0.74%) aerosol. Maritime (0.63%), urban (1.06%) and desert (1.03%) aerosol present positive biases.

Finally, Figure 4.9 shows the scatterplots of ϵ separately for the 14 geometries of Eq.(4.19). The figure also provides the biases and RMS errors. In general, the cluster of simulations is correctly centered with respect to the $\epsilon = 0\%$ line. This bias lies between 0.07% and 0.72%. The RMS error stays relatively constant at $\sim 0.8\%$ for these geometries except for the upper–left plot

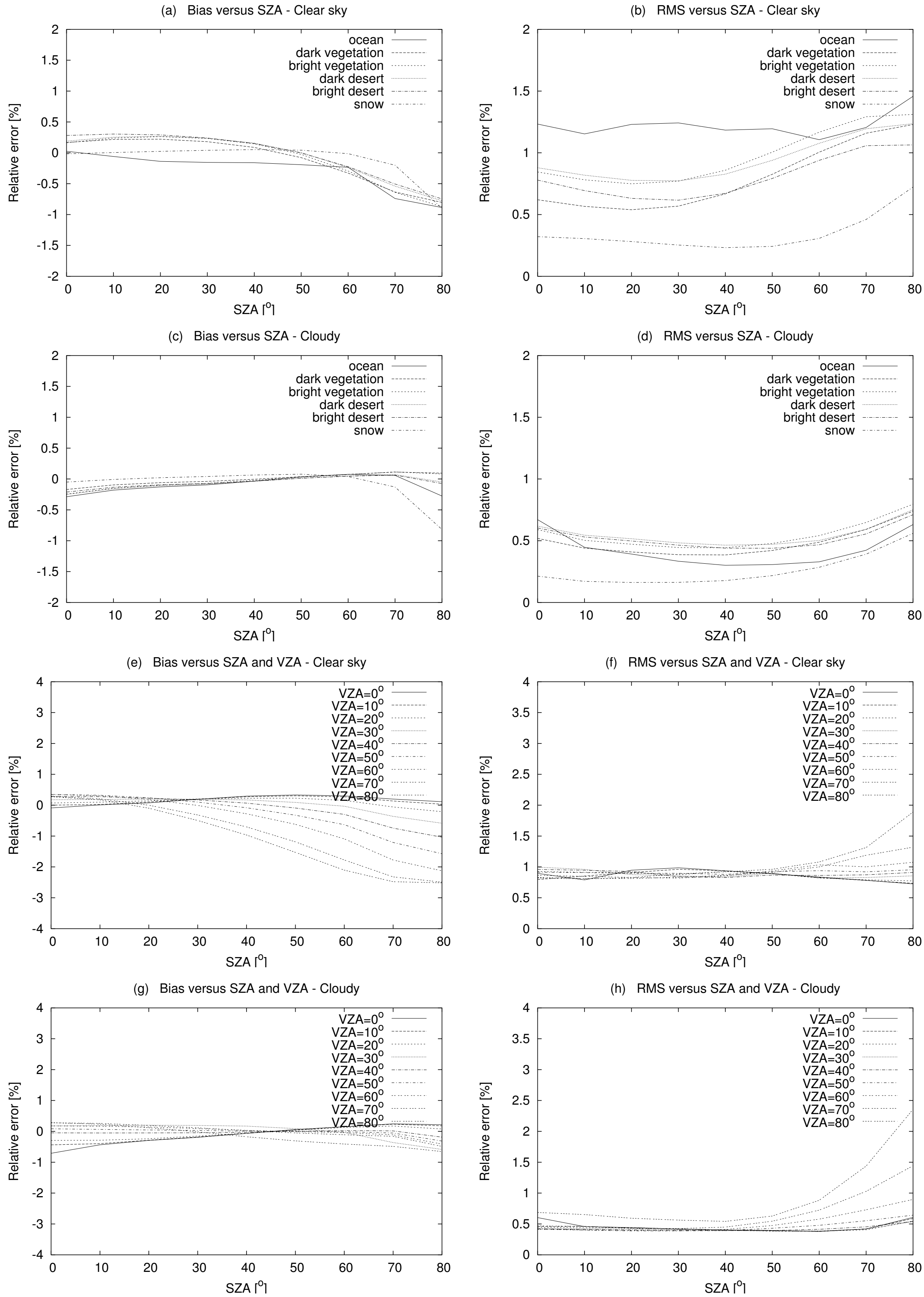

Figure 4.7: Solar zenith angle dependency of the bias (left) and RMS error (right) for clear and cloudy conditions. In panels (a)–(d), the analysis is done for the different surface types (all VZA together), and in panels (e)–(h) for different VZA (all surface type together).

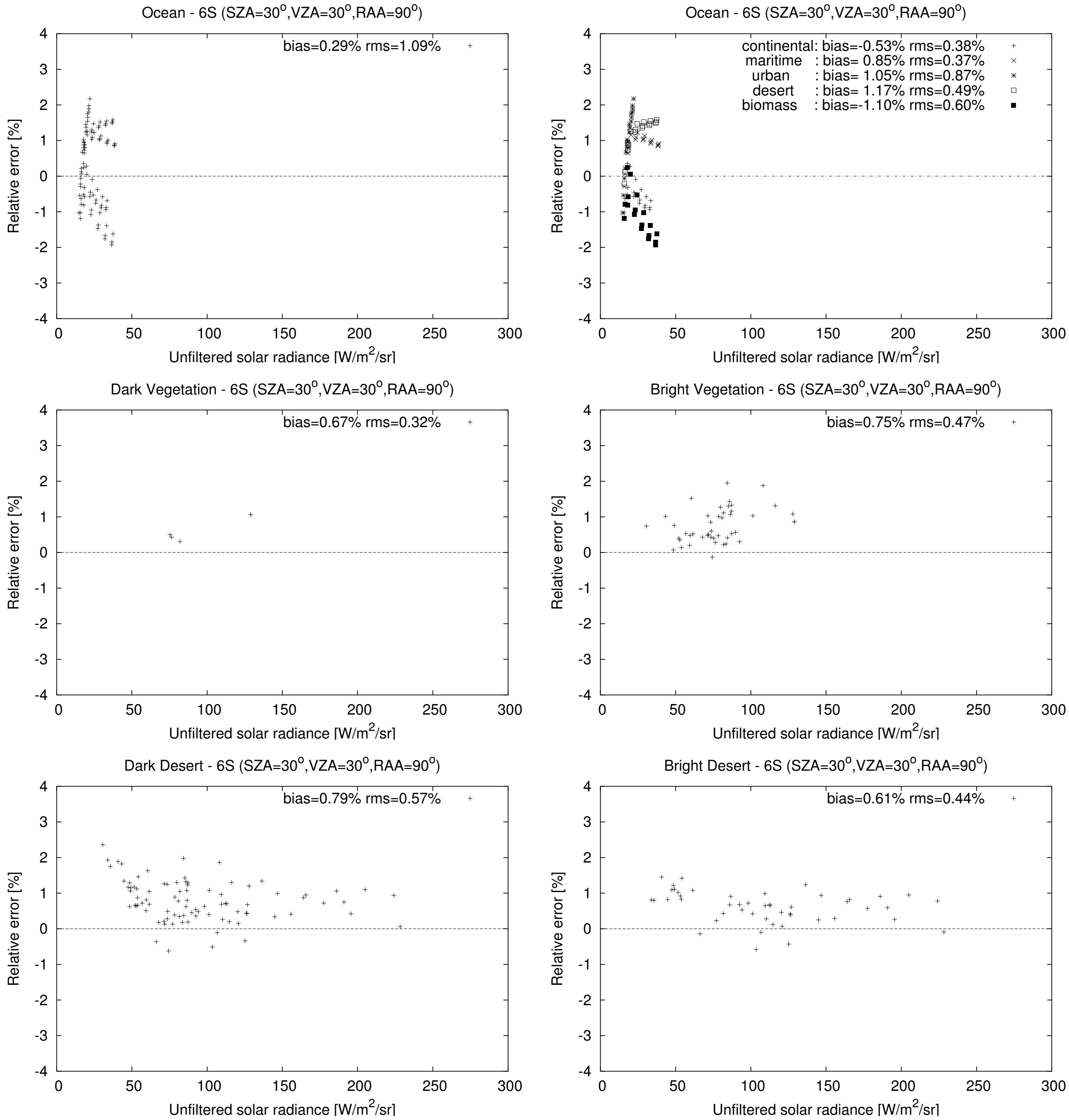

Figure 4.8: Scatterplots of unfiltering error ϵ versus the broadband radiance L_{sol} for the adjusted regressions at the (SZA = 30°, VZA = 30°, RAA = 90°) geometry. The scatterplots are built from the 6S clear sky simulations classified in 5 classes of surface type (no snow scenes are simulated). The upper–right scatterplot shows the unfiltering errors according to the aerosol type over clear ocean.

($\mathrm{SZA} = 0°, \mathrm{VZA} = 0°, \mathrm{RAA} = 90°$) where errors of up to 4% are observed. These higher errors correspond to sun–glint condition over calm clear ocean. At this geometry, the bias for the clear ocean simulations is 2.75% for wind speed at 1 ms^{-1}, 0.89% at 5 ms^{-1}, and only 0.02% at 10 ms^{-1}

Error in the estimated thermal contamination

The estimation of the thermal contamination in the SW channel $L_{sw,th}$ is a spectral modeling problem of the thermal radiation (Chapter 5). For GERB, this quantity is estimated from SEVIRI with Eq.(4.15). The magnitude of the thermal contamination is illustrated in Figure 4.5.

Figure 4.10 shows the scatterplot of the error on $L_{sw,th}$ according to the NB radiance in the 10.8 μm SEVIRI channel for the 4620 thermal simulations at $\mathrm{VZA} = 0°$. The figure shows that the error is in general very small. On the database of thermal simulations, the RMS error is only 0.03Wm^{-2}sr^{-1}. As can be seen in Figure 4.10, some of the LW simulations present higher error which can reach values of up to -0.28Wm^{-2}sr^{-1} (Wm^{-2}sr^{-1} unit is used instead of % because this error does not depend on the intensity of the solar radiance).

In nighttime conditions, the accuracy of this estimation can also be assessed on actual GERB and SEVIRI data. Figure 4.11 shows the scatterplot of the estimated contamination $L_{sw,th}$ versus the GERB measurement L_{sw} for $\mathrm{SZA} > 110°$ conditions between 4:00 UTC and 5:00 UTC, on 8 February 2007. Each point corresponds to average data over a $10° \times 10°$ latitude and longitude box. The figure shows a good correlation although the SEVIRI–based estimation appears overestimated by about 0.07 Wm^{-2}sr^{-1}. This is likely to result from the spectral response definition of the SW channel between 3 and 5 μm or beyond 50μm (leakage of the filter). The overestimation can also result from the in–fly determination of the instrument offset and the possible effect of stray-light on this offset determination.

Subtraction of the thermal contamination

As stated in Section 4.5.1, the implementation of the Edition 1 GERB data processing does not properly compensate for the thermal contamination in the GERB SW measurement. This introduces a small error ϵ which is the difference between Eqs.(4.8) and (4.6)

$$\epsilon = L'_{sol} \frac{L_{sw} - L'_{sw,th}}{L'_{sw,sol}} - L'_{sol} \frac{L_{sw}}{L'_{sw,sol} + L'_{sw,th}} \tag{4.20}$$

Let $\beta = L_{sol}/L'_{sol}$ be the ratio between the actual and the NB–to–BB estimated shortwave radiance. The Eq.(4.20) reduces to

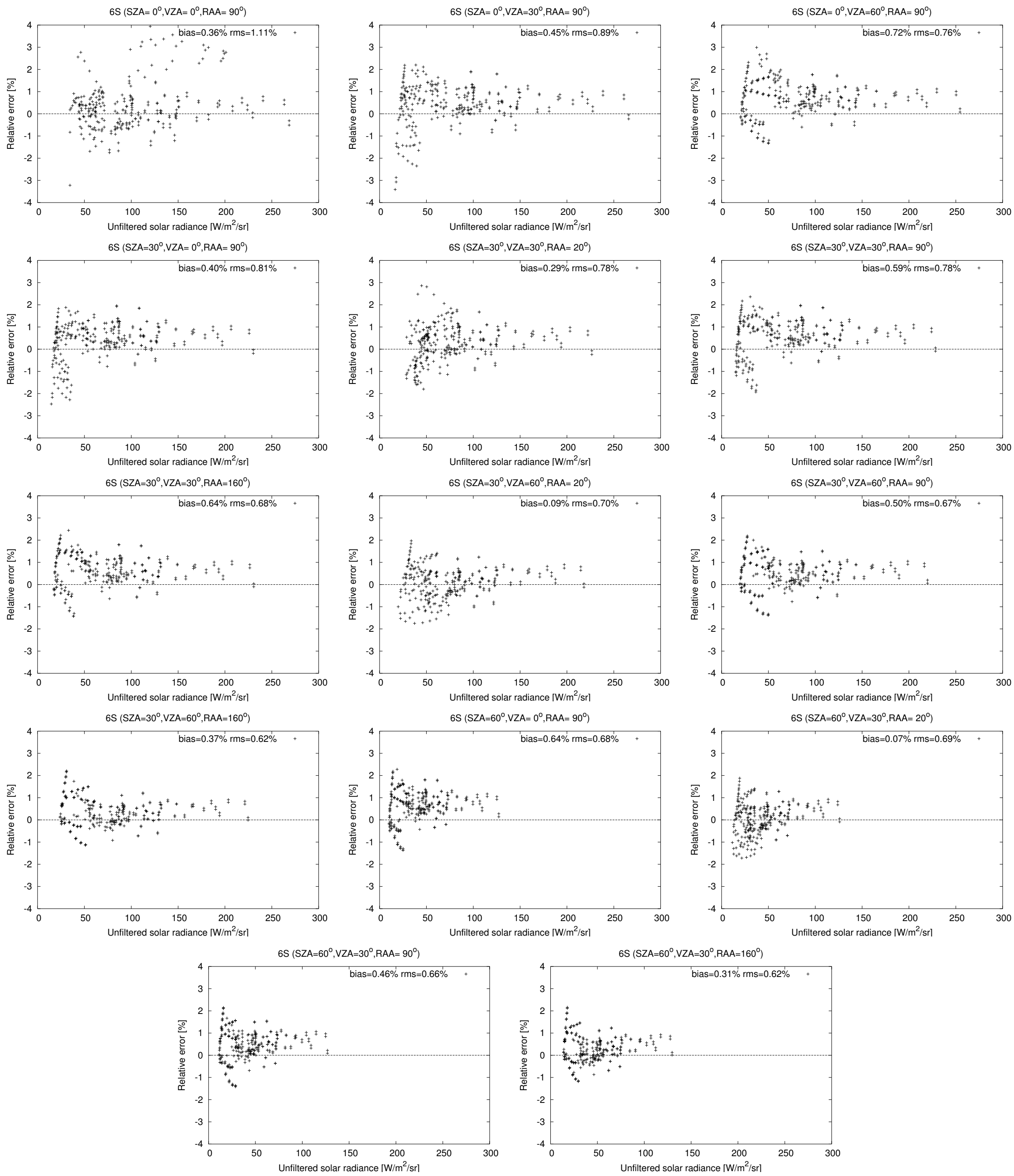

Figure 4.9: Scatterplots of unfiltering error ϵ versus the broadband radiance L_{sol} for the adjusted regressions and for the 14 geometries listed in Eq.(4.19). Each symbol represents one 6S simulation.

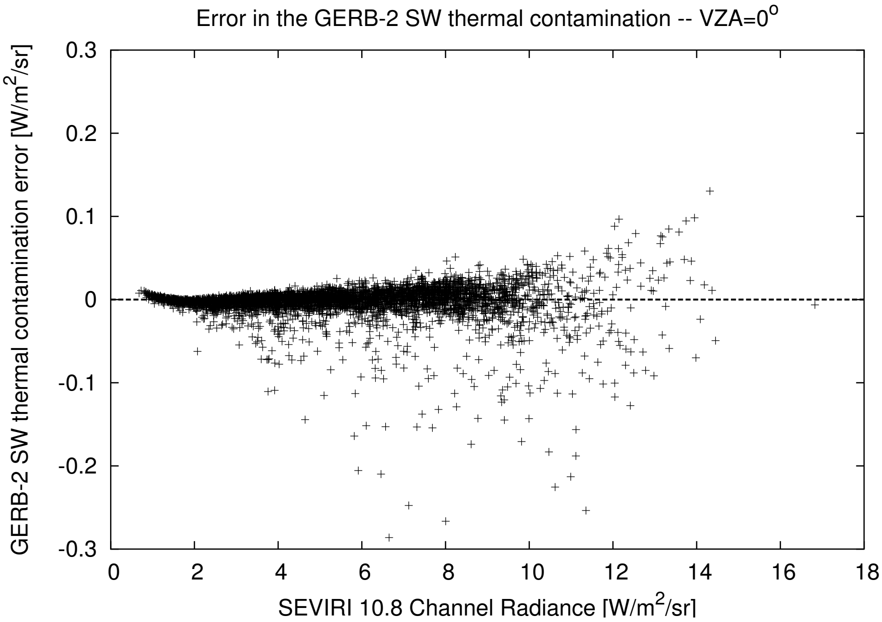

Figure 4.10: Scatterplot of the error on the estimated thermal contamination in the GERB–2 SW channel $L_{sw,th}$ according to the SEVIRI 10.8 μm channel radiance. The dots represent the SBDART thermal simulations at VZA $= 0°$.

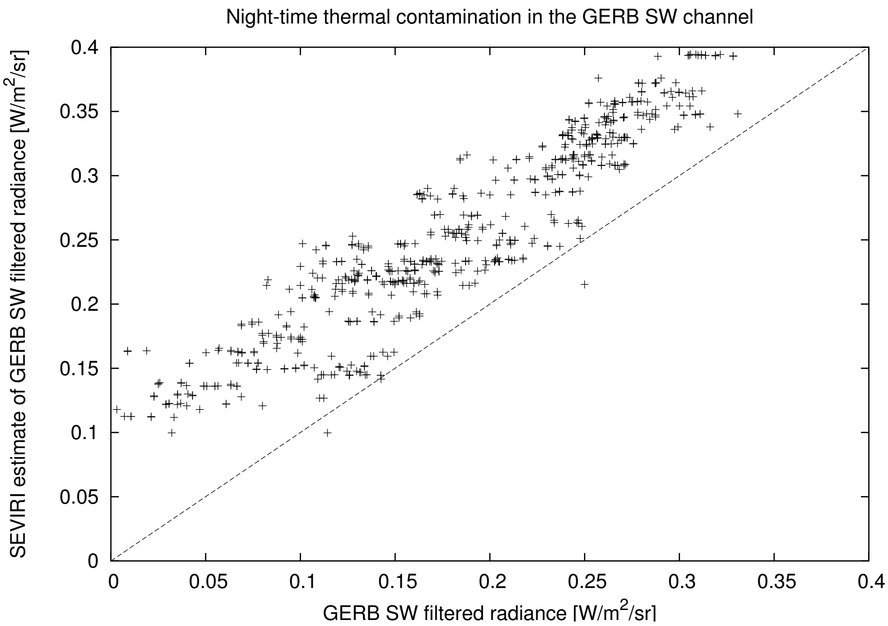

Figure 4.11: Nighttime (SZA $> 110°$) scatterplot of the estimated thermal contamination in the GERB–2 SW channel $L_{sw,th}$ according to the GERB measurement. Each point in the figure corresponds to average data over a $10° \times 10°$ latitude and longitude box for 8 February 2007 between 4:00 and 5:00 UTC.

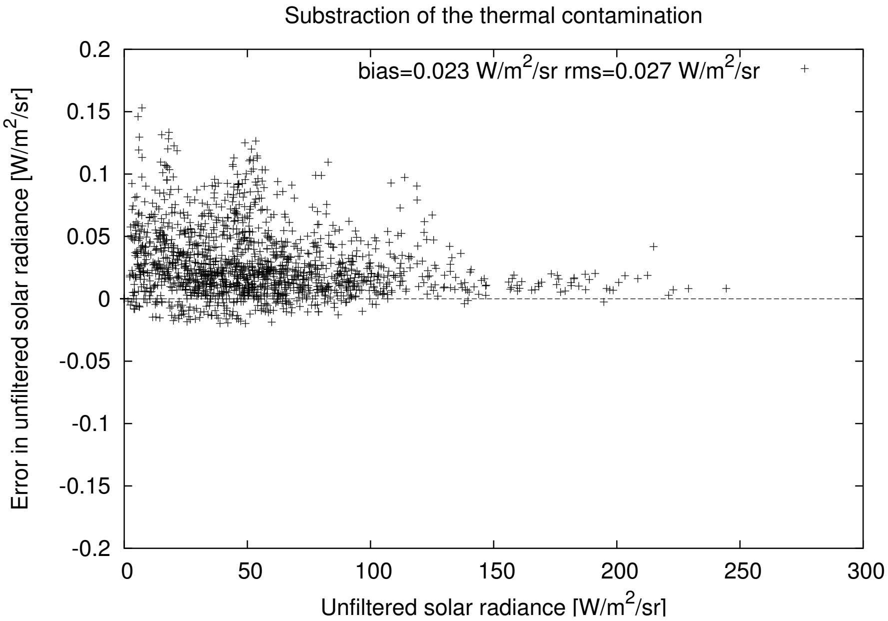

Figure 4.12: Error introduced on the solar radiance due to the incorrect subtraction of the thermal contamination in the SW channel (Eq. 4.21).

$$\epsilon = L'_{sol}(1-\beta)\frac{L'_{sw,th}}{L'_{sw,sol}} \tag{4.21}$$

The highest errors are expected for warm scenes for which the SW NB–to–BB regressions are inaccurate ($\beta \neq 1$). The Figure 4.12 shows the distribution of the error given by Eq.(4.21) evaluated on the actual GERB and SEVIRI data gathered on 20 September 2006 at 7:30 UTC. This error is always small ($\epsilon < 0.2$Wm^{-2}sr^{-1}). However, the relative error can be significant over warm clear ocean scene at low solar elevation angle. Relative errors of up to 4% are observed on the unfiltered radiance L_{sol}.

Sensitivity to SEVIRI absolute calibration

The calibration of the SEVIRI solar channels impacts on the estimation of the unfiltering factor α_{sw} while the calibration of the thermal channel affects the estimation of $L_{sw,th}$. To assess this, the effects of changing the SEVIRI channel calibration by -5%, 0%, $+5\%$ have been simulated. From the unfiltering point of view, the worst case occurs when some solar channels have a positive 5% change while others have -5% change. An overestimation of the unfiltering factor, α_{sw}, by 0.8% is observed for +5% on the 0.6μm channel and -5% on the 0.8μm and 1.6μm channels. The maximum impact on the estimated thermal contamination, $L_{sw,th}$, is observed when all the channels are changed by +5%. This causes an overestimation of the contamination with the same 5% magnitude. As the contamination can reach up to 1.5Wm^{-2}sr^{-1} for very warm scenes (Figure 4.5), the maximum effect on the unfiltered solar radiance is small ($\epsilon = 0.075$ Wm^{-2}sr^{-1}).

4.6 GERB SW radiance comparison with CERES

This Section reports on the comparison between GERB–2 and CERES SW radiances. Similar comparisons are done for the LW radiance (Section 5.6) and for the SW and LW fluxes (Sections 6.5 and 7.5). The methodology and the data used for these comparisons have been presented under Section 3.3.4.

Table 4.6 provides the shortwave radiance comparison results for the $\alpha < 5°$ coangularity criteria (similar results, not shown, are obtained with the $\alpha < 2°$ and $\alpha < 8°$ criteria). For all the GERB formats, all CERES instruments, and all the scene types, the GERB SW radiances are higher than the CERES ones. In all sky conditions, the GERB/CERES ratio m does not depend significantly (i.e. with respect to the uncertainty on m) on the GERB format but shows instead significant differences with respect to the CERES instruments: $m = 1.045$ for FM1, $m = 1.054$ for FM2, $m = 1.072$ for FM3, and $m = 1.068$ for FM4. A straight average of the ratio for the 4 CERES instruments (column with <FM> in the table) indicates that the GERB SW radiance is 5.9% higher than the CERES SW radiance. The ratios for June and December are in good agreement with a (non–significant) difference of about 0.003.

Scene type dependency is observed in the variation of m for overcast and clear conditions over various surfaces. Here significant differences are observed between the GERB ARG format on one side and the BARG and HR formats on the other side. The difference of ratio between clear sky and overcast scenes reaches 5.9% for the ARG but is limited to 2.0% and 2.1% for the BARG and the HR. This is explained by the fact that a number of the ARG pixels classified as clear sky will be contaminated by cloud and visa versa. This contamination is due to the non–correction of the PSF for the ARG, the simple rectification used for the ARG, and the limited accuracy of the GERB geolocation. The net effect is a decrease of m for cloudy scenes and an increase for clear sky scenes. The residual scene type dependency observed in the BARG and HR can be due to the spatial processing but can also be due to imperfect unfiltering of the GERB and/or CERES measurements. The unfiltering error for CERES and GERB is theoretically estimated to less than 1% according to Loeb *et al.* (2001) and Clerbaux *et al.* (2008b) respectively.

Figure 4.13 provides further evidence of scene type dependency affecting the GERB ARG format. On this figure, the GERB/CERES ratio is evaluated in bins of 0.05 of bidirectional reflectance (average of the GERB and CERES reflected radiances divided by the incident Solar irradiance). Unlike the BARG and HR, a significant variation of the GERB/CERES ratio according to the albedo of the scene is observed for the ARG format. This reflectance bin analysis proves that the scene type dependency affecting the ARG in Table 4.6 is not the result of imperfections in the GERB or CERES scene identifications. For instance, it would expect that the ratio will be higher than 1 if the GERB cloud detection fails to detect a significant fraction of the clouds. For the BARG and HR formats, the small decrease of the ratio between

Averaged Rectified Geolocated (ARG)							
Scene Type	FM1	FM2	FM3	FM4	< FM >	$< L_g >$	ΔL
All sky	1.044 ± 0.005	1.054 ± 0.004	1.072 ± 0.004	1.068 ± 0.005	1.059	76.25	4.21
June	1.042 ± 0.008	1.058 ± 0.006	1.073 ± 0.006	1.070 ± 0.007	1.061	70.92	4.02
December	1.046 ± 0.008	1.051 ± 0.006	1.070 ± 0.005	1.066 ± 0.008	1.058	81.46	4.39
Overcast	1.008 ± 0.010	1.026 ± 0.008	1.035 ± 0.009	1.023 ± 0.018	1.023	177.11	3.70
Clear sky	1.077 ± 0.019	1.066 ± 0.004	1.088 ± 0.004	1.097 ± 0.017	1.082	62.06	4.58
ocean	1.120 ± 0.087	1.143 ± 0.025	1.093 ± 0.024	1.076 ± 0.046	1.108	25.70	2.49
dark veg.	1.071 ± 0.020	1.077 ± 0.006	1.098 ± 0.015	1.104 ± 0.018	1.088	50.24	4.03
bright veg.	1.067 ± 0.011	1.063 ± 0.005	1.086 ± 0.008	1.105 ± 0.016	1.080	56.61	4.17
dark desert	-	1.078 ± 0.009	1.083 ± 0.023	-	1.081	77.73	5.78
bright desert	-	1.060 ± 0.004	1.086 ± 0.007	-	1.073	114.18	7.78
Binned Averaged Rectified Geolocated (BARG)							
Scene Type	FM1	FM2	FM3	FM4	< FM >	$< L_g >$	ΔL
All sky	1.045 ± 0.004	1.054 ± 0.003	1.071 ± 0.004	1.067 ± 0.004	1.059	76.51	4.24
June	1.044 ± 0.006	1.057 ± 0.004	1.074 ± 0.007	1.068 ± 0.005	1.061	71.28	4.08
December	1.045 ± 0.006	1.052 ± 0.005	1.068 ± 0.004	1.066 ± 0.005	1.058	81.62	4.40
Overcast	1.041 ± 0.008	1.050 ± 0.005	1.062 ± 0.007	1.064 ± 0.014	1.054	181.28	9.28
Clear sky	1.065 ± 0.012	1.065 ± 0.003	1.087 ± 0.004	1.078 ± 0.014	1.074	55.38	3.88
ocean	1.055 ± 0.024	1.084 ± 0.010	1.067 ± 0.013	1.038 ± 0.019	1.061	24.00	1.33
dark veg.	1.073 ± 0.010	1.072 ± 0.005	1.091 ± 0.008	1.099 ± 0.015	1.084	50.14	3.86
bright veg.	1.070 ± 0.014	1.062 ± 0.005	1.086 ± 0.009	1.105 ± 0.014	1.081	56.81	4.24
dark desert	-	1.062 ± 0.007	1.088 ± 0.011	1.080 ± 0.031	1.077	82.13	5.90
bright desert	-	1.066 ± 0.002	1.093 ± 0.004	-	1.079	114.34	8.40
High Resolution (HR)							
Scene Type	FM1	FM2	FM3	FM4	< FM >	$< L_g >$	ΔL
All sky	1.046 ± 0.003	1.057 ± 0.003	1.071 ± 0.003	1.067 ± 0.003	1.060	74.23	4.17
June	1.045 ± 0.004	1.060 ± 0.005	1.073 ± 0.004	1.069 ± 0.003	1.062	69.25	4.04
December	1.047 ± 0.005	1.054 ± 0.002	1.068 ± 0.004	1.064 ± 0.004	1.058	79.03	4.30
Overcast	1.033 ± 0.008	1.053 ± 0.005	1.061 ± 0.006	1.054 ± 0.008	1.050	171.45	8.05
Clear sky	1.064 ± 0.012	1.066 ± 0.004	1.088 ± 0.004	1.067 ± 0.016	1.071	52.92	3.65
ocean	1.054 ± 0.019	1.081 ± 0.011	1.066 ± 0.013	1.054 ± 0.025	1.064	24.53	1.43
dark veg.	1.080 ± 0.016	1.072 ± 0.005	1.095 ± 0.008	1.096 ± 0.011	1.086	51.65	4.07
bright veg.	1.069 ± 0.015	1.065 ± 0.005	1.086 ± 0.006	1.098 ± 0.011	1.079	56.83	4.12
dark desert	-	1.063 ± 0.006	1.091 ± 0.010	1.078 ± 0.013	1.077	79.01	5.69
bright desert	-	1.067 ± 0.002	1.098 ± 0.005	-	1.082	113.82	8.59

Table 4.6: GERB/CERES SW radiance ratio m and uncertainty for $\alpha < 5°$. The last columns give the average GERB radiance $< L_g >$ and the difference in average GERB and CERES radiance $\Delta L =< L_g > - < L_c >$ both in $\mathrm{Wm^{-2}sr^{-1}}$.

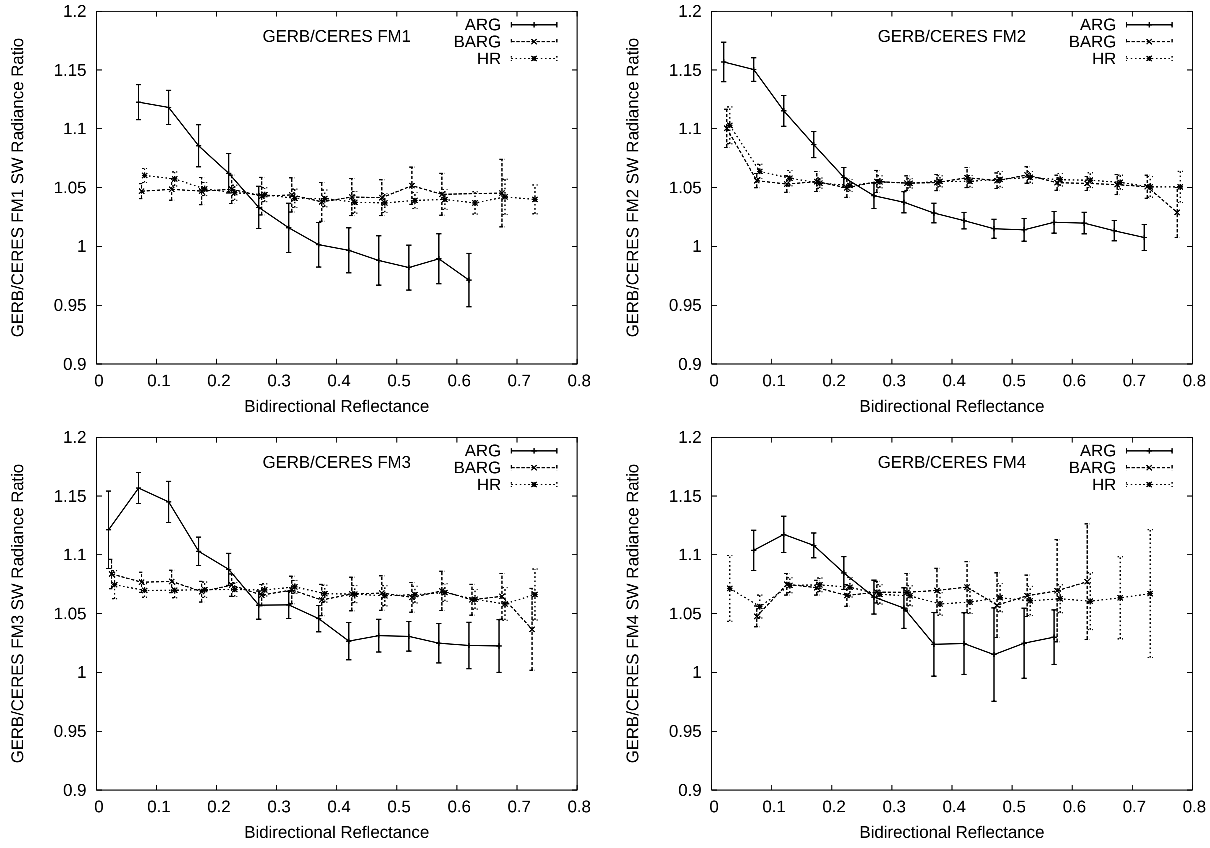

Figure 4.13: GERB/CERES SW radiance ratio m and uncertainty in reflectance bins for the coangularity criterium $\alpha < 5°$ (see Section 3.3.4).

the dark and bright scenes is consistent with the 2% difference between clear and cloudy scenes given in Table 4.6.

Figure 4.14 shows the variation of the ratio m with respect to the Solar Zenith Angle (SZA) and to the Viewing Zenith Angle (VZA) for the 3 GERB formats and for 3 scene types (clear land, clear ocean, and overcast). To get a good sampling of the angles, all the CERES instruments are considered together for this figure. The ratio m does not exhibit significant dependency on the SZA and VZA except for the clear ocean scene. For this case a significant increase of the ratio m with the VZA is observed. This increase is higher for the ARG than for the BARG and HR formats. As the GERB instrument sensitivity is lower in the blue part of the spectrum, the unfiltering is challenging for clear ocean and higher relative error is expected to occur (Clerbaux *et al.*, 2008b). The importance to have stable GERB/CERES ratio with respect to the SZA originates from the fact that the comparisons do not cover equally the different condition of illumination, as CERES is on sun–synchronous orbit.

Finally, Figure 6.2 (Chapter 6) shows the regional analysis of the GERB/CERES SW ratio for all sky radiance (first column) and clear sky radiance (second column). Images are given separately for the 4 CERES instruments, as well as their average (FMX). For these images, the GERB radiances have been taken from the BARG format. As expected from the scene type

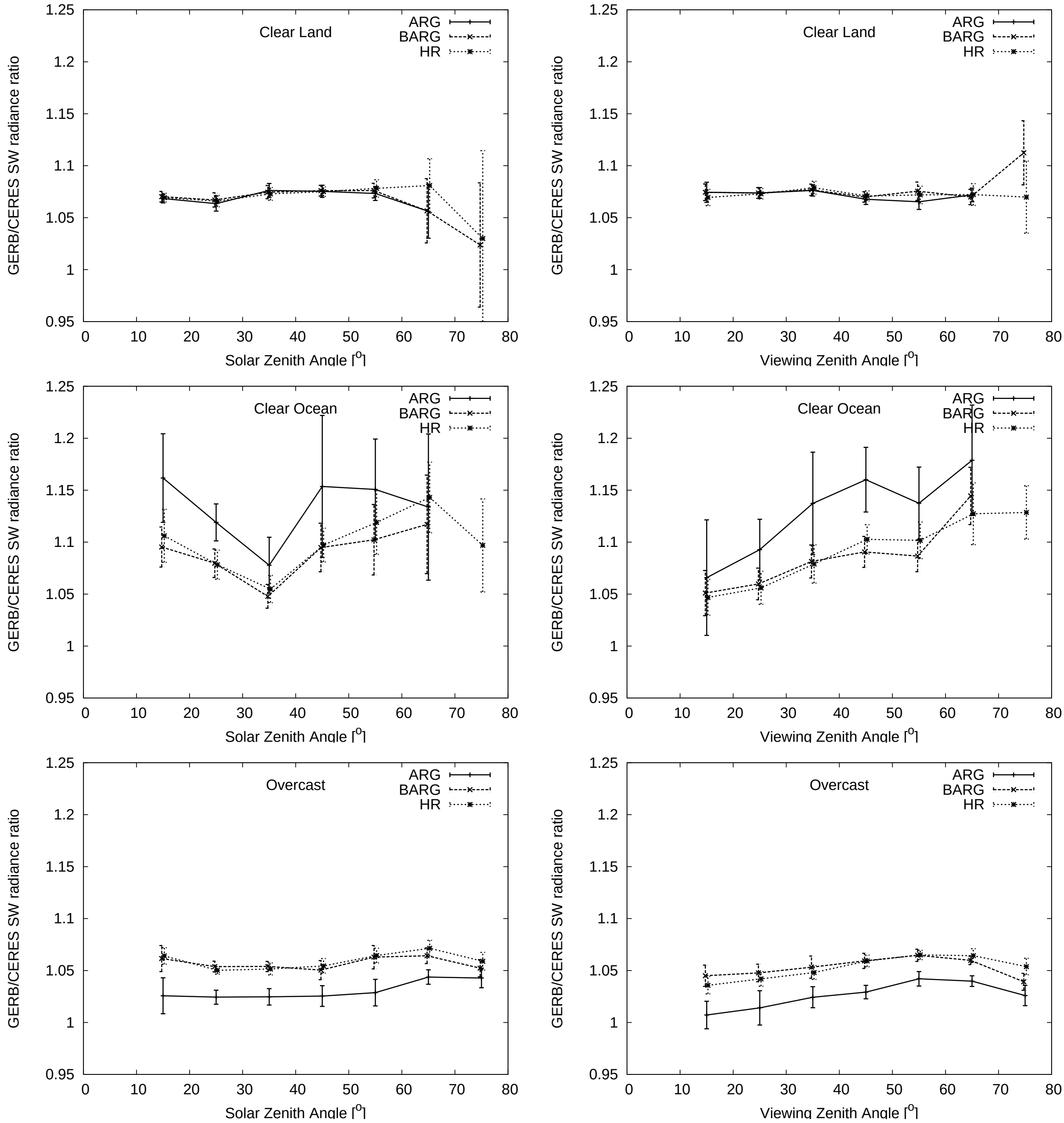

Figure 4.14: Angular dependencies of the GERB/CERES SW radiance ratio m with the Solar Zenith Angle (SZA, left) and the Viewing Zenith Angle (VZA, right). Top, middle and bottom graphs are for clear land, clear ocean and overcast, respectively.

analysis, a slightly lower GERB/CERES ratio is observed in areas with frequent cloudiness in the all sky image.

In summary, the SW GERB radiance is about 5.9% higher than CERES (average over the 4 CERES instruments). Except for the ARG products, scene type dependency of the GERB/CERES ratio is limited to about 1.5% around the $m = 1.069$ value. Therefore a difference in the absolute calibration of the GERB and CERES SW channels seems the most likely cause of the discrepancy. The observed ratio of 1.059 +/- 0.004 for the SW radiance seems to agree with the arithmetic sum of the 95% confidence levels (2 SD) of both GERB (3.8%) and CERES (2%). However, as the calibrations and data processings of the instruments have been kept totally independent, the uncertainty on the difference is the RMS of the uncertainties, thus 4.3% at the 95% confidence level. Assuming normal distributions with the SDs given before, the probability that the ratio of one instrument on the other reaches a value of 1.055 is only 1.4%. It is therefore likely that the absolute accuracy of one or both instruments is poorer than theoretically expected in the SW. Results given here highlight the differences between the GERB products. In particular they show the difficulty of using GERB ARG data to isolate the effect of small regions or individual scene types. Moreover, they illustrate the errors occurring when the full extent and detail of the instrument PSF are not considered. The GERB BARG and HR formats are easier to compare with other instruments and yield more consistent differences with CERES for the comparisons shown here. These formats are in the process of being validated and officially released for scientific use by the GERB team. Further investigations have confirmed that the apparent scene type dependency affecting the ARG format is due to the non–compensation of the PSF (Jacqui Russell and Luis Gonzalez, pers. comm.).

4.7 Pixel–to–pixel variability in spectral response

To address the effect of the GERB pixel–to–pixel variability in spectral response curve $\phi_{sw}^{det}(\lambda)$, the difference $(max - min)$ in filtered SW radiance

$$L_{sw}^{det} = \int \phi_{sw}^{det}(\lambda) L_{sol}(\lambda) d\lambda \tag{4.22}$$

is evaluated over the 256 detectors for each simulation $L_{sol}(\lambda)$. The symbols $'+'$ in Figure 4.15 show that this dispersion increases linearly with the brightness of the scene but remains limited to less than 0.18Wm^{-2}sr^{-1}. The technical note (TN31) proposes to use a linear regression

$$L_{sw} = a^{det} + b^{det}\ L_{sw}^{det} \tag{4.23}$$

to convert the filtered radiance measured by a detector L_{sw}^{det} in the radiance L_{sw} that would have been measured by the (fictive) average detector defined by Eq.(3.1). The values a^{det} and b^{det} in Eq.(4.23) are given in (TN31) for the 256 detectors of GERB–2. The symbols $'\times'$ in Figure 4.15 show that the simple correction significantly reduces the dispersion in filtered radiance between the different detectors. It is worth noting that the work summarized in this section and detailed in (TN31) is based on the Edition 1 spectral response curves $\phi_{sw}^{det}(\lambda)$. These curves differ only by the transmission of the optics, because an equal spectral response curve is used for all of the 256 detectors. Nevertheless, the method has been tested on the early GERB–2 "noisy" detector spectral responses and has proven to work efficiently. In this case, the Eq.(4.23) permits to reduce the pixel–to–pixel dispersion by a factor 3.

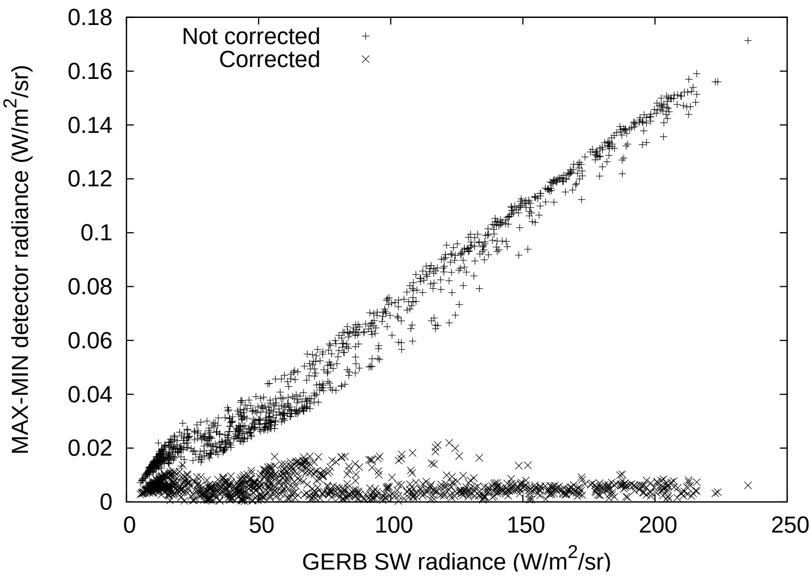

Figure 4.15: Scatterplot of the $(max - min)$ differences for the GERB–2 detectors SW filtered radiance according to the average SW radiance. The $'+'$ and $'\times'$ symbols correspond to the uncorrected and the corrected radiances with Eq.(4.23).

4.8 Unfiltering of the SEVIRI visible channels

4.8.1 Introduction

Different applications require estimating the BB SW radiance from the NB observations of SEVIRI. A review of the existing literature on this topic is given in Table 2.2. In this section, we present different NB-to–BB regressions that have been successively implemented within the GERB and CM–SAF processing systems. Clerbaux *et al.* (2001) provided a preliminary study on the possibility to derive TOA radiative fluxes from the NB measurements of SEVIRI. Using second order regressions on the NB observations, this theoretical (i.e. based on radiative transfer computation) study quantifies to 3.2% the RMS error on the estimated BB reflected solar radiance[1]. These theoretical regressions and their performances are briefly discussed under Section 4.8.3. The first SEVIRI instrument has been operational since the 1 February 2004. Corresponding BB observations are provided by the GERB instrument (in a quasi–continuous manner) and by the CERES instruments on Terra and Aqua satellites (about 4 times per day). A first set of empirical NB–to–BB regressions has been derived using coangular SEVIRI and CERES FM2 and FM3 observations. The methodology and results were presented during the 2005 EUMETSAT conference in Dubrovnik (we refer to them as "Dubrovnik regressions") and are discussed under Section 4.8.4. These regressions are used in the GERB Edition 1 processing. As the GERB and CERES SW radiances differ by about 6% (Section 4.6), from a radiometric point–of–view the Dubrovnik regressions produce more "CERES–like" than "GERB–like" data. For this reason, a correction of these CERES–based BB radiance has been developed and is used in the Climate Monitoring SAF as detailed under Section 4.8.5. Later on, the reprocessing of the GERB–2 dataset with the Edition 1 algorithms allows deriving actual GERB–like regressions. This work, presented in Section 4.8.6, is planned to be implemented in the Edition 2 of the processing. We also consider submitting this work as a manuscript for publication in a peer-reviewed journal, after additional validations and consolidations of the method.

To estimate the BB SW radiance from SEVIRI, the more informative channels are the 0.6 μm and 0.8 μm, while the near infrared 1.6 μm channel is less useful. Although the broadband feature of the High Resolution Visible (HRV) channel could be of interest, the HRV is usually not considered for NB–to–BB regressions. The main reason for this is that the HRV was initially foreseen to cover only a fixed half part of the Meteosat disk (in the east–west direction). However, since August 2005 a new configuration of the HRV coverage has been implemented that optimizes the observation over the illuminated part of the disk. In this configuration, the window moves from east to west to follow the course of the Sun. This configuration makes the

[1] The 3.2% RMS error has been evaluated on the first version of the radiative transfer computation which is not described here. The method has been later consolidated using an improved version of the database of simulations. On this second iteration of the simulations (presented under Section 4.3) the RMS error reaches 4.5%. This indicates that a higher variability of spectra has been simulated.

HRV more suitable for ERB studies over the full Meteosat FOV. In this work, no attempt has been done to combine the HRV BB information with the NB radiances of the other channels.

An often observed limitation of the NB–to–BB technique is that the resulting BB radiances suffer from inaccuracy and drift (aging) in the calibration of the input NB radiances. In this work, the temporal stability is assessed by comparisons with GERB over the full period when MSG–1 has been the operational satellite. These comparisons show that all the regressions present a small positive drift of $\sim 0.3\%$/year. This point is discussed under Section 4.8.7. As said under Section 3.2, although the SSCC method is applied on a regular basis, the calibration provided in NRT in the SEVIRI prologue file is changed by "jumps", when necessary. To avoid that these jumps propagate in the BB estimate and complicate the interpretation of the results, "frozen" calibration coefficients have been used hereafter. For Meteosat–8, we have selected the calibration coefficients that have been disseminated in near real–time from 11 February 2004 up to 1 April 2005. They are given in Table 3.4.

4.8.2 Database of corresponding SEVIRI/GERB radiances

For the validation of the SEVIRI NB–to–BB regressions we can take advantage of the GERB Edition 1 dataset which provides coangular validated BB radiance. With that aim in mind, a database of corresponding SW unfiltered radiance from the GERB-2 BARG products and the corresponding NB radiances from SEVIRI has been elaborated. The BARG format was preferred to the ARG due to the scene dependency affecting the ARG discussed in Section 4.6. The downscaling from the fine 3km SEVIRI spatial resolution to the coarse BARG 45km one is straightforward: it consists in simple averaging in 15×15 pixel boxes. Concerning the temporal matching, each SEVIRI observation is associated with the BARG time interval that contains the time of the SEVIRI observation. With the additional constraints on the SZA $< 80°$ and VZA $< 80°$, the daily number of (perfectly coangular) couples of observation is about 7×10^5. Thanks to this huge number of NB and BB observations, the database is well suited for comprehensive validation, including the validation of the regressions at regional scale. Furthermore, as the database extends over more than 3 years, a first assessment of the cross–stability of GERB and SEVIRI can be carried out.

4.8.3 Theoretical regressions

In the initial design of the RGP, it was foreseen to use theoretical NB–to–BB regressions on the SEVIRI NB radiances. To that end, second order regressions (Eq. 4.9) on the 0.6 μm, 0.8 μm, and 1.6 μm radiances are fit on the RTM simulations. The regressions are not dependent on the surface type but depend on the SZA. The best fit coefficients $\{b_i\}$ of Eq.(4.9) and the residual RMS errors are given in Table 4.2 for SZA $= 0°, 10°, ..., 90°$. The theoretically estimated error on

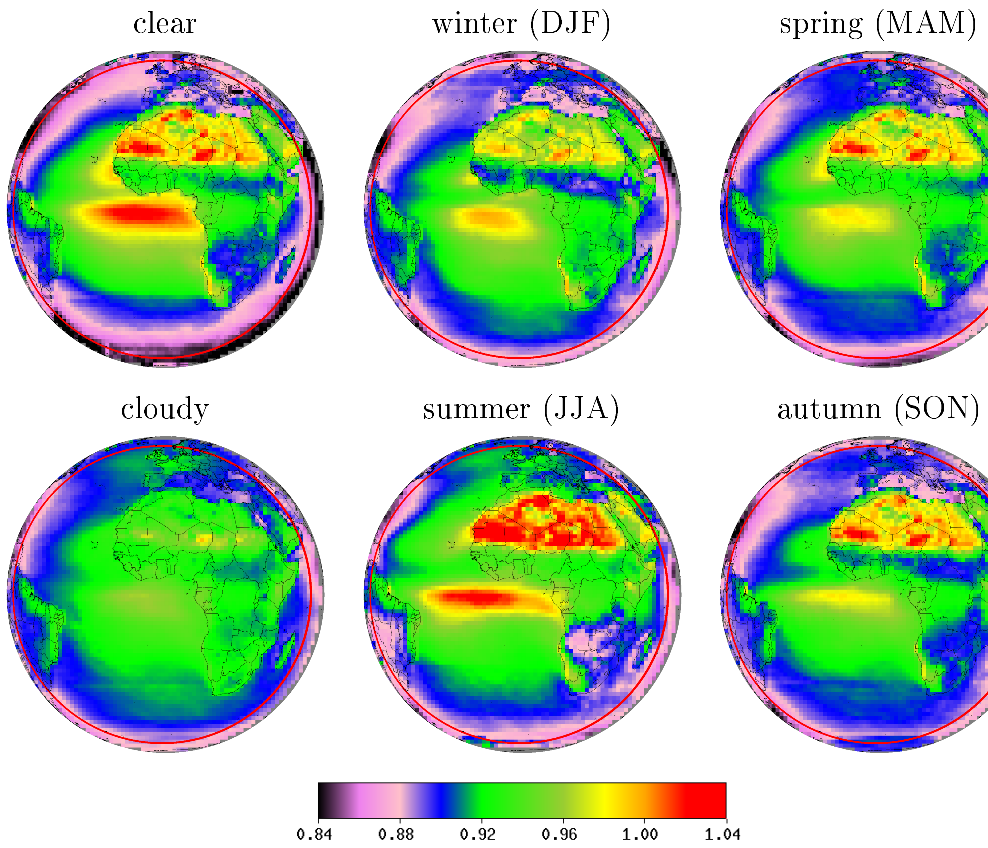

Figure 4.16: Regional scale (135km × 135km boxes) ratio between the theoretical NB–to–BB regressions (Eq. 4.9) and GERB Edition 1. The color palette is centered on 0.94.

the BB radiance is about 4.5%. The comparisons with pre–released GERB data gave evidence of regional problems affecting these theoretical regressions, as well as a residual VZA dependency. Figure 4.16 provides the regional analysis of the <GERB–like>/<GERB> ratio evaluated for clear and cloudy scenes and over the 4 meteorological seasons (DJF=Dec+Jan+Feb, ...). Table 4.7 gives the biases and RMS errors of the regression for different scene types and seasons. In average, the estimated BB radiance lies 8% lower than GERB. According to this overall bias, the RMS error is about 4% for clear sky and 2% for cloudy scenes. Figure 4.20 provides the temporal evolution of the daily values of the ratio.

4.8.4 Dubrovnik regressions

Recognizing the problems affecting the theoretical regressions, a set of CERES–based empirical regressions has been derived in preparation of the Edition 1 GERB processing. The methodology and results were presented during the 2005 EUMETSAT Conference in Dubrovnik. The proceeding paper (Clerbaux *et al.*, 2005) is available from the authors and on the EUMETSAT web site.

The work is based on the CERES ERBE–like (ES8) Edition 2 data for the FM2 (on Terra) and FM3 (on Aqua) instruments for the months of March, April and July 2004. A database of coangular ($\alpha < 15°$) CERES and SEVIRI data has been extracted using a maximum difference of 450s for the temporal matching (so that each CERES observation is associated with one SEVIRI observation). The study of the best–suited regression has been carried out using a least mean square software and a stepwise approach. These investigations have proved that the best performances require the use of regressions dedicated to the surface type. The study also showed that: the best proxy is the $\rho_{0.6\mu m}$ reflectance, the addition of the $\rho_{0.8\mu m}$ reflectance improves the results over vegetation, the $\rho_{1.6\mu m}$ is useful over sandy surfaces, there exists a small dependency on the SZA, there is no significant dependency on neither the VZA nor the RAA (at least when clear and cloudy data are considered together in the regression), there is a small dependency on the Sun–Glint Angle (SGA). Finally, a second order term on the reflectance (e.g. $\rho^2_{0.6\mu m}$) reduces the biases when clear and cloudy scenes are considered separately. Based on these findings, the following regression is proposed

$$\rho'_{bb} = d_0 + d_1\ \rho_{0.6} + d_2\ \rho^2_{0.6} + d_3\ \rho_{0.8} + d_4\ \rho_{1.6} + d_5\ \mathrm{SZA} + d_6\ \mathrm{SGA} \tag{4.24}$$

Table 4.3 gives the best fit parameters $\{d_i\}$ and the residual RMS error for each surface type. Based on the database on SEVIRI/CERES observations, the proceeding paper (Clerbaux *et al.*, 2005) provides validations in terms of bias and RMS error according to the scene type and at regional scale. The RMS error is about 4.5% for land surface, 5.2% for ocean and 2.7% for bright desert. The paper concludes that: "... the SEVIRI NB–to–BB regressions perform well in most parts of the Meteosat FOV. The error remains typically below 3.5%. Higher error could occur over cloud free ocean in case of sun glint, aerosols, non–standard ocean color, and grazing observation angle."

Figure 4.17 and Table 4.7 provide regional validation of the Dubrovnik regressions with the GERB Edition 1 data. In regard to the theoretical regressions, significant improvements are obtained although some VZA dependency remains over clear ocean. The table shows that there remains a significant bias of $\sim 7\%$ but also that the RMS error is reduced by half to about 2% in clear sky and 1% in cloudy sky. The bias is close to the GERB/CERES ratio reported under Section 4.6. The difference (1%) comes from the fact that the Dubrovnik regressions have been fit on CERES Edition 2 data without the Revision 1 and from the limb darkening visible at VZA $\sim 70°$ in Figure 4.17.

This first attempt to derive empirical NB–to–BB regressions for SEVIRI is based on the CERES observations. At that time, the validated CERES data have been preferred to the pre–released un–validated GERB products. This approach suffers however from 2 shortcomings: from a radiometric point–of–view the estimated BB radiance is more "CERES–like" than "GERB–like" and the limited statistics of coangular observations prevents deriving NB–to–BB regressions for fine scene type stratification.

scene type/ season	Theoretical bias	Theoretical rms	Dubrovnik bias	Dubrovnik rms	CM SAF bias	CM SAF rms	Empirical bias	Empirical rms
clear	-7.8%	4.2%	-6.9%	2.0%	-1.1%	1.2%	0.4%	1.3%
cloudy	-8.3%	1.8%	-7.2%	0.9%	-1.1%	0.8%	-0.0%	0.6%
broken cloud	-8.3%	2.8%	-7.0%	1.3%	-0.7%	1.1%	0.2%	0.9%
thin cloud water	-8.0%	3.4%	-7.2%	1.5%	-1.0%	1.2%	-0.0%	1.0%
thin cloud ice	-11.5%	2.1%	-9.5%	1.6%	-3.4%	1.5%	0.1%	0.8%
thick cloud water	-7.7%	1.7%	-7.0%	1.0%	-0.8%	1.0%	-0.1%	0.7%
thick cloud ice	-9.6%	1.1%	-7.7%	1.0%	-1.8%	0.9%	-0.2%	0.7%
winter	-8.1%	3.0%	-6.9%	1.5%	-1.2%	1.2%	0.2%	1.1%
spring	-7.9%	3.2%	-7.1%	1.4%	-1.2%	1.0%	0.1%	1.0%
summer	-6.9%	3.8%	-6.6%	1.8%	-0.6%	1.6%	0.2%	1.3%
autumn	-8.2%	3.2%	-7.2%	1.6%	-1.4%	1.2%	0.0%	1.0%

Table 4.7: Biases (with respect to 1) and RMS errors of the ratio between the NB–to–BB estimates and the GERB Edition 1 evaluated in 135km × 135km boxes. Only the boxes with VZA < 70° (red circle on Figures 4.16, 4.17, 4.18, and 4.19) have been taken into account.

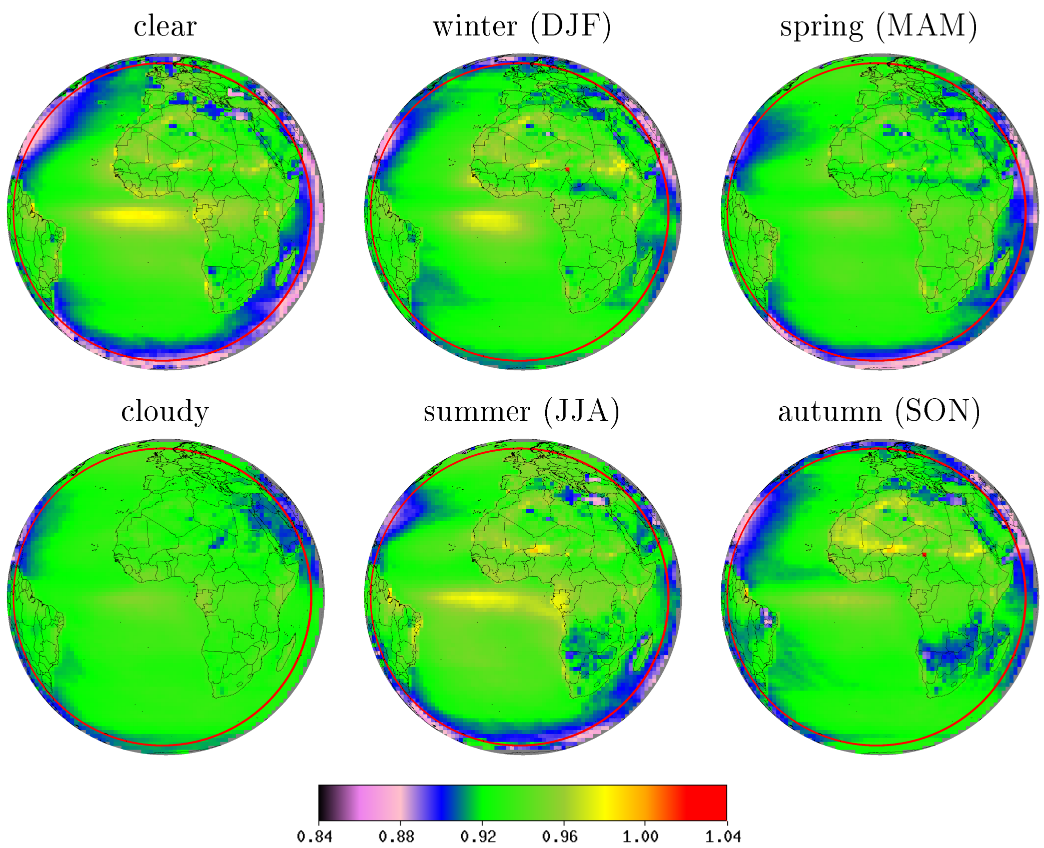

Figure 4.17: Idem as Figure 4.16 but for the Dubrovnik regressions. The color palette is centered on 0.94.

4.8.5 CM–SAF correction of the Dubrovnik regressions

In the Climate Monitoring SAF project, SEVIRI regressions are required to fill the gaps in the GERB dataset (eclipse seasons, instrument outages, ...). In this framework, an objective characterization of the ratio between the Edition 1 GERB High–Resolution (HR) product and the Dubrovnik regressions was done using the April and May 2006 data (the first available GERB Edition 1 data). This scaling of the GERB–like to the GERB level complies with the GERB/CERES homogenization process proposed by Dewitte *et al.* (2002a). Multiplicative factors are estimated for 3 surface types (ocean, vegetation, desert), for 3 cloudiness types (clear sky, partly cloudy, cloudy), and in bins of 10° for the SZA and VZA (no significant dependency on the RAA was observed). A set of tables gives the correction factors that convert the Dubrovnik estimates in radiances and fluxes consistent with GERB. Besides these factors, a daily multiplicative factor is also estimated in the CM–SAF operational chain to correct for a possible drift between the GERB and SEVIRI instruments. This factor is not taken into account here.

Regional validation of the CM–SAF GERB–like is provided on Figure 4.18 and Table 4.7. The correction improves the agreement with GERB both in terms of bias and RMS error. In terms of the VZA dependency, there is a clear improvement with respect to the Dubrovnik regression. Unfortunately, the CM–SAF correction is responsible of new artifacts over clear vegetated surfaces in Africa. The upper graph in Figure 4.20 shows that, with the CM–SAF correction, the BB radiance agrees with GERB when the SEVIRI NRT calibration applied after 1 April 2005 is used ("second part" of the top graph). The bias of $\sim 1\%$ comes from the change in SEVIRI calibration that took place at that date.

4.8.6 Empirical regressions with GERB

True empirical GERB–like regressions have been derived in preparation of the GERB Edition 2 processing. These regressions aim to mimic, as much as possible, the validated GERB Edition 1 data. Thanks to the huge number of corresponding SEVIRI/GERB data it is possible to derive dedicated regressions according to the surface type (6 classes), the SZA (20° bins), the VZA (20° bins), the RAA (45° bins), and the type of cloud cover. To that end, the cloudiness is stratified in 6 classes defined by the cloud cover cc, the cloud optical depth τ, and the cloud phase p (defined in Section 6.3)

- Clear sky : $cc < 10\%$ or $\tau < 1$
- Broken cloud : $10\% < cc < 90\%$ and $\tau >= 1$
- Thin water cloud : $cc > 90\%$ and $1 < \tau < 4$ and $p < 50\%$
- Thin ice cloud : $cc > 90\%$ and $1 < \tau < 4$ and $p >= 50\%$

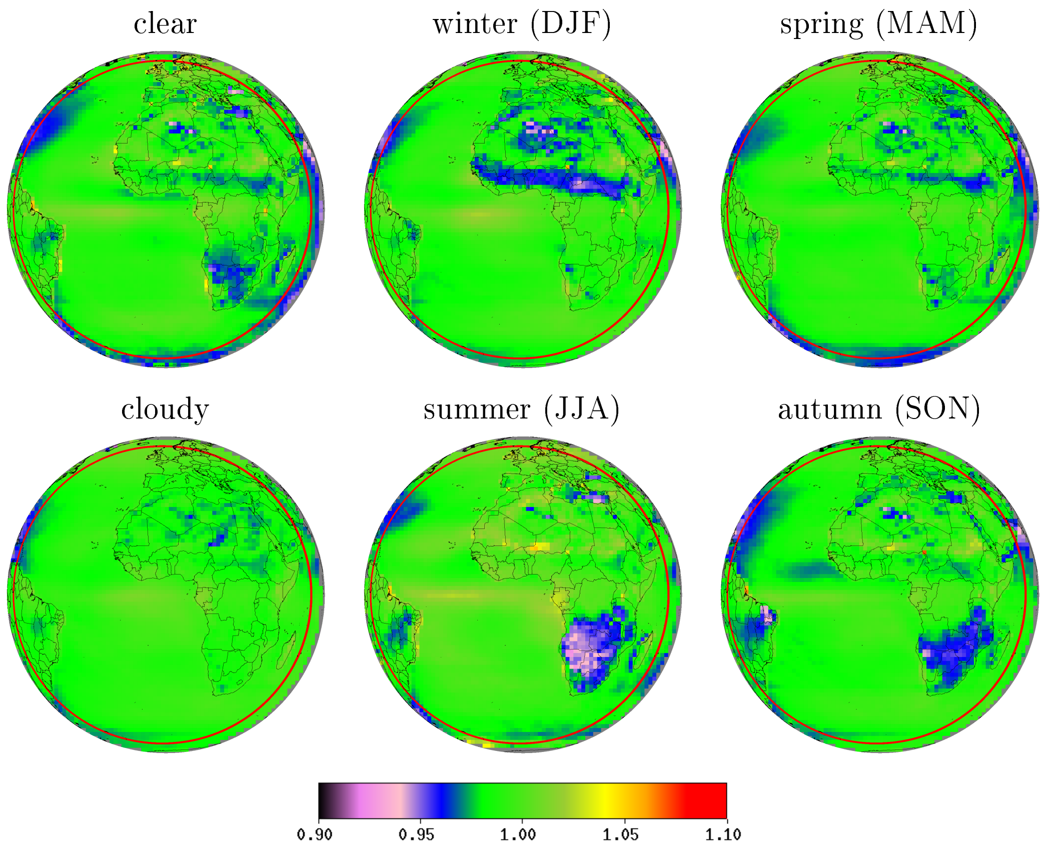

Figure 4.18: Idem as Figure 4.16 but for the Dubrovnik regressions + CM–SAF correction. The color palette is centered on 1.0.

- Thick water cloud : $cc > 90\%$ and $\tau >= 4$ and $p < 50\%$
- Thick ice cloud : $cc > 90\%$ and $\tau >= 4$ and $p >= 50\%$

The cloud retrieval of cc, τ and p is done from SEVIRI using the GERB/SEVIRI scene identification (Ipe *et al.*, 2008). In each of the 2304 bins, a linear regression between the SEVIRI NB reflectances ($\rho_{0.6}$, $\rho_{0.8}$, $\rho_{1.6}$) and the GERB broadband reflectance ρ_{BB}

$$\rho_{BB} = c_0 + c_1\ \rho_{0.6} + c_2\ \rho_{0.8} + c_3\ \rho_{1.6} \tag{4.25}$$

is fit with the least mean square criterium. The regressions have been fit on a subset of the SEVIRI/GERB database that covers only the period from 1 February 2004 until 30 April 2006). This enables the validation of the regressions on a bit more than 1 year of independent data (1 May 2006 to 10 May 2007).

Based on those independent data, Figure 4.19 and Table 4.7 give the ratio of average <GERB–like>/<GERB> for clear and cloudy conditions, on a seasonal basis, and for the 6 classes of cloudiness. The empirical regressions perform very well, with relative error smaller than 2% over most of the FOV. Higher relative errors are however observed over some clear ocean regions due to aerosols, especially in summer, or off the mouth of the Amazon river, due to specific ocean color. The GERB–like works correctly over most of the land surfaces, except over Southern Africa during summer (up to 4% underestimation with respect to GERB). The reason for this is that most of the area is classified as bright vegetation but the vegetation content during this period is very low. Improved performances are expected from regressions dependent on the instantaneous vegetation index (or at least a monthly climatology) instead of constant surface type.

4.8.7 Temporal stability

Figure 4.20 shows the temporal variation of the daily <GERB–like>/<GERB> ratio from 1 February 2004 to 10 May 2007. The drifts are expressed in unit of 0.01/year for the ratio but indicated %/year in the figure. The top graph shows the ratio for the 4 regressions when the NRT SEVIRI calibration is used. The jump that took place, due to the chance in calibration, on 1 April 2005 is clearly visible. A rather constant ratio is obtained using the "frozen" calibration coefficients (middle graph). The observed drift is about +0.3%/year.

The bottom graph shows the daily ratio for the empirical regressions evaluated over 4 scene types: cloud ($cc > 90\%$), and clear ($cc < 10\%$) ocean, vegetation and desert. The scene type dependency of the drifts is consistent with a slow decrease of the GERB sensitivity to the shortest wavelengths (to be confirmed). Another possible explanation is a slow wavelength drift of the SEVIRI filter toward shorter wavelength.

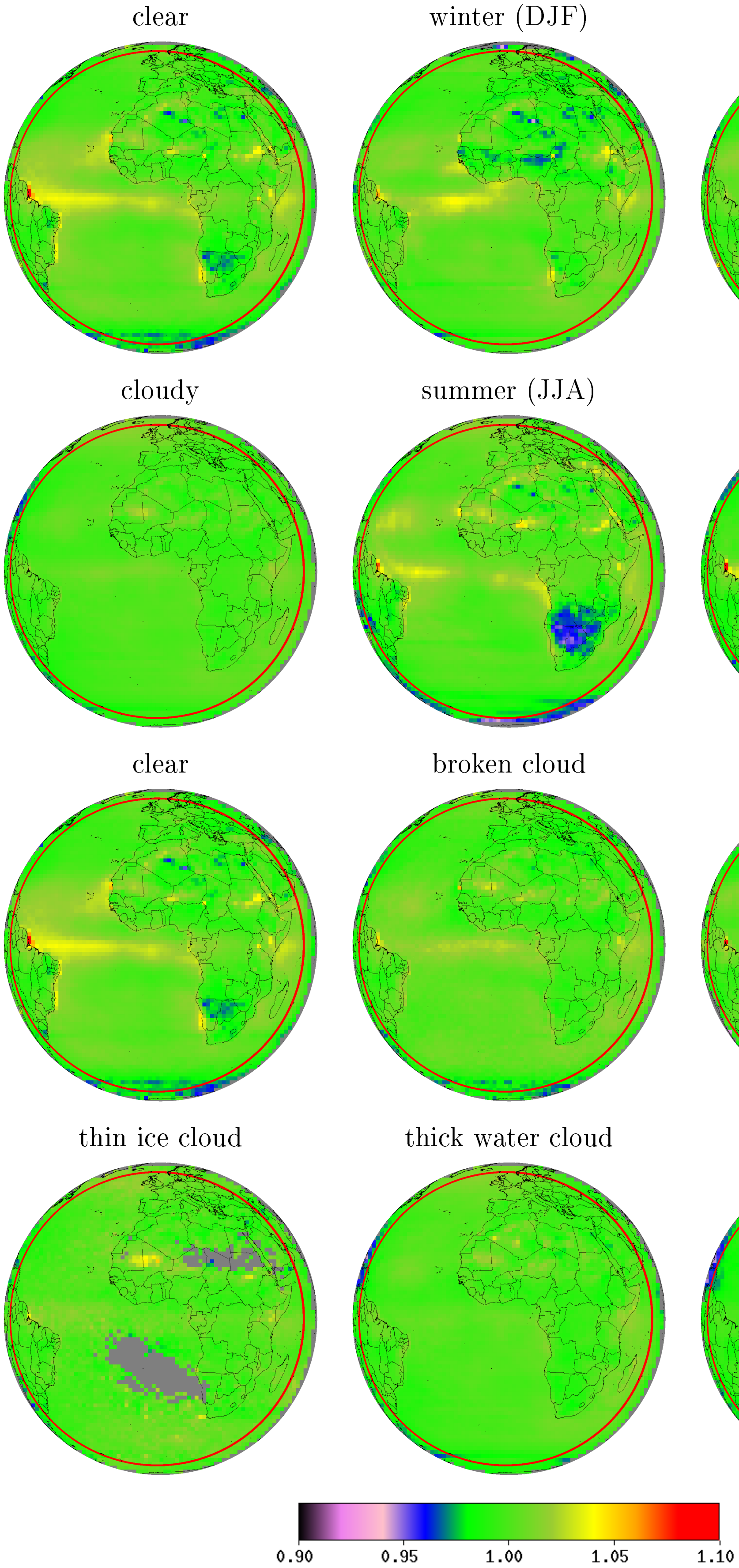

Figure 4.19: Empirical NB–to–BB regressions for SEVIRI. Ratio <GERB–like>/<GERB> in 135km × 135km boxes evaluated on the independent validation dataset (1 May 2006 to 10 May 2007). The color palette is centered on 1.0.

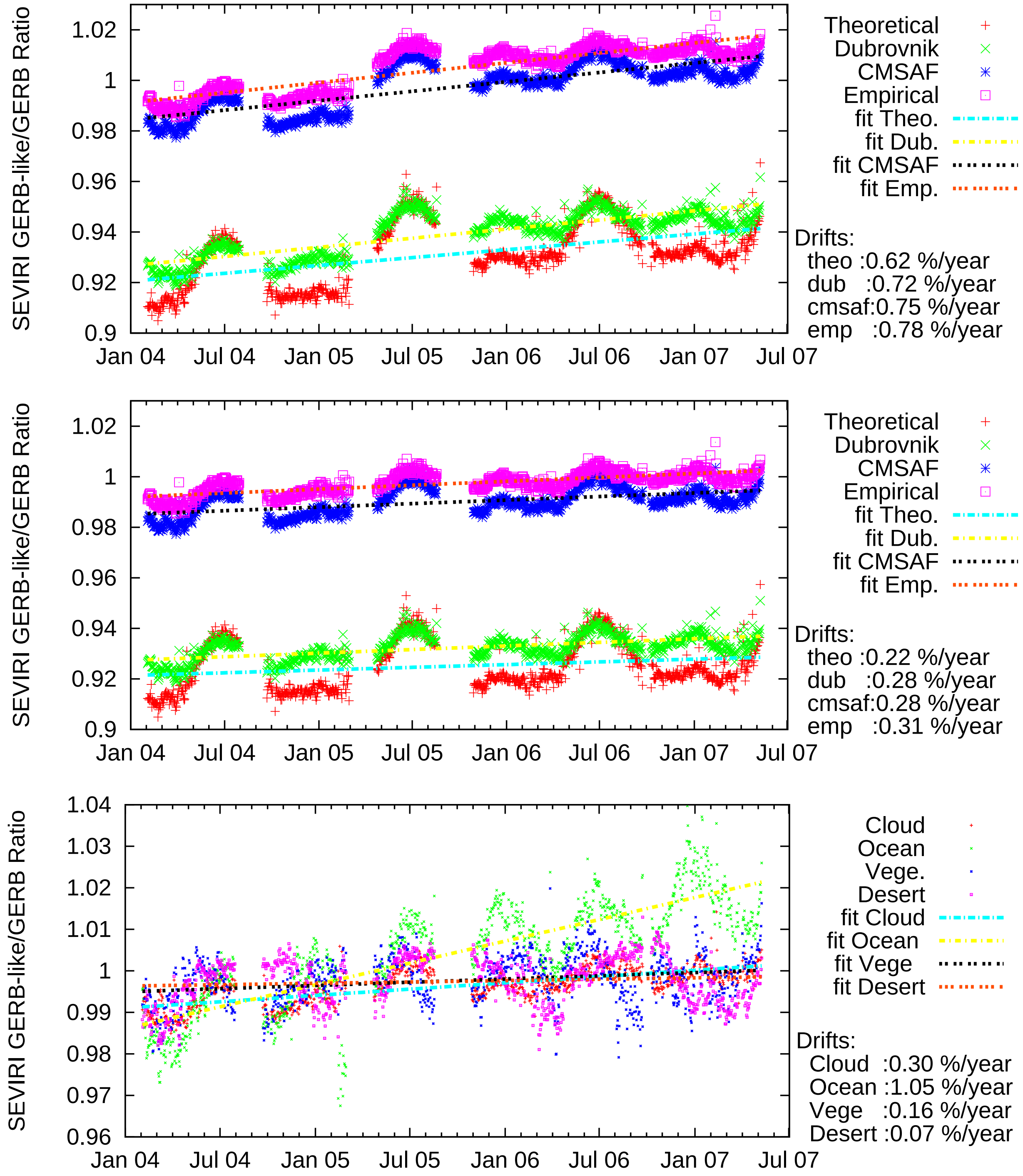

Figure 4.20: Daily ratio of SEVIRI–based <GERB–like>/<GERB>. Top: the 4 regressions with NRT calibration. Middle: the 4 regressions with "frozen" calibration. Bottom: the empirical regression with separation in 4 scene types.

4.9 Unfiltering of the Meteosat visible channel

4.9.1 Introduction

The unfiltering of the MVIRI visible channel observations is of interest for Earth radiation budget studies as it enables to extend the GERB database "toward the past" (processing the data from Meteosat–2 to –7) and toward the east (using Meteosat observations over the Indian Ocean (IODC service). With respect to SEVIRI, the MVIRI channel is relatively broad. On a set of simulated spectra, we can quantify the sensitivity of the MVIRI visible channel to about 58% of the total reflected solar radiation $L_{sol}(\lambda)$. The radiation that is not measured contains 2 contributions of similar magnitude. The first one lies around 0.4μm in the "blue" part of the spectrum . The second is in the near infrared between 1 and 2.5μm.

This Section is organized in a similar way as Section 4.8. First, a database of corresponding MVIRI and GERB radiances is built up. The database is then used to validate theoretical regressions and to derive empirical regressions.

4.9.2 Database of corresponding MVIRI/GERB radiances

Simultaneous Edition 1 GERB and Meteosat–7 data are available from 1 February 2004 to 14 June 2006 (at that date, Meteosat–7 started to move eastward in support of the Indian Ocean Data Coverage). A bit more than 2 years (865 days) of corresponding data are therefore available. The observations are not perfectly coangular as a 3.5° difference in longitudes separated Meteosat–7 and Meteosat–8 during this period. Consequently, the GERB broadband radiance ($L_{3.5^\circ}$) is corrected to infer the radiance (L_{0°) that would have been measured by a GERB instrument from the 0° longitude. This correction is based on the CERES TRMM Angular Dependency Models

$$L_{0^\circ} = L_{3.5^\circ} \frac{R(\mathrm{SZA}_{0^\circ}, \mathrm{VZA}_{0^\circ}, \mathrm{RAA}_{0^\circ})\ Alb(\mathrm{SZA}_{0^\circ})}{R(\mathrm{SZA}_{3.5^\circ}, \mathrm{VZA}_{3.5^\circ}, \mathrm{RAA}_{3.5^\circ})\ Alb(\mathrm{SZA}_{3.5^\circ})} \tag{4.26}$$

where R is the anisotropy factor and Alb the albedo of the best–suited model. The selection of the model is based on the GERB scene identification as described under Section 6.4. The solar zenith angle for Meteosat–7 (SZA_{0°) and for GERB ($\mathrm{SZA}_{3.5^\circ}$) in Eq.(4.26) can differ slightly to compensate difference in time of observation. A maximum time difference of 450s is allowed so that each Meteosat–7 radiance can be associated with a BARG pixel radiance. The downscaling between the 2.5km spatial resolution of the MVIRI visible channel and the 45km BARG pixel is realized by box averaging (i.e. square PSF). With the constraints on the SZA $< 80^\circ$ and VZA $< 80^\circ$ for both instruments, the daily number of observation pairs is about 7×10^5. The Meteosat–7 visible digital count (DC) is converted in physical radiance using the calibration

scene type/ season	Theoretical		Empirical	
	bias	rms	bias	rms
clear	-10.4%	2.0%	-0.4%	1.4%
cloudy	-8.3%	1.0%	-0.4%	0.8%
broken cloud	-7.9%	1.4%	-0.4%	1.1%
thin water cloud	-7.8%	1.4%	-0.4%	1.1%
thin ice cloud	-8.5%	1.2%	-0.3%	0.9%
thick water cloud	-8.3%	1.3%	-0.4%	1.0%
thick ice cloud	-8.6%	1.0%	-0.4%	0.8%
winter	-9.7%	1.9%	-0.3%	1.2%
spring	-9.6%	1.7%	-0.4%	1.2%
summer	-9.3%	2.1%	-0.1%	1.4%
autumn	-9.9%	1.9%	-0.8%	1.2%

Table 4.8: Biases (with respect to 1) and RMS errors of the ratio between the NB–to–BB theoretical and empirical estimates and the GERB Edition 1 evaluated in 135km $\times$ 135km boxes. Only the boxes with VZA $< 70°$ (red curve on Figures 4.21 and 4.22) have been taken into account.

provided by Govaerts *et al.* (2004a): gain at launch of 0.9163 $Wm^{-2}sr^{-1}$/DC and daily drift of 5.5195×10^{-5} (i.e. $\sim 2\%$/year).

4.9.3 Theoretical regressions

Theoretical regressions, adjusted on the database of radiative transfer simulations, have been used from July 1998 until May 2006 to generate the GERB–like product from Meteosat–7. The method involved a third order regression on the visible channel radiance with regression coefficients dependent on the SZA. Among others, these early GERB–like data have been used to study an Etna eruption on 27 October 2002 (Bertrand *et al.*, 2003). Details on the method and results can be found in that paper. Later on, validation of these regressions became possible with the GERB Edition 1 data. Figures 4.21 and 4.23 show respectively the regional and temporal variations of the Meteosat–7 $<$GERB–like$>$/$<$GERB$>$ ratio. Table 4.8 provides the biases and RMS errors for different scene types and seasons.

4.9.4 Empirical regressions with GERB

In this section, we address the possibility to derive empirical GERB–like regressions for the MVIRI visible channel. This work has been presented during the 2007 EUMETSAT conference in Amsterdam. The proceeding paper (Clerbaux *et al.*, 2007) is available from the authors and on the EUMETSAT website.

Regressions are derived with the same scene stratification as for SEVIRI (Section 4.8.6): 6 surface types, 6 cloudiness types, and 4 angular bins for the SZA, VZA, and RAA. In each of the 2304 bins, the best linear fit between the Meteosat VIS reflectance ρ_{VIS} and the GERB broadband reflectance ρ_{BB} is computed using least mean square criteria

$$\rho_{BB} = a + b\ \rho_{VIS} \tag{4.27}$$

The BB reflectance ρ_{BB} is derived from the GERB observation after the angular correction of the radiance using Eq.(4.26). The best fit parameters a and b are derived for each of the bins.

Figure 4.22 shows the <GERB–like>/<GERB> ratio at regional scale for clear and cloudy conditions and over the 4 seasons. High relative errors can occur over some clear ocean regions, but the absolute error remains small. The effects of aerosols over the tropical ocean is well visible during spring and summer. The GERB–like processing works correctly over most of the land surfaces, except over Southern Africa during summer and autumn (up to 4% underestimation with respect to GERB). This problem was already observed with the SEVIRI NB–to–BB conversion and was attributed to vegetation change.

Figure 4.23 shows a temporal drift of +0.98%/year in the GERB–like/GERB ratio. As there is no indication of GERB drift, the +2%/year calibration drift estimated with the SSCC method is likely to over–correct the Meteosat–7 aging during the period 2004–2006. This is consistent with the +1.1%/year drift estimated for Meteosat–5 over a long time period. Not surprisingly, the minimum drift is observed over clear desert (+0.61%/year). Indeed, the MVIRI calibration is based on radiative transfer computation over desert targets. The higher drift observed for the ocean (+1.05%/year), the clouds (+1.0%/year), and the vegetation (+0.99%/year) could be the symptom of a GERB darkening at short wavelengths.

To summarize, on one hand it is observed that the empirical NB–to–BB regressions for the visible channel of the MVIRI instrument work quite well. Concerning the land surface, improved performances are expected by making the regression dependent on the instantaneous vegetation index instead of constant surface type. On the other hand, the study of the temporal stability shows a significant drift of nearly 1%/year, all scenes together. The reason for this should be fully understood and corrected before the GERB–like processing can be successfully applied over the full Meteosat first generation database.

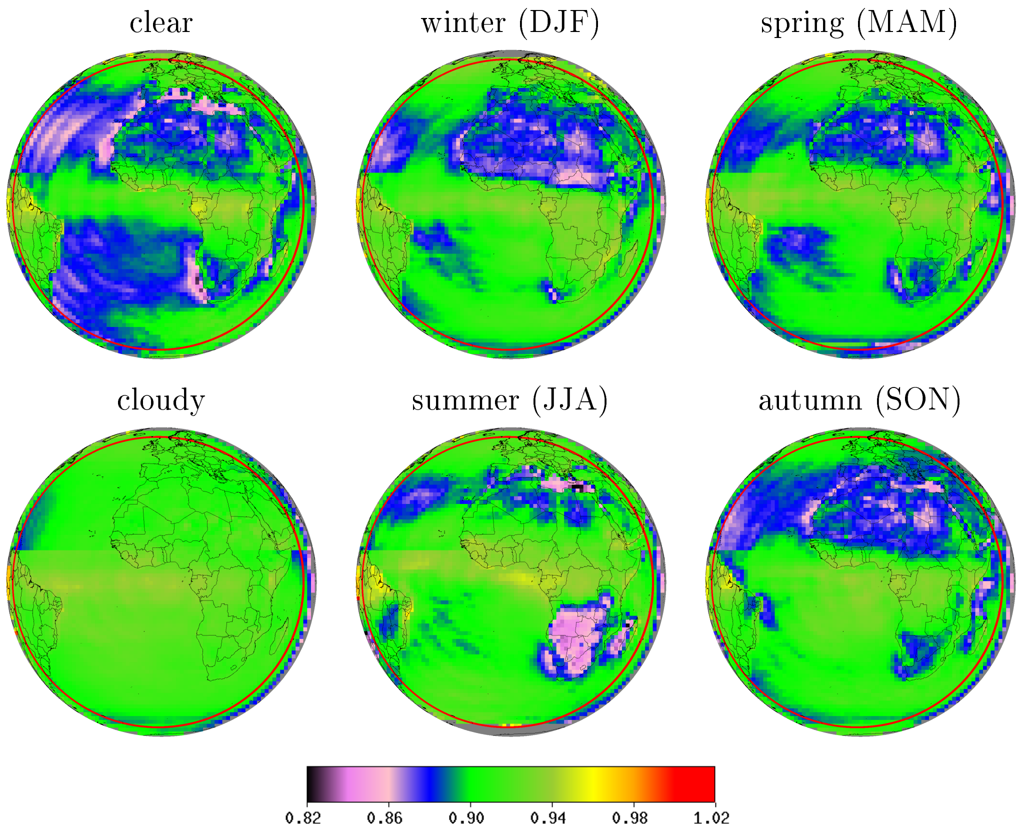

Figure 4.21: Theoretical NB–to–BB regressions for MVIRI. Ratio <GERB–like>/<GERB> in 135km × 135km boxes. The color palette is centered on 0.92.

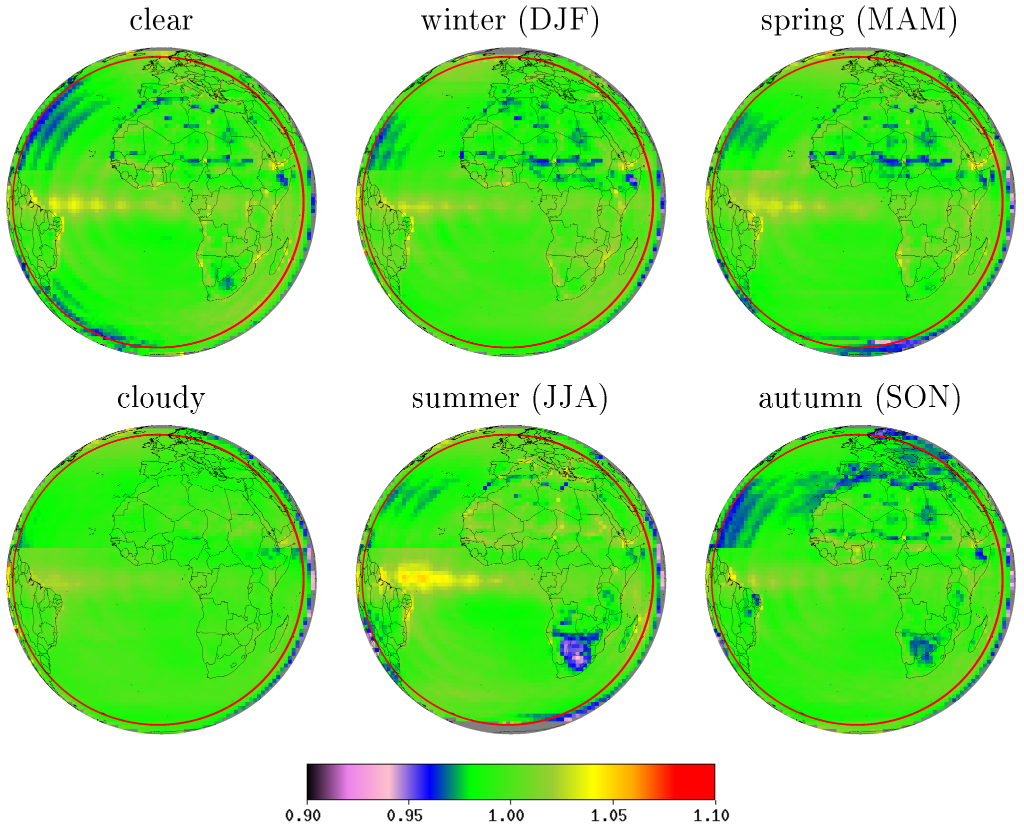

Figure 4.22: Empirical NB–to–BB regressions for MVIRI. Ratio <GERB–like>/<GERB> in 135km × 135km boxes. The color palette is centered on 1.0.

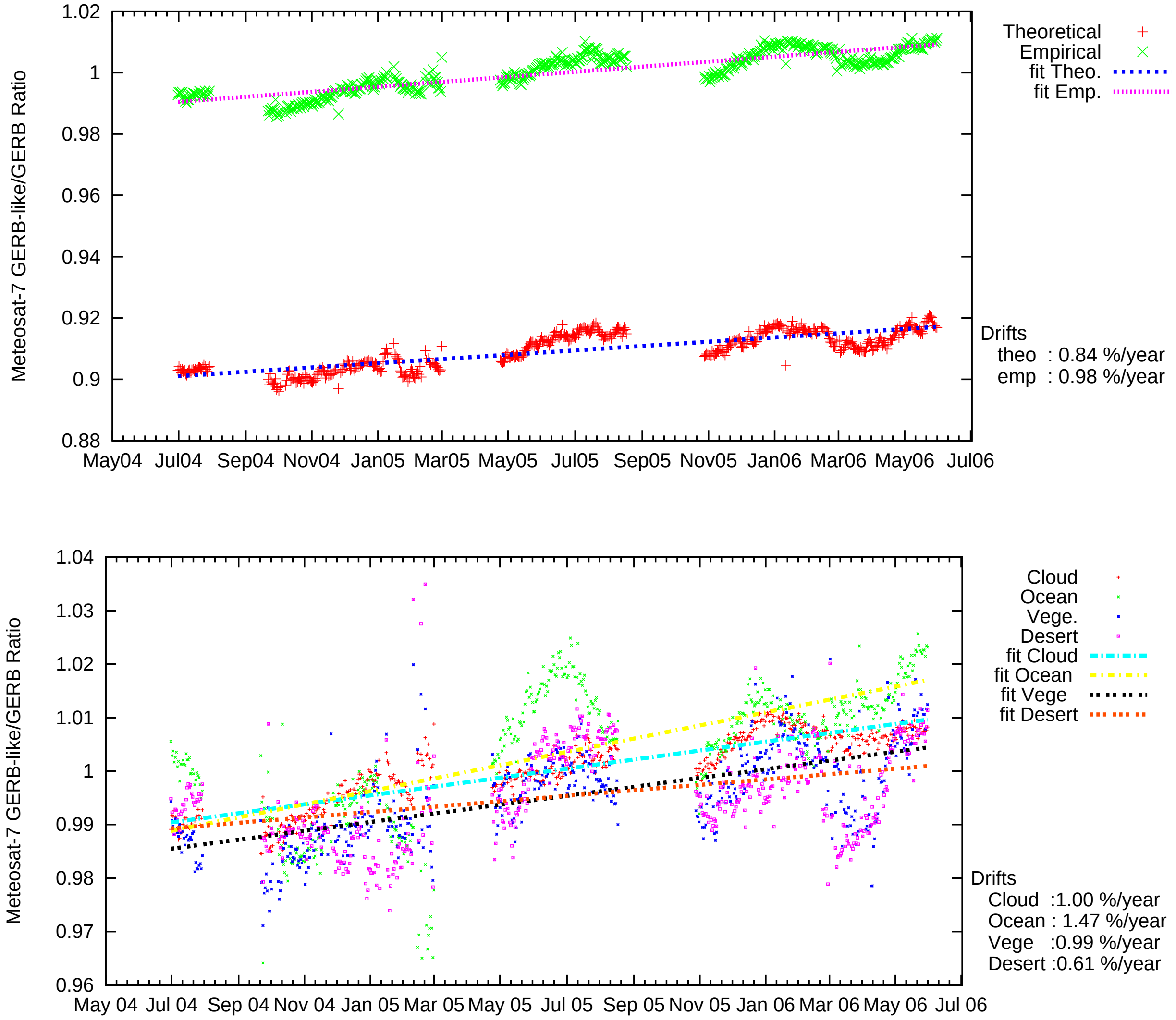

Figure 4.23: Daily ratio of averages Meteosat–7 GERB–like and GERB radiances. Top: theoretical and empirical regressions. Bottom: ratio <GERB–like>/<GERB> for the empirical regressions for cloud and clear ocean, vegetation and desert.

4.10 Discussion

In this chapter, we have addressed a series of problems that require modeling of the reflected solar radiation in its spectral dimension. These problems are mostly worked out using theoretical approaches based on radiative transfer computations. To this end, the SBDART Radiative Transfer Model (RTM) was used to simulate, off–line, a large database of realistic spectra. Although this was not detailed in this document, this database is already the fruit of successive improvements of the model and of the characterization of the Earth–atmosphere system used as input for the model calculations. Future improvements of this database should incorporate a better representation of the mix land/ocean scenes and of the ice crystal size distribution for the cirrus clouds. Spectrally resolved surface BRDF would be desirable but are not yet available in a suitable form. Some of the limitations encountered with the radiative transfer computations could be avoided using observed spectra $L(\lambda)$ instead of simulations. As an example, the Airborne Visible/Infrared Imaging Spectrometer (AVIRIS, Green *et al.*, 1998) provides 224 NB measurements between 0.37μm and 2.51μm. Technical note (TN41) reports on first investigations of using AVIRIS data for SW spectral modeling validation. In addition to their use for validation, it is generally accepted that spectrally resolved observations will play a growing role in radiation budget studies, in conjunction with BB observations and model calculations. For the GERB project, we could benefit from the high spectral resolution data provided by the SCIAMACHY instrument on ENVISAT.

Since a BB radiometer does not provide unfiltered radiance, spectral modeling techniques are needed to estimate the reflected solar radiation. For the GERB instrument, one takes advantage of the spectral information from the NB measurements of the SEVIRI instrument. This information permits generating unfiltered radiances within the scientific goal of 1% accuracy, at 1 SD. Simpler techniques, like the direct unfiltering, do not meet this accuracy. The disagreement of the GERB SW radiances with CERES (about 6%) is however higher than the sum of the theoretically estimated unfiltering errors for both instruments. As discussed previously, it is likely that this difference comes from the absolute on–ground calibration of the GERB and CERES instruments. It is worth noting that a part of the overall disagreement could be introduced by the characterization of the spectral response of the GERB detectors. In particular, as the GERB calibration was performed in the near infrared (tungsten lamps at $\sim$ 3000K), any change in relative sensitivity between the near infrared and the visible could introduce an overall scaling of the calibration when "visible scenes" are observed. Ongoing efforts to improve the spectral response characterization are done at Imperial College using spare detector arrays.

The comparisons with CERES show that the GERB ARG format should be used with caution to study processes over particular scene types and/or over areas of small spatial extension. This work indicates that the BARG, and even the HR, formats agree better with the independent CERES observations.

Empirical regressions to generate GERB–like data from the SEVIRI and MVIRI channels perform surprisingly well, provided they are defined for a sufficient number of surface and cloud types. At regional scale of 135 km, the RMS error of the regression is about 1.3% for clear scenes and 0.7% for cloudy scenes. However, it was shown that higher errors could affect the BB estimate for some specific infrequent scenes and in case of change in the vegetation content. Obviously, the estimated BB radiances suffer from poor calibration and aging of the NB channels of the imager. Regular comparisons with calibrated instruments are therefore essential. For the first generation instrument (MVIRI), improved BB estimates would require a model of the temporal aging of the visible channel spectral response. Further investigations in this direction are foreseen in the frame of our involvement in the Climate Monitoring SAF. In regard to the MVIRI, the aging and calibration problems are significantly reduced with the new generation of instrument (SEVIRI). The routine (each 28 days) full disk imagery with the backup satellite (currently Meteosat–8) will permit verifying this drift over a longer time period. Both for MVIRI and SEVIRI, higher drifts of the GERB–like/GERB ratio are observed for clear ocean than for the other scenes. This could be explained by a slow "darkening" of the GERB sensitivity at the short visible wavelengths.

Chapter 5

Spectral modeling of the emitted thermal radiation

5.1 Introduction

As for the reflected solar radiation, we face different problems that require modeling of the spectral signature of the emitted thermal radiation $L_{th}(\lambda)$. Section 5.2 discusses the factors that govern the spectrum $L_{th}(\lambda)$ of thermal radiation at the TOA. Based on this analysis, a database of simulated spectra has been built using radiative transfer computations. The simulations, described under Section 5.3, are done for various realistic Earth/atmosphere conditions and different viewing geometries. The database is used to address the spectral modeling problems in this chapter and also in Chapter 7 for angular modeling problems.

Sections 5.4 and 5.5 describe respectively the direct and the Edition 1 unfiltering methods for the GERB LW channel. They both comply with the unfiltering objective of 0.5% accuracy. Another spectral modeling problem is the estimation of the SW channel contamination by thermal radiation (Section 4.5.5). Section 5.6 reports on the GERB/CERES unfiltered LW radiance comparisons. The effect of the variability in LW spectral response curves between the 256 GERB detector elements is analyzed in Section 5.7.

Theoretical NB–to–BB conversions have been used since a long time to estimate the Outgoing Longwave Radiation (OLR) from sets of NB observations (e.g. HIRS, GOES, Meteosat, AVHRR, ...). We focused our work on the NB–to–BB conversions for the SEVIRI (Section 5.8) and MVIRI (Section 5.9) instruments. The Edition 1 GERB products allow to validate the theoretical regressions and to derive empirical relations.

A discussion of these works is provided in Section 5.10.

5.2 Factors affecting the TOA LW spectrum

With the atmosphere put aside, the spectrum of emitted thermal radiation $L_{th}(\lambda)$ is mainly dependent on the surface skin temperature T through the Planck's law $B_T(\lambda)$ for the blackbodies. The peak of the spectrum is given by Wien's law, $\lambda_{max} = 2897.768/T$, and the integration (i.e. the "unfiltered" flux quantity) by the Stefan–Boltzmann law $F = 5.67\ 10^{-8}\ T^4$. As Earth surfaces are not perfect blackbodies, the emitted spectrum is also dependent, although to a lesser extent, on the surface spectral emissivity $\epsilon(\lambda)$. Water bodies and most of the land surfaces emit like blackbodies ($\epsilon(\lambda) \sim 1$). An important exception is sandy surface which presents lower emissivities, especially at shorter wavelengths. Another exception is the water surface at grazing observation angle (VZA $\sim 90°$) in calm wind condition. In this case the emissivity decreases quickly and the surface becomes reflective to the infrared radiation. Compared to the SW radiation where the reflectance is usually a slowly varying feature of the surface, important day–by–day changes in surface skin temperature are observed (Gao & Wiscombe, 1994) as a result of cloudiness, air mass temperature and soil humidity.

Concerning the atmosphere, Figure 5.1 shows the ratio between the upward thermal flux at the TOA and at the surface. These curves have been simulated by SBDART using the standard Mac Clatchey mid–latitude summer profile with scalings of the column amounts of H_2O, CO_2 and O_3. Water vapor H_2O is the main absorber in the infrared ($5-8\mu$m and $16-100\mu$m). The carbon dioxide CO_2 absorbs in the bands $2.5-3\mu$m, $4-4.5\mu$m and $14-16\mu$m. The ozone O_3 absorbs around 9.7μm. The amount of other trace gas like CH_4 and CFC can also be retrieved from the infrared spectra (Harries *et al.*, 2001). The spectrum at the TOA is dependent on the atmospheric transmission but also on the temperature at which the absorption/reemission occurs. Therefore, the spectra are linked to the vertical profiles of temperature and humidity, and of the other constituents already discussed. It is observed that, in average, the spectrum is less influenced by the atmosphere over land than over the oceans, due to the smaller atmospheric path.

An optically thick cloud radiates like a blackbody at the temperature of the constituent of the cloud top. For mid– and high–level clouds, the atmospheric absorption is reduced as the distance from the blackbody emission and the TOA is reduced. The shape of the infrared spectrum is therefore dependent on the clouds height. Some clouds are semi–transparent to the infrared radiation. This is the case of the frequently observed cirrus clouds but also of dust clouds and airplane contrails. The spectral signature is modified as the transmission is dependent on the wavelength. This makes these semi–transparent objects detectable by techniques based on brightness temperature difference.

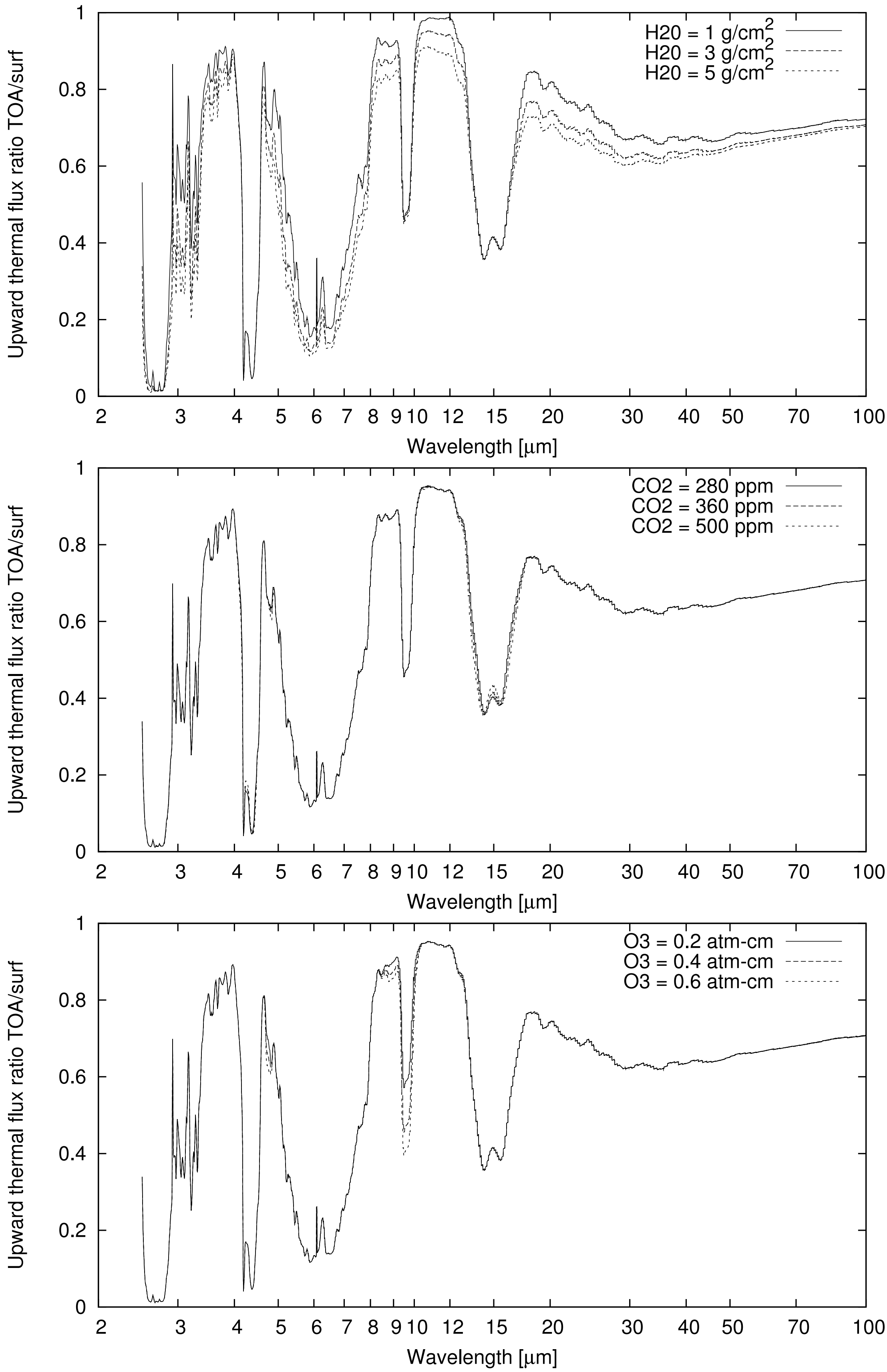

Figure 5.1: Ratio of TOA (100km) and surface upward thermal flux simulated by SBDART Version 2.4. Starting from the standard mid–latitude Mac Clatchey profile, these graphs illustrate the sensitivity to change in column amount of H_2O (top), CO_2 (middle), and O_3 (bottom).

5.3 Radiative transfer simulations

5.3.1 Introduction

This section provides a summary of the longwave radiative transfer simulations and their validations. The full description of this part of the work is available in the technical note (TN30). As written before, the TOA infrared spectrum is mainly affected by the atmospheric profiles of temperature and humidity. Our simulations are based on thousands of observed profiles provided in the TIGR–3 database (Chevallier *et al.*, 2000). A separate technical note (TN29) describes how these profiles are interfaced with SBDART.

5.3.2 Simulations

A large database of simulated spectral radiance curves $L_{th}(\lambda)$ is built up using the version 1.21 of the Santa Barbara DISORT Atmospheric Radiative Transfer (SBDART, Ricchiazzi *et al.*, 1998) model. The simulations are performed for 4622 realistic conditions of the Earth–atmosphere system, as described in Clerbaux *et al.* (2003c). All the simulations are realized with the incoming solar radiation turned off in order to simulate only the radiation due to the planetary thermal emission $L_{th}(\lambda)$. The computations have been done at 431 wavelengths between 2.5μm and 100μm, which are the lower and upper limits for SBDART thermal simulation. From 2.5μm to 20μm a wavelength increment of $\Delta\lambda = 0.05\mu$m is used while from 20μm to 100μm the increment is $\Delta\lambda = 1.0\mu$m, to reduce the computation time. The spectral radiance curves $L(\lambda)$ are then extended up to 500μm using the Planck's law with the brightness temperature given by the radiative transfer model at 100μm. For each wavelength and each simulation, the spectral radiance field is computed with a 5° resolution in VZA (0°, 5°, 10°, ..., 85°). The DISORT computations are performed using 16 streams to obtain an accurate representation of the dependency of the scene spectral signature $L(\lambda)$ with the VZA.

The atmospheric profile is by far the primary input for the radiative transfer computations in the thermal part of the spectrum. For the simulations, the profiles compiled in the TIGR–3 database (Chevallier *et al.*, 2000) have been used. These data have been kindly made available by the French *Laboratoire de Météorologie Dynamique*. The profiles provide, at 40 pressure levels (1013, 955, ..., 0.05hPa), the geopotential height, the temperature, and the concentrations in water vapor and ozone. The technical note (TN29) describes how this database is used as input for SBDART simulations.

For each simulation, the surface skin temperature is set at random and with a uniform distribution of probability between $T_0 - 15$K and $T_0 + 15$K, where T_0 is the temperature at the lowest atmospheric profile level. This aims to account for the radiative heating or cooling of the surface. However, in some daytime situations, a much higher difference between surface and air temperature is observed, as for example over clear desert at the beginning of the afternoon. To simulate this, for 40% of the simulations, the surface skin temperature is set at random and with uniform distribution of probability between T_0 and $T_0 + 50$K. The surface emissivity ϵ must also be specified for the simulations. Ideally, this emissivity should be spectrally dependent $\epsilon(\lambda)$ but, unfortunately, realistic curves $\epsilon(\lambda)$ defined over the 2.5μm $- 100\mu$m interval are not yet available. A spectrally invariant emissivity is therefore used and set at random with a uniform distribution of probability between 0.85 and 1.

Realistic cloud covers are also simulated for half of the simulations, the other half being cloud free. The cloudiness can consist of up to 3 overlapping cloud layers. The characteristics of each layer are independent of those of the other layers. The lower cloud layer is simulated with a probability of occurrence of 50%, is located at a height between 500m and 3500m (with a uniform distribution of probability) and is always constituted of water droplets. The probability of middle level cloud occurrence is 40%, the layer is located between 4000m and 7000m and is constituted of ice crystals in 25% of the cases and water droplets in 75% of the cases. The probability of high level cloud occurrence is 30%, the layer is located between 7000m and 16000m and is always constituted of ice crystals. For a water phase layer, 2 kinds of clouds are simulated with equal probability: precipitating and non-precipitating clouds. The effective radius of the droplet size distribution is then chosen at random and with a uniform distribution of probability within 2μm $- 25\mu$m for non-precipitating clouds and within 25μm $- 128\mu$m for precipitating clouds. For an ice phase layer, the single scattering co–albedo $(1 - a)$, predicted using the Mie theory, is modified by a multiplicative factor chosen at random in the range $0.5 - 1$, as suggested by Ricchiazzi *et al.* (1998). The single scattering co–albedo is the ratio between the probabilities of absorption and scattering. Finally, the optical thickness of the cloud layers must be specified. For each layer, a thickness class is selected at random with equal probability between : thin, medium or thick. The optical thickness (at 0.55μm) is then selected at random within $0 - 3.6$ (thin), $3.6 - 23$ (medium) and $23 - 379$ (thick), in each case with a uniform distribution of probability. These threshold values for cloud optical thickness and cloud height are adopted to match the ISCCP cloud classification (Rossow & Schiffer, 1999).

The type of boundary layer aerosol is chosen at random and with equal probability within: none, rural, urban, oceanic, and tropospheric. The SBDART default parameterizations (optical thickness, wavelength dependency, ...) are used for the selected aerosol type. No stratospheric aerosol is added in the simulations.

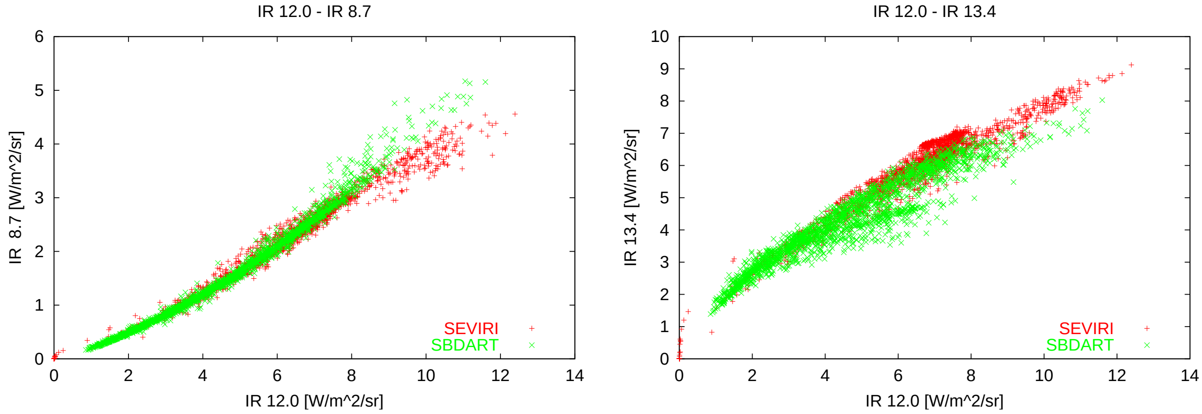

Figure 5.2: Scatterplots between NB radiances as observed by the SEVIRI instrument on MSG–1 (red '+') and as simulated with SBDART (green '×').

This database of spectral radiance curves is then weighted with instrument's spectral response filters to get the BB and NB radiances

$$\begin{aligned}
L_{th} &= \int_{2.5\mu\text{m}}^{500\mu\text{m}} L_{th}(\lambda)d\lambda \\
L_{lw,th} &= \int_{2.5\mu\text{m}}^{500\mu\text{m}} L_{th}(\lambda)\phi_{lw}(\lambda)d\lambda \\
L_{6.2} &= \int_{2.5\mu\text{m}}^{500\mu\text{m}} L_{th}(\lambda)\phi_{6.2}(\lambda)d\lambda \\
(...) & \\
L_{13.4} &= \int_{2.5\mu\text{m}}^{500\mu\text{m}} L_{th}(\lambda)\phi_{13.4}(\lambda)d\lambda
\end{aligned} \tag{5.1}$$

where $\phi_{lw}(\lambda)$ is the GERB–2 average longwave spectral response defined by Eq.(3.2) and $\phi_{6.2}(\lambda)$, ..., $\phi_{13.4}(\lambda)$ are the spectral responses of the thermal channels of the SEVIRI instrument on MSG–1 (available from EUMETSAT).

5.3.3 Validations

Various scatterplots of observed and simulated NB radiances are compared for validation purpose. Figure 5.2 provides two examples of scatterplots while the complete set is available in the technical note (TN30). The left scatterplot in Figure 5.2 shows the principal limitation of the database: the fact that the spectral dependency of the surface emissivity $\epsilon(\lambda)$ is not simulated. For the warmest observed scenes (i.e. hot desert), the radiances in the 8.7μm SEVIRI channel are significantly lower than the simulated radiances.

5.4 Direct unfiltering of the GERB LW channel

Technical note (TN35) describes the direct unfiltering of the LW channel of GERB–2 and GERB–1. Figure 5.3 shows the scatterplots of unfiltering factor $\alpha_{lw,th}$ with respect to $L_{lw,th}$ for the 4622 simulated scenes at VZA = 0°, 25°, 50°, and 75°. A third order regression appears well–suited to estimate the unfiltering factor

$$\alpha_{lw,th} = \frac{L_{th}}{L_{lw,th}} = c_0 + c_1\ L_{lw,th} + c_2\ L^2_{lw,th} + c_3\ L^3_{lw,th} \tag{5.2}$$

The best fit parameters $\{c_i\}$ and the RMS error are given in (TN35) for the different VZA and for GERB-2 and GERB-1. The residual RMS error on the longwave unfiltering factor α is typically about 0.1%.

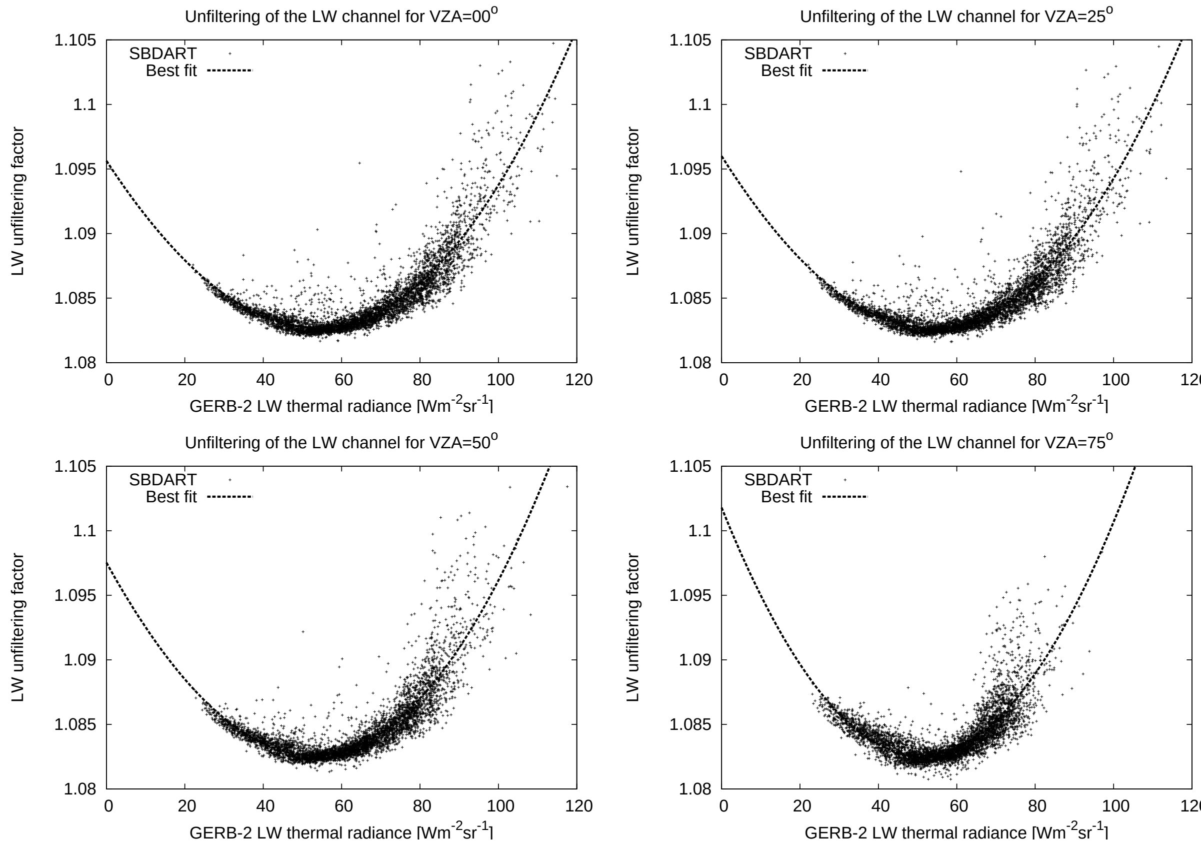

Figure 5.3: Scatterplots of GERB-2 longwave unfiltering factor $\alpha_{lw,th}$ with respect to $L_{lw,th}$ radiance for VZA = 0°, 25°, 50°, and 75°. The direct unfiltering with the best fit of Eq.(5.2) is shown.

5.5 Edition 1 GERB LW channel unfiltering

5.5.1 Introduction

This section contains a summary of a more detailed study of the GERB LW channel unfiltering published in the *Journal of Atmospheric and Oceanic Technology* (Clerbaux *et al.*, 2008a). The GERB unfiltering problem is illustrated in Figure 5.4 that shows the variability of the unfiltering factors $\alpha_{lw,th} = L_{th}/L_{lw,th}$ according to the cloudiness type (ISCCP classification) for GERB–2 (left) and CERES FM2 (right).

As for the SW (see section 4.5.1), the GERB LW unfiltering is based on a ratio of unfiltered and filtered BB radiances estimated from SEVIRI

$$L_{th} = L_{lw}\left(\frac{L'_{th}}{L'_{lw,sol}+L'_{lw,th}}\right) \tag{5.3}$$

$$= L'_{th}\left(\frac{L_{lw}}{L'_{lw,sol}+L'_{lw,th}}\right) \tag{5.4}$$

5.5.2 Theoretical regressions

A set of theoretical regressions has been derived from the radiative transfer computations to estimate the BB radiances L'_{th} and $L'_{lw,th}$ as a function of the SEVIRI thermal channel radiances. To that end, second order polynomial regressions have been adopted

$$\begin{aligned} L'_{th} &= a_0 + a_1L_{6.2} + a_2L_{7.3} + a_3L_{8.7} + a_4L_{9.7} + a_5L_{10.8} + a_6L_{12} + a_7L_{13.4} + \\ &\quad a_8L^2_{6.2} + a_9L_{7.3}L_{6.2} + a_{10}L^2_{7.3} + a_{11}L_{8.7}L_{6.2} + a_{12}L_{8.7}L_{7.3} + \ldots + a_{35}L^2_{13.4} \qquad (5.5) \\ L'_{lw,th} &= b_0 + b_1L_{6.2} + b_2L_{7.3} + b_3L_{8.7} + b_4L_{9.7} + b_5L_{10.8} + b_6L_{12} + b_7L_{13.4} + \\ &\quad b_8L^2_{6.2} + b_9L_{7.3}L_{6.2} + b_{10}L^2_{7.3} + b_{11}L_{8.7}L_{6.2} + b_{12}L_{8.7}L_{7.3} + \ldots + b_{35}L^2_{13.4} \qquad (5.6) \end{aligned}$$

The regression coefficients $\{a_i\}$ and $\{b_i\}$ are estimated as a best fit on the database of 4622 spectral radiance curves for each VZA $= 0°, 5°, \ldots, 85°$. These NB–to–BB conversions are only dependent on the VZA and are neither dependent on the surface type nor on the cloudiness. Clerbaux *et al.* (2008a) provide the coefficients $\{a_i\}$ and $\{b_i\}$ for the GERB–2 instrument, and the residual RMS error of the fit. The RMS error associated with these NB–to–BB regressions is about 0.45$\mathrm{Wm^{-2}sr^{-1}}$ (0.7%). Before fitting the Eqs.(5.5) and (5.6) on the simulations, the NB radiances $\{L_{ch}\}$ are modified at random with a noise having Gaussian distribution with a standard deviation equal to 5% of the average radiance in the channel. This is necessary to avoid

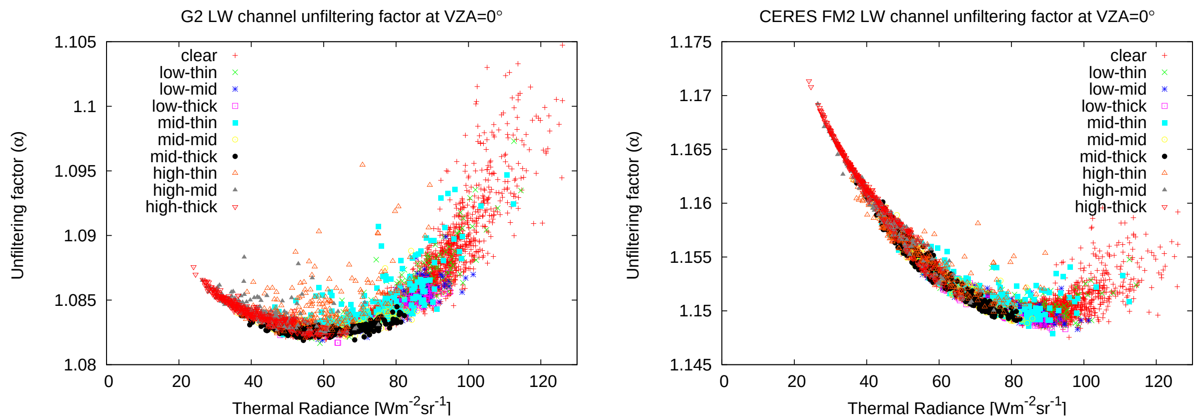

Figure 5.4: Unfiltering factor $\alpha_{lw,th}$ for the GERB–2 (left) and the CERES FM2 (right) LW channels. Each dot corresponds to a SBDART simulation at VZA $= 0°$.

that the fits exploit excessively slight correlations among the SEVIRI channels (overfitting of the data). The value of 5% is a conservative limit for the SEVIRI thermal channels calibration accuracy (Schmetz *et al.*, 2002).

5.5.3 Estimation of the solar contamination in the GERB LW channel

For the GERB LW channel unfiltering the contamination of the channel by reflected solar radiation $L_{lw,sol}$ must be estimated. A direct estimation of this quantity proportional to the GERB SW measurement is proposed in (TN35)

$$L_{lw,sol} = a(\mathrm{SZA}) L_{sw,sol} \tag{5.7}$$

The parameterization is performed using the database of spectral radiance curves described under Section 4.3. The values of a are given in (TN35), as well as the residual error which is about 0.04Wm^{-2}sr^{-1}. For the operational GERB unfiltering, the contamination $L_{lw,sol}$ must be estimated from the visible channel radiances of the SEVIRI instrument. A second order regression on the $L_{0.6\mu\mathrm{m}}$, $L_{0.8\mu\mathrm{m}}$ and $L_{1.6\mu\mathrm{m}}$ is therefore used

$$\begin{aligned} L'_{lw,sol} = \quad & c_0 \quad + c_1 L_{0.6} + c_2 L_{0.8} + c_3 L_{1.6} + c_4 L_{0.6}^2 + c_5 L_{0.8} L_{0.6} + \\ & c_6 \quad L_{0.8}^2 + c_7 L_{1.6} L_{0.6} + c_8 L_{1.6} L_{0.8} + c_9 L_{1.6}^2 \end{aligned} \tag{5.8}$$

with the coefficients of the regression $\{c_i\}$ being dependent on the SZA. Table 5.1 provides the $\{c_i\}$ values at SZA $= 0°$, $10°$, ..., $80°$. Before fitting the Eq.(5.8) on the database of simulations, the simulated NB radiances are modified at random by a Gaussian noise with a standard deviation equal to 5% of the average radiance in the channel. Both methods to

SZA	c_0	c_1	c_2	c_3	c_4	c_5	c_6	c_7	c_8	c_9	RMS $(Wm^{-2}sr^{-1})$
0°	-0.04092	-0.02797	-0.05608	-0.00197	0.00038	-0.00077	0.00012	-0.00088	0.00025	-0.00018	0.046
10°	-0.03727	-0.02910	-0.05530	-0.00456	0.00035	-0.00050	-0.00023	-0.00139	0.00145	-0.00046	0.044
20°	-0.03811	-0.03002	-0.05304	-0.00836	0.00038	-0.00050	-0.00034	-0.00140	0.00136	0.00046	0.042
30°	-0.03778	-0.03025	-0.05222	-0.00888	0.00043	-0.00057	-0.00044	-0.00155	0.00156	0.00062	0.039
40°	-0.03587	-0.03097	-0.04827	-0.01949	0.00058	-0.00097	-0.00036	-0.00110	0.00012	0.00443	0.037
50°	-0.03474	-0.03071	-0.04548	-0.03431	0.00078	-0.00163	-0.00002	-0.00089	-0.00177	0.01217	0.034
60°	-0.02893	-0.03147	-0.04687	-0.02704	0.00070	-0.00140	-0.00050	-0.00042	0.00199	0.00330	0.033
70°	-0.01866	-0.03399	-0.04176	-0.03700	0.00106	-0.00111	-0.00264	-0.00288	0.00708	0.00605	0.022
80°	-0.01112	-0.03229	-0.04482	-0.03705	0.00226	-0.00797	0.00371	0.00620	-0.00638	0.01312	0.012

Table 5.1: Regression parameters $\{c_i\}$ used to estimate the solar contamination in the GERB-2 LW channel.

estimate the contamination, the direct estimation and the estimation from SEVIRI, present the same accuracy.

5.5.4 Theoretical assessment of unfiltering errors

In this section, the different sources of error that affect the unfiltering process are addressed using the radiative transfer simulations. All the errors are expressed as the difference between the estimated and the actual unfiltered radiances. So, positive (negative) error means that the unfiltering process overestimates (underestimates) the resulting BB unfiltered radiance.

Error due to the NB–to–BB regressions

Although the SEVIRI NB–to–BB theoretical regressions Eqs.(5.5) and (5.6) are affected by a RMS error of about 0.45$\mathrm{Wm^{-2}sr^{-1}}$ or 0.7% (Clerbaux *et al.*, 2008a), the unfiltering error is expected to be much smaller. This assumption must be verified on the database of simulations. For each simulation $L_{th}(\lambda)$, the BB (L_{th} and $L_{lw,th}$) and the NB ($L_{6.2}$, $L_{7.3}$, ..., $L_{13.4}$) radiances are computed with the Eqs.(5.1). The unfiltering error for this simulated scene is then evaluated as

$$\epsilon[\%] = 100.0 \frac{L_{lw,th}\frac{L'_{th}}{L'_{lw,th}} - L_{th}}{L_{th}} \tag{5.9}$$

where L'_{th} and $L'_{lw,th}$ are the BB radiances estimated from the SEVIRI NB radiances through the Eqs.(5.5) and (5.6). Figure 5.5 shows scatterplots of the unfiltering factor α_{lw} (left) and of the unfiltering error ϵ (right) versus L_{th} at VZA $= 0°, 40°, 80°$. The figure also provides the unfiltering bias (the average of the unfiltering error) and RMS error

$$\text{bias} = \frac{1}{N}\Sigma_{i=1}^{N}\epsilon_i \tag{5.10}$$

$$\text{rms} = \sqrt{\frac{1}{N}\Sigma_{i=1}^{N}(\epsilon_i - \text{bias})^2} \tag{5.11}$$

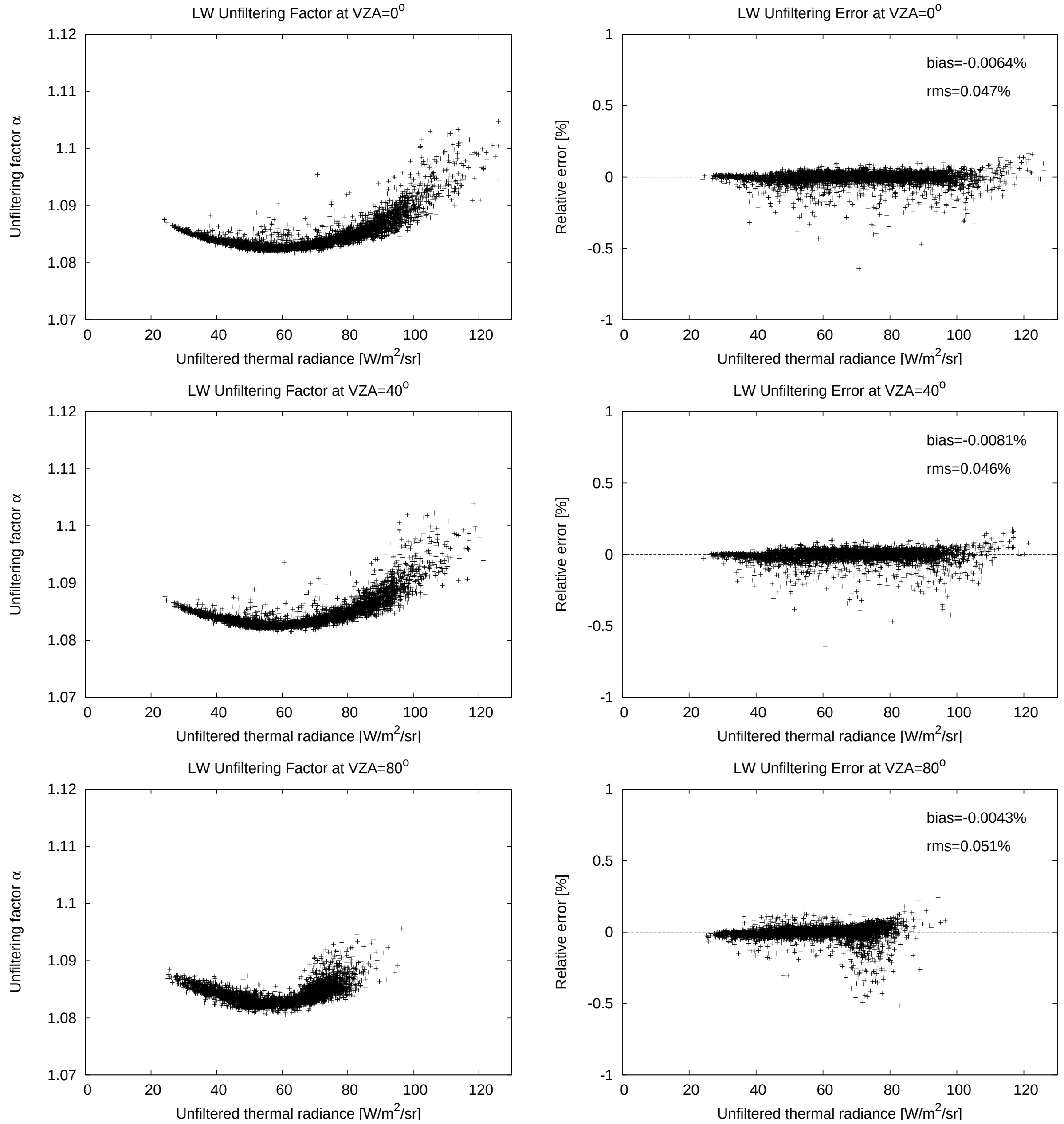

Figure 5.5: Theoretical unfiltering factor (left) and unfiltering error $\epsilon[\%]$ (right) for VZA = $0°, 40°, 80°$.

scene type	$< L_{th} >$ $Wm^{-2}sr^{-1}$	bias $Wm^{-2}sr^{-1}(\%)$	rms $Wm^{-2}sr^{-1}(\%)$
clear sky	81.3	-0.0009 (-0.0011)	0.0343 (0.0422)
cumulus	78.8	-0.0106 (-0.0134)	0.0452 (0.0574)
stratocumulus	73.8	0.0103 (0.0140)	0.0300 (0.0407)
stratus	72.3	0.0174 (0.0240)	0.0209 (0.0288)
altocumulus	70.6	-0.0265 (-0.0375)	0.0549 (0.0778)
altostratus	60.4	0.0022 (0.0036)	0.0223 (0.0370)
nimbostratus	59.4	0.0085 (0.0144)	0.0146 (0.0245)
cirrus	57.1	-0.0456 (-0.0798)	0.0779 (0.1366)
cirrostratus	43.3	-0.0096 (-0.0223)	0.0237 (0.0547)
deep convection	41.5	-0.0013 (-0.0031)	0.0095 (0.0230)

Table 5.2: Unfiltering error according to scene type for the VZA $= 0°$ simulations.

where the summations are done on the $N = 4622$ simulations. The figure shows that the unfiltering does not introduce significant error. The RMS error of the unfiltering process is about 0.05%. However, an unfiltering error of up to approximately -0.5% (i.e. an underestimation) is observed for some cloud conditions. Table 5.2 gives the unfiltering error according to the ISCCP cloud classification. The highest error is observed for high and semi–transparent clouds (cirrus). However, even in this case, the bias and the rms errors remain very small (bias $< 0.05 Wm^{-2}sr^{-1}$ and rms $< 0.08 Wm^{-2}sr^{-1}$)

Estimation of the solar contamination

The RMS error on the estimated solar contamination in the GERB–2 SW channel is estimated from the database of solar simulations. Figure 5.6 shows the scatterplot of the error ($L'_{lw,sol} - L_{lw,sol}$) according to the L_{sol} for a given geometry (SZA $= 0°$, VZA $= 50°$, RAA $= 90°$). The error can reach up to $+/- 0.2 Wm^{-2}sr^{-1}$ for reflective scene. The RMS of this error is $0.046 Wm^{-2}sr^{-1}$ which is, surprisingly, the same order of magnitude than the LW unfiltering error. In general, the contamination is slightly overestimated for the cloudy scenes. As the contamination is subtracted, this leads to a small underestimation of the unfiltered thermal radiance. For the reflective desert scenes, the opposite error is observed.

Subtraction of the solar contamination

As stated in Section 4.5.1, the implementation of the Edition 1 GERB data processing does not properly compensate for the solar contamination in the GERB LW measurement. This introduces a small error ϵ equal to

$$\epsilon = L'_{th} \frac{L_{lw}}{L'_{lw,th} + L'_{lw,sol}} - L'_{th} \frac{L_{lw} - L'_{lw,sol}}{L'_{lw,th}} \tag{5.12}$$

Let $\beta_{lw} = L_{lw}/L'_{lw}$ be the ratio between the actual and NB–to–BB estimated longwave radiance. Eq.(5.12) reduces to

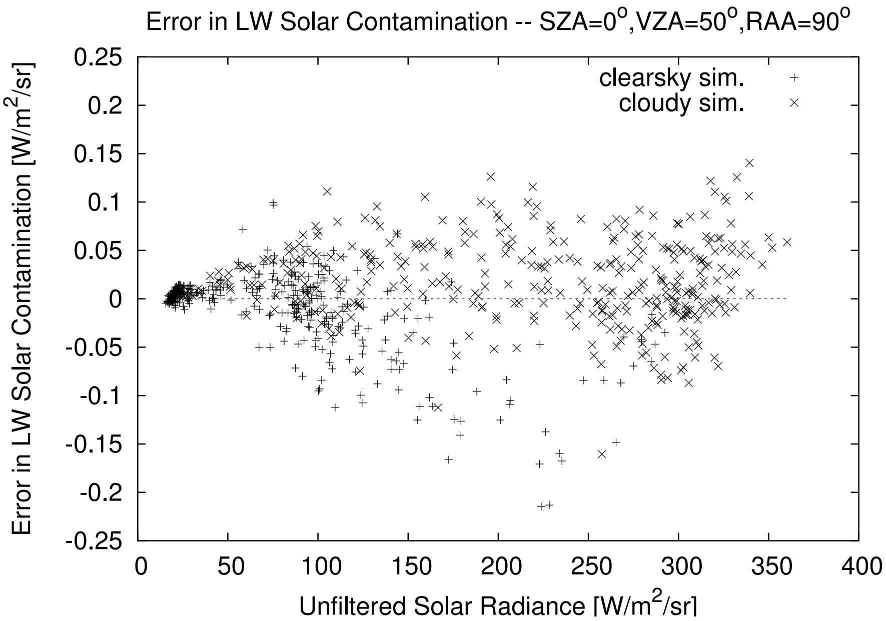

Figure 5.6: Theoretical error in the estimation of the LW solar contamination ($L'_{lw,sol} - L_{lw,sol}$) for the simulations at the geometry (SZA = 0°, VZA = 50° and RAA = 90°).

$$\epsilon = L'_{th}(1 - \beta_{lw})\frac{L'_{lw,sol}}{L'_{lw,th}} \tag{5.13}$$

The highest errors are then expected for highly reflective scenes (i.e. high $L'_{lw,sol}$ values) for which the LW NB–to–BB regression are inaccurate ($\beta_{lw} \neq 1$). Figure 5.7 shows the distribution of the error ϵ given by Eq.(5.13) evaluated on actual GERB and SEVIRI data from 19 November 2006 at 12:00 UTC. On these data, errors up to 0.13$\text{Wm}^{-2}\text{sr}^{-1}$ are observed. On average, the error is 0.013$\text{Wm}^{-2}\text{sr}^{-1}$ and the standard deviation 0.016$\text{Wm}^{-2}\text{sr}^{-1}$.

Dependency on SEVIRI calibration error

The calibration of the SEVIRI thermal channels impacts the estimation of the unfiltering factor α_{lw} while the calibration of the solar channels affects the estimation of $L_{lw,sol}$. To assess this, the effects of changing the SEVIRI channel calibration by −5%, 0% and +5% have been simulated.

From the unfiltering point of view, the worst case occurs when some thermal channels have a positive 5% change while others have -5% change. An overestimation of the GERB unfiltering factor by 0.09% is observed for -5% on 6.2μm, 7.3μm, 12μm and 13.4μm SEVIRI channels and +5% on 8.7μm, 9.7μm and 10.8μm channels.

For the estimation of the reflected sunlight contamination via Eq. 5.9, the worst case is observed when the 0.6, 0.8 and 1.6μm SEVIRI channels are decreased by -5%. In this case, the estimate $L'_{lw,sol}$ is underestimated by 5%. As the sunlight contamination can reach up to $-2.5\text{Wm}^{-2}\text{sr}^{-1}$ for very reflective scenes, the error on the unfiltered thermal radiance is $\epsilon = 0.12\text{Wm}^{-2}\text{sr}^{-1}$.

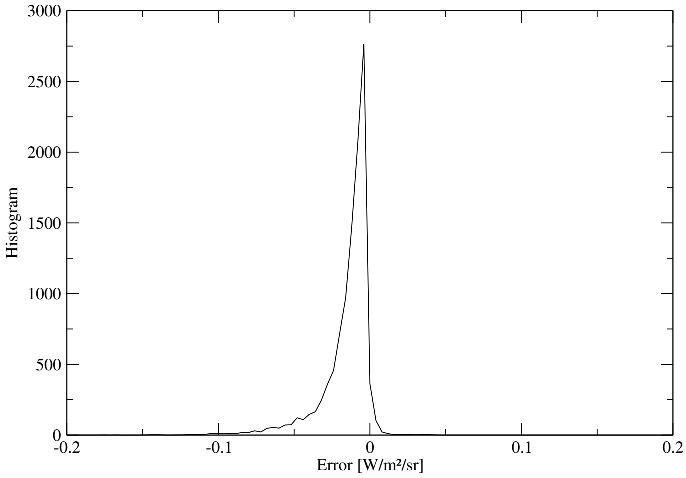

Figure 5.7: Error introduced on the thermal radiance due to the incorrect subtraction of the solar contamination in the LW channel (Eq.5.13).

This is a small relative error for typical scenes ($L_{th} \sim 100\mathrm{Wm^{-2}sr^{-1}}$) but can represent 0.5% of the signal for a very cold cloud with $L_{th} \sim 25\mathrm{Wm^{-2}sr^{-1}}$. The use of calibrated GERB shortwave observations could improve the estimate of the $L'_{lw,sol}$ contamination, but this is not possible today because of the current implementation of the data processing system.

5.6 GERB LW radiance comparison with CERES

Table 5.3 reports the GERB/CERES LW radiance comparison results, with the data and methodology presented under Section 3.3. In contrast with the SW, the GERB LW radiance is generally lower than the CERES one. The GERB/CERES longwave radiance ratio m differs significantly between the 4 CERES instruments and lies between $m = 0.981$ (FM4) and $m = 0.993$ (FM2). In addition to the average all sky ratio, the results are shown separately for June and December, for day (SZA $< 85°$) and night (SZA $> 95°$) conditions, and for clear and cloudy scenes. Overall, the GERB LW radiance is 1.3% lower than CERES. This is consistent with the combined stated 1 SD accuracies of 0.75% for CERES and 0.9% for GERB (the combined RMS is 1.2%).

For cloudy scenes, the GERB/CERES ratio is slightly higher for the ARG than for the BARG and HR formats. The explanation for this is the same as for the SW radiance comparison over clear ocean, except that here the cloudy scenes have the lower radiances. Figure 5.8 shows the dependency of the ratio with the LW radiance. In addition to the scene type dependency affecting the ARG format for very cold scenes, a significant day/night difference is observed with the FM1 (1.1%) and to a lesser extend with the FM2 (0.5%). As the problem is not present with the FM3 and FM4, it is assumed to be due to the LW separation for the CERES instruments on Terra. For the BARG and HR formats the GERB/CERES ratio is lower for cold

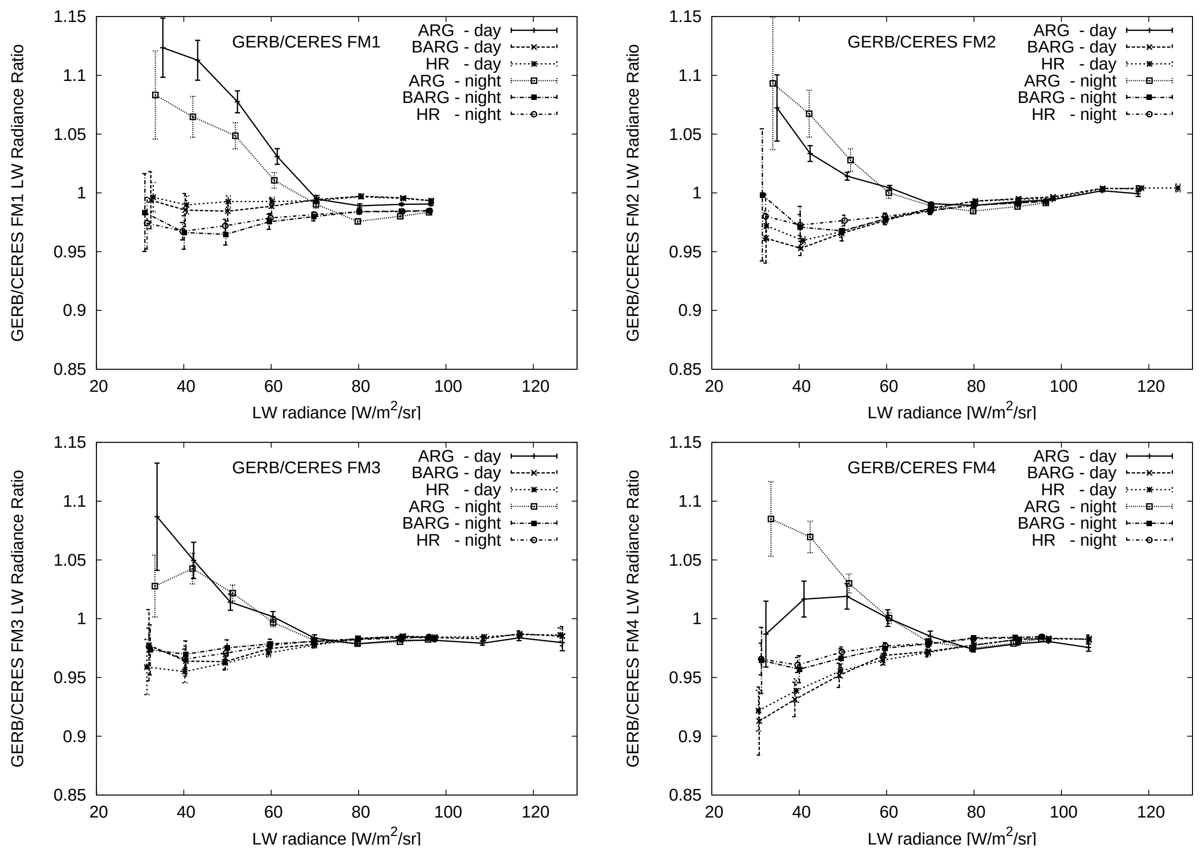

Figure 5.8: GERB/CERES LW radiance ratio in radiance bins.

Averaged Rectified Geolocated (ARG)							
Scene Type	FM1	FM2	FM3	FM4	$<$ FM $>$	$< L_g >$	ΔL
All sky	0.989 ± 0.001	0.993 ± 0.001	0.983 ± 0.001	0.981 ± 0.001	0.986	84.22	-1.17
June	0.989 ± 0.001	0.993 ± 0.001	0.984 ± 0.001	0.982 ± 0.001	0.987	86.64	-1.14
December	0.989 ± 0.001	0.993 ± 0.001	0.981 ± 0.001	0.980 ± 0.001	0.986	81.90	-1.20
Day	0.994 ± 0.001	0.994 ± 0.001	0.983 ± 0.001	0.981 ± 0.001	0.988	85.80	-1.05
Night	0.983 ± 0.001	0.989 ± 0.002	0.982 ± 0.001	0.981 ± 0.002	0.984	82.23	-1.34
Clear sky	0.983 ± 0.001	0.995 ± 0.001	0.982 ± 0.001	0.980 ± 0.001	0.985	95.44	-1.45
Cloudy	1.015 ± 0.005	0.998 ± 0.003	0.998 ± 0.006	0.999 ± 0.005	1.002	67.26	0.14
Binned Averaged Rectified Geolocated (BARG)							
Scene Type	FM1	FM2	FM3	FM4	$<$ FM $>$	$< L_g >$	ΔL
All sky	0.989 ± 0.001	0.993 ± 0.001	0.983 ± 0.001	0.981 ± 0.001	0.987	84.15	-1.15
June	0.989 ± 0.001	0.993 ± 0.001	0.984 ± 0.001	0.983 ± 0.001	0.987	86.46	-1.12
December	0.989 ± 0.001	0.993 ± 0.001	0.981 ± 0.001	0.980 ± 0.001	0.986	81.94	-1.18
Day	0.995 ± 0.001	0.994 ± 0.001	0.983 ± 0.001	0.981 ± 0.001	0.988	85.71	-1.04
Night	0.983 ± 0.001	0.989 ± 0.001	0.983 ± 0.001	0.982 ± 0.001	0.984	82.22	-1.30
Clear sky	0.986 ± 0.001	0.997 ± 0.001	0.984 ± 0.001	0.984 ± 0.001	0.988	95.52	-1.19
Cloudy	0.991 ± 0.003	0.983 ± 0.002	0.982 ± 0.002	0.978 ± 0.003	0.983	65.73	-1.11
High Resolution (HR)							
Scene Type	FM1	FM2	FM3	FM4	$<$ FM $>$	$< L_g >$	ΔL
All sky	0.989 ± 0.001	0.993 ± 0.001	0.983 ± 0.001	0.982 ± 0.001	0.987	84.93	-1.15
June	0.990 ± 0.001	0.993 ± 0.001	0.984 ± 0.001	0.983 ± 0.001	0.987	87.00	-1.11
December	0.989 ± 0.001	0.993 ± 0.001	0.982 ± 0.001	0.980 ± 0.001	0.986	82.95	-1.18
Day	0.995 ± 0.001	0.993 ± 0.001	0.983 ± 0.001	0.981 ± 0.001	0.988	86.57	-1.05
Night	0.984 ± 0.001	0.990 ± 0.001	0.983 ± 0.001	0.982 ± 0.001	0.985	83.10	-1.29
Clear sky	0.987 ± 0.001	0.998 ± 0.001	0.985 ± 0.001	0.984 ± 0.001	0.988	95.78	-1.12
Cloudy	0.988 ± 0.002	0.980 ± 0.002	0.977 ± 0.001	0.976 ± 0.002	0.981	68.28	-1.35

Table 5.3: GERB/CERES LW radiance ratio m and uncertainty for $\alpha < 5°$. The last columns give the average GERB radiance $< L_g >$ and the difference in average GERB and CERES radiance $\Delta L =< L_g > - < L_c >$ both in $\mathrm{Wm^{-2}sr^{-1}}$.

(i.e. cloudy) scenes than for warm (i.e. clear) scenes. Theoretical studies show that the CERES LW radiances are expected to be slightly overestimated for cloudy scenes. Loeb *et al.* (2001) have shown that although the CERES LW unfiltering error remains in general below 0.2% it can reaches 0.4% for deep convective clouds (overestimation). On the other hand, the GERB unfiltering is expected to slightly underestimate the radiance for cloudy scenes (Clerbaux *et al.*, 2008a). The cumulative effect of these 2 error sources explains the observed drop in ratio for the coldest scenes in Figure 5.8 for the BARG and HR.

The images on the first and second columns in Figure 7.5 (Chapter 7) show the radiance ratio in all sky and clear sky conditions. For the FM2 instrument, a slightly higher LW radiance ratio is observed over warm desert. This corresponds to the ratio increase seen with the FM2 for warm scenes in the upper right graph of Figure 5.8.

5.7 Correction of the dispersion

To assess the magnitude of the pixel–to–pixel variability in the GERB LW spectral response the difference $(max - min)$ of simulated filtered LW radiance is computed on the database of simulated spectra. Figure 5.9 shows that the $(max - min)$ dispersion increases with the LW radiance up to a value of $(max - min) = 1$ W m^{-2} sr^{-1}. In a similar way as for the SW channel, (TN31) proposes to use a linear fit to convert the detector radiance L_{lw}^{det} in "GERB radiance" L_{lw}, the radiance corresponding to the average spectral response defined by Eq.(3.2)

$$L_{lw} = c^{det} + d^{det} L_{lw}^{det} \tag{5.14}$$

Figure 5.9 shows that this simple correction reduces significantly the dispersion. After correction (symbols '×'), the $(max - min)$ differences remain mostly below 0.1 W m^{-2} sr^{-1}. The detector's coefficients c^{det} and d^{det} of the best fit Eq.(5.14) are given in (TN31) for the 256 detectors of GERB–2. The analysis of the LW filtered radiance according to the detector number shows that the filtered radiance is linearly decreasing. Over the database of simulations, the average filtered radiance is 61.99 W m^{-2} sr^{-1} for the northernmost detector and 61.65 W m^{-2} sr^{-1} for the southernmost detector. So, for a same scene, a half percent difference in filtered radiance is expected to exist between the bottom and the top of the GERB LW images due only to the optics, since for Edition 1 the detectors have the same response. Since this difference is not correct in the Edition 1 processing, a similar north–south variation should be present in the GERB longwave unfiltered radiances and fluxes. This assumption has to be confirmed.

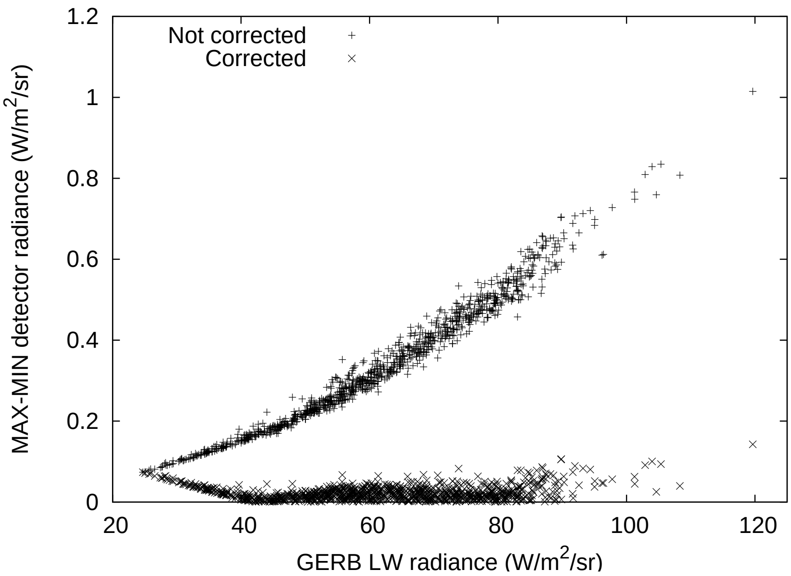

Figure 5.9: Scatterplot of $(max - min)$ difference of GERB-2 LW filtered radiance according the average detector radiance without (symbols '+') and with (symbols '×') correction with Eq.(5.14).

5.8 Unfiltering of the SEVIRI thermal channels

5.8.1 Introduction

Based on a preliminary version of the database of simulated spectra (Section 5.3), Clerbaux *et al.* (2001) quantified to 0.7% the RMS error when second order regressions are used to estimate the BB unfiltered radiance from the thermal channels of SEVIRI. The theoretical approach has been adopted in the GERB and GERB–like data processing, and is still used. The method together with some pieces of validation are given in Section 5.8.2. For the validation, we have taken advantage of the availability of the Edition 1 GERB LW radiance.

The empirical approach is also investigated using CERES and GERB BB observations. In a first attempt, CERES has been used (Dubrovnik regressions, Clerbaux *et al.*, 2005). Since March 2006, the availability of Edition 1 GERB data has permitted deriving actual GERB–like regressions for the LW radiation. This work is presented under Section 5.8.4 and is planned to be implemented in the Edition 2 of the processing.

A database of corresponding LW unfiltered radiance from the GERB–2 BARG products and the corresponding NB radiances from SEVIRI has been built. To this end, the SEVIRI images at the synoptic hours (0, 3, 6, 9, 12, 15, 18, 21 UTC) have been used as from 1 February 2004 to 10 May 2007. The criteria for temporal and spatial matchings are identical to the ones considered for the SW case (Section 4.8.2). From each SEVIRI repeat cycle, about 40 000 couples of coangular observations are extracted.

5.8.2 Theoretical regressions

Second order regressions on the 7 thermal channels[1] (Eq.5.5) have been selected with coefficients dependent on the VZA. The GERB and GERB–like Edition 1 data have been processed using these theoretical regressions.

Figure 5.10 shows the ratio of the monthly means GERB–like and GERB data for June and December 2006 at 00:00, 06:00, 12:00 and 18:00 UTC. Similar plots, not shown, have been analyzed for the other months and synoptic hours. Table 5.4 shows that an overall overestimation of about 1.7% is observed on the theoretically estimated BB radiance with respect to GERB. The ratio shows regional patterns that are related to the high–level cloudiness in the Intertropical Convergence Zone (ITCZ) and to the VZA.

The SEVIRI radiances that are used as input of the regressions are spectral radiances, but the theoretical regressions expect effective radiance (see definition in Section 3.2.3). In Figure 5.11

[1] The 3.9μm SEVIRI channel has not been considered for the NB–to–BB due to its contamination by daytime solar radiation.

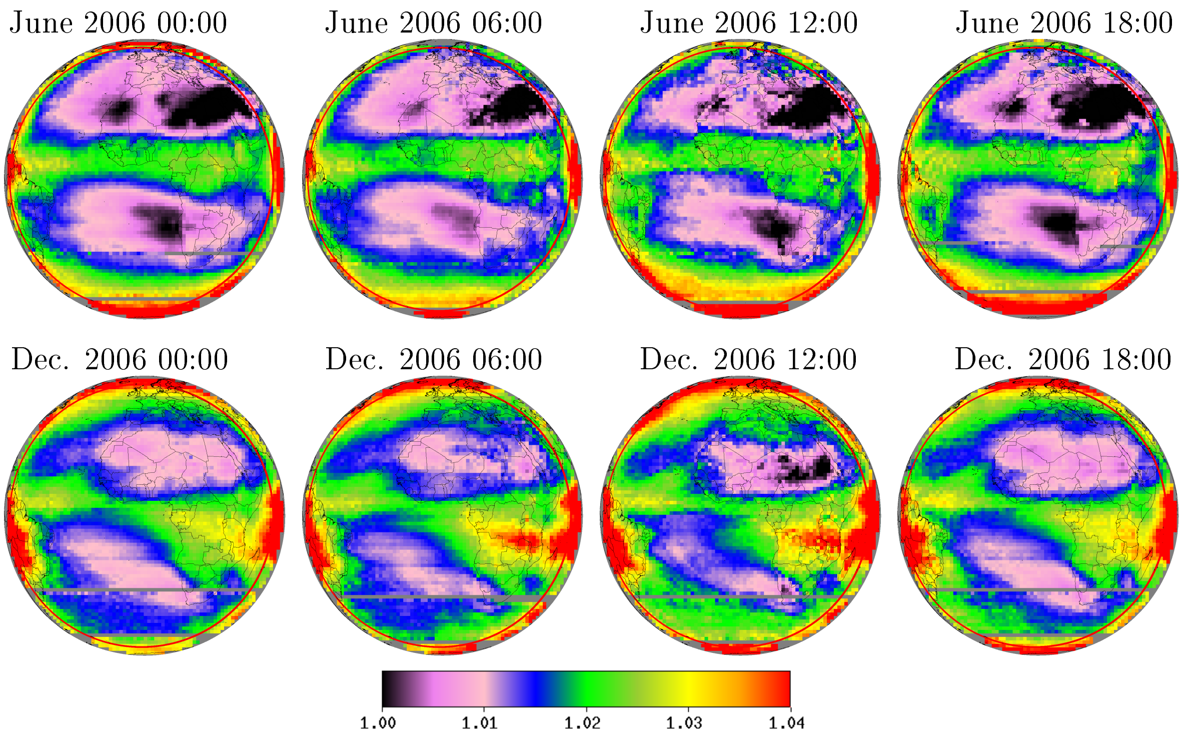

Figure 5.10: Regional scale (135km × 135km boxes) GERB–like/GERB ratio between the theoretical LW NB–to–BB regressions and GERB Edition 1. The color palette is centered on 1.02.

the input SEVIRI radiances have been converted from spectral to effective radiances before their use in the regressions. The regional patterns are not modified but the overall difference increases by an additional 0.4% (to 2.1%) as stated in Table 5.4. Figure 5.14 shows the daily ratio between the theoretical regressions and GERB. Over 3 years, a non–significant drift of 0.05%/year is observed.

5.8.3 Dubrovnik regression

The SEVIRI-CERES collocation methodology described in (Clerbaux *et al.*, 2005) has been followed for the LW radiation. The simple linear regression is selected to estimate the BB radiance from the NB radiances and the VZA (in degree)

$$\begin{aligned} L'_{bb} &= 17.71 + 1.86 L_{6.2} + 8.52 L_{7.3} + 5.01 L_{8.7} - 3.86 L_{9.7} + \\ &\quad 1.73 L_{10.8} - 0.551 L_{12} + 6.14 L_{13.4} + 0.0166 \text{ VZA} \end{aligned} \tag{5.15}$$

Regional validation of the Dubrovnik regressions is provided in Figure 5.12. The problem affecting the ITCZ in the theoretical regressions is corrected. However, the VZA term in

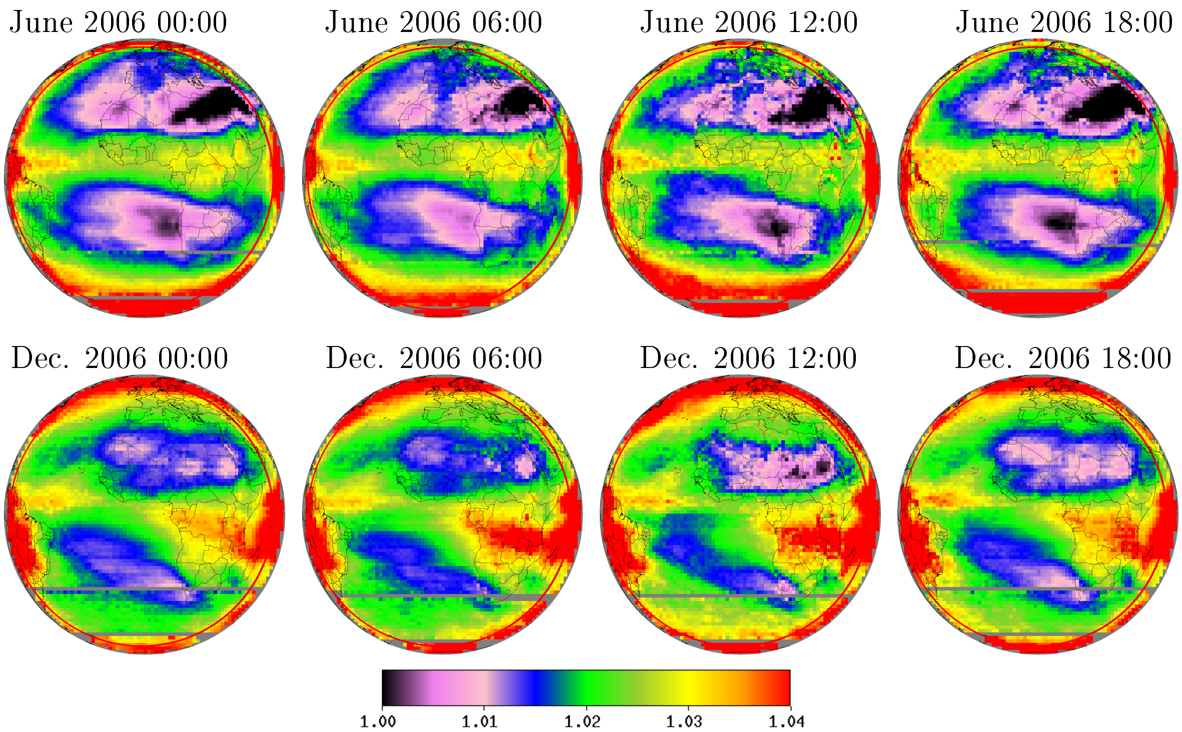

Figure 5.11: Idem as Figure 5.10 but with SEVIRI effective radiance.

month hour	Theoretical		Theo. Eff.		Dubrovnik		Empirical	
	bias	rms	bias	rms	bias	rms	bias	rms
200606 0000	1.4%	0.9%	1.8%	1.0%	1.3%	0.7%	0.0%	0.2%
200606 0600	1.5%	0.8%	1.9%	0.9%	1.4%	0.7%	0.1%	0.2%
200606 1200	1.6%	0.9%	2.0%	1.0%	1.4%	0.8%	0.3%	0.2%
200606 1800	1.5%	1.0%	1.9%	1.1%	1.3%	0.8%	0.1%	0.2%
200612 0000	1.8%	0.7%	2.3%	0.8%	1.2%	0.7%	0.0%	0.2%
200612 0600	1.9%	0.8%	2.4%	0.8%	1.4%	0.6%	0.1%	0.2%
200612 1200	2.0%	0.9%	2.5%	1.0%	1.4%	0.7%	0.3%	0.2%
200612 1800	1.9%	0.8%	2.3%	0.9%	1.2%	0.6%	0.1%	0.2%

Table 5.4: Biases (with respect to 1) and RMS errors of the ratio between the LW NB–to–BB estimates and the GERB Edition 1 evaluated in 135km × 135km boxes. Only the boxes with VZA $< 70°$ (red curves on the Figures 5.10, 5.11, 5.12 and 5.13) have been taken into account.

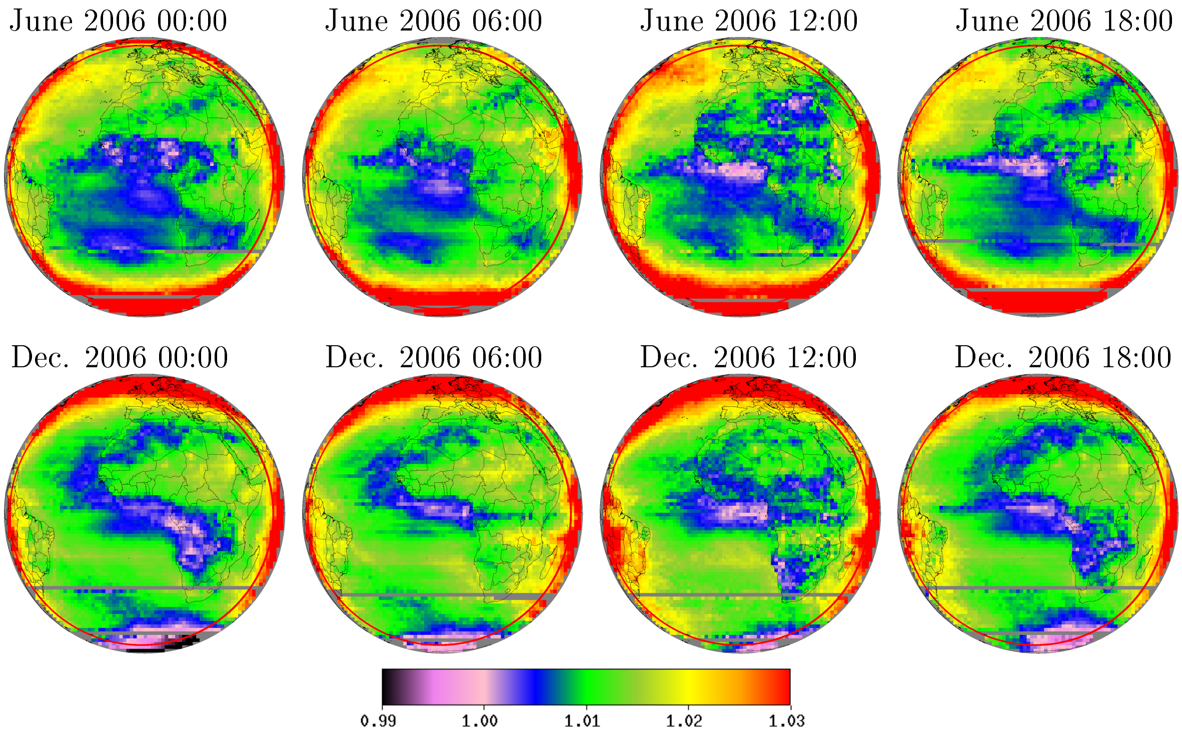

Figure 5.12: Idem as Figure 5.10 but for the Dubrovnik regression. The color palette is centered on 1.01.

Eq.(5.15) seems to overestimate the BB radiance, especially at high latitude in the winter hemisphere.

Figure 5.14 shows the daily ratio value between the Dubrovnik estimate and the actual GERB. In comparison with the theoretical regressions, reduced seasonal variations of the ratio is observed. On the other hand, higher jumps of the daily ratio occur during the SEVIRI decontamination (January 2005 and 2006). The Dubrovnik regression seems to rely more on the 13.4μm channel than the theoretical regressions.

5.8.4 Empirical regressions with GERB

For the Edition 2 of the GERB/GERB–like data processing, it is proposed to use the following second order regression (without crossed terms)

$$\begin{aligned} L'_{bb} &= c_0 + c_1\ L_{6.2} + c_2\ L_{7.3} + c_3\ L_{8.7} + c_4\ L_{9.7} + c_5\ L_{10.8} + c_6\ L_{12} + c_7\ L_{13.4} + \\ & \quad c_8\ L^2_{6.2} + c_9\ L^2_{7.3} + c_{10}\ L^2_{8.7} + c_{11}\ L^2_{9.7} + c_{12}\ L^2_{10.8} + c_{13}\ L^2_{12} + c_{14}\ L^2_{13.4} \end{aligned} \tag{5.16}$$

The 15 coefficients of the regressions are derived in boxes of 12×12 BARG pixels (i.e. 540km $\times$ 540km) on a monthly basis (Jan, Feb, ..., Dec). To facilitate independent validation, the

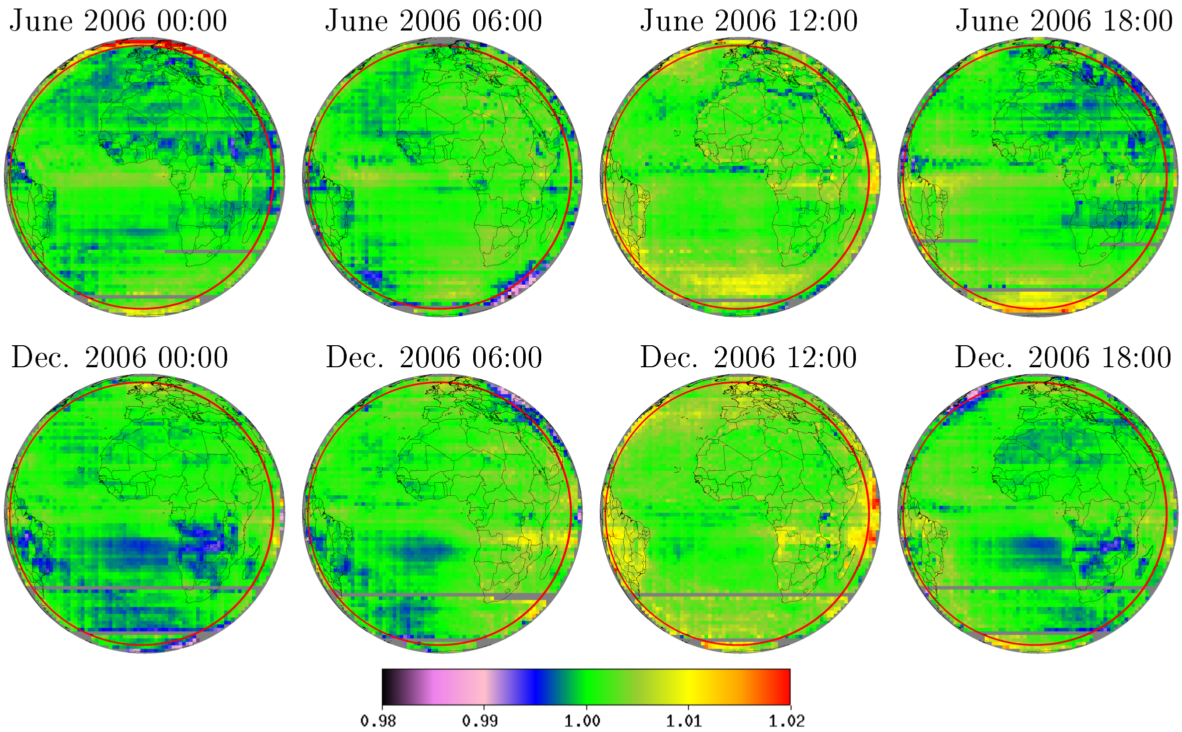

Figure 5.13: Idem as Figure 5.10 but for the empirical regression. The color palette is centered on 1.

regressions are fit on the data from 1 February 200 to 30 April 2006. One complete year of independent data is kept for the validation. Figure 5.13 shows the improvement obtained with respect to the theoretical and Dubrovnik regressions. Figure 5.14 shows that the daily means ratio GERB–like/GERB is very stable in time. Table 5.4 shows that there is nearly no overall bias during the night and a small overestimation of $\sim 0.3\%$ during daytime. The RMS error of the ratio at the 135km $\times$ 135km scale is $\sim 0.2\%$.

5.8.5 Temporal stability

Figure 5.14 shows an excellent temporal stability between the SEVIRI–based estimate BB LW radiance and the GERB observations. This is made possible by the inboard calibration blackbodies of both instruments. It is worth noting that the calibration of the SEVIRI thermal channels is carried out without the instrument front optics. The observed good stability suggest therefore that there is no significant change in transmission of the SEVIRI telescope.

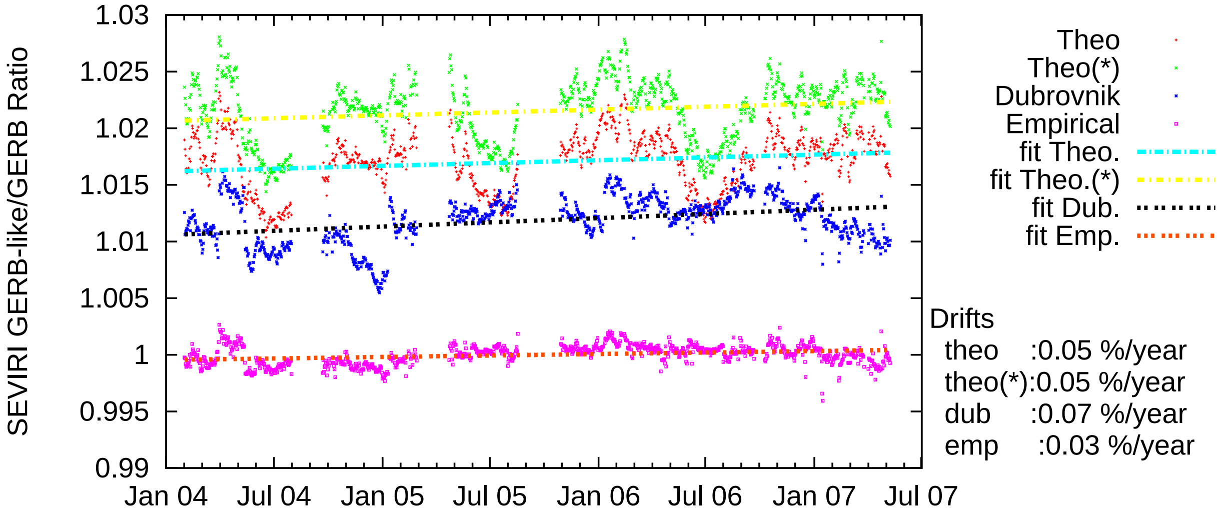

Figure 5.14: Daily ratio of the SEVIRI LW NB–to–BB with GERB Edition 1 for the theoretical regressions in spectral and in effective radiances (Theo *), for the Dubrovnik regression, and for the empirical regressions.

5.9 Unfiltering of the Meteosat IR and WV channels

5.9.1 Introduction

Using the same methodology as for the visible channel (Section 4.9), a database of coangular Meteosat–7 WV and IR radiances and corresponding GERB LW unfiltered radiance has been built. Using the BARG format for GERB, the number of corresponding pairs of NB and BB observations is about $2\ 10^6$ per day. The GERB–2 radiance measured from 3.5° west is corrected to simulate what would have been observed from the position of the Meteosat–7 position at 0°. This correction is based on a simple model of the LW unfiltered radiance anisotropy given by Eq.(7.1) under Section 7.3

$$L_{0^\circ} = L_{3.5^\circ} \frac{R(0^\circ, L_{3.5^\circ})}{R(-3.5^\circ, L_{3.5^\circ})} \tag{5.17}$$

5.9.2 Theoretical regressions

Theoretical regressions, adjusted on the dataset of radiative transfer simulations, have been used to generate GERB–like data from Meteosat–7 from July 1998 to May 2006 (Dewitte & Clerbaux, 1999a). The broadband emitted thermal radiance was estimated using the following regression on the water vapor (WV) and infrared window (IR) measurements of the MVIRI instrument on Meteosat–7

$$L_{bb} = c_0 + c_1 L_{wv} + c_2 L_{ir} + c_3 L_{ir}^2 \tag{5.18}$$

The coefficients of the regression are dependent on the VZA. These early GERB–like data have been used to study an anomaly of OLR over the Sahara due to a large desert dust event in July 2003 (Haywood *et al.*, 2005) and the radiative effects of an eruption of the Etna on the 27 October 2002 (Bertrand *et al.*, 2003). Details on the method and results can be found in these 2 papers. The images on the first row in Figure 5.15 show the regional validation on the theoretical regressions using GERB data (using the angular correction expressed in Eq.5.17). These monthly means ratios show important differences (±2%) at regional scale.

5.9.3 Empirical regressions with GERB

For a first survey of empirical regressions, it is decided to fit the Eq.(5.18) in super boxes of 12×12 BARG pixels (540km × 540km and on a seasonal basis (DJF, MAM, JJA, SON). This aims to account for the spatial and seasonal patterns of water vapor in the atmosphere and for

month	Theoretical bias (%)	Theoretical rms (%)	Empirical bias (%)	Empirical rms (%)
200410	1.7	0.8	0.1	0.4
200501	1.4	0.8	0.1	0.3
200507	1.7	1.1	-0.1	0.3
200604	0.8	0.6	-0.1	0.4

Table 5.5: Biases (wrt 1.0) and RMS of the <GERB–like>/<GERB> ratio in the 135km $\times$ 135km boxes with VZA $< 70°$ for the theoretical and empirical Meteosat–7 NB–to–BB regressions.

local variation of the surface emissivity. It is worth noting that these empirical regressions are fitted on the Meteosat 0° FOV and can therefore not process data from the IODC.

The images on the second row in Figure 5.15 provide monthly means validation at regional scale. The improvement with respect to the theoretical regression is significant. In general, better NB–to–BB results are observed over the ocean than over the land surfaces. Most of the monthly mean residual errors seem to result from changes in desert surface emissivity. The aridity of the surface modifies the emission in the ranges $3\mu m - 5\mu m$ and $7.5\mu m - 10.5\mu m$ where Meteosat–7 does not sample the radiation. The method could certainly be improved using a stratification of the regression as a function of the type of surface emissivity. A good proxy for this could be the $8.7\mu m$ surface emissivity derived from MSG/SEVIRI in the Land Surface Analysis (LSA) SAF. Similar surface characterization is made available in the IREMIS database (Seemann *et al.*, 2008).

5.9.4 Temporal stability

Figure 5.16 shows the day–by–day variation of the <GERB–like>/<GERB> ratio. The theoretical regressions show important variations and an overall decrease of the ratio by -0.45%/year. For the empirical regressions, the temporal variations of the ratio are limited to about a quarter of percent around 1. Over the 2 years of data considered here, a small drift of about -0.2%/year is observed with the empirical regression although it is not known if the drift is significant or not. If significant, the drift could be attributed to Meteosat–7 as GERB proved to be stable with respect to SEVIRI. In this case, it is likely that the drift comes from the calibration of the Meteosat–7 WV channel. Indeed, this would explain why the drift is higher for the theoretical regressions as they rely more on the WV radiance than the empirical regressions.

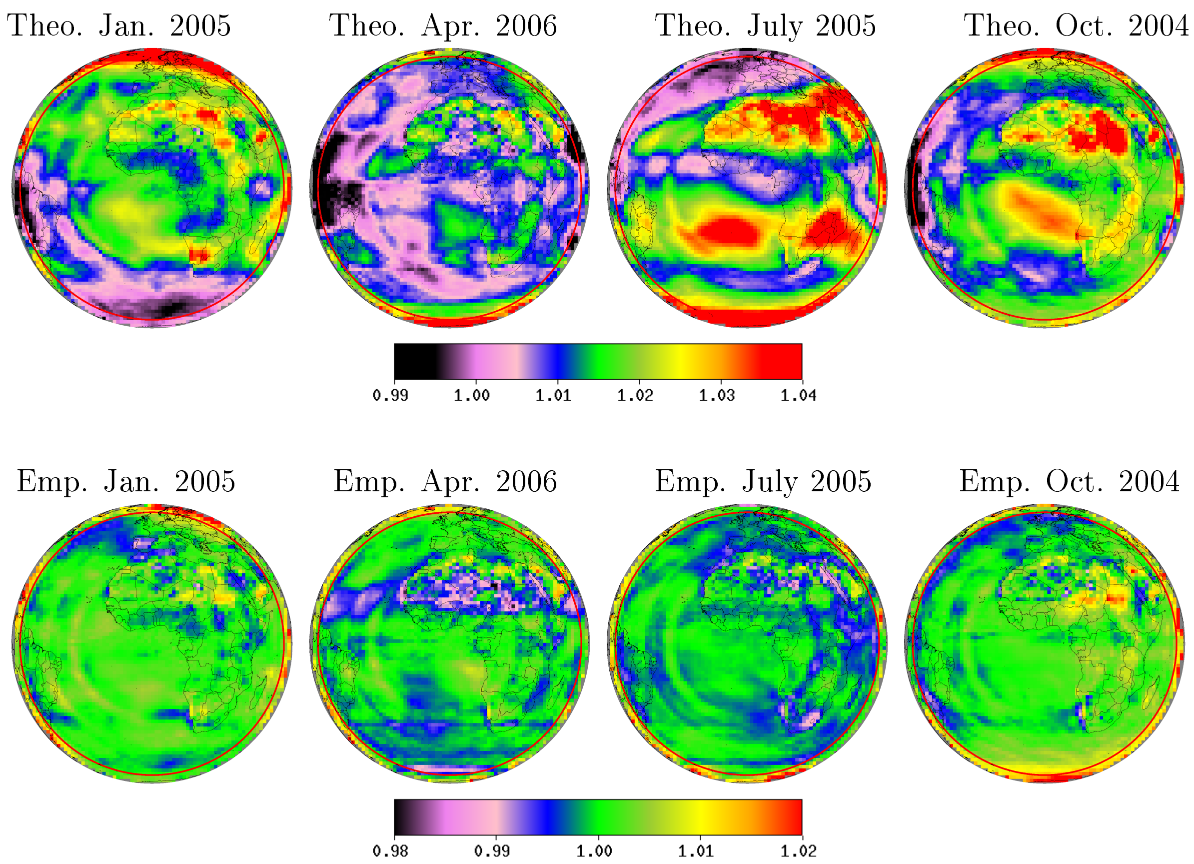

Figure 5.15: LW NB–to–BB regressions for Meteosat–7. Ratio <GERB-like>/<GERB> in 135km × 135km boxes. The images show monthly mean ratio for the theoretical regressions (top) and the empirical regressions (bottom). For the theoretical regressions, the color palette is centered on 1.015.

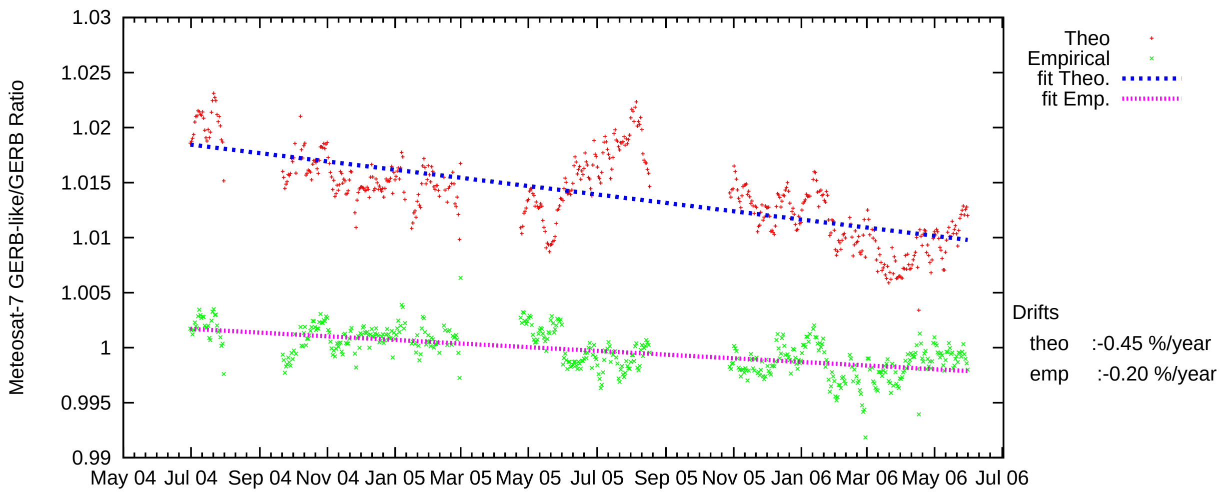

Figure 5.16: Daily value of the ratio of average GERB–like from Meteosat–7 and GERB radiance.

5.10 Discussion

Radiative transfer computations are powerful tools to simulate the spectral signature in the thermal part of the spectrum. The physics in the models is now very accurate and the limitations we encountered are mainly due to difficulties of providing realistic atmosphere and surface descriptions as input for the simulations. We used the TIGR database which provides sufficient atmosphere description but unfortunately without the corresponding surface properties in terms of spectral emissivity and (radiometric) skin temperature. Although this appears not to be critical for the problems faced in this chapter, a better representation of the surface spectral emissivity is desirable. For this purpose, it is foreseen to use the IREMIS dataset (Seemann *et al.*, 2008) in a next issue of our database of thermal simulations. In parallel with the theoretical approach, an empirical approach of the spectral modeling problems is possible based on observed spectra instead of simulations. As an example, the Infrared Atmospheric Sounding Interferometer (IASI) instrument on the MetOp satellites provides more than 8000 samples between 3.62μm and 15.5μm. A large part of the spectrum (the far IR) is however not measured and must be simulated.

Although some spectral variation of sensitivity exists, the unfiltering of the GERB instrument LW channel is not an issue. Simple methods produce unfiltered thermal radiances well within the scientific goal of 0.5% for the unfiltering. As an example, the RMS error for the direct unfiltering is about 0.1%. Using spectral information from 7 thermal channels of SEVIRI, this error is further reduced to about 0.05% in the Edition 1 unfiltering. Surprisingly, the daytime error due to the subtraction of the solar contamination can reach the same error level for some bright scenes (up to 0.2$\mathrm{Wm}^{-2}\mathrm{sr}^{-1}$ error is reported). With respect to these small theoretical error sources, more significant unfiltering errors could arise from improper characterization of the instrument sensitivity, including in the far infrared, beyond 25μm. For GERB, this sensitivity is not measured but is inferred from measurements made on a witness sample (up to 55μm) and extrapolated up to 140μm. Similarly, it has been theoretically shown that the error due to the pixel–to–pixel variability in optical paths in the instrument optics could reach 0.25%. Further investigations are needed to confirm this finding, for instance by analyzing the GERB/CERES unfiltered radiances ratio in latitude bins.

When broadband measurement is not available, the BB radiance has been widely inferred using narrowband–to–broadband techniques. Thanks to the number of channels in the infrared and the blackbody calibration of these channels, the SEVIRI regressions perform very well over the whole FOV and no significant day–to–day variation is observed. For the MVIRI instrument the regressions suffer clearly from the absence of measurements between 8μm and 10μm, at wavelengths where the surfaces present large variability in emissivity.

Chapter 6

Angular modeling of the reflected solar radiation

6.1 Introduction

As stated in Section 2.5 (scientific background), in itself the radiance measured by a BB radiometer is of little interest for Earth radiation budget studies. Indeed, the scientific community requires reflected solar and emitted thermal fluxes leaving the TOA in the full upper hemisphere. A model of the angular distribution of the radiance is therefore needed to infer the hemispheric flux from the directional measurement. This chapter concentrates on the solar radiation while Chapter 7 deals with the thermal one.

As for the spectral modeling, we first discuss the factors that govern the anisotropy of the radiance field at the TOA (Section 6.2).

Since the anisotropy is dependent on the type of observed scene, a scene identification process is required for selecting the adequate model. Section 6.3 describes the scene identification algorithm that has been developed for the GERB data processing. Then, Section 6.4 details the application of the CERES–TRMM SW ADMs to convert the GERB SW radiance in flux. In these two sections, the discussion focuses mainly on the strengths and weaknesses of the adopted approaches and suggests improvements of the processing system.

Section 6.5 reports on the comparison of the GERB and CERES solar fluxes. Taking into account the results already obtained at the radiance level (Section 4.6), the flux comparisons are key elements of the overall validation of the GERB angular conversion (scene identification + ADM).

Section 6.6 concludes this part of the work.

6.2 Main sources of anisotropy

A number of effects contribute to the anisotropy of the TOA radiance field: the scattering by atmospheric constituents, the bi–directional reflection at the surface, the effects of the cloudiness and aerosols.

In the clear atmosphere, the Rayleigh scattering mainly affects the short wavelengths, with a λ^{-4} dependency. This scattering is not isotropic as the intensity of the scattered beam is proportional to $(1 + \cos^2(\theta))$, where θ is the scattering angle. The angular distribution is therefore symmetric between forward and backward directions. At the TOA, the main systematic effect is related to the increase of scattering with the VZA due to the atmospheric path. In general, this induces a limb brightening in the SW that is apparent on the clear sky images as illustrated in Figure 6.1 (left).

A highly anisotropic radiance field is observed over the clear ocean. Out of the specular beam, quite low anisotropy factors ($R \sim 0.7$ in Eq. 2.3) are generally observed. On the opposite, high values (up to $R \sim 5$) are common in the sun glint region. The width of the specular reflected beam depends on the sea state: calm sea produces specular reflection in a narrow beam while rough sea produces more diffuse glint. The effect of a long wavelength ocean swell (that can travel thousands of nautical miles from the storm wind that created it) is small compared to the effect of the normal waves. For this reason, the local surface wind speed is a good proxy of the sea surface bi–directional reflectance. A statistical model of the sea surface roughness is available from Cox & Munk (1955) and has been improved since then.

For land surfaces, the BRDF is physically dependent on both the geometric structure and on the optical properties of its constituents (absorption, scattering). An often observed effect of the geometric structure is the increase of radiation in the backward direction due to the cancellation of the shadows when the sun lies behind the observer. For vegetated surface, geometric structure of the canopy also explains the dependency of the BRDF on type and density of vegetation. In this case, it is generally accepted that the vegetation indices are good proxies for the bi–directional reflectance.

In case of cloudiness, the TOA anisotropy is dependent on the clouds macro– and micro–physical properties. For the former, enhanced anisotropy occurs in broken cloud fields: the apparent cloud fraction depends on the VZA, and limb brightening is frequent. The transparency (i.e. the optical depth) of the cloud is obviously another macro–physical properties that governs the TOA anisotropy. The Mie "theory" provides the analytical solution of the equations of Maxwell for scattering of the radiation by spherical droplets in water clouds. At the TOA, the light scattered by these clouds is relatively isotropic, due to the multiple scattering processes. However, a small increase of the radiance could be observed in the forward direction due single scattering, especially at low sun elevation. The particle size distribution affects the overall reflectivity of the cloud (numerous small particles give a brighter cloud than few large particles) but does not affect significantly the anisotropy. The high level clouds are often constituted of ice crystals which can not be modeled as spherical anymore. Numerous empirical refractivity indexes are proposed for ice crystal particles. The ice particles are responsible for numerous optical phenomena like the 22° and 44° halos, the 120° parhelion and the glory.

Due to large particle size compared to the radiation wavelength, the single and multiple scattering by atmospheric aerosols is relatively isotropic. With respect to an "aerosol–free" condition, the aerosols reduce in general the TOA anisotropy (Loeb *et al.*, 2003b). This effect is especially significant over the clear ocean.

6.3 SEVIRI scene identification

From the previous analysis, it is clear that an accurate SW radiance–to–flux conversion requires the characterization of the footprint in terms of surface type (especially the water fraction and vegetation content), cloudiness (especially the cloud fraction, the cloud optical depth, and type of particles), and aerosols (especially the optical depth). Additional scene type information (e.g. altitude of the surface and of the cloudiness, droplets size distribution, type of aerosols, ...) are not expected to provide significant improvement in the SW angular modeling.

A point discussed at the GERB International Science Team (GIST) meetings concerns the need to develop our own scene identification for the GERB data processing. External products (e.g. MPEF cloud mask) or software (e.g. SAFNWC) are available with the associated documentation and validation activities. But, the science team is of the opinion that an own scene identification is preferable to ensure the constancy of the processing software and the independence of the fluxes to external sources like NWP fields.

For the GERB Edition 1 processing, the surface type is derived from the invariant land cover type classification of the International Geosphere and Biosphere Program (IGBP). Based on AVHRR observations, this project provides a global surface classification into 17 geotypes at 1km spatial resolution (Townshend *et al.*, 1994). Following the merging done for the CERES–TRMM ADMs (Loeb *et al.*, 2003b), these 17 geotypes have been grouped in 6 surface types: ocean, dark vegetation (low–to–moderate tree/shrub), bright vegetation (moderate–to–high tree/shrub), dark desert, bright desert and snow. The downscaling in the larger GERB pixels (ARG , BARG, HR), provides percentages of coverage for each class. These percentages are used in the processing. An image of the surface type is provided to the user of the GERB products. This surface type is the one with the maximum coverage value. This is debatable for the mixed pixels since, for example, a pixel with 40% water and 30% of both vegetation and desert is classified as a water pixel. Figure 6.1 (right) shows the surface type assigned to the GERB HR pixels. The use of invariant geotype performs correctly in most parts of the FOV, validating the underlying assumption that the surface properties do not change significantly at the GERB pixel scale. A series of regional problems observed in the GERB and GERB–like products are however attributed to surface change in spectral or bidirectional reflectances. It is the case of seasonal variations of water level in some African lakes (e.g. Lake Chad), of the vegetation content in the Sahel Belt and South African sub-continent, and of snow coverage in Europe and Asia. For these last 2 points, the consequences on the GERB SW fluxes are addressed in (Bertrand *et al.*, 2008) and (Bertrand *et al.*, 2006c), respectively.

The cloud detection is performed as a cloud mask at the SEVIRI 3km pixel scale, i.e. each pixel is labeled as clear or cloudy. For this, the reflectances in the SEVIRI 0.6 μm and 0.8 μm bands are compared with reference clear sky values for these bands (Ipe *et al.*, 2003). The clear sky reflectances are estimated by fitting a model of the TOA reflectance (BRDF) on the observations done during the last 60 days. To cope with changes in surface properties and sun illumination, the clear sky images are updated on a weekly basis. The use of the 0.6 μm and 0.8 μm bands gives optimal performances over both land and ocean surfaces. Indeed, as the land surface reflection is usually lower at 0.6 μm, this band presents a higher contrast between clear and cloudy situations. Over the water, the contrast is higher in the 0.8 μm channel as it is less affected by Rayleigh scattering. Figure 6.1 (left) shows an example of color composite of clear sky reflectance images for the 0.6μm and 0.8μm bands. The clear sky and actual reflectance are used as input in Look-Up Tables (LUTs) that provide estimates of the cloud optical depth at 0.55μm. These LUTs have been built off–line using the STREAMER radiative transfer model (Key & Schweiger, 1998). Each SEVIRI pixel is classified as cloudy if the cloud optical depth provided by the LUTs is higher than a threshold. A threshold value of 0.6 proved to provide cloud fractions consistent with more complex multi–spectral algorithms involving the thermal channels. For some pixels, it is however needed to increase locally the threshold to avoid persistent false detection of clouds. This problem affects areas where high spatial gradient of reflectance exists, like the coastal pixels. In these areas, the clear sky reflectance presents day–to–day variations that are attributed to the IMPF rectification. In practice, the threshold value is estimated from the max and min reflectance values in the 3×3 pixels neighborhood as

$$\tau_{th} = 0.6 + 3.0(\max - \min) \tag{6.1}$$

The brightness temperature (BT) in the 10.8μm infrared window channel is used to assign a "floating point" cloud phase to each cloudy pixel. For $BT > 265$ K the top of the cloud is supposed to contain only water droplets, for $BT < 245$ K only ice crystal particles, and a mix is assumed between these limits.

The 3–km cloud information is then downscaled to the GERB pixels to get the cloud fraction, the average of the logarithm of the cloud optical depth, and the average of the cloud phase. For fractional cloud cover, these averages are evaluated on the cloudy part of the GERB pixel. This retrieved cloud information is used to select the SW ADM at the HR pixel resolution. The information is also provided to the users as part of the GERB level 2 products. Ipe *et al.* (2008) provide the full description and validation of the cloud retrieval for GERB Edition 1. The paper is currently under review.

In a manner similar to the cloud characterization, retrieval of the aerosol optical depth over clear ocean is implemented in the Edition 1 processing (De Paepe *et al.*, 2008) using LUTs providing by NOAA. Ocean regions with high aerosol content are bright and are often classified as cloudy by the cloud scheme. For this reason, a dedicated discrimination between cloud and aerosols is implemented in the GERB processing following the method proposed by Brindley & Russell (2006). The aerosols optical depth is not used in the processing but is made available to the users as part of the level 2 data.

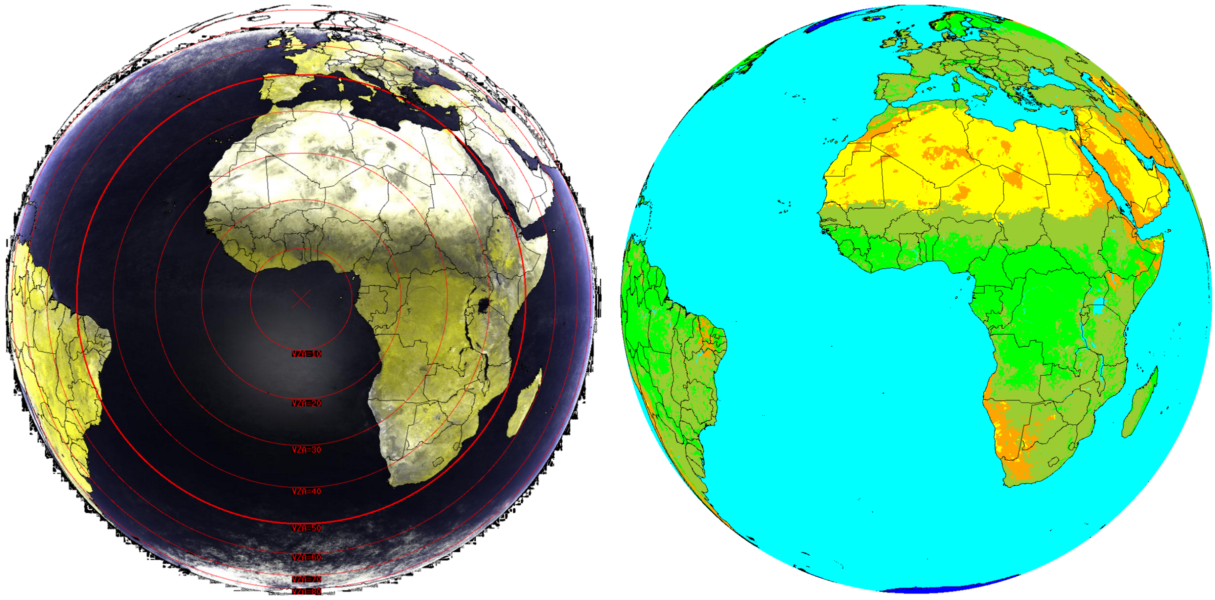

Figure 6.1: Left: composite clear sky image with the viewing zenith angle at the Earth surface (from a geostationary satellite at 0°). Right: surface type (ocean, dark and bright vegetation, dark and bright desert, snow) for the GERB HR pixels.

With respect to the GERB mission objectives, this SEVIRI scene identification presents the following strengths:

- Based on LUTs, the cloud retrieval is fast. On a standard computer, the full disk scene identification requires less than 1 minute. This enables to process the data in near real–time and also allows reprocessing of the GERB dataset in a limited time period.
- The processing is causal in the sense that no data from the future are required to process the near real–time observations. This allows delivering data to the near real–time users with a good timeliness.
- The processing does not rely on any Numerical Weather Prediction (NWP) model field. The GERB scene identification is therefore not affected by modifications of the NWP model and/or of the observational data assimilated by the model.
- The scheme presents only a limited sensitivity to the SEVIRI instrument calibration. The clear sky reflectance images that serve as reference for the cloud detection follow, with a small time delay, any drift of the SEVIRI solar channel sensitivities. This feature has been proved during the switch between Meteosat–8 and Meteosat–9 on 1 May 2007: although the 0.6 μm and 0.8 μm radiances differed by about 1.7% between the satellites, the cloud fraction was not significantly affected.

On the other hand, the following weaknesses have been identified:

- Based on the visible channels, the retrieval does not work during the night and in grazing sun illumination (SZA $> 80°$).
- For the same reason, the retrieval is not reliable in the sun glint region: clouds are hard to distinguish from the bright specular reflection in the solar channels.
- Optically thin clouds are hardly detected over bright surface (cirrus cloud over the Sahara).
- There are problems due to the use of invariant surface geotype as discussed before.
- The wish to maintain a causal processing impedes some kind of post–processing in the cloud retrieval. In particular, it has been shown that the cloud retrieval in the sun glint region could be improved combining observations just before and after the sun glint contamination (Bertrand *et al.*, 2006a).
- Similarly, although this has not yet been addressed, it is expected that the accuracy of the clear sky reflectance maps should be better if based on 60 days of observation centered on the processing time instead of using the previous 60 days.
- The need of 60 days of SEVIRI observations to built the clear sky images prohibits to process short periods of data. This proved to be a problem in case of short switches to the backup satellite (e.g. during decontamination).
- Comparison with CERES retrieval reveals important dispersion in cloud phase. The use of the 1.6 μm channel (Nakajima & King, 1990) is expected to improve the agreement with CERES.

6.4 GERB processing with the CERES TRMM ADM set

Applying the sorting by angular bin method to the 9 months of CERES–TRMM data, Loeb *et al.* (2003b) have derived a set of 592 SW ADMs. These models are well–suited to process geostationary observations since the precessing orbit of TRMM provides a full coverage in terms of solar illumination. On the other hand, as the inclination of the TRMM orbit is only 35° above the Equatorial plane[1], the mid– and high–latitude regions have not been sampled. The CERES–TRMM models are therefore representative of the scenes between 38°S and 38°N but may fail to describe the anisotropy of higher latitude, not observed. Another important feature of these models is the spatial resolution of 10 km for the nadir view footprints of CERES on TRMM. For partly cloudy scenes, the empirical models reproduce therefore the anisotropy over area of this size. For this reason, the models are used to estimate the GERB flux on the High Resolution grid. The 9km × 9km spatial resolution of this grid is close to the 10km size of the CERES–TRMM models. The manner the models are applied within the GERB processing does not follow exactly the recipes given in (Loeb *et al.*, 2003b), the differences are detailed hereafter.

A first difference concerns the way the ADM is interpolated according to the VZA, SZA, and RAA. For GERB a tri–linear interpolation of the anisotropy factor R is realized while for CERES the tri–linear interpolation is done on the flux F. The interpolation according to the cloud fraction and the cloud optical depth is also different. For CERES a bi–linear interpolation is realized on the flux F while for GERB no interpolation is done. The reason for these differences lies in the fact that most of the data processing was implemented before the publication of the (Loeb *et al.*, 2003b) paper.

The processing also differs over pixels that contain a mix of different surface types. In this case, CERES does not interpolate the models, while GERB performs an interpolation. The reason is that the CERES team concluded that with the small 10 km CERES–TRMM footprint, mixed pixels should be quite rare. For GERB the anisotropy factor is estimated as

$$R = \frac{\sum_{i=1}^{6} f_i Alb_i(\mathrm{SZA}) R_i(\mathrm{SZA}, \mathrm{VZA}, \mathrm{RAA})}{\sum_{i=1}^{6} f_i Alb_i(\mathrm{SZA})} \tag{6.2}$$

where Alb_i(SZA) and f_i are respectively the model albedo and the percent coverage of the surface type i in the HR pixel (Bertrand *et al.*, 2005). The Eq.(6.2) is used even for cloudy pixels. Thanks to this interpolation, the GERB fluxes are supposed to be more accurate in regions where water and land coexist (e.g. archipelagoes).

For clear ocean, ADMs are provided for different wind speed intervals. For CERES, wind speed analysis from an NWP model is used to interpolate the ADM. For GERB a monthly climatology

[1]The main mission of TRMM is the study of the tropical convection.

of wind speed derived from the ERS scatterometer observations is used to select the model.

CERES performs a theoretical adjustment of the clear ocean ADM to account for the reduction of anisotropy in presence of aerosols. Basically, the adjustment is proportional to the difference between the observed BB radiance and the radiance of the ADM. Although this correction was implemented in the GERB processing, it was decided not to activate it for the Edition 1 processing. The reason for this is that no actual BB measurement at the 10 km resolution is available (GERB footprints are much larger). Therefore, the adjustment would have been based on estimates of the BB radiance from SEVIRI. It was not possible to prove that the accuracy of these estimates was sufficient to use them in the aerosol adjustment scheme. Consequently it was decided to develop a specific adjustment based on the retrieved aerosol optical depth. This is an ongoing activity performed by Helen Brindley at Imperial College.

In the sun glint region, CERES does not estimate the flux from the observed radiance using Eq.(2.3) but uses the model albedo. The same processing is implemented for GERB up to $25°$ for the SGA. Later, it was decided to mask the flux in the SGA $< 15°$ region in the final Edition 1 products (by mistake also over the land!). This keeps the GERB dataset as independent as possible from the CERES absolute level, except in the $15° - 25°$ SGA region.

Due to the infrequent observation of snow in the sampled area, CERES–TRMM does not provide empirical models for snow covered surfaces. For Edition 1, the angular conversion for the GERB pixels with permanent snow/ice is done using the bright desert ADMs (which are the closest model in terms of albedo). Empirical snow ADMs are now available from Kato & Loeb (2005). They might be used in future Editions of the dataset.

Finally, the GERB TOA fluxes are provided at the surface reference level, while CERES rescales the fluxes to the 20 km reference level proposed by Loeb *et al.* (2002). The difference is a simple multiplicative factor of $(r_e + 20\ \mathrm{km})^2/r_e^2 = 1.0063$, where $r_e = 6378$ km is the Earth Equatorial radius. The users are warned of this difference via the GERB Quality Summary (Russell, 2006).

Although there is clearly room for improvements of the GERB SW angular modeling in subsequent Editions of the dataset, the next section demonstrates that this part of the processing does not introduce significant problems in the resulting fluxes.

6.5 GERB SW flux comparison with CERES

For the shortwave flux comparison, there is no restriction on the coangularity angle α and consequently the number of GERB/CERES pairs is much higher than for the radiance comparison. Table 3.5 shows that this number reaches nearly 2.5 millions per CERES instruments over June and December 2004.

Table 6.1 summarizes the SW flux comparison in a similar form to that given in Table 4.6 for the SW radiance. The (BARG) SW GERB/CERES flux ratio in all sky conditions lies between 1.066 (FM1 and FM2) and 1.086 (FM4). Similarly as for the radiances intercomparison the agreement is better with the FM1 and FM2 than with the FM3 and FM4. All together, the flux ratio are about 1.5% higher than the ratio observed in radiance. This increase of m between radiance and flux comparisons is higher for the FM1 and FM4 instruments (+2.1% and +1.9%) than for the FM2 and FM3 (+1.2% and +0.9%). This is consistent with the change of sampled area between radiance and flux for the CERES instruments in cross–track scanning. For the FM1 and FM4, the radiances comparisons are in the tropical region, where the GERB/CERES ratio is in general slightly lower than for the rest of the FOV.

As expected, the SW flux comparison shows the same scene type dependency as the radiance comparison: it is larger for the ARG and much more limited for the BARG and HR formats.

Figure 6.2 shows the regional analysis of the GERB/CERES SW ratio for all sky and clear sky radiance (1st and 2nd columns) and flux (3rd and 4th columns). Due to the increased number of matches, the spatial noise is reduced in the flux comparisons compared to the radiance. Figure 6.3 separates the flux comparisons for the June and December periods, for these plots, results from the CERES instruments on the same satellite and therefore sharing the same overpass time have been combined.

Regional patterns are apparent in the flux comparisons which are not visible in the radiance results. As the CERES fluxes are observed from a range of different viewing geometries, errors in the radiance to flux conversion, specific to a particular geometry should be minimal in the average quantity used in this comparison, whereas the GERB viewing geometry for each location is fixed. Thus these differences highlight problems in the radiance to flux conversions for specific geometries which result in errors in the GERB fluxes for particular locations.

The most obvious feature in the flux plots is a lowering of the ratio, off the West coast of Africa. Around the gulf of Guinea this feature is visible in all the flux comparisons, regardless of instrument or season, although it is clearly most pronounced in the clear sky and larger in June than December. Lowered ratios off the African coast at higher and lower latitudes are also seen in some of the plots. To some extent the lowered ratio in the Gulf of Guinea region is present in the radiance comparison, and this could be due to the spectral response

Averaged Rectified Geolocated (ARG)							
Scene Type	FM1	FM2	FM3	FM4	< FM >	$< F_g >$	ΔF
All sky	1.066 ± 0.002	1.066 ± 0.002	1.079 ± 0.001	1.085 ± 0.001	1.074	253.22	17.44
June	1.068 ± 0.002	1.069 ± 0.002	1.078 ± 0.002	1.086 ± 0.002	1.075	233.73	16.34
December	1.065 ± 0.002	1.063 ± 0.002	1.080 ± 0.002	1.084 ± 0.002	1.073	272.13	18.50
Overcast	1.038 ± 0.003	1.043 ± 0.003	1.056 ± 0.003	1.056 ± 0.003	1.048	493.24	22.52
Clear sky	1.077 ± 0.003	1.074 ± 0.002	1.096 ± 0.003	1.099 ± 0.002	1.086	262.34	20.84
ocean	1.081 ± 0.014	1.093 ± 0.012	1.090 ± 0.012	1.085 ± 0.013	1.087	94.06	7.54
dark veg.	1.071 ± 0.004	1.069 ± 0.004	1.085 ± 0.007	1.095 ± 0.006	1.080	160.25	11.83
bright veg.	1.084 ± 0.004	1.078 ± 0.004	1.111 ± 0.007	1.118 ± 0.006	1.098	197.87	17.52
dark desert	1.091 ± 0.004	1.084 ± 0.004	1.108 ± 0.006	1.114 ± 0.005	1.099	240.54	21.60
bright desert	1.072 ± 0.003	1.070 ± 0.003	1.091 ± 0.003	1.093 ± 0.003	1.082	356.88	26.80
Binned Averaged Rectified Geolocated (BARG)							
Scene Type	FM1	FM2	FM3	FM4	< FM >	$< F_g >$	ΔF
All sky	1.066 ± 0.002	1.066 ± 0.002	1.080 ± 0.002	1.086 ± 0.001	1.075	253.98	17.59
June	1.067 ± 0.002	1.069 ± 0.002	1.080 ± 0.003	1.087 ± 0.002	1.076	234.58	16.51
December	1.065 ± 0.002	1.063 ± 0.002	1.081 ± 0.002	1.085 ± 0.002	1.073	272.69	18.64
Overcast	1.059 ± 0.002	1.066 ± 0.003	1.079 ± 0.002	1.080 ± 0.002	1.071	506.21	33.36
Clear sky	1.076 ± 0.002	1.073 ± 0.002	1.096 ± 0.002	1.098 ± 0.002	1.085	246.67	19.41
ocean	1.046 ± 0.009	1.058 ± 0.008	1.063 ± 0.009	1.057 ± 0.008	1.056	91.26	4.83
dark veg.	1.071 ± 0.005	1.068 ± 0.005	1.082 ± 0.006	1.092 ± 0.006	1.078	160.67	11.58
bright veg.	1.083 ± 0.004	1.077 ± 0.004	1.113 ± 0.007	1.120 ± 0.006	1.098	195.42	17.30
dark desert	1.070 ± 0.004	1.066 ± 0.005	1.083 ± 0.004	1.088 ± 0.003	1.076	235.00	16.58
bright desert	1.078 ± 0.003	1.076 ± 0.002	1.098 ± 0.003	1.100 ± 0.003	1.088	357.18	28.71
High Resolution (HR)							
Scene Type	FM1	FM2	FM3	FM4	< FM >	$< F_g >$	ΔF
All sky	1.067 ± 0.002	1.066 ± 0.002	1.082 ± 0.002	1.086 ± 0.002	1.075	253.65	17.65
June	1.069 ± 0.002	1.069 ± 0.002	1.082 ± 0.003	1.088 ± 0.003	1.077	231.39	16.50
December	1.065 ± 0.003	1.064 ± 0.002	1.081 ± 0.002	1.084 ± 0.002	1.073	275.22	18.76
Overcast	1.055 ± 0.003	1.062 ± 0.003	1.078 ± 0.003	1.077 ± 0.003	1.068	481.40	30.54
Clear sky	1.077 ± 0.002	1.075 ± 0.002	1.096 ± 0.003	1.097 ± 0.003	1.086	231.32	18.32
ocean	1.056 ± 0.011	1.061 ± 0.011	1.069 ± 0.009	1.064 ± 0.008	1.063	91.68	5.39
dark veg.	1.074 ± 0.004	1.069 ± 0.004	1.091 ± 0.007	1.095 ± 0.006	1.082	164.11	12.41
bright veg.	1.084 ± 0.005	1.081 ± 0.005	1.112 ± 0.009	1.117 ± 0.007	1.099	196.15	17.54
dark desert	1.077 ± 0.005	1.072 ± 0.005	1.089 ± 0.005	1.092 ± 0.005	1.083	237.55	18.06
bright desert	1.078 ± 0.004	1.076 ± 0.003	1.100 ± 0.004	1.101 ± 0.003	1.089	355.91	28.85

Table 6.1: GERB/CERES SW flux ratio m and uncertainty. The last columns give the average GERB SW flux $< F_g >$ and the difference in average GERB and CERES SW fluxes $\Delta F =< F_g > - < F_c >$ both in Wm^{-2}.

characterization in the blue band and the GERB SW radiance unfiltering (Clerbaux *et al.*, 2008b).

However, there is clearly an additional issue affecting the fluxes. Considering the region $3°N - 3°S$ and $20°W - 2°W$, in cloudy conditions the average SW flux ratio, m is 1.061, which is similar to the average overcast value shown in Table 6.1. However, in clear sky the ratio falls to 0.996 that is clearly different from the values seen over most of the rest of the field of view. The ratio for the co–angular radiances for clear scenes in this region is 1.022, which although lower than the surrounding regions is clearly not sufficient to explain the flux effect. Although this affected region is subject to significant aerosol contamination, this can be shown not to be the cause of the problem, because decomposing the result by aerosol loading using the aerosol parameters present in the CERES SSF files indicates that the disagreement is actually reduced in the presence of aerosol.

However considering the GERB/CERES ratio in the region as a function of sun glint angle shows that the low GERB/CERES SW flux ratio occur when the GERB direction of observation is close to the sun specular reflection. To explain this it must be understood what happens to the GERB fluxes for clear ocean scenes in the region of the glint angle. For glint angles between 0 and 15 degrees, no GERB flux is produced in the Edition 1 and V003 products, due to the problem of obtaining an accurate scene identification. For glint angles between 15 and 25 degrees the GERB radiance is not used as the basis of the flux due to the problem of determining an accurate anisotropy factor for these angles. In these cases a climatological value of the flux from the CERES TRMM ADM is used. Thus for these angles a comparison is actually being made between a CERES based climatology and a CERES instantaneous estimate and thus it is not surprising that the ratio is close to 1. As the glint angle varies with time of day and season, the location of the lowered ratios varies according to which CERES instrument (i.e. overpass time) and in which season the comparison is made.

A much more localized, but nevertheless persistent difference is observed in the form of elevated flux ratios some (small) regions of the desert on the African continent and in Spain. These are most obvious in the clear sky flux comparisons and more apparent in the December comparisons than in the June results. These differences relate to a known problem with the radiance to flux conversion for these scenes and hence improved angular dependency models for semi–desert regions are planned (Bertrand *et al.*, 2008).

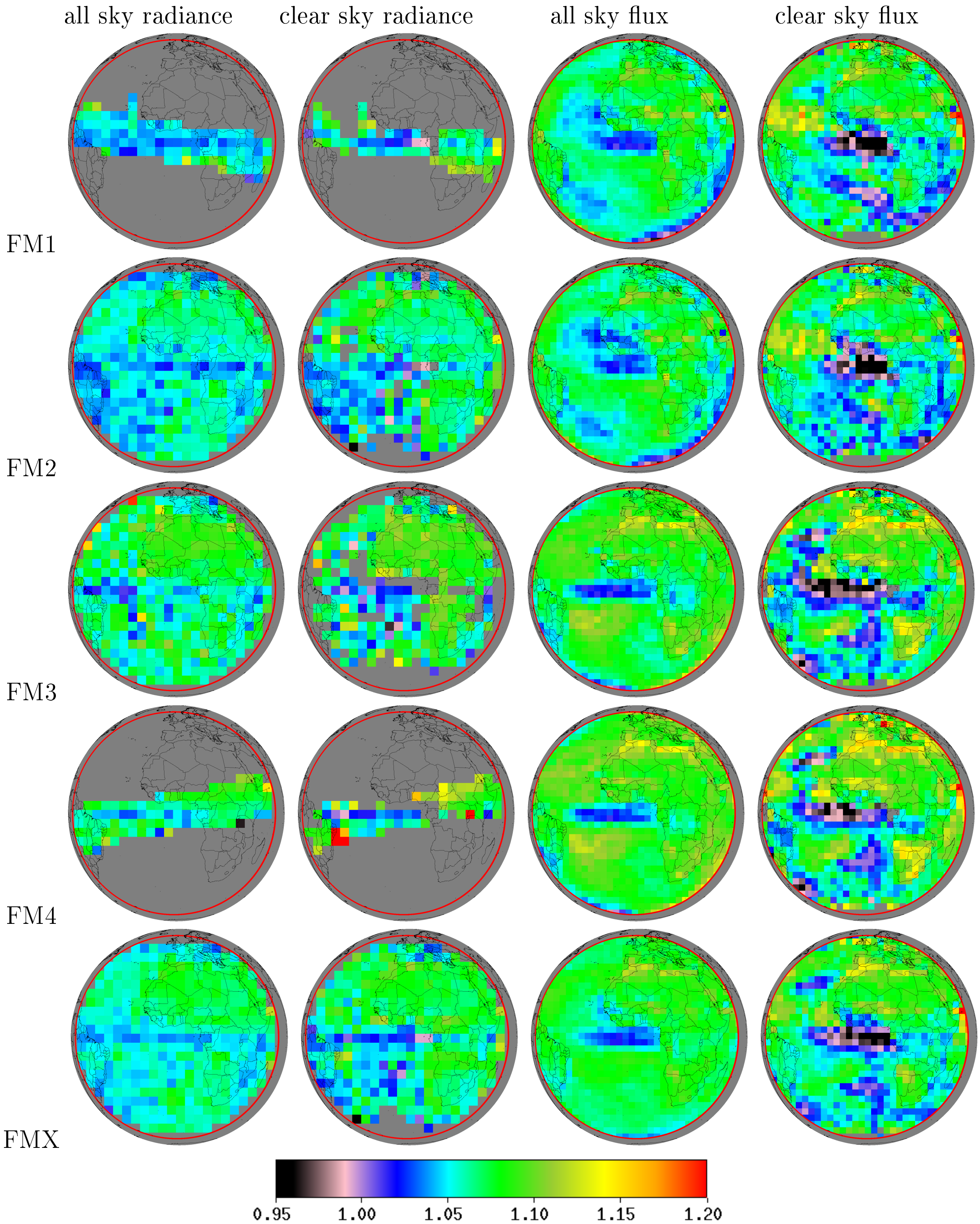

Figure 6.2: GERB (BARG)/CERES SW ratio for the different CERES instruments and altogether (FMX). The red circle indicates VZA = 70°.

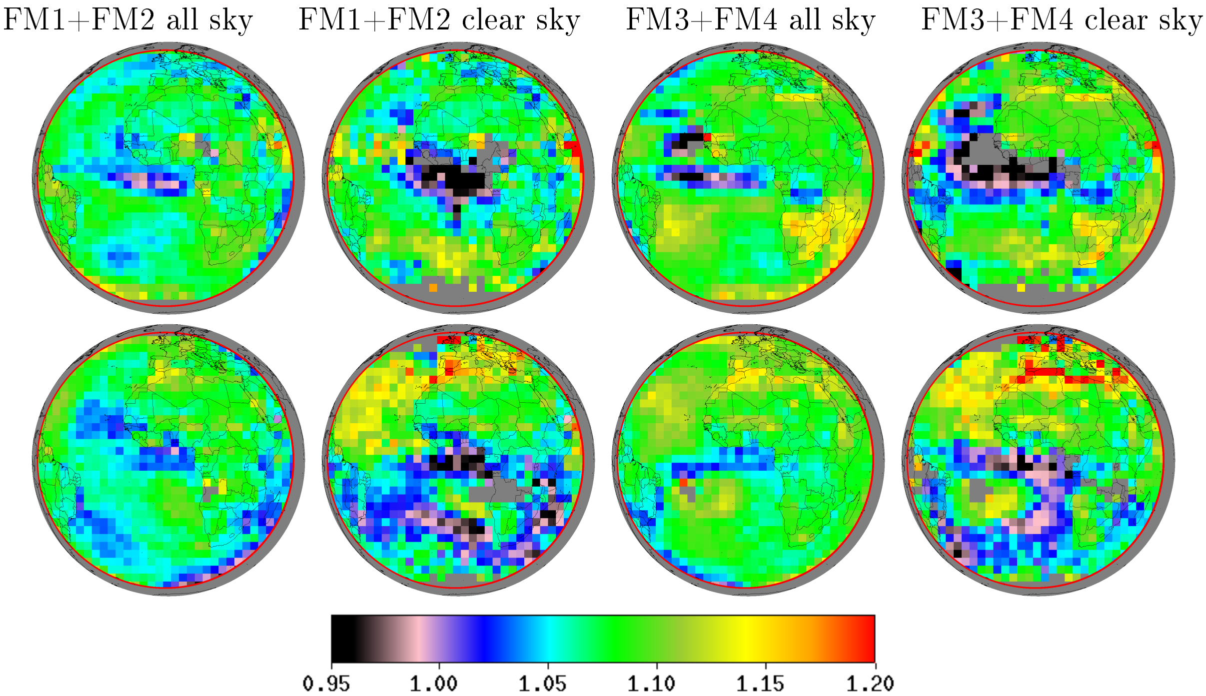

Figure 6.3: GERB (BARG)/CERES SW flux ratio for (FM1+FM2) and (FM3+FM4) in clear sky and all sky condition. Upper panels are for June 2004 and lower ones for December 2004.

6.6 Discussion

This chapter presents the radiance–to–flux conversion method implemented for the GERB SW channel. The method relies on an accurate SEVIRI–based scene identification that allows selecting the most–adequate anisotropy model among the CERES–TRMM ADMs set. As well the scene identification, the angular models, and the manner they are selected and applied, are potential sources of error for the resulting GERB fluxes.

An overall validation of the whole scheme, namely the comparison with collocated SW fluxes provided by the CERES instruments, has been done. Most of the difference observed between the GERB and CERES SW fluxes is explained by a multiplicative factor: the GERB fluxes are about 7.5% higher than the CERES ones. However, a large part of this difference is already present at the radiance level, although to a slightly lower value of 6%. When analyzed at regional scale, the GERB/CERES ratio shows a series of local patterns. Investigations have been carried out and explanations have been proposed for the most obvious of them. The underlying reason for some of these patterns lies at the level of the scene identification. For instance, there is no detection of the snow coverage in the current scheme. Other patterns come from the angular model, the most obvious one is observed in the sun glint region over clear ocean.

It is worth noting that the GERB/CERES comparisons reported in this chapter are only possible at the time of CERES overpass (10:30 and 13:30 solar time). Therefore, the validation does not cover the full diurnal cycle and sun–Earth–satellite geometries. Another validation technique for the radiance–to–flux conversion consists in the comparison of the GERB fluxes taken at identical solar zenith angle during the morning and the afternoon. If the cloudiness does not change during the day, the fluxes are expected to be the same. When applied to the pre–release GERB fluxes, the method highlighted significant morning/afternoon asymmetry (Bertrand *et al.*, 2006b). It has not yet been investigated if a similar problem affects the Edition 1 fluxes and, if it is the case, to what extent.

A series of improvements are foreseen for the Edition 2 that should improve the GERB/CERES agreement. Before release, similar GERB/CERES comparisons as those described in Section 6.5 must be done to check that the improvement objectives are reached. In turn, this could make apparent new (hopefully minor) problems affecting the Edition 2 GERB SW fluxes.

Chapter 7

Angular modeling of the emitted thermal radiation

7.1 Introduction

Although the emission of thermal radiation is nearly Lambertian for most of the natural materials, a number of effects makes the TOA longwave radiance field anisotropic. The main factors governing this anisotropy are discussed in Section 7.2.

A preliminary study of the correlation between the angular and spectral behaviors of the LW radiation has been published in (Clerbaux *et al.*, 2003c). This work, summarized in Section 7.3, involves the following steps: (i) the generation of a realistic set of Earth–atmosphere conditions, (ii) the radiative transfer computations with sufficient spectral and angular resolutions to simulate the TOA radiance field in its spectral and angular properties, (iii) the computation of the anisotropy factor R and corresponding NB radiances $\{L_{nb}\}$ through spectral convolution, (iv) finally, regressions are fitted to estimate the anisotropy R from the NB radiances.

This approach is followed for the Edition 1 GERB LW radiance–to–flux conversion. In this case, the NB measurements are provided by a subset of 4 thermal channels of SEVIRI. The method is discussed in Section 7.4. Like the radiances and the SW fluxes, the GERB LW fluxes have been validated by comparison with CERES as reported in Section 7.5. The comparisons highlight several limitations of the method. The main one concerns the angular conversion for cloudy scenes which is discussed under Section 7.6. A method is proposed for reducing the magnitude of the problem in Edition 2. In Section 7.7, the assumption of azimuthal isotropy of the infrared radiance is addressed using CERES data in RAPS mode. It is shown that significant azimuthal effects occur over mountainous areas. In case of geostationary observation, this leads more easily than for polar observation to regional biases in the field–of–view (Clerbaux *et al.*, 2003d). Section 7.8 concludes this last part of the work.

7.2 Main sources of anisotropy

Most of the TOA anisotropy originates from the temperature difference between the Earth surface and the atmospheric constituents and clouds. For this reason, higher anisotropy is in general observed during daytime and in the Tropics. The main sources of anisotropy are:

The **atmospheric profiles** of temperature and humidity, as well as the profiles of other absorbers like CO_2 and O_3. The water vapor is by far the highest absorber in the infrared and therefore the main source of limb darkening. However, the effect is highly related to the altitude where the absorption takes place: the boundary layer humidity does not act as strongly as in the upper troposphere. Concerning the ozone, as it is mainly located in the stratosphere, it may introduce limb–brightening at its absorbing wavelengths.

The **surface skin temperature** drives the emission by the surface. This temperature can depart significantly from the temperature in the lower atmospheric profile level due to surface warming during daytime. This is the source of the enhanced anisotropy observed over hot desert regions during the afternoon. Connected to this is the azimuthal anisotropy introduced by solar warming, for example in mountainous areas (Clerbaux *et al.*, 2003d) or vegetation (Otterman *et al.*, 1995).

The height of the **cloud layer** and its infrared transparency (i.e. the cloud emissivity). For an optically thick cloud the anisotropy usually decreases with the height of the cloud top. The difference of temperature between the cloud top and the atmosphere above this top is indeed reduced. On the other hand, the opposite behavior is observed for **semi–transparent clouds**. The highest anisotropy is observed for cloud with visible optical depth $\tau \sim 1.5$ located close to the tropopause (Clerbaux *et al.*, 2003c).

Enhanced anisotropy is also observed for **broken cloud** fields (Duvel & Kandel, 1984; Naber & Weinman, 1984). The highest anisotropy is observed for aspect ratio (height/width) close to 1. In this case, Naber & Weinman (1984) reports a difference of brightness temperature of 7K between the observations at VZA $= 0°$ and $50°$. However, the difference decreases quickly at lower aspect ratio (e.g. $\Delta T = 2$K for aspect ratio of 0.5). In practice, most of the broken cloud fields have aspect ratio of about 0.1, except the small cumulus in the trade-wind zones (Stubenrauch *et al.*, 1993).

A part of the TOA anisotropy can result from **3–dimensional effects at the surface**. This is the case for example when 2 constituting elements of the surface do not have equal temperature. Otterman *et al.* (1997) reports the case of a forest with trees free of snow while the ground is snow covered. When illuminated by the sun, the trees become warmer than the ground and this induces limb brightening (at least at the surface level).

The **ocean emissivity** is close to 1 but presents a rapid decrease at grazing observation angle, especially for calm sea state. At these angles, the water surface reflects the downward infrared radiation.

The **desert dust cloud** is often semi–transparent to the infrared radiation and could therefore enhance the anisotropy in a similar way as the cirrus clouds. However, as these desert aerosols are usually located in the lower part of the troposphere, the temperature difference with the surface is much smaller than for the cirrus. Angular modeling in case of desert dust cloud has been addressed theoretically by Helen Brindley who reported acceptable results of the GERB LW ADM in case of dust cloud (Helen Brindley, pers. comm.).

7.3 Angular modeling using spectral information

7.3.1 Introduction

This section summarizes a paper (Clerbaux *et al.*, 2003c) published in *Remote Sensing of Environment*. The study analyzes how spectral information can be used to improve the radiance–to–flux conversion of broadband longwave radiance measurements. Such an improvement is possible if and only if a correlation exists between the spectral and the angular behaviors of the radiation field.

7.3.2 Methodology

To address the correlation between the spectral signature $L(\lambda)$ and the anisotropy $R(\mathrm{VZA})$, a database of spectral radiance fields $L(\mathrm{VZA}, \lambda)$ was built as described under Section 5.3.

Figure 7.1 shows the scatterplots of the anisotropy factor R versus the thermal radiance L for the 4622 elements in the database for nadir, oblique and grazing angles of observation. The scatterplot at $\mathrm{VZA} = 0°$ (top) shows that, in average, the anisotropy factor at nadir increases linearly with the radiance L. This illustrates the increase of anisotropy for increasing surface temperature. The strong anisotropy observed over semi–transparent cold clouds is clearly visible in this figure. This scatterplot shows that, even using a plane–parallel radiative transfer model like SBDART, it is possible to generate TOA radiance fields with large dispersion in terms of anisotropy. The scatterplot at $\mathrm{VZA} = 50°$ (middle) indicates that, for this angle of observation, the R values are close to 1 and there is little dispersion of the anisotropy factor values. At $\mathrm{VZA} \sim 52°$ (not shown) an even smaller dispersion is simulated. Such a result was reported in numerous theoretical studies (Otterman *et al.*, 1997; Stubenrauch *et al.*, 1993) and also directly from satellite observations as in the ERBE models (Suttles *et al.*, 1989). The oblique observation permits an easy and accurate estimation of the thermal flux. This is the main reason why the BB radiometer on the future EarthCARE mission will perform forward and backward observations at $\mathrm{VZA} \sim 55°$, in addition to the nadir observation. At grazing observation angle ($\mathrm{VZA} = 75°$, bottom), the R values are usually lower than 1 and they decrease at increasing radiance L.

Since SBDART is a plane–parallel RTM, the simulations represent neither the anisotropy due to structured surfaces (Otterman *et al.*, 1995) nor the anisotropy due to broken cloud fields (Duvel & Kandel, 1984; Naber & Weinman, 1984). On the other hand, the database is representative of the anisotropy due to the surface temperature, the atmospheric constituents, and the stratiform cloudiness, including the strong anisotropy of high semi–transparent clouds (cirrus).

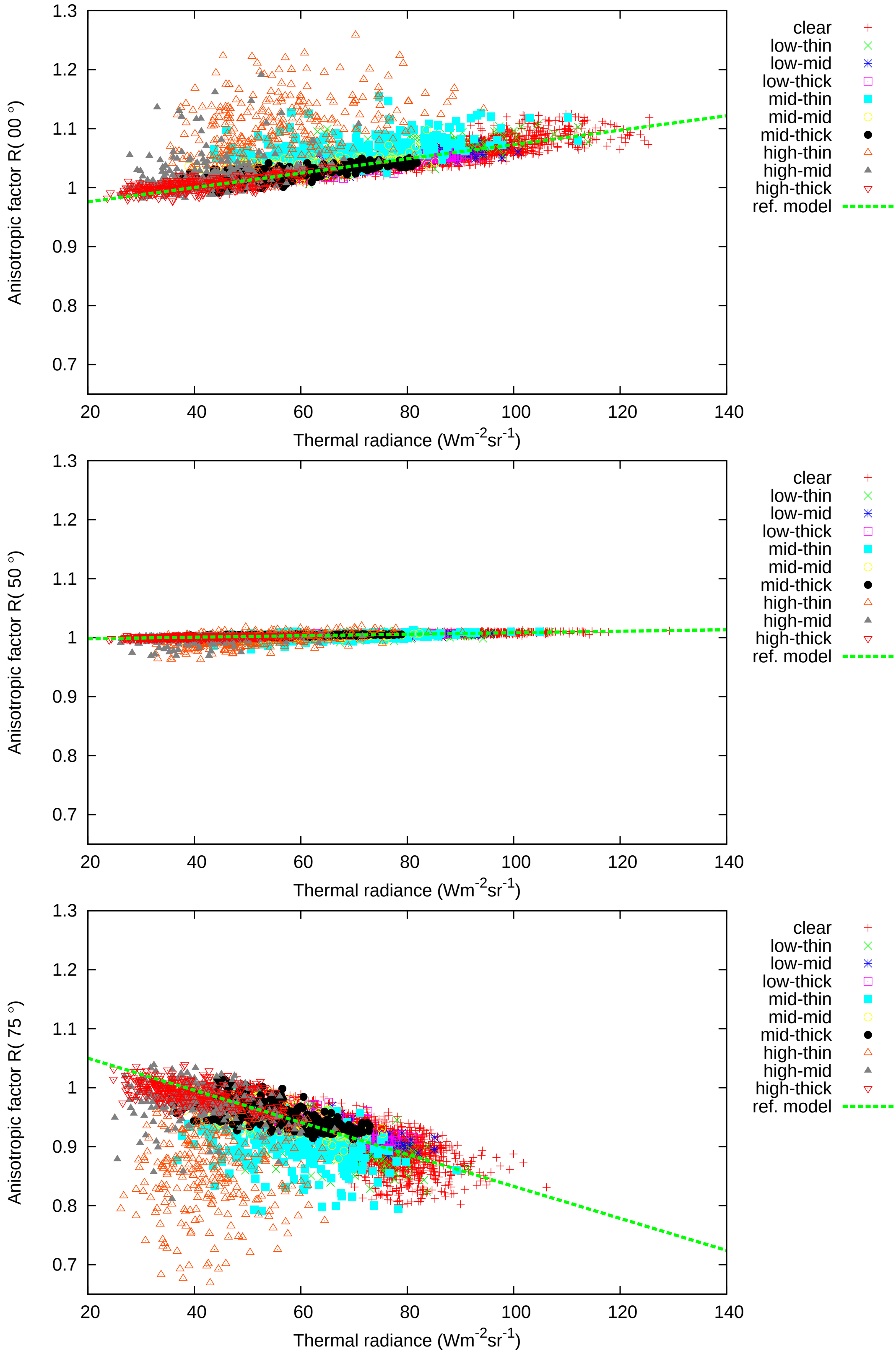

Figure 7.1: Scatterplots of the anisotropy factor R versus the thermal radiance L at 3 observation angles: VZA = 0° (top), VZA = 50° (middle), and VZA = 75° (bottom). The 4622 simulated scenes are displayed with symbols according to the ISCCP cloud classification (Rossow & Schiffer, 1999).

From the simulations, the NB radiances are easily estimated by spectral convolution with the spectral response curves of the instruments using Eq.(5.1). Measurement of NB radiance is usually done with instruments with poorer calibration than the BB measurement. For this reason, the NB radiances L_{nb} are altered in this study by adding a random calibration error with a Gaussian distribution that has a standard deviation of $\eta = 2\%$ of the average signal in the channel. This value was chosen as typical for a state–of–the–art imager (Pili, 2000a).

The database is split in two equal parts of 2311 elements. Half of the data is used to fit the models (i.e. parameterize the regressions) while the second half is used to evaluate the performances of these models. To this end, the root mean square (rms) error which is introduced in the flux by the radiance–to–flux conversion is evaluated.

Firstly, a simple non–spectral model of the anisotropy is analyzed. Its performance is used as a reference to quantify the improvement obtained when using spectral information. Secondly, models of the anisotropy using spectral information in the form of a single NB radiance are presented and evaluated. Finally, we will discuss models based on multiple NB measurements.

7.3.3 Non–spectral model (reference model)

From the different scatterplots of Figure 7.1, a simple model for the anisotropy takes the linear form

$$R(\mathrm{VZA}, L) = c_0(\mathrm{VZA}) + c_1(\mathrm{VZA})\ L(\mathrm{VZA}). \tag{7.1}$$

For each viewing zenith angle VZA $= \{0°, 5°, 10°, ..., 85°\}$, the model is fit to the database and the rms error is evaluated. The best fits are drawn on the scatterplots of Figure 7.1 and the variation of the error according to the VZA is given in Figure 7.2. This figure shows a local maximum of the error at nadir which appears as the worst observation angle within the $0° - 65°$ VZA range. For this reason, our analysis is restricted to the nadir observation angle. If the radiance–to–flux conversion can be improved at nadir using spectral information, we expect that similar improvements could be obtained for viewing angles in the $0° - 65°$ VZA range. For nadir observation, the non–spectral model (Eq.7.1) leads to a TOA flux error of $4.63\mathrm{Wm}^{-2}$ (2.2%). In the following parts of the study, this value will be used as a reference to quantify the improvement obtained using spectral information.

7.3.4 Models using spectral information from one NB measurement

Radiance–to–flux conversion using information from a single NB radiance is of interest since the Earth observing BB radiometers often have a single NB window channel in addition to

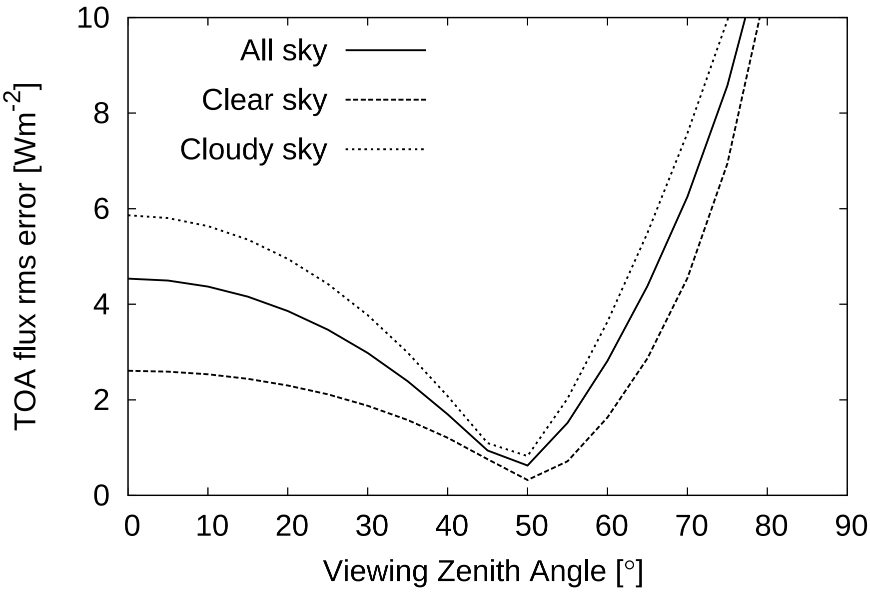

Figure 7.2: Radiance–to–flux conversion error versus the VZA for the non–spectral model (Eq.7.1). The curves give the performances in all sky, clear sky and cloudy sky.

their BB channels. This is the case for the ScaRaB (window channel $10.5 - 12.5$ μm) and CERES (window channel $8 - 12$ μm) instruments. These channels are not designed to help in the radiance–to–flux conversion but rather to supplement the broadband measurement in better understanding the underlying physics (e.g. greenhouse effect).

For the ScaRaB thermal radiance–to–flux conversion, Stubenrauch *et al.* (1993) introduce the concept of atmospheric "pseudoabsorptance"

$$A(\text{VZA}) = 1 - \frac{L(\text{VZA})}{\frac{\sigma}{\pi} T_B(\text{VZA})^4} \tag{7.2}$$

where σ is the Stefan–Boltzmann constant, T_B is the brightness temperature in the window channel of ScaRaB, and L is the BB unfiltered radiance. Using a database of spectral radiance fields generated with the LOWTRAN–7 RTM, Stubenrauch *et al.* (1993) suggested the following analytical form to estimate the BB anisotropy factor

$$R(\text{VZA}) = 1 + (0.55 - e^{-\cos(\text{VZA})}) A(\text{VZA}) \tag{7.3}$$

This method was not used for the operational ScaRaB data processing, the ERBE models have been preferred for the sake of consistency. The performances of the Stubenrauch approach are addressed as a function of the wavelength of the NB channel. To this end, the NB radiance L_{nb} is estimated using Eq.(5.1) with a narrow ($\Delta\lambda = 0.1$ μm) rectangular filter $\phi(\lambda)$ centered at increasing wavelength. The NB radiance is then converted into brightness temperature T_B and the "pseudoabsorptance" is estimated with Eq.(7.2).

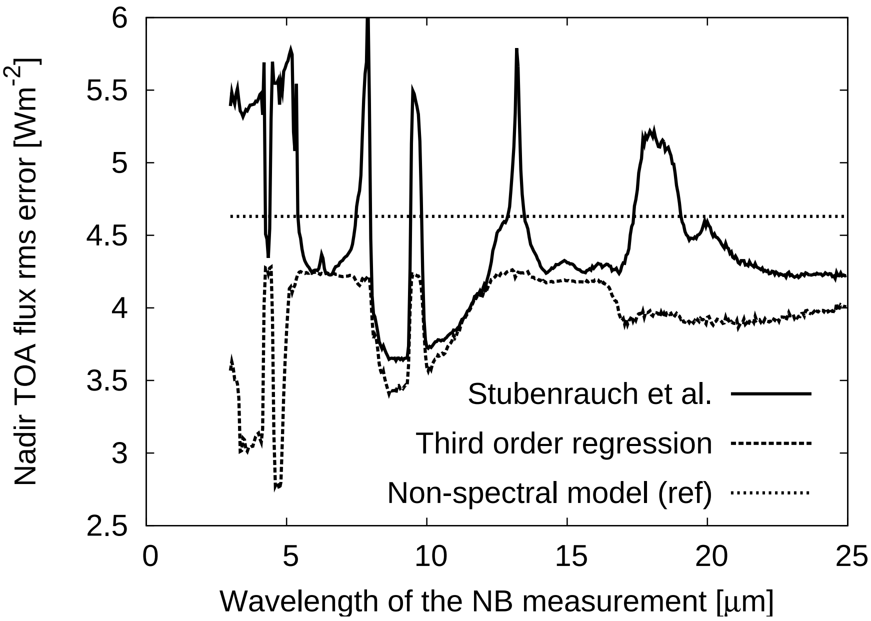

Figure 7.3: Radiance–to–flux conversion error at nadir for the: non–spectral model (Eq.7.1), the "pseudoabsorptance" regression (Eq.7.4) and the third order regression (Eq.7.5). The error is dependent on the wavelength of the NB measurement.

A generalization of the Eq.(7.3) is then used to estimate the anisotropy at nadir

$$R(0°) = c_o + c_1 A(0°) \tag{7.4}$$

where the best fit coefficients c_0 and c_1 depend on the wavelength of the NB measurement. The solid–line curve in Figure 7.3 gives the rms error when the Eq.(7.4) is used according to the wavelength used to estimate the "pseudoabsorptance" (the horizontal line at 4.6Wm^{-2} corresponds to the non–spectral model). The figure shows that the best performance is obtained with a NB measurement done in the atmospheric transmission window. Within the main window ($8 - 12$ μm), the short wavelengths give the best result. The minimal error (3.65Wm^{-2} or 1.73%) is observed at $\lambda = 8.6\mu$m. In regard to the non–spectral model, this is a reduction of the error of about 20%.

By–passing of the conversion to "pseudoabsorptance" allows to obtain a slightly better radiance–to–flux conversion. To show this, the anisotropy factor at nadir is estimated directly as a third order regression on the BB and NB radiances

$$\begin{aligned} R(0°) = \quad & c_0 + c_1 L + c_2 L_{nb} + c_3 L^2 + c_4 L L_{nb} + c_5 L_{nb}^2 + \\ & c_6 L^3 + c_7 L^2 L_{nb} + c_8 L L_{nb}^2 + c_9 L_{nb}^3. \end{aligned} \tag{7.5}$$

This form is used as a general non-linear fit without any physical meaning for the regression coefficients. The performance of this model according to the wavelength of the NB measurement

channel	type	rms error Wm^{-2} (%)
$3.9\mu m$	WIN	3.09 (1.47)
$6.2\mu m$	WV	4.23 (2.01)
$7.3\mu m$	WV	4.21 (2.00)
$8.7\mu m$	WIN	3.43 (1.63)
$9.7\mu m$	O_3	4.21 (2.00)
$10.8\mu m$	WIN	3.76 (1.79)
$12.0\mu m$	WIN	4.10 (1.95)
$13.4\mu m$	CO_2	4.26 (2.02)

Table 7.1: Radiance–to–flux conversion rms error at nadir when the anisotropy factor is estimated using the third order regression (Eq.7.5) on the BB radiance and one of the 8 SEVIRI thermal radiances.

is displayed in Figure 7.3. As for the Stubenrauch model, the best performance is obtained in the atmospheric windows. Close to 12 μm the performances of the 2 models are similar but at shorter wavelength the third order regression presents a significant improvement compared to the Stubenrauch approach based on the "pseudoabsorptance". Discarding the $\lambda < 5$ μm region, the best performance (rms error of $3.41 Wm^{-2}$ or 1.62%) is observed at the same wavelength $\lambda = 8.6$ μm as for the "pseudoabsorptance". Here, the improvement is about one quarter with respect to the non–spectral model. NB radiance at $\lambda < 5$ μm can be used provided that it only contains thermal radiation. The narrow wavelength interval $4.6\mu m - 4.9\mu m$ (located between the CO_2 and WV absorption bands in Figure 5.1) appears to be very informative for the radiance–to–flux conversion (rms error of $2.76 Wm^{-2}$ or 1.31%). On the other side of the CO_2 absorption peak ($\lambda < 4.2\mu m$), the radiance–to–flux conversion error is about $3.01 Wm^{-2}$ (1.43%).

Eqs. (7.4) and (7.5) are evaluated for narrow ($\Delta\lambda = 0.1\mu m$) rectangular spectral filters. Table 7.1 gives the rms error of the third order regression (Eq.7.5) when L_{nb} is provided by one of the 8 SEVIRI thermal channels. The errors in Table 7.1 agree with Figure 7.3, therefore the width of the NB measurement seems not to impact on the spectral information.

The previous results were obtained under the assumption that the NB measurements are contaminated with a typical 2% Gaussian noise level. Figure 7.4 shows a strong dependency on the angular conversion error according to the noise level when the third order regression (Eq.7.5) is used. To obtain a significant spectral improvement, the NB measurement(s) must be done with a relatively well–calibrated device. In practice, for NB thermal measurements from weather satellites, a noise level/calibration error below $\eta = 2$ % can be expected.

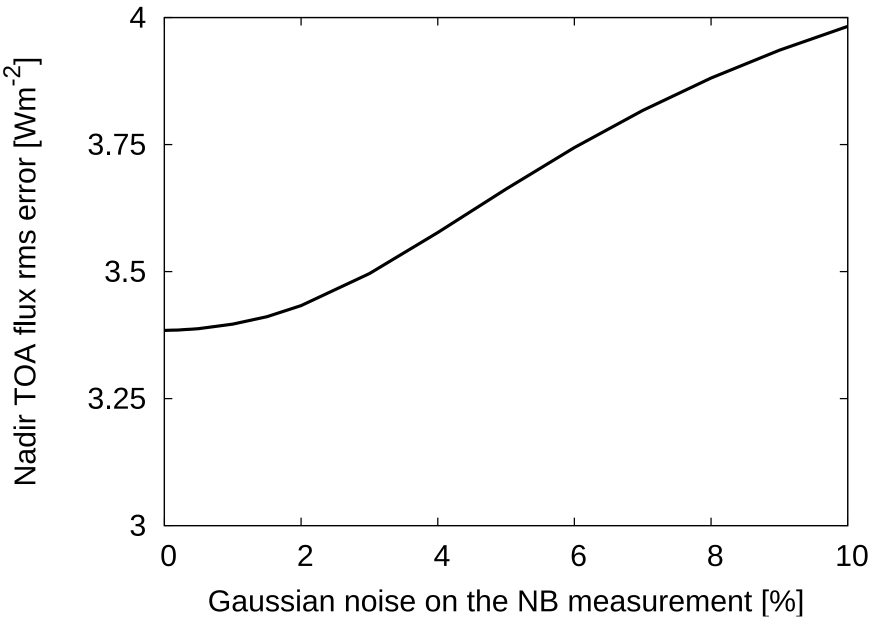

Figure 7.4: Radiance–to–flux conversion error at nadir versus the noise level on the SEVIRI 8.7μm measurement when the AEF at nadir is estimated using the 3th order regression (Eq.7.5).

7.3.5 Models involving multiple NB measurements

The improvement in the radiance–to–flux conversion is analyzed when information about the spectral signature $L(\lambda)$ is available through a set of NB measurements $\{L_{nb}\}$. This is done for 3 different cases of spectral information: the one provided by the SEVIRI, the one provided by MODIS, and the one available when the entire spectral signature $L(\lambda)$ is known (case of a spectrometer like IASI). Here, the large number of NB measurements (8 for SEVIRI, 16 for MODIS and 431 for the spectrometer) impedes a direct use of these measurements in high order regressions. For instance, a third order regression on the 16 thermal radiances of MODIS contains about a thousand coefficients. For this reason, the spectral information is first projected using the Principal Components Analysis (PCA) and the anisotropy models are built as regressions on a restricted set of components. This is just a linear transformation of the $\{L_{nb}\}$ set that facilitates the exploitation of the same spectral information using a restricted number of input quantities in the regressions. The radiance–to–flux conversion error is not modified by such transformation.

The SEVIRI case is of interest because the instrument is used during the radiance–to–flux conversion for the GERB data. Here, the anisotropy factor is dependent on the BB radiance L and on the 8 NB SEVIRI thermal radiances. These NB radiances were converted into 8 components $\{c_i\}$ using the PCA and the model of the anisotropy takes the form $R(\text{VZA}) = R(\text{VZA}, L, c_1, c_2, ..., c_8)$. The estimation of the anisotropy factor at nadir $R(0°)$ has been analyzed for different regression orders and for increasing numbers N of coefficients $\{c_i\} = \{c_1, c_2, ..., c_N\}$. The minimal radiance–to–flux conversion error (2.65Wm^{-2} or 1.26%) is observed with a second order regression on the BB radiance L and the first $N = 7$ components

$\{c_i\}$. The spectral signature provided by the SEVIRI instrument enables reducing the radiance–to–flux conversion error by about 43% compared to the non–spectral model. Discarding the SEVIRI window channel at 3.9 μm (due to possible daytime contamination by solar radiation), the error is only a slightly higher (2.76Wm^{-2} or 1.31%).

The MODIS case is of interest because this spectral information might be used for the CERES data processing. The MODIS imager provides 16 NB measurements in the thermal part of the spectrum. The best radiance–to–flux conversion at nadir (with an error of 2.48Wm^{-2} or 1.17%) is observed using a third order regression on the BB radiance and the first $N = 5$ components $\{c_i\}$. Despite the fact that MODIS has twice as many channels as SEVIRI, the improvement in the spectral conversion is quite limited. The underlying reason is that MODIS provides measurements in the same parts of the thermal spectrum as SEVIRI.

Finally, the database also permits to investigate the improvement that can be obtained when the full spectral signature $L(\lambda)$ is known. This case study is of interest because it places a theoretical limit on the improvements using spectral information and also because infrared spectrometers are planned to fly in some future Earth observation missions, for instance the Fourier Transform Spectrometer of the ESA Earth Explorers EarthCARE mission. The analysis is performed in a similar manner as for SEVIRI and MODIS. The instrument is supposed to provide 431 narrow radiance measurements between 2.5 and 100μm. The need to project the spectral signature $L(\lambda)$ on the principal component axes is obvious as it is impossible to deal with high order regressions on such a large number of input quantities. The best radiance–to–flux conversion is obtained using a second order regression on the first $N = 13$ EOFs. In this case, the angular conversion error for nadir observation reaches 2.12W m^{-2} (or 1%), which is just below the half of the error of the non–spectral model.

7.3.6 Discussion

The possibility to improve the radiance–to–flux conversion for BB thermal radiation using spectral information is addressed. This work is based on a database of spectral radiance fields $L(\text{VZA}, \lambda)$ at the TOA. As the RTM used to build up the database is a plane–parallel model, it is not possible to deal with the anisotropy due to broken cloud fields or structured surface. Nevertheless, the database is representative of the others sources of anisotropy, including the strong anisotropy observed for semi–transparent cirrus clouds.

Different case studies have outlined a weak correlation between spectral signature $L(\lambda)$ and angular behavior $L(\text{VZA})$ for the thermal radiation field. This weak correlation can be exploited to improve the conversion into fluxes of the thermal radiances measured by BB radiometers like CERES, ScaRaB or GERB. The improvement is quantified according to a simple non–spectral radiance–to–flux conversion model. It depends on the number, the kind and the accuracy of the spectral measurements. The use of a single NB measurement as spectral information should be done in an atmospheric transmission window and at the shortest possible wavelength. The exploitation of spectral signature from multi-channel imagers like SEVIRI or MODIS permits a reduction of the error of about 45%. When the entire thermal spectrum $L(\lambda)$ is known, the analysis shows a possible reduction of the radiance–to–flux conversion error up to about 55 %. In the case of nadir observation, this corresponds to a reduction of the radiance–to–flux conversion error of 1.98Wm^{-2} (SEVIRI) and 2.51Wm^{-2} (entire spectrum).

Obviously the spectral information is not the only variable that can be exploited to obtain accurate thermal fluxes at the TOA from BB radiance measurements. All information about the surface temperature, the atmospheric profiles (T, WV and other greenhouse gas concentrations) and about the cloud cover is useful to characterize the TOA anisotropy and hence to improve the accuracy of the inferred thermal flux.

Another important point is that, for this early analysis, the LW anisotropy model relies on a single regression valid for all scene types. At a later stage, it became evident that better performances could be obtained by using dedicated regressions according to scene types. This requires a scene identification that works also during nighttime (See Section 7.6).

7.4 Edition 1 GERB LW ADMs

Contrary to the SW radiation, the GERB thermal flux is not estimated via the CERES–TRMM empirical models but rather through a spectral model based on the SEVIRI NB measurements. This choice is motivated by the complexity of the development of a cloud retrieval that works during nighttime. The model is based on the work presented in the previous section and on the radiative transfer simulations presented in Section 5.3. At a given VZA, the anisotropy factor R is estimated as a second order regression on the 7 SEVIRI thermal radiances

$$R(\text{VZA}) = R(\text{VZA}, L_{6.2}, L_{7.3}, L_{8.7}, L_{9.7}, L_{10.8}, L_{12}, L_{13.4}) \tag{7.6}$$

The 3.9μm channel is not considered here due to its daytime solar contamination. This model has been applied to generate the pre–released GERB data. Validation activities, as the comparisons with CERES presented in the next section, have pointed out 2 main shortcomings.

Firstly, the Eq.(7.6) underestimates the anisotropy over hot desert surface. Detailed analysis of the problem showed that it is due to the lower surface emissivity in the $L_{7.3}$, $L_{8.7}$ and $L_{9.7}$ channels. As a rapid fix for the Edition 1 data release, it was therefore decided not to use those channels in the regression. The regression takes therefore the form

$$R(\text{VZA}) = R(\text{VZA}, L_{6.2}, L_{10.8}, L_{12}, L_{13.4}) \tag{7.7}$$

Secondly, due to the presence of high semi–transparent clouds, the model underestimates the anisotropy in the tropical convective region. In Section 7.6 it is shown that the problem can be solved by the development of a dedicated anisotropy model for this kind of cloudiness. This improvement was however not included in the Edition 1 GERB processing.

The effect of error in SEVIRI channel intercalibration is evaluated by simulating calibration changes of +/-5% for the 4 channels used in Eq.(7.7). In the worst case (+5% for IR 10.8μm and -5% for the other channels), the RMS difference and bias in estimated thermal flux are just less than 1Wm^{-2}. Similarly, the effect of the change from SEVIRI spectral to effective radiances has been quantified. The change introduces an increase of the residual limb darkening of the GERB thermal fluxes by about 0.2% (see Section 3.2.3).

7.5 GERB LW flux comparison with CERES

Table 7.2 summarizes the LW flux comparisons in a similar form to the one given in Table 5.3 for the LW radiance. The GERB/CERES flux ratio in all sky conditions lies between $m = 0.983$ (FM4) and $m = 0.992$ (FM2). The average across the 4 CERES instruments is $m = 0.987$ which is in line with the radiance comparison. Just as for the shortwave, the compliance is better with the FM1 and FM2 than with the FM3 and FM4. All together, the GERB LW flux appears to be about 1.3% lower than the CERES LW flux ($m = 0.987$). Similarly to all the previous comparisons, the difference between the clear and cloudy GERB/CERES ratios is higher for the ARG (1.7%) than for the BARG (0.3%) and HR (0.1%) formats.

The third and fourth columns in Figure 7.5 show the flux ratio in all sky and clear sky conditions respectively. In clear sky conditions, there is no obvious problem affecting the GERB fluxes at the regional scale, at least for GERB VZA lower than 70° (red circle). On the other hand, the all sky plots give further evidence of GERB LW flux error over cloudy scenes. This problem was already reported by Dewitte *et al.* (2008). The GERB LW radiance–to–flux conversion does not fully compensate for the limb darkening associated with high level clouds. A similar radiance–to–flux conversion error is suspected in case of aerosol (Ali Bahmal, pers. comm.).

Averaged Rectified Geolocated (ARG)							
Scene Type	FM1	FM2	FM3	FM4	$<$ FM $>$	$< F_g >$	ΔF
All sky	0.988 ± 0.001	0.992 ± 0.001	0.986 ± 0.001	0.983 ± 0.001	0.987	257.35	-3.28
June	0.987 ± 0.001	0.992 ± 0.001	0.987 ± 0.001	0.984 ± 0.001	0.988	263.96	-3.34
December	0.989 ± 0.001	0.992 ± 0.001	0.986 ± 0.001	0.982 ± 0.001	0.987	250.94	-3.22
Day	0.992 ± 0.001	0.994 ± 0.001	0.988 ± 0.001	0.983 ± 0.001	0.989	262.63	-2.86
Night	0.983 ± 0.001	0.990 ± 0.001	0.985 ± 0.001	0.984 ± 0.001	0.986	251.87	-3.71
Clear sky	0.982 ± 0.001	0.990 ± 0.001	0.982 ± 0.001	0.979 ± 0.001	0.983	291.98	-4.99
Cloudy	1.003 ± 0.001	1.001 ± 0.001	1.000 ± 0.002	0.995 ± 0.001	1.000	204.56	-0.01
Binned Averaged Rectified Geolocated (BARG)							
Scene Type	FM1	FM2	FM3	FM4	$<$ FM $>$	$< F_g >$	ΔF
All sky	0.988 ± 0.001	0.992 ± 0.001	0.987 ± 0.001	0.983 ± 0.001	0.987	257.20	-3.26
June	0.987 ± 0.001	0.992 ± 0.001	0.987 ± 0.001	0.984 ± 0.001	0.987	263.76	-3.35
December	0.989 ± 0.001	0.992 ± 0.001	0.986 ± 0.001	0.983 ± 0.001	0.987	250.83	-3.18
Day	0.992 ± 0.001	0.994 ± 0.001	0.988 ± 0.001	0.983 ± 0.001	0.989	262.56	-2.85
Night	0.983 ± 0.001	0.990 ± 0.001	0.985 ± 0.001	0.984 ± 0.001	0.986	251.89	-3.67
Clear sky	0.984 ± 0.001	0.991 ± 0.001	0.984 ± 0.001	0.981 ± 0.001	0.985	292.12	-4.51
Cloudy	0.991 ± 0.001	0.990 ± 0.001	0.989 ± 0.002	0.983 ± 0.002	0.988	202.02	-2.38
High Resolution (HR)							
Scene Type	FM1	FM2	FM3	FM4	$<$ FM $>$	$< F_g >$	ΔF
All sky	0.985 ± 0.001	0.989 ± 0.001	0.983 ± 0.001	0.981 ± 0.001	0.984	255.37	-4.03
June	0.984 ± 0.001	0.989 ± 0.001	0.984 ± 0.001	0.982 ± 0.001	0.985	262.42	-4.03
December	0.985 ± 0.001	0.989 ± 0.001	0.982 ± 0.001	0.980 ± 0.001	0.984	248.52	-4.04
Day	0.989 ± 0.001	0.991 ± 0.001	0.984 ± 0.001	0.980 ± 0.001	0.986	260.51	-3.71
Night	0.981 ± 0.001	0.987 ± 0.001	0.982 ± 0.001	0.981 ± 0.001	0.983	250.27	-4.37
Clear sky	0.981 ± 0.001	0.989 ± 0.001	0.981 ± 0.001	0.979 ± 0.001	0.983	290.66	-5.15
Cloudy	0.985 ± 0.001	0.983 ± 0.001	0.981 ± 0.001	0.978 ± 0.001	0.982	205.39	-3.85

Table 7.2: GERB/CERES LW flux ratio m and uncertainty. The last columns give the average GERB LW flux $< F_g >$ and the difference between the average GERB and CERES LW flux $\Delta F =< F_g > - < F_c >$ both in Wm^{-2}.

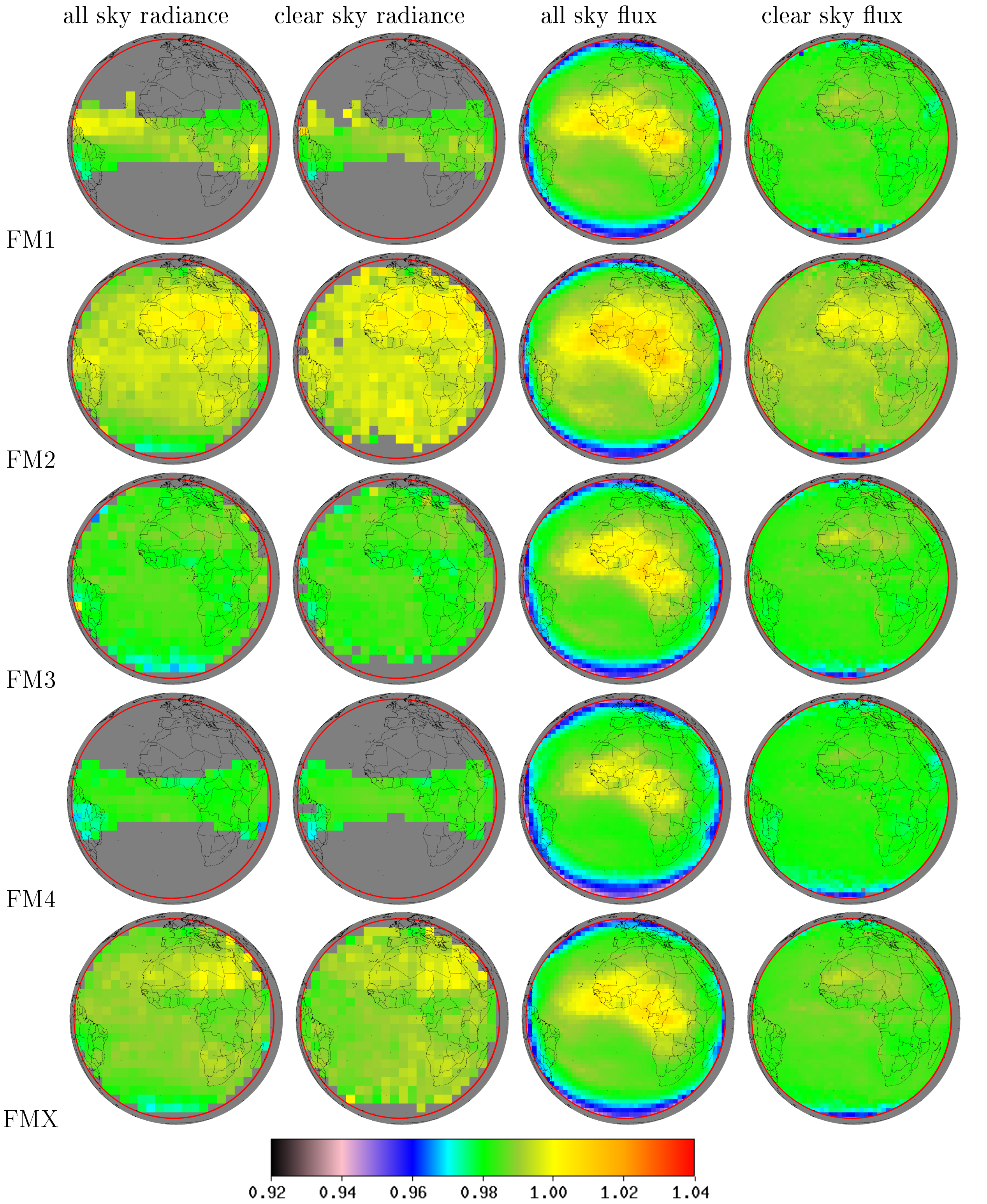

Figure 7.5: GERB (BARG)/CERES LW ratio for the different CERES instruments and altogether (FMX). The red circle indicates VZA = 70°.

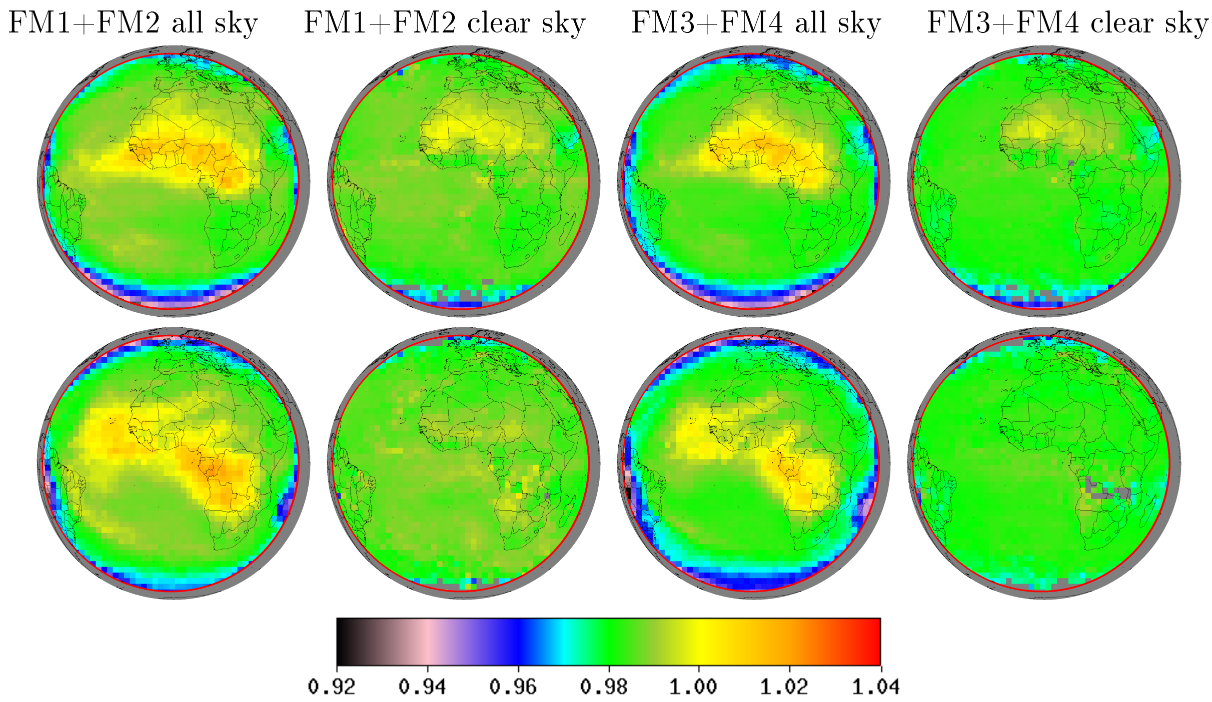

Figure 7.6: GERB (BARG)/CERES LW flux ratio for (FM1+FM2) and (FM3+FM4) in clear sky and all sky condition. Upper panels are for June 2004 and lower ones for December 2004.

This is the cause of the high ratio observed for viewing angles close to nadir (center of the disk) and the lower ratio on the borders of the disk. As expected, the lowest errors are associated with viewing zenith angles close to VZA $\sim 52°$ due to the near independence of the anisotropy on the scene type around this angle (Otterman *et al.*, 1997).

Although the observation angle is favorable (VZA $\sim 55°$), an increase of the GERB/CERES ratio is observed over the Alps in clear sky conditions. Compared to the surrounding area there is a local increase of the LW flux ratio of about 1%. This is an effect of azimuthal anisotropy which is not taken into account in the GERB LW radiance–to–flux conversion. Due to its geostationary orbit the GERB instrument mainly measures radiance emitted by the south faces of the mountains in the northern hemisphere (and the opposite in the southern hemisphere). This could introduce small bias as south faces present higher temperatures than north faces (Clerbaux *et al.*, 2003d).

7.6 Anisotropy of high semi-transparent clouds

High semi–transparent clouds affect strongly the LW anisotropy. The effect increases with the cloud height and is maximum for cloud with visible optical depth of about $\tau \sim 1.5$. Theoretical studies (Section 7.3), as well as the comparison with CERES (Section 7.5), show that a single regression can not successfully simulate the strong anisotropy for semi–transparent cirrus clouds. As proposed in the technical note (TN39), a rough detection of this kind of cloudiness is obtained by the difference of brightness temperature in the 10.8μm and 12.0μm SEVIRI channels. The following simple test is used to detect the high semi-transparent clouds

$$\begin{aligned} T_{10.8\mu\mathrm{m}} &< T_{max} \\ T_{10.8\mu\mathrm{m}} - T_{12\mu\mathrm{m}} &> \Delta T_{min} \end{aligned} \tag{7.8}$$

The thresholds T_{max} and ΔT_{min} are given in (TN39). They depend on the VZA and are estimated on the database of simulations in such a way that the number of selected clouds is 10% of the total number of cloudy simulations (i.e. 229). Figure 7.7 (right) illustrates this simple detection of high semi-transparent clouds. The Eqs. (7.8) have been used to select the high semi–transparent clouds in the database and to derive a specific regression valid for this kind of cloudiness. The following regression is proposed

$$R = c_0 + c_1\ (T_{10.8} - 268K) + c_2\ (T_{10.8} - T_{12} - 2.65K) \tag{7.9}$$

where the regression coefficients $\{c_i\}$ are dependent on the VZA and are given in (TN39).

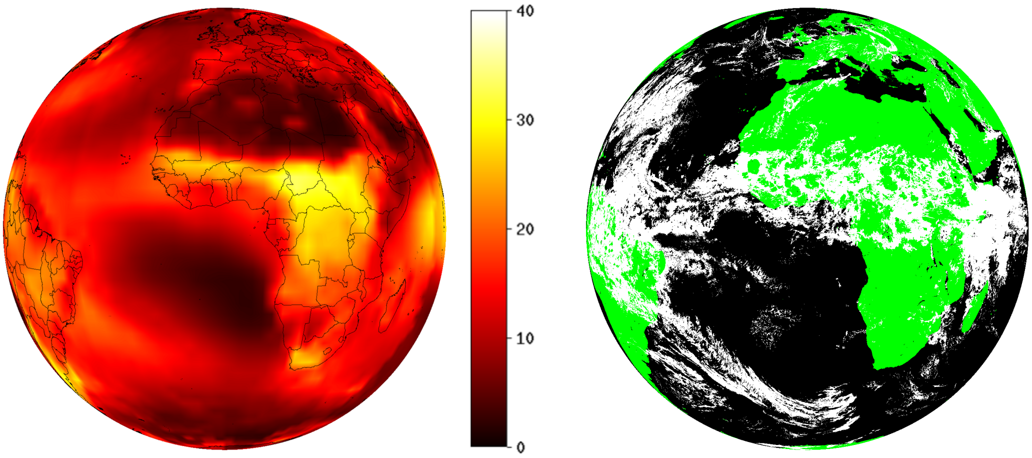

Figure 7.7: Left: ISCCP mean annual cirrus cloud probability in the Meteosat FOV. Right: illustration of the semi–transparent cloud (in white) detected by Eqs. (7.8) for July 10 2004, 00:00.

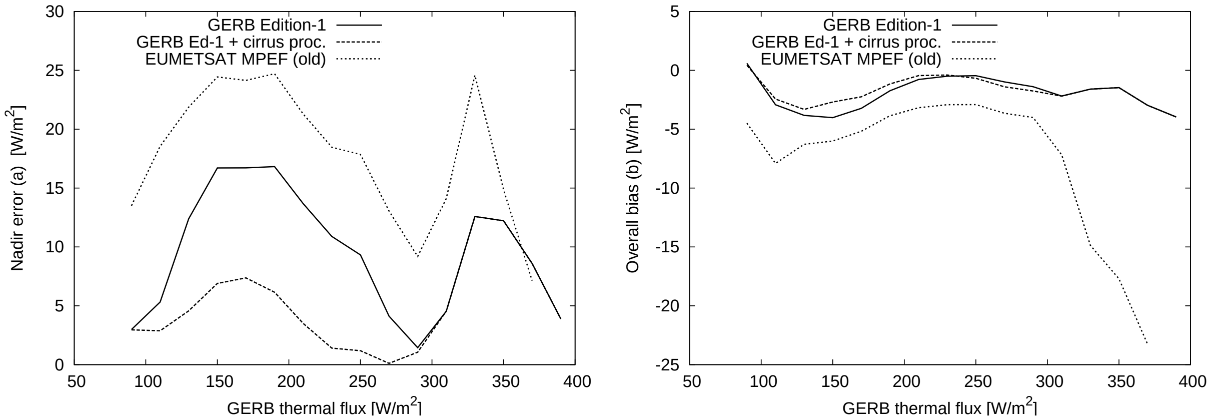

Figure 7.8: Parameters a (left) and b (right) of Eq.(7.10) for the Edition 1 LW ADM without (solid line) and with (dashed line) the cirrus processing. The MPEF curves refer to the first version of the SEVIRI OLR .

To quantify the improvement that can be obtained with this dedicated cirrus regression, two databases of collocated GERB–like and CERES FM3 ES8 OLR have been compiled. They differ by the radiance–to–flux conversion. In the first database, the GERB Edition 1 method is used while the second database includes the detection (Eqs. 7.8) and specific processing (Eqs. 7.9) for the cirrus clouds. A total of 63 millions of OLR pairs have been extracted from July and December 2004 data. Since the ERBE LW models (Suttles *et al.*, 1989) rely on a crude cloud identification (clear, partly cloudy, mostly cloudy and overcast), they do not reproduce the cirrus cloud anisotropy. For this reason, the GERB/CERES comparisons hereafter only use the CERES OLR derived from observations with VZA in the range $40° - 65°$.

The technical note (TN39) illustrates the improvements obtained at regional scale with the dedicated cirrus processing To quantify the residual limb–darkening with and without the cirrus processing, we have followed the method developed by Dewitte *et al.* (2008). The difference between the GERB–like and the CERES OLR is analyzed as a function of the VZA

$$F_{GERB} - F_{CERES} = a(F_{GERB})\,\frac{52.5° - \mathrm{VZA}_{GERB}}{52.5°} + b(F_{GERB}) \tag{7.10}$$

The parameters $a(F_{GERB})$ and $b(F_{GERB})$ are estimated in bins of $20\mathrm{Wm}^{-2}$ of the F_{GERB} flux. If the GERB limb darkening is corrected by the ADM, the parameter a must be close to 0. On the other hand, the parameters b can depart from 0 due to calibration and unfiltering. Figure 7.8 shows how these parameters vary according to the F_{GERB} for the 2 databases (without and with the cirrus processing). The improvement of the angular modeling is significant for the cloudy scenes with flux between 100 and 250 Wm^{-2}. It is worth noting that the MPEF faced the same problem with the SEVIRI OLR product. They have therefore derived 3 specific regressions: a first one for clear scenes, a second one for opaque clouds and a last one for semi–transparent clouds.

7.7 Azimuthal dependency of the thermal radiation field

This section is mainly a compilation of a paper (Clerbaux *et al.*, 2003d) published in the International Journal for Remote Sensing and a poster (Clerbaux *et al.*, 2002) presented at the EUMETSAT data user conference in 2002. Further advances on the topic of azimuthal anisotropy have been performed later by the CERES team (Minnis *et al.*, 2004).

The infrared narrowband and broadband radiances at the TOA are usually supposed to be dependent on the Viewing Zenith Angle (VZA) but not on the Viewing Azimuth Angle (VAA). Azimuthal variability of the thermal emission just above vegetated surfaces has been described in various studies and explained as a result of differential solar warming of the vegetation structure (e.g. in Kimes (1981)). Logically, the anisotropy at the surface level should propagate up to the TOA albeit reduced due to the atmosphere and cloudiness. Lipton & Ward (1997) have simulated the anisotropy for mountainous areas in North America using digital elevation data and an atmospheric model. They have shown that the variation of the incoming solar flux with the surface slope can lead to large biases in satellite retrieval of the surface temperature. Using simultaneous IR radiances from GOES-8, -9 and -10 satellites, Minnis & Khaiyer (2000) were able to observe the anisotropy in the azimuth direction. They have shown that the phenomenon is closely correlated with surface slopes, as suggested by Lipton & Ward (1997). Nevertheless, using only observations from geostationary satellites (thus located over the Equator) the Minnis & Khaiyer (2000) analysis may underestimate the magnitude of the azimuthal anisotropy (they compare 2 observations taken from different azimuths but both are however taken "from the south"). On the other hand, this approach permits to address the diurnal cycle.

In (Clerbaux *et al.*, 2003d), we provide further evidence of azimuthal anisotropy using a statistical analysis of the CERES data. The data and methodology used enable us to estimate the annual average of the azimuthal variability at regional scale. In addition, the study quantifies the relationship between the azimuthal anisotropy in the atmospheric infrared window and in the broadband longwave radiance.

The study is based on 12 months of the Cloud and the Earth's Radiant Energy System (CERES) data from the Terra spacecraft. The satellite is operating in a sun–synchronous orbit with the descending node crossing time at 10:30 Local Time (LT). This implies that the satellite observations are done close to 10.30 LT and 22:30 LT. The CERES instrument is a 3–channels broadband radiometer providing accurate measurement of shortwave ($0.3 - 5$ μm), longwave ($5 - 50$ μm) and infrared window ($8 - 12$ μm) radiances. There are two identical CERES instruments aboard Terra. One instrument is operating in a cross–track scan mode and the other in a biaxial scan mode. The first mode is used to obtain the complete spatial coverage of the Earth while the biaxial scan mode is mainly used to characterize the angular distribution of the radiation (Angular Distribution Model). In the second mode there is a complete sampling in zenith VZA and azimuth VAA angles. For the analysis, 314 days of CERES–Terra data in biaxial scan mode are used, ranging from November 2000 to November 2001. This amounts to about 1.6 10^9 observations, half of them realized during the morning pass and half of them during the evening pass. Due to the quantity of data, the ES8 CERES format is used in this study.

According to the VAA, each CERES observation of the Earth is classified as an observation *from the south* or *from the north*. An observation *from the south* corresponds to a viewing azimuth VAA in the range $90° - 270°$. An observation *from the north* corresponds to a viewing azimuth VAA in the range $270° - 90°$. The averaged CERES longwave and infrared window radiances measured *from the south* L_S and *from the north* L_N are evaluated on a $1° \times 1°$ latitude-longitude box grid. For the data used, there are about 13 000 *south* and *north* observations for each box and CERES instrument channel (LW and WIN). The difference $(L_S - L_N)$ between these two average radiances is a rough indicator of the anisotropy in azimuth. In the following, the relative difference Δ, expressed in percent, will be used as the measurement of the anisotropy:

$$\Delta = \frac{L_S - L_N}{(L_S + L_N)/2}. \tag{7.11}$$

Figure 7.9(a) shows the regional variation of Δ for the CERES infrared window channel for the morning orbit (10:30 LT). This figure provides evidence that, on average, the anisotropy in azimuth Δ is positive in the northern hemisphere and negative in the southern. The largest anisotropy is observed over mountain and desert areas like the Himalaya region, the Alps, the Atlas, the North and South American Cordilleras, the South African and Australian deserts. For land surface at latitude $> 20°$ N and S, the typical annual average anisotropy at 10:30 LT ranges between 1% and 5%.

Applying the same analysis on data from the evening orbit at 22:30 does not produce these areas of large azimuthal anisotropy over mountains or deserts (not shown). Therefore, the anisotropy appears to be caused by a difference in the daytime solar warming of north and south faces of the surface. For example, the anisotropy for the CERES infrared window channel in the Himalaya region (area between $29°N$ and $38°N$ and between $69°E$ and $104°E$) was 3.14% and 0.54% for the 10:30 and 22:30 times, respectively.

Regional anisotropy for the CERES longwave channel is given in Figure 7.9(b). Compared to the infrared window case, the anisotropy is reduced due to the atmosphere absorption/emission in spectral regions outside of the atmospheric windows. The scatterplot in Figure 7.10 shows the correlation between broadband and window anisotropy in the $1° \times 1°$ grid boxes. On this graph, the anisotropy for broadband longwave radiance appears to be about 57% of the one in the infrared window channel.

To study the influence of the cloud cover on the anisotropy, the Earth Radiation Budget Experiment (ERBE) scene identification is used. This scene identification is done using the Maximum

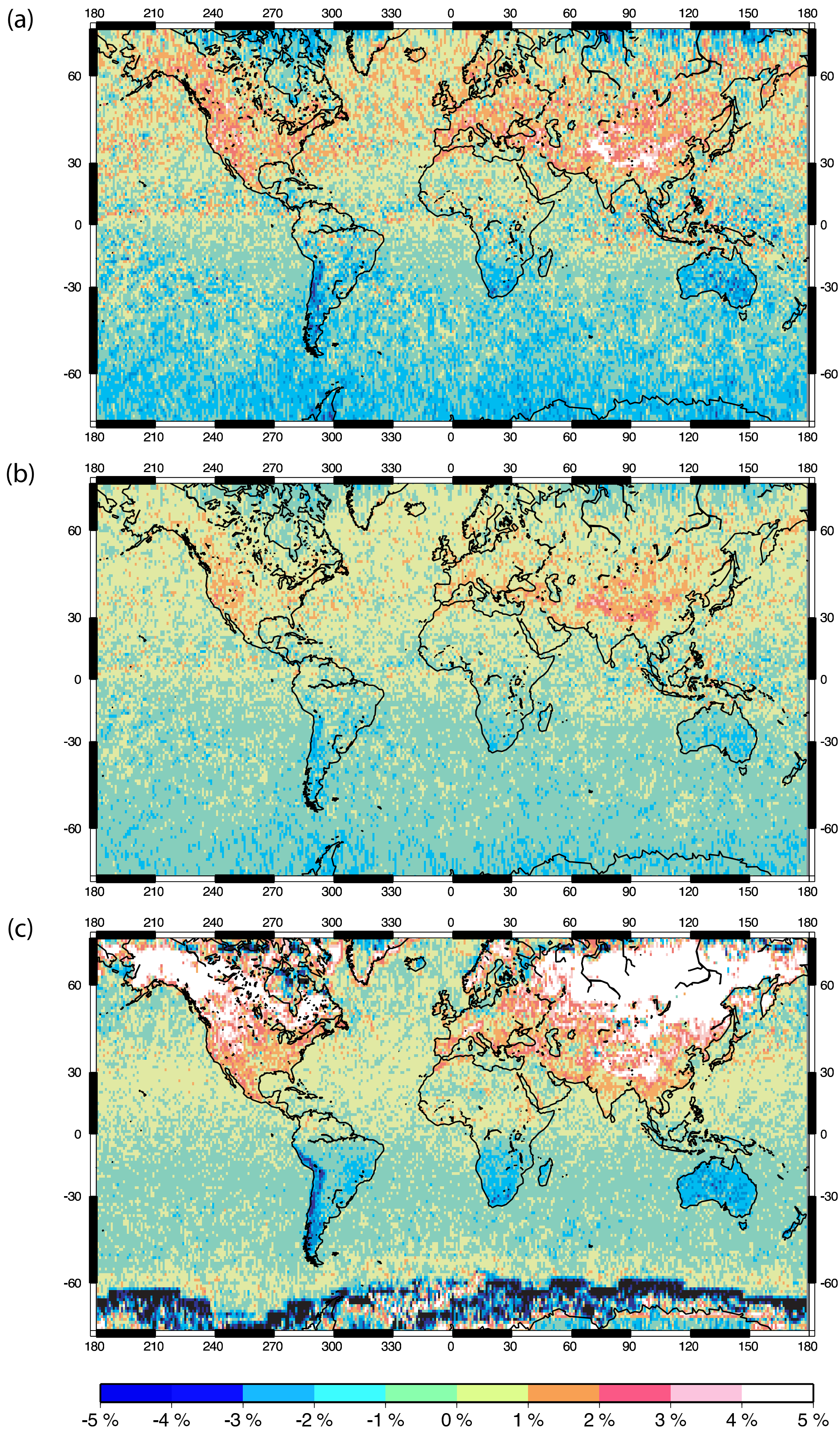

Figure 7.9: Annual average of the azimuth anisotropy Δ[%] for the CERES: (a) infrared window channel, (b) broadband longwave channel and (c) infrared window channel under clear and partly cloudy conditions only.

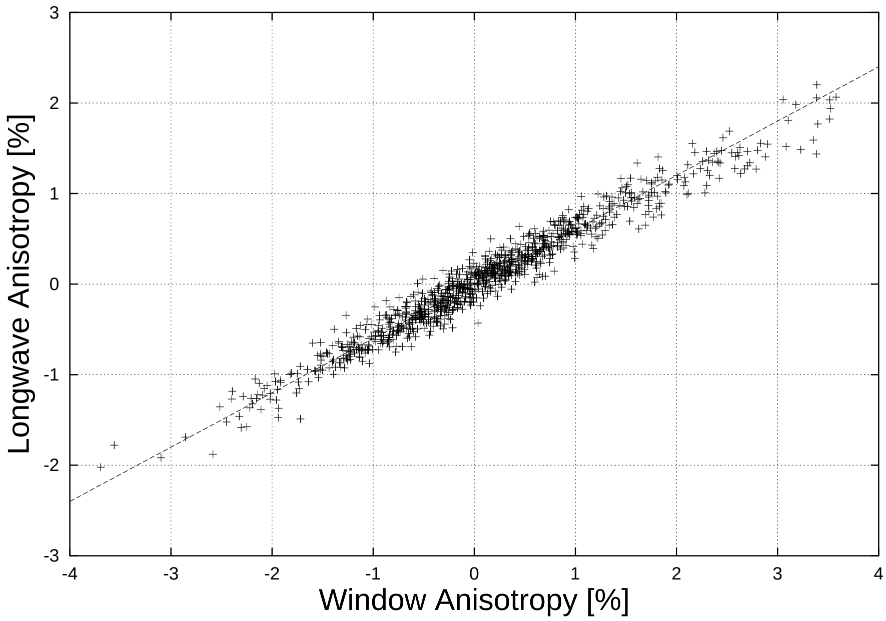

Figure 7.10: Scatterplot of the longwave versus the window anisotropies Δ (Eq. 7.11). Each cross corresponds to a $1° \times 1°$ box.

Likelihood Estimation (MLE) algorithm of Wielicki & Green (1989) which classifies the cloudiness according to the cloud fraction as clear ($< 5\%$), partly cloudy ($5 - 50\%$), mostly cloudy ($50-95\%$) or overcast ($> 95\%$). Figure 7.9(c) shows the regional variation of Δ when only the CERES clear or partly cloudy measurements are used to evaluate the *south* and *north* radiances in Eq.(7.11). The main result here is that, for cloud free conditions, the infrared radiance does not show azimuthal anisotropy over the ocean ($|\Delta| < 1\%$). This is a valuable result for the remote sensing of the sea surface temperature. In Figure 7.9(c), the values of the azimuthal anisotropy measured over the ice packs near Antarctica and over Canadian tundra and Siberia appear to be unrealistic and do not follow the general behavior. This artifact is probably due to the fact that over reflective surfaces, such as ice and snow, the ERBE scene identification (MLE) mainly relies on the CERES longwave measurement and is then correlated to the (small) signal we want to highlight.

This simple statistical analysis of CERES–Terra data shows a significant dependency on azimuth for the thermal radiance field at the TOA, mainly over arid and mountain regions. The regional analysis has only been done for the 10:30 and 22:30 LT (Terra overpass). The data from the CERES instruments on the Aqua satellite would be appropriate to perform a similar analysis at 01:30 and 13:30 LT.

This azimuthal anisotropy affects the GERB thermal flux as it is observed in the GERB/CERES comparisons under Section 7.5.

7.8 Discussion

Radiative transfer computations are powerful tools to simulate the TOA infrared radiance field in both its spectral and angular dimensions. These simulated radiance fields allow to derive models of the TOA anisotropy which take as input a set of NB infrared radiances. Compared to the empirical ADMs, an asset of this approach is that no explicit scene identification is required. On the other hand, the theoretical approach is more likely to introduce biases and comprehensive validations of the inferred thermal flux are therefore needed.

The theoretical approach is followed for GERB Edition 1. The resulting fluxes have been validated by comparison with the independent CERES observations. It was shown that the radiance–to–flux conversion performs correctly for clear sky scenes but does not totally compensate for the anisotropy for some cloudy scenes. A residual limb–darkening of the LW flux is observed in cloudy condition.

For a series of scene types like the cirrus clouds, it is shown that some kind of scene identification is desirable to improve the GERB fluxes in future Editions. It was observed that a single universal regression can not perform correctly over so different anisotropy behaviors. As an example, for an optically thick cloud the anisotropy decreases with the cloud height, while it is the opposite for a semi–transparent cloud. Other teams, like the MPEF at EUMETSAT and the group of Ellingson and Lee at the University of Maryland (development of HIRS and GOES-R OLR products), have faced the same problem and arrived at similar conclusions. For the GERB Edition 2 data, it is proposed to implement a simple cirrus cloud detection and to use a dedicated regression for this type of cloudiness. The work presented in Section 7.6 can serve as a starting point to that end. In parallel, performances over desert surface could be improved by a better treatment of the surface emissivity. For this, it is foreseen to issue a new version of the LW radiative transfer computations taking as input parameters realistic values of surface emissivity extracted from the IREMIS database (Seemann *et al.*, 2008).

As in the Edition 1, the LW angular modeling is a major source of error on the flux over semi–transparent objects like the cirrus clouds, but also the airplane contrails and the desert dust clouds. If possible, the effect of these phenomena on the ERB should be quantified using fluxes derived from GERB observations with VZA $\sim 52°$, as at these viewing angles most of the radiance–to–flux conversion error cancels.

Chapter 8

Summary and outlook

8.1 Summary

In this work we have reviewed many aspects of the GERB data processing at RMIB. This highlighted the strengths but also some limitations of the involved methods. These limitations have been discussed and quantified, and improvement proposals have been made in the text and are summarized in the next section. It is however worth remembering that the main objective is reached: quasi–continuous, 24h/7days, calibrated and validated TOA fluxes are provided over the Meteosat field of view. The diurnal cycles of outgoing radiations are fully resolved with unprecedented temporal resolution. For GERB Edition 1, the data processing is ensured through relatively simple algorithms and methods. This permits the estimation of the TOA fluxes in near real–time through the synergetic processing of the GERB and SEVIRI level 1.5 data. Reprocessing capability has also been demonstrated.

With the exception of the SW radiance–to–flux conversion, the GERB spectral and angular modelings are based on radiative transfer computations. It is shown that this approach is well–suited for BB instrument unfiltering and LW radiance–to–flux conversion. State–of–the–art radiative transfer models provide accurate simulations of the TOA radiation in both its spectral and angular properties. This requires as input a comprehensive physical characterization of the Earth–atmosphere system which is not obvious to provide in a realistic manner. Indeed, these characteristics are available in separate sources (TIGR atmospheric profiles, IREMIS surface emissivities, IGBP for the geotype, aerosols or wind speed climatology, ...) which are not easy to combine. Another difficulty appears when fitting a regression on the database of simulations: the usual "a single regression fits all" assumption proved not to be valid for all the problems we faced. Sometimes, better results are obtained by using dedicated regressions according to the scene type.

As an important step in the GERB Edition 1 data release, the GERB SW and LW radiances and fluxes have been compared with corresponding quantities from the CERES instruments. Overall, the GERB unfiltered radiances are found to be 5.9% higher than the CERES ones for the shortwave, and 1.3% lower than the CERES ones for the longwave. Regarding the SW radiation, the scene type dependency around this mean value is limited to ±1% (except for the ARG format). The observed SW difference suggests that one or both instruments are out of the stated accuracies of 1% (CERES) and 1.99% (GERB) at 1 SD. The overall difference comes probably from the absolute on–ground calibration of the GERB and/or CERES SW channels.

The GERB/CERES comparison reveals differences between the different GERB data formats that should be taken into account by the user of the data. It appeared that the released ARG format should be used cautiously to study processes over particular scene types and/or over areas of small spatial extension. The comparisons proved that the BARG and HR GERB formats agree better with the independent CERES observations. These formats will be officially released soon.

Concerning the LW radiation, the observed overall 1.3% difference in radiance is consistent with the GERB (0.9%) and the CERES (0.75%) accuracies at 1 SD. The LW flux comparison shows angular dependency problems affecting the GERB dataset in cloudy regions. The future reprocessings of GERB (Edition 2) and CERES (Edition 3 expected by the end of 2008) will probably improve the agreement between these two missions.

The interest of BB observations is proven by pointing out the difficulties to obtain efficient narrowband–to–broadband regressions for all the scene types at all viewing and solar geometries. At this level, empirical regressions fitted on the GERB BB observations provide much better results than the usual radiative transfer approach. The empirical approach has been tested for Meteosat first (MVIRI) and second (SEVIRI) generations. The temporal stability of the estimated BB radiance remains a problem although significant improvement is observed with SEVIRI.

As it is generally accepted that an enhanced number of NB observations should confine the NB–to–BB error to less than 1%, it was decided that Meteosat Third Generation (MTG) will not continue the BB measurements done by MSG. Our investigations suggest to collect at least one complete year of overlapping MSG and MTG data to enable empirical GERB–like regressions beyond MSG.

8.2 Outlook

This document mainly deals with the performances and the limitations of the Edition 1 GERB data. The work suggests the following improvements to be implemented for a subsequent Edition of the GERB data set:

Improved RTM simulations. As discussed in the text (Sections 4.3 and 5.3), there is room for improvement of the radiative transfer simulations. Concerning the SW simulations, the priorities should be (in the order of expected difficulties or required amount of "man–months"): to add simulations for mixed ocean/land scenes, to use more realistic crystal size distributions for the ice clouds, and to use land surface BRDFs, if possible with spectral dependency. The limitations for the LW simulations concern the surface characterization in terms of emissivities and temperature and their link with the atmospheric profile. For the next version of the database of simulations, it is proposed to use the surface spectral emissivity provided in the IREMIS database and collocated atmospheric profiles from the ECMWF analysis.

Use of empirical narrowband–to–broadband regressions. The whole processing would benefit from the empirical regressions presented in Sections 4.8 and 5.8. For the SW regression, our work also suggests relying on "frozen" calibration for the SEVIRI solar channels instead of the MPEF near real–time calibration. The rapidly growing GERB/SEVIRI database will allow additional validations at regional scale and the assessment of the temporal stability of the GERB–like products on longer time periods.

Spectral response and unfiltering. Based on the improved radiative transfer simulations databases, and possibly spectral response reprocessed by Imperial College, an update of the unfiltering parameters will be issued. For the SW unfiltering, a simplification of the current scheme, which involves 3 different methods, is desirable. For the LW radiation, the pixel–to–pixel variability, which is theoretically expected from the telescope throughput (Section 5.7), could be empirically validated using the databases of GERB/CERES coangular observations.

GERB SW channel aging. The ratios GERB–like/GERB SW radiance present a small positive drift for both Meteosat–7 and MSG–1. The scene type dependency of the drift could be the sign of an aging of the GERB SW channel for the short wavelength. Further investigations are foreseen by analysis of the level 1.5 data over clear ocean scenes.

LW angular modeling. The work realized under Section 7.6 must be consolidated and possibly submitted for publication. In particular, a more reliable cirrus cloud detection could be made possible using the infrared cloud mask under development. This processing step could also benefit from the improvements of the RTM simulations, in particular using more realistic surface emissivity data.

SW angular modeling. A series of improvements is foreseen for the Edition 2 data: a better processing of snow covered areas, a better processing of semi–arid areas, a better modeling of the anisotropy for aerosol over clear ocean, the use of an empirical GERB model for the clear ocean flux in the sun glint region. For this region, the detection of clear sky pixels should benefit from the infrared retrieval under development. Before release of the Edition 2, those improvements will be validated using the GERB/CERES comparison methodology presented in this work.

Appendix: a note about regression

Introduction

Scientific activities make frequent use of regression to estimate (to model) a quantity y (the *response*) as a function on a set of predictors x_i (the *inputs*). In this work, the response y was either unfiltering factor (for GERB unfiltering problems, Sections 4.4, 4.5, 5.4, and 5.5) or broadband radiance (for the narrowband–to–broadband problems, Sections 4.8, 4.9, 5.8, and 5.9). The input variables x_i are usually the narrowband radiances measured by the SEVIRI instrument. The general form of the model is

$$y = f(x) + \epsilon \tag{8.1}$$

where ϵ is the noise on the y. The inversion process consists in finding the function f from the x and y. In practice, before inversion, some assumptions have to be done about the mathematical form of the relationship f. In this frame, linear models are widely used as they provide simpler inversion of the model. The regressions have been fit on either simulated or observational data. In this work, this is performed by minimizing the mean square differences between the y and their estimate $f(x)$

$$\frac{1}{N}\sum_{i=1}^{N}(y_i - f(x_i))^2 \tag{8.2}$$

It can be demonstrated that, under some conditions, the least square provides the best model in the sense of the maximum likelihood estimator (Tarantola, 2005). These conditions concern the distribution of the errors affecting the y and the x_i, namely (Faraway, 2002):

- The distribution of the noise ϵ on the y must be normally distributed and with mean value zero.
- The noise level (standard deviation of the distribution) must be the same for the y.
- The errors must be uncorrelated.
- The predictors x_i are not subject to significant noise level.

Hereafter, we investigate 3 situations encountered during the thesis for which these conditions are not fulfilled.

Heterogeneous errors ϵ

The first one concerns the fit used for the direct unfiltering of the GERB–2 LW channel. Details are given in Section 5.4. In this case, the data are not observational data but radiative transfer simulations for which error is difficult to assess. However, a quick look at the scatterplots in Figures 5.3 and 8.1 suffices to convince that the unfiltering factor exhibits significantly more dispersion for warm scenes (like warm desert) than for cold ones (deep convective clouds). To address the effect of this on the regression, the simulations have been binned in intervals of 5 $Wm^{-2}sr^{-1}$ of LW radiance. Within each interval the average values $< L_{lw,th} >$ and $< \alpha_{lw,th} >$, and the standard deviation $\sigma_{\alpha_{lw,th}}$ are computed. Figure 8.1 shows the original scatterplot (red dots), the binned quantities (in green with error bars at 1 SD), and 3 regression fits. The first one ("fit dots") corresponds to the standard fit of the dots, assuming homogeneous error on the y (or no error at all). The second ("fit bin") is obtained by fitting the centers of interval, without any weighting (a weighting according to the population of the bin could have be done). The third fit ("fit bin weighted") takes into account the standard deviation σ_{y_i} within the bins. This was done by minimization, with respect to a, b, c, d of

$$\frac{1}{N}\sum_{i=1}^{N}\frac{(y_i - a - bx_i - cx_i^2 - dx_i^3)^2}{\sigma_{y_i}^2} \tag{8.3}$$

where $y =< \alpha_{lw,th} >$, $x =< L_{lw,th} >$ and $\sigma_y = \sigma_{\alpha_{lw,th}}$. Except when used in "extrapolation" mode (which is clearly not the aim of the direct unfiltering), the differences between the regression curves remain negligible.

Errors in predictors

A second case study, concerns the regressions on predictors affected by random error. As an example, let consider the fit of Eq.(4.27), used to generate GERB–like data from the Meteosat–7 VIS channel (Section 4.9). In this case, the regression $\rho_{BB} = a + b\rho_{VIS}$ is fit on observation data. The BB reflectances ρ_{BB} are derived from the GERB SW observations which are featured with 1.99% error at 1 Standard Deviation (SD), see Section 3.1.6. The NB reflectances ρ_{VIS} are obtained from the VIS channel of Meteosat–7. which is featured with 5% error at 1 SD (Govaerts *et al.*, 2004a). The solution (a and b) with maximum likelihood is the one that minimizes

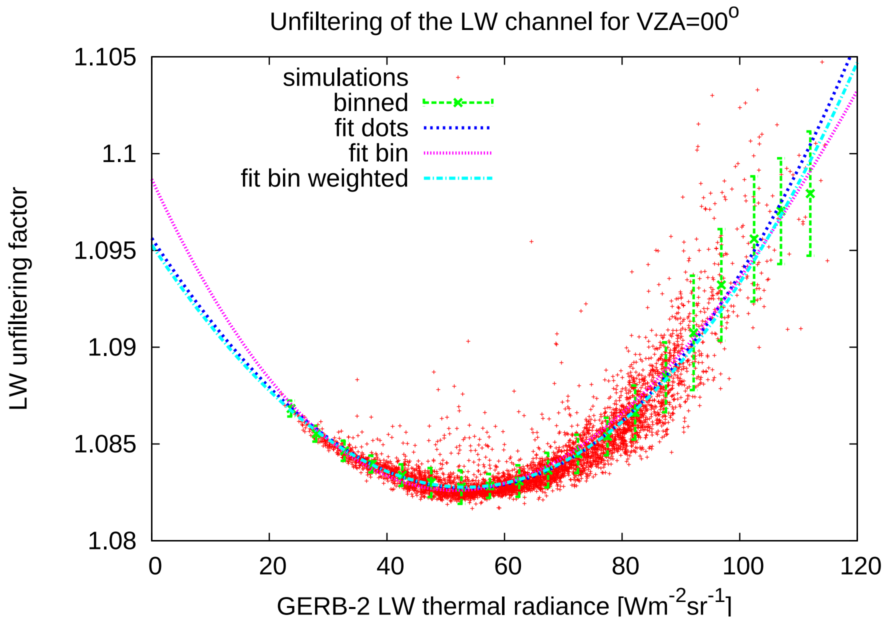

Figure 8.1: Weighted least square.

$$\frac{1}{N}\sum_{i=1}^{N}\frac{(y_i - a - bx_i)^2}{\sigma_{y_i}^2 + b^2\sigma_{x_i}^2} \tag{8.4}$$

As an illustration, Figure 8.2 displays the scatterplot (ρ_{BB}, ρ_{VIS}) for bright vegetation surface, thin water cloud ($cc > 90\%$, $1 < \tau < 4$, $p < 50\%$), $40° <$ SZA $< 60°$, $40° <$ VZA $< 60°$, and $0° <$ RAA $< 45°$. The regressions "fit" (green) and "weighted fit" (blue) are close one to the other as the 1.99% error on the y is a small quantity. Taking into account the 5% error on the predictor x leads to regression ("generalized least square" in pink) with higher slope value b. This illustrates the well–known fact that the error in the predictors tend in general to bias the regression slope(s) in the direction of zero (Faraway, 2002).

From this analysis, one can think that the generalized least square regression should be preferred to the standard least square. Indeed, taking into account the error on the predictor reduces the bias on the model. However, as our model $\rho_{BB} = a + b\rho_{VIS}$ is built for prediction purpose only (i.e. we are not interested to know what are the exact values of a and b), with input data ρ_{VIS} affected with the same error level, the standard fit could be use (Faraway, 2002).

Assessing the error in the temporal drift

Simple linear regression have been used to model temporal drift between GERB–like and GERB daily mean values (Sections 4.8.7, 4.9.4, 5.8.5 and 5.9.4). A difficulty here is that the residual exhibits an apparent seasonal cycle. The assumption of uncorrelated Gaussian noise is therefore not verified. To deal with this we have first deseasonalized the data as illustrated on Figure 8.3 for the SEVIRI GERB–like SW radiances (see Section 4.8.7). After correction for the seasonal

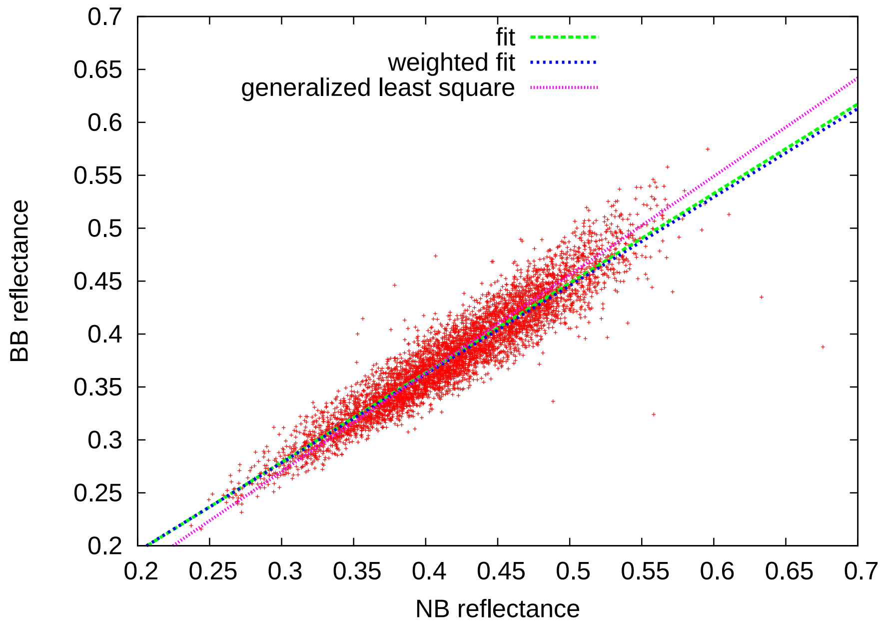

Figure 8.2: Generalized Least Square.

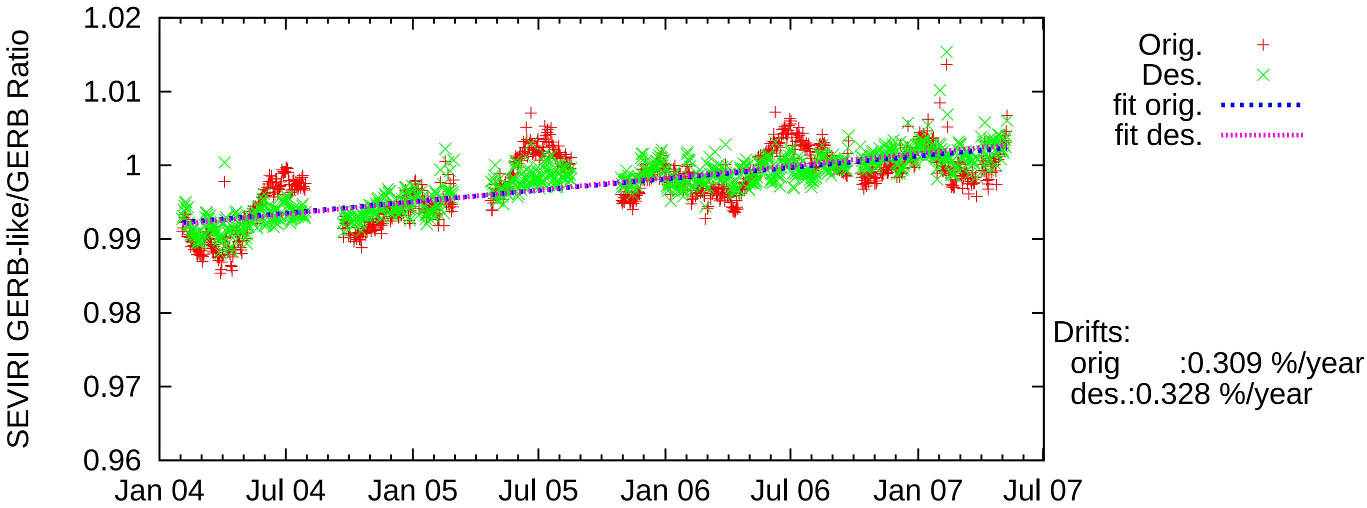

Figure 8.3: Temporal drift.

variations, the standard least square fit is done, giving a drift of 0.328%/year. Under the assumption of normal noise on the y, the uncertainty on the drift (at 1SD) can be estimated from the residual error $\sigma_{res,y}$, the number of points N and the dispersion in time σ_x as (Faraway, 2002)

$$\text{S.D.(drift)} = \frac{\sigma_{res,y}}{\sqrt{N}\ \sigma_x} \tag{8.5}$$

In the case of Figure 8.3, one get a residual of $\sigma_{res,y} = 0.001683$, a number of point of $N = 962$ and a time dispersion of $\sigma_x = 0.984$year. Therefore, under the assumption that the residual errors are normally distributed, the drift is 0.328 ± 0.016 %/year, at 3 SD uncertainty.

Bibliography

Allan, R., Slingo, A., Milton, S. & Culverwell, I. (2005). Exploitation of Geostationary Earth Radiation Budget data using simulations from a numerical weather prediction model: Methodology and data validation. *Journal of Geophysical Research*, **110**, D14111. 29

Allan, R., Slingo, A., Milton, S. & Brooks, M. (2007). Evaluation of the Met Office global forecast model using Geostationary Earth Radiation Budget (GERB) data. *Quarterly Journal of Royal Meteorological Society*, **133**, 1993–2010. 9, 29

Atlas, R., Hoffman, R., Bloom, S., Jusem, J. & Ardizzone, J. (1996). A Multiyear Global Surface Wind Velocity Dataset Using SSM/I Wind Observations. *Bulletin of the American Meteorological Society*, **77(5)**, 869–882. 57

Barkstrom, B.R. (1984). The Earth Radiation Budget Experiment (ERBE). *Bulletin of the American Meteorological Society*, **65**, 1170–1186. 11, 17

Bates, M., Smith, A., Allan, P., Coan, B., Lepine, D., Ricketts, M. & Stewart, B. (2004). Geolocation accuracy of GERB data. In *Proc. of the 2004 EUMETSAT Meteorological Satellite Conference*, 505–511. 32

Berk, A., Anderson, G., Bernstein, L., Acharya, P., Dothe, H., Matthew, M., Adler-Golden, S., Chetwynd, J.J., Richtsmeier, S., Pukall, B., Allred, C., Jeong, L. & Hoke, M. (1999). MODTRAN4 Radiative Transfer Modeling for Atmospheric Correction. In *Proceedings of SPIE*, vol. 3756, 348–353. 55

Bertrand, C., Clerbaux, N., Ipe, A. & Gonzalez, L. (2002). Use of GERB–like fluxes to validate NWP models. In *Geophysical Research Abstracts*, vol. 4. 29

Bertrand, C., Clerbaux, N., Ipe, A. & Gonzalez, L. (2003). Estimation of the 2002 Mount Etna eruption cloud radiative forcing from Meteosat-7 data. *Remote Sensing of Environment*, **87**, 257–272. 29, 98, 128

Bertrand, C., Clerbaux, N., Ipe, A., Dewitte, S. & Gonzalez, L. (2005). Angular distribution models anisotropic correction factors and mixed clear scene types: a sensitivity study. *IEEE Transactions on Geoscience and Remote Sensing*, **43(1)**, 92–102,. 32, 140

Bertrand, C., Clerbaux, N., Ipe, A., Dewitte, S. & Gonzalez, L. (2006a). Angular distribution models anisotropic correction factors and sun glint: a sensitivity study. *International Journal for Remote Sensing*, **27**, 1741–1757. 139

Bertrand, C., Futyan, J., Ipe, A., Gonzalez, L. & Clerbaux, N. (2006b). Diurnal Asymmetry in the GERB SW Fluxes. *IEEE Transactions on Geoscience and Remote Sensing*, **44(12)**, 3585–3600. 147

Bertrand, C., Gonzalez, L., Ipe, A., Clerbaux, N. & Dewitte, S. (2006c). Improvement in the GERB short wave flux estimations over snow covered surfaces. *Advances in Space Research*, **41(11)**, 1894–1905. 136

Bertrand, C., Ipe, A., Clerbaux, N. & Gonzalez, L. (2008). GERB SW flux anomalies over the Sahel region: an ADM related issue. *Advances in Space Research*, **submitted**. 29, 136, 144

Brindley, H. & Ignatov, A. (2006). Retrieval of mineral aerosol optical depth and size information from Meteosat Second Generation SEVIRI solar reflectance bands. *Remote Sensing of Environment*, **102**, 344–363. 29

Brindley, H. & Russell, J. (2006). Improving GERB scene identification using SEVIRI: Infrared dust detection strategy. *Remote Sensing of Environment*, **104**, 426–446. 29, 137

Caprion, D., Clerbaux, N., Dewitte, S., Bertrand, C., Depaepe, B., Gonzalez, L. & Ipe, A. (2005). Initial operation of the CM-SAF TOA flux products. In *Proc. of the 2005 EUMETSAT Meteorological Satellite Conference (P46)*. 2, 29

Chevallier, F., Chédin, A., Chéruy, F. & Morcrette, J. (2000). TIGR-like atmospheric-profile databases for accurate radiative-flux computation. *Quarterly Journal of Royal Meteorological Society*, **126**, 777–785. 108

Clerbaux, N., Dewitte, S., Gonzalez, L., Ipe, A. & Nicula, B. (2001). Derivation of Top Of the Atmosphere Radiative Fluxes from SEVIRI: Methodology, Accuracy and Perspectives. In *Proc. of the 2001 EUMETSAT Meteorological Satellite Conference*, 69–76. 87, 122

Clerbaux, N., Dewitte, S., Bertrand, C., Ipe, A., Gonzalez, L. & Nicula, B. (2002). Regional Bias in the OLR Estimated from the Geostationary Orbit. In *Proc. of the 2002 EUMETSAT Meteorological Satellite Conference*, 677–681, Dublin. 167

Clerbaux, N., Bertrand, C., Dewitte, S., Gonzalez, L., Ipe, A. & Nicula, B. (2003a). Estimation of the TOA radiative fluxes from the GERB instrument data. In *SPIE Infrared Spaceborne Remote Sensing XI*, vol. 5152, 305–315, San Diego. 31

Clerbaux, N., Dewitte, S., Bertrand, C., Ipe, A., Gonzalez, L., Nicula, B. & Joukoff, A. (2003b). Generation of TOA radiative fluxes from the GERB instrument data. Part II: First Results. In *Proc. of the 2003 EUMETSAT Meteorological Satellite Conference*, 228–235, Weimar. 31

Clerbaux, N., Dewitte, S., Gonzalez, L., Bertand, C., Nicula, B. & Ipe, A. (2003c). Outgoing Longwave Flux Estimation: Improvement of Angular Modelling Using Spectral Information. *Remote Sensing of Environment*, **85**, 389–395. 108, 149, 150, 152

Clerbaux, N., Ipe, A., Bertrand, C., S., D., Nicula, B. & Gonzalez, L. (2003d). Evidence of Azimuthal Anisotropy for the Thermal Infrared Radiation Leaving the Earth's Atmosphere. *International Journal for Remote Sensing*, **24**, 3005–3010. 149, 150, 164, 167

Clerbaux, N., Bertrand, C., Caprion, D., Depaepe, B., Dewitte, S., Gonzalez, L. & Ipe, A. (2005). Narrowband-to-broadband Conversions for SEVIRI. In *Proc. of the 2005 EUMETSAT Meteorological Satellite Conference (P46)*, 351–357. 33, 66, 67, 89, 90, 122, 123

Clerbaux, N., Dewitte, S., Bertrand, C., Caprion, D., De Paepe, B., Gonzalez, L. & Ipe, A. (2007). GERB–like data from Meteosat first generation. In *Proc. of the 2007 EUMETSAT Meteorological Satellite Conference (P48)*. 29, 98

Clerbaux, N., Dewitte, S., Bertrand, C., Caprion, D., Depaepe, B., Gonzalez, L., Ipe, A. & Russell, J. (2008a). Unfiltering of the Geostationary Earth Radiation Budget (GERB) data. Part II: Longwave Radiation. *Journal of Atmospheric and Oceanic Technology*, **25(7)**, 1106–1117. 14, 16, 32, 69, 112, 114, 120

Clerbaux, N., Dewitte, S., Bertrand, C., Caprion, D., Depaepe, B., Gonzalez, L., Ipe, A., Russell, J. & Brindley, H. (2008b). Unfiltering of the Geostationary Earth Radiation Budget (GERB) data. Part I: Shortwave Radiation. *Journal of Atmospheric and Oceanic Technology*, **25(7)**, 1087–1105. 14, 16, 32, 63, 81, 83, 144

Clerbaux, N., Russell, J., Dewitte, S., Bertrand, C., Caprion, D., Depaepe, B., Gonzalez, L., Ipe, A., Bantges, R. & Brindley, H. (2008c). Comparison of GERB Instantaneous Radiance and Flux Products with CERES Edition-2 Data. *Remote Sensing of Environment*, **in press**. 34, 46

Comer, R., Slingo, A. & Allan, R. (2007). Observations of the diurnal cycle of outgoing longwave radiation from the Geostationary Earth Radiation Budget instrument. *Geophysical Research Letters*, **34**, L02823. 29

Cox, C. & Munk, W. (1955). Some problems in optical oceanography. *Journal of Marine Research*, **14**, 63–78. 134

Crommelynck, D. & Dewitte, S. (1999). Metrology of total solar irradiance monitoring. *Advances in Space Research*, **24(2)**, 195–204. 11

De Paepe, B., Ignatov, A., Dewitte, S. & Ipe, A. (2008). Aerosol retrieval over ocean from SEVIRI for the use in GERB Earth's radiation budget analyses. *Remote Sensing of Environment*, **112(5)**, 2455–2468. 29, 137

Derrien, M. & Le Gléau, H. (2005). MSG/SEVIRI cloud mask and type from SAFNWC. *International Journal for Remote Sensing*, **26(21)**, 4707–4732. 22

Desormeaux, Y., Rossow, W., Brest, C. & Campbell, G. (1993). Normalization and Calibration of Geostationary Satellite Radiances for the International Satellite Cloud Climatology Project. *Journal of Atmospheric and Oceanic Technology*, **10**, 304–325. 38

Dewitte, S. (1997). *Local Instantaneous Earth Radiation Budget Terms Measured from Geostationary and Polar Satellites*. Ph.D. thesis, Vrije Universiteit Brussel. 1

Dewitte, S. & Clerbaux, N. (1999a). First Experience with GERB Ground Segment processing Software: Validation with CERES PFM Data. *Advances in Space Research*, **24**, 925–929. 128

Dewitte, S. & Clerbaux, N. (1999b). The need of Angular Dependency Models for the Geostationary Earth Radiation Budget Short Wave Flux Estimation. In *Proc. of the ALPS'99 conference.*, CNES. 19

Dewitte, S., Clerbaux, N. & Nicula, B. (2002a). Homogenisation of reflected solar fluxes in the Climate Monitoring SAF. In *Proc. of the 2002 EUMETSAT Meteorological Satellite Conference*, 690–695, Dublin. 29, 92

Dewitte, S., Nicula, B. & Clerbaux, N. (2002b). Comparison of satellite measurements of the monthly mean diurnal cycle of radiative fluxes at the top of the atmosphere over Europe and Africa. In *Proceedings of the European Conference of Applied Climatology*. 29

Dewitte, S., Clerbaux, N., Bertrand, C., Ipe, A., Gonzalez, L., Nicula, B. & Joukoff, A. (2003). Generation of TOA radiative fluxes from the GERB instrument data. Part I: Methods. In *Proc. of the 2003 EUMETSAT Meteorological Satellite Conference*, 227–227, Weimar. 31

Dewitte, S., Caprion, D., Clerbaux, N., Gonzalez, L., Ipe, A., Bertrand, C. & De Paepe, B. (2007). The European climate anomaly in 2006 as seen by the Geostationary Earth Radiation Budget instrument. In *Proc. of the 2007 EUMETSAT Meteorological Satellite Conference (P48)*. 29

DEWITTE, S., GONZALEZ, L., CLERBAUX, N., IPE, A. & BERTRAND, C. (2008). The Geostationary Earth Radiation Budget Edition 1 data processing algorithms. *Advances in Space Research*, **41**, 1906–1913. 14, 31, 32, 63, 162, 166

DUVEL, J. & KANDEL, R. (1984). Anisotropy of Longwave Radiation Emergent from a Broken Cloud Field and its Effect on Satellite Estimates of Flux. *Journal of Climate and Applied Meteorology*, **23**, 1411–1420. 19, 150, 152

ELLINGSON, R. & BA, M. (2003). A Study of Diurnal Variation of OLR from the GOES Sounder. *Journal of Atmospheric and Oceanic Technology*, **20**, 90–98. 24

ELLINGSON, R., YANUK, D., LEE, H.T. & GRUBER, A. (1989). A Technique for Estimating Outgoing Longwave Radiation from HIRS Radiance Observations. *Journal of Atmospheric and Oceanic Technology*, **6**, 706–711. 13, 21

ELLINGSON, R., LEE, H.T., YANUK, D. & GRUBER, A. (1994). Validation of a Technique for Estimating Outgoing Longwave Radiation from HIRS Radiance Observations. *Journal of Atmospheric and Oceanic Technology*, **11**, 357–365. 21

FARAWAY, J. (2002). *Practical regression and ANOVA using R*. Department of Mathematical Sciences, University of Bath (UK): self-published at http://www.maths.bath.ac.uk/ jjf23/book/. 177, 179, 180

FORSTER, P., RAMASWAMY, V., ARTAXO, P., BERNTSEN, T., BETTS, R., FAHEY, D., HAYWOOD, J., LEAN, J., LOWE, D., MYHRE, G., NGANGA, J., PRINN, R., RAGA, G., SCHULZ, M. & VAN DORLAND, R. (2007). *Changes in Atmospheric Constituents and in Radiative Forcing. In Climate Change 2007: The Physical Science Basis. Contribution of Working Group I to the Fourth Assessment Report of the Intergovernmental Panel on Climate Change [Solomon, S., D. Qin, M. Manning, Z. Chen, M. Marquis, K.B. Averyt, M.Tignor and H.L. Miller (eds.)].*, chap. 2, 129–234. Cambridge University Press. 7

FUTYAN, J. (2005). *Satellite Observations of the Radiative Effects of Tropical Clouds*. Ph.D. thesis, Imperial College London. 9, 29

FUTYAN, J. & DEL GENIO, A. (2007). Deep Convective System Evolution over Africa and the Tropical Atlantic. *Journal of Climate*, **20**, 5041–5060. 29

FUTYAN, J. & RUSSELL, J. (2005). Developing clear sky flux products for the Geostationary Earth Radiation Budget Project. *Journal of Applied Meteorology*, **44**, 1361–1374. 24, 29

FUTYAN, J., RUSSELL, J. & HARRIES, J. (2005). Determining Cloud forcing by cloud type from geostationary satellite data. *Geophysical Research Letters*, **32**, L08807. 29

Gao, B. & Wiscombe, W. (1994). Surface-Induced Brightness temperature variations and their effects on detecting thin cirrus clouds using IR emission channels in the 8-12 μm region. *Journal of Applied Meteorology*, **33**, 568–570. 106

Gonzalez, L., Hermans, A., Dewitte, S., Ipe, A., Sadowski, G. & Clerbaux, N. (2000). Resolution Enhancement of GERB Data. In *Proc. of the 2000 EUMETSAT Meteorological Satellite Conference*, 619–625, Bologna, Italy. 31

Govaerts, Y. (1999). Correction of the Meteosat-5 and -6 radiometer solar channel spectral response with the Meteosat-7 sensor spectral characteristics. *International Journal for Remote Sensing*, **20**, 3677–3682. 37

Govaerts, Y., Arriaga, A. & Schmetz, J. (2001). Operation Vicarious calibration of the MSG/SEVIRI Solar Channels. *Advances in Space Research*, **28(1)**, 21–30. 40, 65

Govaerts, Y., Clerici, M. & Clerbaux, N. (2004a). Operational Calibration of the Meteosat Radiometer VIS Band. *IEEE Transactions on Geoscience and Remote Sensing*, **42**, 1900–1914. 37, 38, 98, 178

Govaerts, Y., Lattanzio, A., Pinty, B. & Schmetz, J. (2004b). Consistent surface albedo retrieval from two adjacent geostationary satellites. *Geophysical Research Letters*, **31**, L15201. 21, 42

Green, R. & Avis, L. (1996). Validation of ERBS Scanner Radiances. *Journal of Atmospheric and Oceanic Technology*, **13**, 851–862. 14, 15

Green, R. & Hinton, P. (1996). Estimation of angular distribution models from radiance pairs. *Journal of Geophysical Research*, **101**, 16951–16960. 17

Green, R., Eastwood, M., Sarture, C., Chrien, T., Aronsson, M., Chippendale, B., Faust, J., Pavri, B., Chovit, C. & Solis, M. (1998). Imaging spectroscopy and the Airborne Visible/Infrared Imaging Spectrometer (AVIRIS). *Remote Sensing of Environment*, **65**, 227–248. 102

Halthore, R. & al. (2005). Intercomparison of shortwave radiative transfer codes and measurements. *Journal of Geophysical Research*, **110**, D11206. 55

Hansen, J., Nazarenko, L., Ruedy, R., Sato, M., Willis, J., Del Genio, A., Koch, D., Lacis, A., Lo, K., Menon, S., Novakov, S., Perlwitz, J., Russell, G., Schmidt, G. & Tausnev, N. (2005). Earth's Energy Imbalance: Confirmation and Implications. *Science*, **308**, 1431–1435. 7

Harries, J. & Crommelynck, D. (1999). The Geostationary Earth Radiation Budget experiment on MSG-1 and its potential applications. *Advances in Space Research*, **24**, 915–919. 27

HARRIES, J., BRINDLEY, H., SAGOO, P. & BANTGES, R. (2001). Increases in greenhouse forcing inferred from the outgoing longwave radiation spectra of the Earth in 1970 and 1997. *Letters to Nature*, **410**, 355–357. 106

HARRIES, J., RUSSELL, J., HANAFIN, J., BRINDLEY, H., FUTYAN, J., RUFUS, J., KELLOCK, S., MATTHEWS, G., WRIGLEY, R., LAST, A., MUELLER, J., MOSSAVATI, R., ASHMALL, J., SAWYER, E., PARKER, D., CALDWELL, M., ALLAN, P., SMITH, A., BATES, M., COAN, B., STEWART, B., LEPINE, D., CORNWALL, L., CORNEY, D., RICKETTS, M., DRUMMOND, D., SMART, D., CUTLER, R., DEWITTE, S., CLERBAUX, N., GONZALEZ, L., IPE, A., BERTRAND, C., JOUKOFF, A., CROMMELYNCK, D., NELMS, N., LLEWELLYN-JONES, D., BUTCHER, G., SMITH, G., SZEWCZYK, Z., MLYNCZAK, P., SLINGO, A., ALLAN, R. & RINGER, M. (2005). The Geostationary Earth Radiation Budget Project. *Bulletin of the American Meteorological Society*, **86(7)**, 945–960. 1, 11, 27

HARRISON, E., MINNIS, P., BARKSTROM, B. & GIBSON, G. (1993). *Radiation budget at the top of the atmosphere. In Atlas of satellite observations related to global change.*, 19–38. Cambridge University Press. 6

HARTMANN, D.L., OCKERT-BELL, M.E. & MICHELSEN, M.L. (1992). The Effect of Cloud Type on Earth's Energy Balance: Global Analysis. *Journal of Climate*, **5**, 1281–1304. 9

HAYWOOD, J., ALLAN, R., CULVERWELL, I., SLINGO, T., MILTON, S., EDWARDS, J. & CLERBAUX, N. (2005). Can desert dust explain the outgoing longwave radiation anomaly over the Sahara during July 2003? *Journal of Geophysical Research*, **110**, D05105. 29, 128

HOLLMANN, R., MULLER, R. & GRATZKI, A. (2006). CM-SAF surface radiation budget: First results with AVHRR data. *Advances in Space Research*, **37**, 2166–2171. 29

IPE, A., CLERBAUX, N., BERTRAND, C., S., D. & GONZALEZ, L. (2003). Pixel–Scale Composite TOA Clear–Sky Reflectances for Meteosat–7 Visible Data. *Journal of Geophysical Research*, **108(D19)**, 4612–4612. 22, 136

IPE, A., CLERBAUX, N., BERTRAND, C., DEWITTE, S. & GONZALEZ, L. (2004). Validation and homogenisation of cloud optical depth and cloud fraction retrievals for GERB/SEVIRI scene identification using Meteosat-7 data. *Atmospheric Research*, **72**, 17–37. 21

IPE, A., BERTRAND, C., CLERBAUX, N., DEWITTE, S. & GONZALEZ, L. (2008). The GERB Edition 1 products SEVIRI scene identification - Part I: Methodology. *IEEE Transactions on Geoscience and Remote Sensing*, **submitted**. 21, 32, 48, 68, 93, 137

JACOBOWITZ, H., SOULE, H.V., KYLE, H.L. & HOUSE, F.B. (1984). The Earth Radiation Budget (ERB) experiment - An overview. *Journal of Geophysical Research*, **89**, 5021–5038. 11

KANDEL, R., VIOLLIER, M., RABERANTO, P., DUVEL, J.P., PAKHOMOV, L.A., GOLOVKO, V.A., TRISHCHENCO, A.P., MUELLER, J., RASCHKE, E., STUHLMANN, R. & THE ISSWG (1998). The ScaRaB Earth Radiation Budget Dataset. *Bulletin of the American Meteorological Society*, **79**, 765–783. 11

KATO, S. & LOEB, N. (2005). Top-of-atmosphere shortwave broadband observed radiance and estimated irradiance over polar regions from Clouds and the Earth's Radiant Energy System (CERES) instruments on Terra. *Journal of Geophysical Research*, **110**, D07202. 18, 141

KEY, J. & SCHWEIGER, A. (1998). Tools for atmospheric radiative transfer: Streamer and FluxNet. *Computers and Geosciences*, **24**, 443–451. 55, 137

KIEHL, J. & TRENBERTH, K. (1997). Earth's Annual Global Mean Energy Budget. *Bulletin of the American Meteorological Society*, **78(2)**, 197–208. 5, 6, 7, 10

KIMES, D. (1981). Azimuthal radiometric temperature measurements of wheat canopies. *Applied Optics*, **20**, 1119–1121. 167

KING, M., KAUFMAN, Y., TANRÉ, D. & NAKAJIMA, T. (1999). Remote sensing of tropospheric aerosols from space: Past, present, and future. *Bulletin of the American Meteorological Society*, **80(11)**, 2229–2260. 57

LE BORGNE, P., LEGENDRE, G. & MARSOUIN, A. (2004). Meteosat and GOES-East Imager Visible Channel Calibration. *Journal of Atmospheric and Oceanic Technology*, **21**, 1701–1709. 37

LEE, H., GRUBER, A., ELLINGSON, R. & LASZLO, I. (2007). Development of the HIRS Outgoing Longwave Radiation Climate Dataset. *Journal of Atmospheric and Oceanic Technology*, **24**, 2029–2047. 13

LINTZ, J. & SIMONETT, D. (1976). *Remote Sensing of Environment*. Addison-Wesley Publishing Company. 53

LIPTON, A. & WARD, J. (1997). Satellite–view biases in retrieved surface temperature in mountain areas. *Remote Sensing of Environment*, **60**, 92–100. 167

LOEB, N., HINTON, P. & GREEN, R. (1999). Top-of-atmosphere albedo estimation from angular distribution models: A comparison between two approaches. *Journal of Geophysical Research*, **104**, 31255–31260. 17

LOEB, N., PRIESTLEY, K., KRATZ, D., GEIER, E., GREEN, R., WIELICKI, B., HINTON, P. & NOLAN, S. (2001). Determination of Unfiltered Radiances from the Clouds and the Earth's Radiant Energy System instrument. *Journal of Applied Meteorology*, **40**, 822–835. 14, 15, 16, 61, 81, 120

Loeb, N., Kato, S. & Wielicki, B. (2002). Defining Top-of-the-Atmosphere Flux Reference Level for Earth Radiation Budget Studies. *Journal of Climate*, **15**, 3301–3309. 46, 141

Loeb, N., Loukachine, K., Smith, N., Wielicki, B. & Young, D. (2003a). Angular distribution models for top-of-atmosphere radiative flux estimation from the Clouds and the Earth's Radiant Energy System instrument on the Tropical Rainfall Measuring Mission Satellite. Part II: Validation. *Journal of Applied Meteorology*, **42**, 240–265. 18, 19

Loeb, N., Smith, N., Kato, S., Miller, W., Gupta, S., Minnis, P. & Wielicki, B. (2003b). Angular distribution models for top-of-atmosphere radiative flux estimation from the Clouds and the Earth's Radiant Energy System instrument on the Tropical Rainfall Measuring Mission Satellite. Part I: Methodology. *Journal of Applied Meteorology*, **42**, 240–265. 12, 18, 19, 20, 67, 135, 136, 140

Loeb, N., Kato, S., Loukachine, K. & Smith, N. (2005). Angular distribution models for top-of-atmosphere radiative flux estimation from the Clouds and the Earth's Radiant Energy System instrument on the Terra Satellite. Part I: Methodology. *Journal of Atmospheric and Oceanic Technology*, **22**, 338–351. 19

Loeb, N., Wielicki, B., Doelling, D., Smith, G., Keyes, D., Kato, S., Manalo-Smith, N. & Wong, T. (2008). Towards Optimal Closure of the Earth's Top-of-Atmosphere Radiation Budget. *Journal of Climate*, **in press**. 7, 43

Lopez-Baeza, E., Alonso, S., Bates, M., Bodas, A., Dewitte, S., Diaz-Pabon, C., Domenech, C., Gimeno Ferrer, J., Harries, J., Jorge, J., Labajo, A., Pineda, N., Pino, D., Rius, A., Rocadenbosch, F., Russell, J., Sicard, M., Smith, G., Szewczyk, Z., Tarruella, R., Torrobella, J. & Velazquez, A. (2004). First GERB/CERES Ground Validation Campaign at the Valencia Anchor Station (Spain). In *Proc. of the 2004 EUMETSAT Meteorological Satellite Conference*. 29

Loukachine, K. & Loeb, N. (2004). Top-of-Atmosphere Flux Retrievals from CERES Using Artificial Neural Networks. *Remote Sensing of Environment*, **93(3)**, 381–390. 19

Manalo-Smith, N., Smith, G.L., Tiwari, S.N. & Staylor, W.F. (1998). Analytic forms of bidirectional reflectance functions for application to Earth radiation budget studies. *Journal of Geophysical Research*, **103**, 19733–19752. 19

Miller, M. & Slingo, A. (2007). The Arm Mobile Facility and Its First International Deployment: Measuring Radiative Flux Divergence in West Africa. *Bulletin of the American Meteorological Society*, **88**, 1229–1244. 29

Minnis, P. & Harrison, E. (1984a). Diurnal Variability of Regional Cloud and Clear-Sky Radiative Parameters Derived from GOES Data. Part I: Analysis Method. *Journal of Applied Meteorology*, **23(7)**, 993–1011. 11

Minnis, P. & Harrison, E. (1984b). Diurnal Variability of Regional Cloud and Clear-Sky Radiative Parameters Derived from GOES Data. Part II: November 1978 Cloud Distributions. *Journal of Applied Meteorology*, **23(7)**, 1012–1031. 11

Minnis, P. & Harrison, E. (1984c). Diurnal Variability of Regional Cloud and Clear-Sky Radiative Parameters Derived from GOES Data. Part III: November 1978 Radiative Parameters. *Journal of Applied Meteorology*, **23(7)**, 1032–1051. 11

Minnis, P. & Khaiyer, M. (2000). Anisotropy of Land Surface Skin Temperature Derived from Satellite Data. *Journal of Applied Meteorology*, **39**, 1117–1129. 167

Minnis, P., Young, D., Wielicki, B., Heck, P., Dong, X., Stowe, L. & Welch, R. (1999). CERES Cloud Properties Derived from Multispectral VIRS Data. In *Proceedings of the EOS/SPIE Symposium on Remote Sensing*, vol. 3867, 91–102. 22

Minnis, P., Gambheer, A. & Doelling, D. (2004). Azimuthal anisotropy of longwave and infrared window radiances from the Clouds and the Earth's Radiant Energy System on the Tropical Rainfall Measuring Mission and Terra satellites. *Journal of Geophysical Research*, **109**. 167

Mlynczak, P., Smith, G., Szewczy, P., Russell, J., Harries, H., Dewitte, S. & Clerbaux, N. (2006). Comparisons of GERB and CERES measurements. In *Proc. 13–th Satellite Meteorology and Oceanography*. 61

Naber, P. & Weinman, J. (1984). The Angular Distribution of Infrared Radiances Emerging From Broken Fields of Cumulus Clouds. *Journal of Geophysical Research*, **89**, 1249–1257. 150, 152

Nakajima, T. & King, M. (1990). Determination of the Optical Thickness and Effective Particle Radius of Clouds from Reflected Solar Radiation Measurements. Part I: Theory. *Journal of Atmospheric Sciences*, **47**, 1878–1893. 53, 139

Nicula, B., Dewitte, S. & Clerbaux, N. (2002). CM-SAF high resolution radiation budget products. In *Proceedings of the SPIE 9th International Symposium on Remote Sensing*, vol. 4882-04. 29

Nowicki, S. & Merchant, C. (2004). Observations of diurnal and spatial variability of radiative forcing by equatorial deep convective clouds. *Journal of Geophysical Research*, **109**, D11202. 29

Ohring, G., Wielicki, B., Spencer, R., Emery, B. & Datla, R. (2005). Satellite Instrument Calibration for Measuring Global Climate Change (Report of a Workshop). *Bulletin of the American Meteorological Society*, **86(9)**, 1303–1314. 2, 14

Otterman, J., Susskind, J., Brakke, T., Kimes, D., Pielke, R. & Lee, T. (1995). Inferring the thermal-infrared hemispheric emission from sparsely-vegetated surface by directional measurements. *Boundary-Layer Meteorology*, **74**, 163–180. 150, 152

Otterman, J., Starr, D., Brakke, T., Davies, R., Jacobowitz, H., Mehta, A., Chéruy, F. & Prabhakara, C. (1997). Modeling Zenith-Angle Dependence of Outgoing Longwave Radiation: Implication for Flux Measurements. *Remote Sensing of Environment*, **62**, 90–100. 20, 150, 152, 164

Pili, P. (2000a). Calibration of SEVIRI. In *Proc. of the 2000 EUMETSAT Meteorological Satellite Conference*, 33–39, Bologna, Italy. 39, 154

Pili, P. (2000b). SEVIRI Instrument Level 1.0 Data. In *Proceedings of the 1st MSG RAO Workshop*, vol. ESA-SP 452, 19–28, Bologna, Italy. 38, 39

Ramanathan, V. & coauthors (2001). Indian Ocean Experiment: An integrated analysis of the climate forcing and effects of the great Indo-Asian haze. *Journal of Geophysical Research*, **106 (D22)**, 28371–28398. 36

Raschke, E., Vonder Haar, T., Bandeen, W. & Pasternak, M. (1973). The Annual Radiation Balance of the Earth-Atmosphere System During 1969-70 from Nimbus 3 Measurements. *Journal of the Atmospheric Sciences*, **30**, 341–364. 21

Ricchiazzi, P., Yang, S., Gautier, C. & Sowle, D. (1998). SBDART: A Research and Teaching Software Tool for Plane-Parallel Radiative Transfer in the Earth's Atmosphere. *Bulletin of the American Meteorological Society*, **79**, 2101–2114. 55, 58, 108, 109

Rieland, M. & Raschke, E. (1991). Diurnal variability of the Earth Radiation Budget: Sampling requirements, time integration aspects and error estimates for the Earth Radiation Budget Experiment (ERBE). *Theoretical and Applied Climatology*, **44**, 9–24. 2

Rigollier, C., Lefèvre, M., Blanc, P., & Wald, L. (2002). The Operational Calibration of Images Taken in the Visible Channel of the Meteosat Series of Satellites. *Journal of Atmospheric and Oceanic Technology*, **19**, 1285–1293. 36, 38

Rossow, W. & Schiffer, R. (1999). Advances in Understanding Clouds from ISCCP. *Bulletin of the American Meteorological Society*, **80(11)**, 2261–2287. 7, 9, 57, 59, 109, 153

Roujean, J.L., Leroy, M. & Deschanps, P.Y. (1992). A bidirectional reflectance model of the Earth's surface for the correction of remote sensing data. *Journal of Geophysical Research*, **97 (D18)**, 20455–20468. 19

Russell, J. (2006). Quality Summary for GERB Edition 1 L2 ARG Product. Reference document, Imperial College. 32, 34, 141

Russell, J., Futyan, J., Allan, R., Harries, J., Slingo, A., Dewitte, S. & Clerbaux, N. (2004). Strategies for determining clear-sky fluxes from GERB data. In *Proc. of the 2004 EUMETSAT Meteorological Satellite Conference*, 490–497. 24

Schmetz, J. & Liu, Q. (1988). Outgoing longwave radiation and its diurnal variation at regional scales derived from Meteosat. *Journal of Geophysical Research*, **93**, 11192–11204. 21

Schmetz, J., Pili, P., Tjemkes, S., Just, D., Kerkmann, J., Rota, S. & Ratier, A. (2002). An introduction to Meteosat Second Generation (MSG). *Bulletin of the American Meteorological Society*, **83**, 977–992. 1, 2, 36, 113

Seemann, S., Borbas, E., Knuteson, R., Stephenson, G. & Huang, H.L. (2008). Development of a Global Infrared Land Surface Emissivity Database for Application to Clear Sky Sounding Retrievals from Multispectral Satellite Radiance Measurements. *Journal of Applied Meteorology and Climatology*, **47**, 106–123. 129, 131, 171

Slingo, A. (1990). Sensitivity of the Earth's radiation budget to changes in low clouds. *Nature*, **343**, 49–51. 9

Slingo, A., Hodges, K.I. & Robinson, G.J. (2004). Simulation of the diurnal cycle in a climate model and its evaluation using data from Meteosat 7. *Quarterly Journal of Royal Meteorological Society*, **130**, 1449–1467. 29

Slingo, A., Ackerman, T.P., Allan, R.P., Kassianov, E.I., McFarlane, S.A., Robinson, G.J., Barnard, J.C., Miller, M.A., Harries, J.E., Russell, J.E. & Dewitte, S. (2006). Observations of the impact of a major Saharan dust storm on the atmospheric radiation balance. *Geophysical Research Letters*, **33**, L24817. 29

Smith, G., Szewczyk, Z., Mlynczak, P., Lee III, R., Wielicki, B., Priestley, K., Harries, J., Dewitte, S. & Clerbaux, N. (2003). Method for comparison of GERB and CERES radiances. In *Proc. 10th Int. Symp. Remote Sensing.*, vol. SPIE 5234. 46

Smith, G.L., Green, R.N., Avis, L.M., Suttles, J.T., Wielicki, B.A., Raschke, E. & Davies, R. (1986). Inversion methods for satellite studies of the Earth Radiation Budget - Development of algorithms for the ERBE mission. *Reviews of Geophysics*, **24**, 407–421. 15

Stubenrauch, C., Duvel, J. & Kandel, R. (1993). Determination of Longwave Anisotropic Emission Factors from Combined Broad- and Narrowband Radiance Measurements. *Journal of Applied Meteorology*, **32**, 848–856. 21, 150, 152, 155

Suttles, J., Green, R., Minnis, P., Smith, G., Staylor, W., Wielicki, B., Walker, I., Young, D., Taylor, V. & Stowe, L. (1988). Angular Radiation Models for Earth-Atmosphere System: Volume I - Shortwave Radiation. Reference Publication 1184, NASA. 11, 19

SUTTLES, J., GREEN, R., SMITH, G., WIELICKI, B., WALKER, I., TAYLOR, V. & STOWE, L. (1989). Angular Radiation Models for Earth-Atmosphere System. Volume II - Longwave Radiation. Reference Publication 1184, NASA. 11, 19, 20, 152, 166

SUTTLES, J., WIELICKI, B. & VEMURY, S. (1992). Top-of-Atmosphere Radiative Fluxes: Validation of ERBE Scanner Inversion Algorithm Using Nimbus-7 ERB Data. *Journal of Applied Meteorology*, **31(7)**, 784–796. 19

SZEWCZYK, Z., SMITH, G. & PRIESTLEY, K. (2005). Validation of Clouds and Earth Radiant Energy System instruments aboard the Terra and Aqua satellites. *Journal of Geophysical Research*, **110**, D02103. 43

TARANTOLA, A. (2005). *Inverse Problem Theory and Model Parameter Estimation*. Society for Industrial and Applied Mathematics. 177

TAYLOR, V.R. & STOWE, L.L. (1984). Reflectance characteristics of uniform earth and cloud surfaces derived from Nimbus-7 ERB. *Journal of Geophysical Research*, **89**, 4987–4996. 17

TOWNSHEND, J., JUSTICE, C., SKOLE, D., MALINGREAU, J.P., CIHLAR, J., TEILLET, P., SADOWSKI, F., & RUTTENBERG, S. (1994). The 1-km AVHRR global data set: needs of the International Geosphere Biosphere Program. *International Journal for Remote Sensing*, **15**, 3319–3332. 67, 136

VELAZQUEZ-BLAZQUEZ, A., CANO, A., DOMENECH, C., FERREIRA, A., VIDAL, S., LOPEZ-BAEZA, E., CLERBAUX, N., DEWITTE, S., GONZALEZ, L., ESTELLES, V., SANCHEZ, J.J., TARRUELLA, R., LOEB, N., PINO, D., RIUS, A., TORROBELLA, J., SMITH, G. & SZEWCZYK, Z. (2007). Simulation of CERES and GERB TOA products over the Valencia anchor station for GERB validation purposes. In *Proc. of the 2007 EUMETSAT Meteorological Satellite Conference (P48)*. 29

VERMOTE, E., TANRE, D., DEUZE, J., HERMAN, M. & MORCRETTE, J.J. (1997). Second Simulation of the Satellite Signal in the Solar Spectrum, 6S: An Overview. *IEEE Transactions on Geoscience and Remote Sensing*, 675–686. 55, 74

VIOLLIER, M., KANDEL, R. & RABERANTO, P. (1995). Inversion and space-time-averaging algorithms for ScaRaB (Scanner for the Earth Radiation Budget). Comparison with ERBE. *Annales Geophysicae*, **13**, 959–968. 15

VIOLLIER, M., KANDEL, R. & RABERANTO, P. (2004). Combination of ScaRaB-2 and CERES with Meteosat-5 to remove time sampling bias and improve radiation budget estimations in the INDOEX region. *Journal of Geophysical Research*, **109**, D05105. 38

WIELICKI, B., BARKSTROM, B., BAUM, B., CHARLOCK, T., GREEN, R., KRATZ, D., LEE, R., MINNIS, P., SMITH, G. & WONG, T. (1998). Clouds and the Earth's Radiant Energy System (CERES): Algorithm Overview. *IEEE Transactions on Geoscience and Remote Sensing*, **36**, 1127–1141. 43

WIELICKI, B., WONG, T., ALLAN, R., SLINGO, A., KIEHL, J., SODEN, B., GORDON, C., MILLER, A., YANG, S.K., RANDALL, D., ROBERTSON, F., SUSSKIND, J. & JACOBOWITZ, H. (2002). Evidence for Large Decadal Variability in the Tropical Mean Radiative Energy Budget. *Science*, **295**, 841–844. 12

WIELICKI, B.A. & GREEN, R.N. (1989). Cloud Identification for ERBE Radiative Flux Retrieval. *Journal of Applied Meteorology*, **28**, 1133–1146. 22, 170

WIELICKI, B.A., BARKSTROM, B.R., HARRISON, E.F., LEE III, R.B., SMITH, G.L. & COOPER, J.E. (1996). Clouds and the Earth's Radiant Energy System (CERES): An Earth Observing System Experiment. *Bulletin of the American Meteorological Society*, **77**, 853–868. 3, 11, 22, 43

WILSON, R. (1993). *Solar irradiance. In Atlas of satellite observations related to global change.*, 5–18. Cambridge University Press. 5

WOICK, H., DEWITTE, S., FEIJT, A., GRATZKI, A., HECHLER, P., HOLLMANN, R., KARLSSON, K., LAINE, V., LOWE, P., NITSCHE, H., WERSCHECK, M. & WOLLENWEBER, G. (2002). The Satellite Application Facility on climate monitoring. *Advances in Space Research*, **30(11)**, 2405–2410. 1, 29

YOUNG, D., MINIS, P., DOELLING, D., GIBSON, G. & WONG, T. (1998). Temporal Interpolation Methods for the Clouds and the Earth's Radiant Energy System (CERES) Experiment. *Journal of Applied Meteorology*, **37**, 572–590. 24

Technical Notes

The technical notes hereafter can be downloaded from the RMIB GERB team web site at the address http://gerb.oma.be in the "Documents" section.

[TN29] Clerbaux, N. (2001). Use of TIGR-3 Atmospheric Profiles as Input for SBDART. Technical Note MSG-RMIB-GE-TN-0029, RMIB.

[TN30] Clerbaux, N. (2005). Generation of a Database of TOA Spectral Radiance Fields. Technical Note MSG-RMIB-GE-TN-0030, RMIB.

[TN31] Clerbaux, N. (2007). Correction of the Dispersion in the GERB's Detector Spectral Response Curves. Technical Note MSG-RMIB-GE-TN-0031, RMIB.

[TN35] Clerbaux, N. (2007). Direct Unfiltering of GERB data. Technical Note MSG-RMIB-GE-TN-0035, RMIB.

[TN38] Clerbaux, N. (2006). Regional Scale Comparison of SSF and ES8 Fluxes from CERES FM2 Instrument in RAPS Mode. Technical Note MSG-RMIB-GE-TN-0038, RMIB.

[TN39] Clerbaux, N. (2006). Proposal to Modify the GERB Longwave ADM. Technical Note MSG-RMIB-GE-TN-0039, RMIB.

[TN41] Clerbaux, N. (1999). Exploiting AVIRIS Data for the Solar Reflected Part of the GERB Ground Segment Validation. Technical Note MSG-RMIB-GE-TN-0041, RMIB.

[TN42] Clerbaux, N. and S. Dewitte (2006). GERB-2 Edition-1 ARG Radiances and Fluxes Intercomparison with CERES SSF Data. Technical Note MSG-RMIB-GE-TN-0042, RMIB.

[TN43] Clerbaux, N. (2007). Equivalence Between the ARG, BARG and HR GERB Formats. Technical Note MSG-RMIB-GE-TN-0043, RMIB.

[TN44] Clerbaux, N. (2008). Impact of the Change in SEVIRI Radiance Definition on the GERB Products. Technical Note MSG-RMIB-GE-TN-0044, RMIB.

Nomenclature

Acronyms

ADM	Angular Dependency Model or Angular Distribution Model
AMMA	African Monsoon Multidisciplinary Analyses
ARG	Averaged Rectified Geolocated level 2 GERB product
ATS	Applications Technology Satellite
AVHRR	Advanced Very High Resolution Radiometer
BARG	Binned Averaged Rectified Geolocated level 2 GERB product
BB	BroadBand
BRDF	Bidirectional Reflectance Distribution Function
BT	Brightness Temperature
CERES	Clouds and Earth's Radiant Energy System
CM-SAF	Climate Monitoring SAF
DC	Digital count
DI	Direct Integration (of the radiance field)
DJF	December + January + February
EOCF	Earth Observation Characterisation Facility
EOF	Empirical Orthogonal Functions
EOS	Earth Observing System
ERB	Earth Radiation Budget
ERBE	Earth Radiation Budget Experiment
ERBE-like	CERES data processed with the ERBE algorithms
ERBS	Earth Radiation Budget Satellite/Sensor
ES8	ERBE-like S8
ESSC	Environmental Systems Science Centre
EUMETSAT	European organisation for the exploitation of meteorological satellites
FM	Flight Model
FOV	Field–Of–View
GERB	Geostationary Earth Radiation Budget
GERB–like	SEVIRI–based estimate of the BB fluxes.
GGSPS	GERB Ground Segment Processing System
GIST	GERB International Science Team

GOES	Geostationary Operational Environmental Satellite
HIRS	High-resolution InfraRed Sounder
HR	High Resolution level 2 GERB product
HRV	High Resolution Visible
IASI	Infrared Atmospheric Sounding Interferometer
IC	Imperial College
IGBP	International Geosphere and Biosphere Program
IMPF	IMage Processing Facility
IODC	Indian Ocean data Coverage
IPCC	Intergovernmental Panel on Climate Change
IR	Infrared
IREMIS	InfraRed EMISsivity
ISCCP	International Satellite Cloud Climatology Project
ITCZ	InterTropical Convergence Zone
JJA	June + July + August
LSA SAF	Land Surface Analysis SAF
LT	Local Time
LUT	LookUp Table
LW	LongWave
MAM	March + April + May
MFG	Meteosat First Generation
MLE	Maximum Likelihood Estimation
MODIS	Moderate resolution Imaging Spectroradiometer
MPEF	Meteorological Product Extraction Facility
MSG	Meteosat Second Generation
MTG	Meteosat Third Generation
MVIRI	Meteosat Visible and InfraRed Imager
NANRG	Non–Averaged Non–Rectified Geolocated level 1.5 GERB product
NASA	National Aeronautics and Space Administration
NB	NarrowBand
NCEP	National Centers for Environmental Prediction
NOAA	National Oceanic and Atmospheric Administration
NPL	National Physical Laboratory
NPOESS	National Polar-orbiting Operational Environment Satellite System
NPP	NPOESS Preparatory Project
NRT	Near Real–Time
NWP	Numerical Weather Prediction
OLR	Outgoing Longwave Radiation (equivalent to the thermal flux)
OSI SAF	Ocean and Sea Ice SAF

PAPS	Programmable Azimuth Plane Scan
PCA	Principal Components Analysis
PFM	Proto Flight Model
PSF	Point Spread Function
RAA	Relative Azimuth Angle
RADAGAST	Radiative Atmospheric Divergence using Arm mobile facility, GERB and Amma STations
RAL	Rutherford Appleton Laboratory
RAPS	Rotating Azimuth Plane Scan
RGP	RMIB GERB Processing
RMIB	Royal Meteorological Institute of Belgium
ROLSS	RMIB On Line Short-term Service
RTM	Radiative Transfer Model
SAA	Solar Azimuth Angle (w.r.t. the North)
SAB	Sorting–into–Angular–Bins
SAF	Satellite Application Facility
SBDART	Santa Barbara DISORT Atmospheric Radiative Transfer Model
ScaRaB	Scanner for Radiation Budget
SD	Standard Deviation
SEVIRI	Spinning Enhanced Visible and InfraRed Imager
SGA	Sun Glint Angle
SON	September + October + November
SRB	Surface Radiation Budget
SSCC	SEVIRI Solar Channel Calibration
SSF	Single Scanner Footprint
SW	ShortWave
SZA	Solar Zenith Angle
TIGR	TIROS Initial Guess Retrieval
TIROS	Television Infrared Observation Satellite
TIS	TOA Incoming Solar (radiation)
TN	Technical Note
TOA	Top Of Atmosphere
TOT	Total (= Shortwave + Longwave)
TOVS	TIROS Operational Vertical Sounder
TRMM	Tropical Rainfall Measurement Mission
TSI	Total Solar Irradiance
UKMO	United Kingdom Met–Office
UMARF	Unified Meteosat Archive and Retrieval Facility.
UTC	Universal Time Coordinated

VAA	Viewing Azimuth Angle (w.r.t. the North)
VIRS	Visible and InfraRed Scanner
VIS	VISisble
VZA	Viewing Zenith Angle
WIN	WINdow
WV	Water Vapor
Symbols	
$< x >$	average value of x
σ	RMS error (= standard deviation)
τ	optical thickness
A	Pseudoabsorptance
Alb	Albedo
F	Flux ($\mathrm{Wm^{-2}}$)
L	Radiance ($\mathrm{Wm^{-2}sr^{-1}}$)
RMS	Root Mean Square ($\sqrt{< x^2 >}$)
Subscripts	
lw	refers to the longwave radiation
sol	refers to reflected solar radiation
sw	refers to the shortwave radiation
th	refers to emitted thermal emission